ENSEMBLE-AVERAGED DYNAMICS OF PREMIXED, TURBULENT, HARMONICALLY EXCITED FLAMES

A Dissertation
Presented to
The Academic Faculty

by

Luke Humphrey

In Partial Fulfillment
of the Requirements for the Degree
Doctor of Philosophy in the
Georgia Institute of Technology School of Aerospace Engineering

Georgia Institute of Technology
May 2017

ENSEMBLE-AVERAGED DYNAMICS OF PREMIXED, TURBULENT, HARMONICALLY EXCITED FLAMES

Approved by:

Dr. Tim Lieuwen, Advisor
School of Aerospace Engineering
Georgia Institute of Technology

Dr. Wenting Sun
School of Aerospace Engineering
Georgia Institute of Technology

Dr. Jerry Seitzman
School of Aerospace Engineering
Georgia Institute of Technology

Dr. Lakshmi Sankar
School of Aerospace Engineering
Georgia Institute of Technology

Dr. Devesh Ranjan
School of Mechanical Engineering
Georgia Institute of Technology

Date Approved: March 29, 2017

To those who lit and carried the torch of knowledge before us

ACKNOWLEDGEMENTS

Although the work of conducting research is often solitary, it would not have been possible without the support and guidance of so many people who have helped me along the way. As an incoming graduate student, Donghyuk Shin was instrumental in introducing me to the obscure world of the level set *G*-equation, oscillating flame holders, and premixed flames. He has provided an always friendly and invaluable source of help, as well as providing the foundation of my work.

My research has also been aided by many of the other students and staff working in our research group, including Alberto Amato, Vishal Acharya, Ben Emerson, Bobby Noble, Chris Douglas, Travis Smith, Ianko Chetrev, Debolina Dasgupta, Vedanth Nair, Sukruth Somappa, Julia Lundrigan, Matthew Sirignano, and Nicholas Magina.

Despite the help of my peers, I am certain I would not be writing these words today without the support and guidance of Dr. Tim Lieuwen, my PhD adviser. His quick insight into research problems, as well as the breadth and depth of his knowledge, is astonishing and inspiring. However, it his kindness and understanding for which I am most grateful, as it was he who convinced me to continue toward a PhD when I was ready to leave, and that more than once.

My parents were both understanding and encouraging when I chose to return to school to earn a second undergraduate degree in a new field, and then continue to graduate school. I cannot thank them enough for all they have done for me. Finally, I must acknowledge my wife, Julia, to whom I owe the deepest debt. Quite simply, without her patience, support, and love I would never would have completed this journey, and quite possibly never started.

Financial support for this work was partially provided by the NASA Aeronautics Scholarship Program through grant number NNX14AE98H, and the Georgia Institute of Technology President's Fellowship.

TABLE OF CONTENTS

LIST OF TABLES

LIST OF FIGURES

LIST OF SYMBOLS AND ABBREVIATIONS

λ_a	acoustic length scale
ω_d	angular forcing frequency
$u_{x,n,s}$	axial, normal, and tangential velocity components, respectively
τ_F	characteristic chemical time scale
τ_t	characteristic turbulent time scale
ξ_1	coherent flame position fluctuation
λ_c	convective length scale
u_c	convective velocity disturbance phase speed
a	coherent forcing amplitude
Da	τ_t/τ_F = Damköhler number, the ratio of the characteristic flow to chemical time
$\mathscr{D}$	diffusion coefficient
$u_{s,eff}$	effective tangential velocity
$\langle C \rangle$	ensemble-averaged flame curvature
$\hat{\varepsilon}_{ref}$	ensemble-averaged flame holder oscillation amplitude, in flame normal direction
$S_{T,Disp/T,C}$	ensemble-averaged, turbulent displacement (*T*,*Disp*) or consumption (*T*,*C*) speed
ε	excitation amplitude
l_0	excitation normalization length
β	flame aspect ratio
s, n, z	flame axis, flame normal, and transverse coordinates

$s_{I,W}$	flame axis integration start location or end (wall) location
FDF	flame describing function
L_f	flame integration length
Σ	flame surface density
FTF	flame transfer function
$FTF_{I/W/S/Tot}$	flame transfer function gain due to the starting correction (I), wall correction (W), consumption speed (S), or the sum of the individual components (Tot)
$\breve{c}$	Favre averaged progress variable
$\vec{u}$	flow velocity
f_0	forcing frequency
f	frequency
$\hat{\xi}'$	Fourier space flame position fluctuation
$\Delta\hat{s}_{I,W}$	Fourier space integration limit start or end correction
A	flame area
l_F	global flame length scale
Q	global heat release rate
$S_{T,GC}$	global turbulent consumption speed
Δh_R	heat of combustion per unit mass
$Q'_{A,S}$	heat release fluctuation due to area (A), or flame speed (S)
ξ	instantaneous flame position
L_{11}	integral length scale
$Ka_{K,\delta}$	τ_F/τ_t = Karlovitz number, a ratio of characteristic chemical and flow times (based on Kolmogorov (K) or reaction zone (δ)

η	Kolmogorov length scale
ℓ_F	laminar flame thickness
S_L	laminar local burning velocity
$\mathscr{L}_M$	laminar Markstein length
σ_M	laminar Markstein number
q'	local heat release rate fluctuation
ΔA	local incremental flame area
p'	local pressure fluctuation
$S_{T,LC}$	local turbulent consumption speed
$\mathscr{L}_i$	losses from acoustic field via path *i*
α	molecular thermal diffusivity
$U_{x,0}$	nominal mean flow velocity
γ	non-dimensional convective velocity disturbance amplitude decay rate
$\vec{n}$	normal vector with regard to the flame
$\mathscr{S}_{T,C}$	normalized ensemble-averaged turbulent consumption speed
$\mathscr{S}_T$	normalized ensemble-averaged turbulent displacement speed
$\mathscr{M}_{T,D/C}$	normalized turbulent displacement (*T*,*D*) or consumption (*T*,*C*) Markstein number
ℓ_δ	reaction zone thickness
$\hat{l}'_{ref}$	reference excitation length
u'	root mean square of the turbulent velocity fluctuation
G	scalar field variable

c	speed of sound
I_0	stretch factor
κ	$(1/A)\,dA/dt$ = stretch rate of flame
St	$\left(f_0 \cdot L_f\right)/u_c$ = Strouhal number
$St_{I/W/L_f}$	$\left(\omega_d \cdot s_{I,W,L_f}\right)/u_{s,0}$ = Strouhal number based on s_I, s_W, or L_f
$\bar{C}$	turbulent flame progress variable
$\lambda_{\xi,t}$	turbulent flame wrinkling length scale
$\sigma_{T,D/C}$	turbulent Markstein displacement (D) speed length or consumption (C) speed length
ΔL_f	two-dimensional flame length fluctuation
ρ	unburned density
$\vec{v}_f$	velocity of flame in laboratory reference frame

Subscripts, Superscripts, and Accents

$\overline{(\ )}$	Average taken over all points of phase
$(\ )_{A,N,T}$	axial, normal, or transverse coordinate system reference
$(\ )_1$	coherent fluctuating component
$(\ )_0$	mean component
$(\ )$	non-dimensional quantity
$\underset{\sim}{(\cdot)}$	reactant-conditioned quantity
$(\ )_2$	stochastic component

$( )_t$ tangential direction along flame

$( )^u$ unburned value

$( )^0$ unstretched or uncurved flame speed

SUMMARY

Increasing awareness of the negative impacts of pollutant emissions associated with combustion is driving increasingly stringent regulatory limits. In particular, oxides of nitrogen, generally referred to as NO_x, now face strict limits. These restrictions have driven development of cleaner burning combustion systems. Because NO_x formation increases significantly at elevated temperatures, one method to reduce NO_x emissions is to burn the fuel at lower temperatures. By premixing the fuel and oxidizer prior to combustion significantly lower flame temperatures can be achieved, with corresponding reductions in NO_x emissions. Unfortunately, premixed combustion systems are generally more prone to potentially problematic feedback between the unsteady heat release from the flame and unsteady pressure oscillations. This self-excited feedback loop is known as combustion instability. Because these oscillations are associated with unsteady pressure fluctuations they can degrade system performance, limit operability, and even lead to catastrophic failure. Understanding combustion instability is the primary motivation for the work presented in this thesis.

The interaction of quasi-coherent and turbulent flame disturbances changes the spatio-temporal flame dynamics and turbulent flame speed, yet this interaction is not fully understood. Therefore, this thesis concentrates on identifying, understanding, and modeling these interactions. In order to address this topic, two primary avenues of research are followed: development and validation of a flame position model and experimental investigations of predicted ensemble-averaged flame speed sensitivity to flame curvature.

First, a reduced order modeling approach for turbulent premixed flames is presented, based on the ensemble-averaged flame governing equation proposed by Shin and Lieuwen [1]. The turbulent modeling method is based on the *G*-equation approach used in laminar flame position and heat release studies. In order to capture the dependence of the ensemble-averaged turbulent flame speed on the ensemble-averaged flame curvature, the turbulent flame model incorporates a flame speed closure proposed by Shin and Lieuwen [1]. Application of the *G*-equation approach in different coordinate systems requires the inclusion of time-varying integration limits when calculating global flame area. This issue is discussed and the necessary corrections derived. Next, the reduced order turbulent modeling approach is validated by comparison with three-dimensional simulations of premixed flames, for both flame position and heat release response. The reduced order model is the linearized, in order to develop fully analytical flame position and heat release expressions. The use of the flame speed closure is shown to capture nonlinear effects associated with kinematic restoration.

Second, the development of and results from a novel experimental facility are described. This facility has the capability to subject premixed flames to simultaneous broadband turbulent fluctuations and narrowband coherent fluctuations, which are introduced on the flame through the use of an oscillating flame holder. Mie scattering images are used to identify the instantaneous flame edge position, while simultaneous high speed PIV measurements provide flow field information.

Results from this experimental investigation include analysis of the ensemble-averaged flame dynamics, the ensemble-averaged turbulent displacement speed, the local ensemble-averaged area and consumption speed, and the dependence of both the

displacement speed and consumption speed on the ensemble-averaged flame curvature. Finally, the flame speed sensitivity to curvature is quantified through calculation of the normalized turbulent Markstein displacement and consumption numbers.

The results show that the amplitude of coherent flame wrinkles generally decreases with both downstream distance and increasing turbulence intensity, providing the first experimental validation of previous isothermal results. The average displacement and consumption speeds increase with downstream distance and turbulence intensity, reflecting the increasing wrinkled flame surface. The ensemble-averaged, phase dependent displacement and consumption speeds demonstrate clear modulation with the shape of the ensemble-averaged flame. Specifically, these turbulent flame speeds increase in regions of negative curvature. For both the displacement and consumption speed, the magnitude of the normalized turbulent Markstein length increases with ratio of the turbulent flame wrinkling length to the coherent wrinkling length when $u'/S_L^0 > 2.5$. For $u'/S_L^0 \leq 2.5$ the trends are less clear due to the presence of convecting disturbances which introduce additional fine scale wrinkles on the flame.

Together the results presented in this thesis provide a foundation for modeling turbulent flames in the presence of quasi-coherent disturbances. The flame position can be modeled using the ensemble-averaged governing equation with the dynamical flame speed closure, and the corresponding heat release can be calculated from the turbulent consumption speed closure. The turbulent Markstein numbers and uncurved flame speed may be extracted from experimental or numerical data.

CHAPTER 1. INTRODUCTION

1.1 Motivation

The ability to control and use fire for cooking, warmth, light, and protection marks a distinct turning point in the development of human civilization. The use of fire by early hominins dates at least to one million years ago, and possibly as long ago as 1.9 million years ago [2]. In fact, it is hypothesized that cooking food may have provided the necessary caloric requirements which enabled the evolution of modern human intelligence in early hominins [3].

More recently, modern humans used fire for the extraction and forming of metals. Although the exact location and date of the first extractive metallurgy is (apparently) contentiously debated, there is evidence of early copper smelting at least as long ago as 7,000 years, near what is now Belovode, in Eastern Serbia [4]. Later use of combustion for metals production allowed the development of bronze, iron, and eventually steel and other metals.

The advent of the industrial revolution in the mid eighteenth century expanded the role of fire and combustion from heating, cooking, light, and smelting to that of an industrial power source. Coal gradually replaced wood and charcoal for metals production, heating, and other uses such as salt production, brewing, and soap-boiling [5]. After the invention of the steam engine, the use of steam power came to replace water and wind power as a primary industrial mover. Further development of the steam engine set the stage for a revolution in transportation in the form of the first steam driven railways and ships. Although the first patent for a gas turbine was also granted during this

period (to John Barber, in 1791), it would be more than a century before practical gas turbines were developed [6].

The importance of combustion further expanded with the invention of the first internal combustion engines and the development of the modern gas turbine engine. Although Frank Whittle's 1930 patent for the first successful gas turbine was intended for aircraft propulsion [7], it was only nine years later, in 1939, that the first electrical power generation gas turbine, providing 4 MWe, was installed in Neuchâtel, Switzerland. Amazingly, this gas turbine set ran until 2002 when the generator broke, and has since been restored as an ASME landmark [6].

Gas turbines are now widely used for aircraft propulsion (i.e. jet and turboshaft engines), marine propulsion, to drive pipeline pumps and other industrial applications, and have even been used to power automobiles and motorcycles [8]. In addition, gas turbines now provide the majority of the electricity generated in the United States.

1.1.1 Environmental Concerns

Despite the great value and utility provided by combustion, growth in the use of combustion systems as a source of motive and industrial power has, unfortunately, also resulted in significant environmental degradation due to pollutant emissions. For gas turbines, the air pollutants of most interest include NO_x (primarily NO, NO_2, and other oxides of nitrogen), unburned hydrocarbons (UHC), particulate matter (i.e. smoke) and CO. In addition, carbon dioxide (CO_2) is of significant concern in regard to global climate change [9, 10].

Another major potential pollutant from combustion is SO_x (i.e oxides of sulphur). However, unlike nitrogen, which makes up the bulk of air, the sulphur which reacts to

form SO_x derives entirely from sulphur in the fuel. Because natural gas contains only trace amounts of sulphur and sulphur compounds [9], it is not a significant concern for natural gas fueled systems. Similarly, reducing fuel-bound sulphur in aircraft jet fuels reduces SO_x emissions from aircraft gas turbines. However, for systems fueled by low-grade fuel oils, SO_x remains a significant pollutant.

The demands of a given application constrain gas turbine operating conditions. For example, flight gas turbine engines are constrained by the necessity of maintaining combustion, at appropriate power levels and with sufficiently fast response time, throughout different phases of the flight as well as preserving engine re-light ability should the engine flameout. These demands result in variations in fuel-to-air ratio, pressure, temperature, and residence time across the operational envelope, which can cause increased pollutant emissions. Similarly, the use of gas turbines in ground-based power generation for load following can require fast power ramp up and operation at off-design conditions.

These primary engine use constraints complicate emissions reduction. For instance, formation of particulate emissions and NOx increases during high-power conditions (i.e. during takeoff), and although modern aircraft gas turbine engines do not emit visible smoke trails, particulate emissions remain of significant concern. Conversely, CO and UHC emissions are most significant at low power conditions [11].

The production and emission of UHCs, particulate matter, CO, and NO_x are all functions of the design of the combustion system. However, although control and mitigation of each of these pollutants remains important, the motivation for this thesis stems most directly from efforts to limit NO_x emissions. Therefore, the following

discussion is limited to NO_x-related health and environmental effects, abatement strategies, and implications on combustor design.

1.1.2 Effects of NOx Pollution on Health and the Environment

Nitrogen oxide emissions from combustion are primarily composed of NO (nitric oxide), but also includes NO_2 (nitrogen dioxide), and N_2O (nitrous oxide). Additional nitrogen oxides, such as N_2O_2, N_2O_3, N_2O_4, and N_2O_5, may be produced, depending on the nitrogen valence state, but are not generally produced in large quantities by combustion processes [12]. Generally, NO and NO_2 are collectively referred to as NO_x. These NO_x compounds are both primary pollutants (i.e. they have direct, negative impacts on the public and environment) and react in the atmosphere with other gases and water to produce different, additional pollutants, as shown in Figure 1.1.

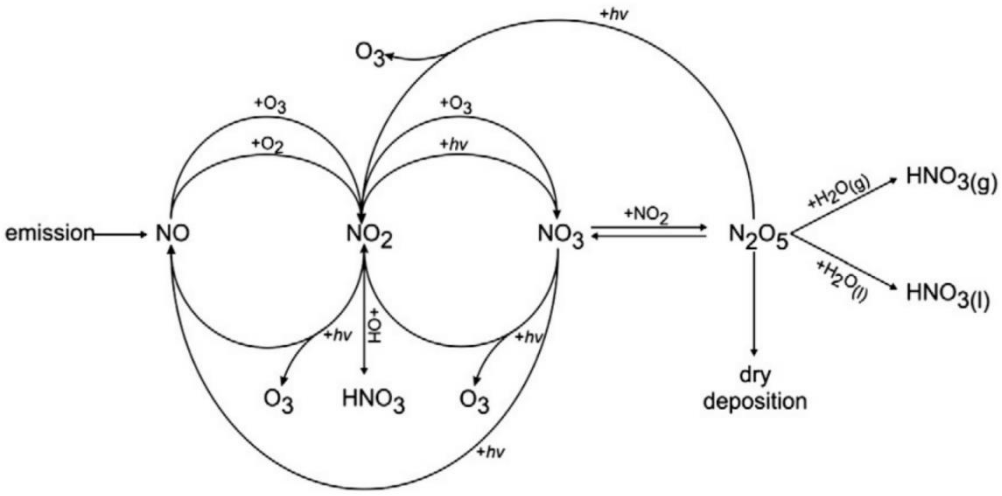

Figure 1.1. Atmospheric NOx pathways, from Skalska et al. [13].

Once emitted into the environment, NO is readily converted to NO_2 by reaction with oxygen. Even in low amounts, NO_2 has direct health impacts, including acute lung

injury, fulminant pulmonary edema, increased likelihood of respiratory and cardiovascular diseases, and associated mortality [13].

Moreover, a variety of secondary reactions produce an array of additional pollutants. Both NO and NO_2 dissolve in water (as in clouds) to produce acid rain, which in turn may cause deforestation and plant death, with potential impacts on agriculture [12, 13]. The action of UV sunlight and volatile organic compounds (VOCs), which are also produced by UV light, with NO_x also causes the formation of photochemical smog. As shown in Figure 1.1 NO and NO_2 are also involved in the production of ground-level ozone, which is a pollutant.

As well as these direct health and environmental impacts, N_2O is a powerful greenhouse gas, with a warming effect 270 times stronger than CO_2 and a half-life of 100 to 150 years [13]. Furthermore, while NO and NO_2 are involved in the *production* of ground-level ozone, N_2O, with its long half-life, can travel to the stratosphere where it reacts with and *destroys* stratospheric ozone, which protects the earth from ionizing radiation.

Clearly, the effects of NO_x emissions are manifold and detrimental to human health and the environment. As a result, the US Environmental Protection Agency (EPA) and other governing bodies have implemented increasingly stringent restrictions for NO_x emissions.

1.1.3 Environmental Regulations

The environmental impact of pollutant emissions from combustion systems, including gas turbines, has motived increasingly stringent environmental regulations. In the United States, the US Environmental Protection Agency, as required by the Clean Air

Act, regulates allowable limits on ambient NO_2 levels, which are measured as a proxy indicator of overall NO_x levels [14].

Similarly, the European Commission has introduced NO_x regulations governing members of the European Union [15]. Increasing environmental concerns in China have also motivated new limits on NO_x emissions from power plants [16]. In the US, the air quality regulations are divided into primary and secondary standards. Primary standards are intended to protect at risk or sensitive populations, including children, the elderly, or individuals with relevant health issues. Secondary standards are intended to protect against general environmental degradation and its impacts, such as haze, and weathering due to acid rain [14]. These standards are summarized in Table 1.1.

Table 1.1. NO2 / NOx allowable limits for the United States [14] and Europe [15].

Regulatory Agency	Averaging Period	Level	Form
US Environmental Protection Agency	1 Hour*	100 ppb	98th Percentile of 1-hour daily maximum concentrations averaged over 3 years; Primary Standard
	1 Year	53 ppb	Annual Mean; Primary and Secondary Standard
European Commission	1 Hour	200 µg/m3 (~100 ppb)	Hourly Mean
	1 Year	40 µg/m3 (~19.7 ppb)	Annual Mean

In the US these regulations have been effective in reducing ambient levels of NO_x as shown in Figure 1.2. In fact, the measured average concentration of NO_x decreased 57% between 1980 and 2014 [17], and average values have been consistently below the national limit standard since circa 1989.

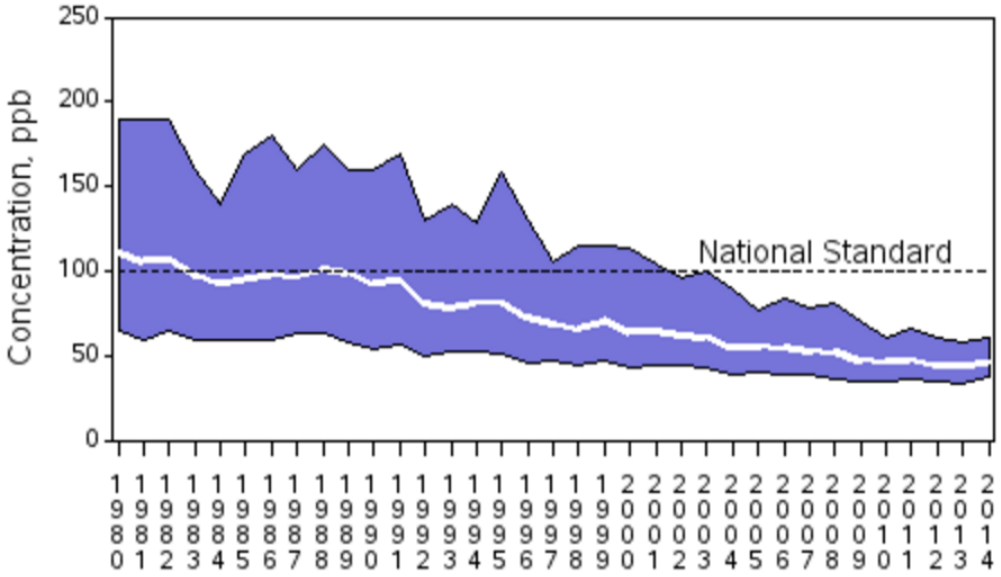

Figure 1.2. NO_2 trends in the United States. The white line indicates the annual 98th percentile for the daily maximum one hour average, based on 26 sites, reproduced from [17].

For ground-based, (particularly coal-fueled) power generation systems, post-combustion exhaust cleaning is widely used to remove SO_x, mercury, and other toxic pollutants. Indeed, this approach is also used in some cases for NO_x abatement, discussed in the following section. However, for aircraft propulsion, such post-combustion pollution control strategies, which typically require large installations as well as injection of additional reducing or sorbent chemicals, are impractical. Thus, pollution mitigation for aircraft propulsion has necessitated carefully designed gas turbine combustors which attempt to *prevent* the formation of pollutants, rather than clean them from combustion products.

1.1.4 NO_x Formation Pathways

The formation of NO_x occurs through four main chemical pathways. These pathways are: 1) the Zeldovich/thermal mechanism, 2) the Fenimore/prompt mechanism,

3) the N_2O pathway, and 4) the NNH pathway [9, 11]. Furthermore, fuel-bound nitrogen, as for coal, can also produce NO_x.

The amount of NO produced by the thermal pathway increases significantly if the flame temperature exceeds 1800 K. The rate limiting step in this pathway depends on the concentration of atomic oxygen, which is an exponential function of temperature. Note that super-equilibrium concentrations of atomic oxygen can be as high as 1000 times the equilibrium concentration [9]. Because of the dependence on oxygen concentration, the amount of NO produced by this pathway is also, essentially, an exponential function of temperature [11] and can increase significantly with atomic oxygen concentration. Yet, despite its importance, the thermal pathway may not be the major NO_x production pathway, particularly for flames with lower peak temperatures (i.e. < 1800K) and low residence times.

A second important pathway is the prompt mechanism, which was discovered due to observations of greater than expected NO concentrations at relatively cold locations, which is unexplained by the thermal mechanism. This pathway depends primarily on the presence of CH radicals which form during hydrocarbon combustion. The CH radicals react with molecular nitrogen to form NCN and H. The NCN then reacts with OH and O to form NO. Because this mechanism depends on the presence of the CH radical, and other hydrocarbon radicals, it is particularly important in fuel rich conditions. This mechanism contributes significantly as burning pockets form [18]. For this same reason, it is not a significant NO source in post-combustion / downstream regions [11].

A third NO_x formation route is the N_2O pathway, which produces both NO and N_2O. This pathway is initiated by the reaction of atomic oxygen with molecular nitrogen,

forming N_2O. The N_2O then reacts with atomic oxygen or hydrogen to form two NO molecules, or an NO and NH molecule, respectively [11]. This pathway is most important for lean, cool flames, because of relatively favorable kinetic formation rates under these conditions. Therefore, this pathway may be a significant source of NO in modern, lean-premixed gas turbines [11].

A more recently discovered pathway is the NNH route. The molecule NNH forms through the reaction of molecular nitrogen and a hydrogen atom. The NNH subsequently reacts with atomic oxygen to form NO and NH. At higher combustion temperatures, NNH is consumed by other reaction pathways, and is therefore less available for the formation of NO, resulting in a relatively small contribution to total NO formation [11]. Yet, combustion modeling with perfectly stirred reactors (PSR) at lean, premixed, pre-vaporized conditions, indicates that the NNH pathway may come to dominate over the other NO formation pathways [18].

1.1.5 NO_x Mitigation and Limiting Strategies

Approaches to controlling NO_x can be broadly categorized into two strategies: those focused on removing NO_x from the combustion products by some type of treatment of the combustion products and those focused on minimizing NO_x production during the primary combustion process itself.

A variety of methods of have been developed to reduce the amount of NO in combustion products. These approaches generally require the addition of some reacting agent. For example, one approach is to chemically reduce NO_x by the use of fuel reburning, whereby additional fuel is introduced into the primary combustion products. This fuel forms hydrocarbon radicals through reactions with oxygen, and these radicals

reduce NO to N_2 and HCN [19]. Alternatively, selective catalytic and selective non-catalytic schemes reduce NO to N_2 by the use of a catalyst or addition of a reacting agent (such as urea or ammonia), respectively [11]. Another approach is to oxidize NO_x compounds by introduction of ozone, a catalyst or other oxidizing agent into N_2O_5, which is more easily removed [12].

Two additional methods are to simply remove the nitrogen from the oxidizer and burn the fuel in a pure oxygen environment. However, this results in very high combustion temperatures which then require cooling / quenching. If the quenching agent contains nitrogen, NO may still be formed. Lastly, NO_x compounds can be sequestered from combustion products using chemicals (sorbents) which absorb NO_x compounds, similar to post-combustion flue gas processing used to remove SO_x compounds. Interestingly, it is sometimes possible to process the used sorbent materials into saleable materials [12].

The second type NO_x control strategy aims to prevent the formation of NO during the primary combustion process. As discussed in Section 1.1.4 above, and shown in Figure 1.3, the formation of NO (and NO_x) during combustion depends strongly on temperature. Thus, an obvious approach to reducing NO_x emissions is to reduce the maximum combustion temperature, or reduce residence time at maximum temperature [11, 12]. As will be discussed further below, reduction of peak temperature is the NO_x abatement method underpinning the motivation for this thesis.

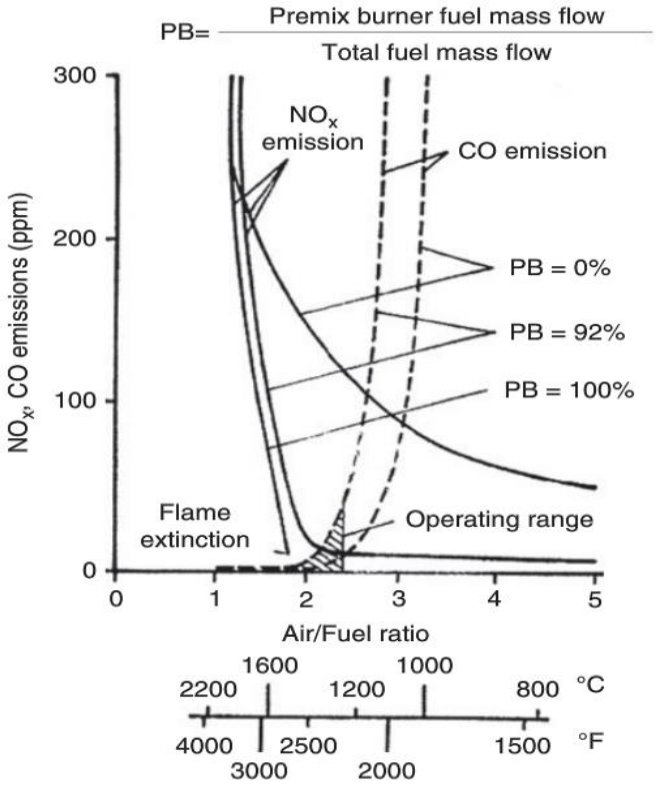

Figure 1.3. NO_x and CO emissions versus temperature and normalized fuel-to-air ratio. PB indicates the degree of premixing, from Gokulakrishnan and Klassen [11], originally in [20].

A variety of methods are available for lowering peak combustion temperatures, particularly in ground-based applications. A straightforward approach is to inject an energy diluting agent, such as water, steam, or cooled exhaust gas recirculation (EGR) [12]. However, injection of water (or steam) can result in reduced efficiencies, and erosion on downstream components. Both EGR and water injection may result in increased CO emissions due to premature quenching during CO burnout [21, 22].

A widely used approach to reducing peak combustion temperatures is to operate at either lean or rich conditions, thereby avoiding the highest combustion temperatures which occur near stoichiometric equivalence ratios. This approach has been used in aircraft combustors in a scheme known as Rich-Quench-Lean (RQL). RQL combustors are designed so that at low power conditions the front of the combustor is near a

stoichiometric equivalence ratio, which helps to prevent blowout. Diluting air is added through liner holes downstream. At high power, the equivalence ratio in the front end of the combustor shifts to a fuel rich condition, with an equivalence ratio near two, and thus a lower peak temperature. The downstream addition of quenching air through the liner holes allows complete combustion. The additional air also increases the temperature, and thus NO formation, but because of the fast mixing, the residence time at this temperature is short, thereby limiting overall NO_x formation [10].

A conceptually related approach known as air staging manipulates the amount of air at different operational points in order to control temperature and pollutant formation. Similarly, it is also possible to manipulate the addition of fuel to avoid peak temperatures and chemistries which produce the greatest NO_x formation [23]. These approaches often incorporate active controls to adjust fuel and air streams in order to achieve stable combustion across the range of operating conditions.

Although all the approaches discussed above provide a means of reducing NO_x emissions, many have specific drawbacks as well. For instance, the use of reducing agents or selective catalytic and non-catalytic approaches have inherent cost and durability issues. The RQL approach may produce excess soot and particulate matter. The drawbacks with these approaches, increasingly strict environmental regulations, and the growth in the use of gas turbines for electrical power generation, have motivated continued work to develop superior methods for NO_x. One approach, now widely used with ground-based power generation is the use of lean, premixed combustion (LPM).

In LPM combustion systems the fuel, if gaseous, is mixed with the oxidizer (typically air) before reaching the combustion zone. The advantages of doing so are

twofold. First, creating a lean fuel-air mixture lowers the theoretical peak combustion temperature. Second, because the fuel-air mixture is fully premixed, there is no opportunity for the formation locally stoichiometric or near stoichiometric pockets of combustion, with their increased temperature and NO_x creation rates [24]. If a liquid fuel is used the fuel must be prevaporized also. Doing so brings attendant challenges, and as of 2013, there are no airplanes which utilize fully premixed combustion [25]. An alternative approach is the use of Lean Direct Injection (LDI), where fuel is injected into a highly turbulent region of the flame. If the turbulence time scale is less than the chemical time scale it is possible to approach something like LPM [23].

The major advantage of LPM combustion systems is that NO_x formed through the thermal mechanism is essentially eliminated [24]. However, (and it is a large 'however', however) LPM systems are prone to combustion instability.

Combustion instability, discussed further in the following section, is a coupling between the fluctuating heat release from the flame and one or more acoustic modes in the combustion environment, which may occur through a variety of pathways. The associated pressure oscillations can increase maintenance expenses, limit operability, induce blow-off or flashback, and in some cases cause severe damage of the combustion system [26]. Better understanding these instabilities provides the motivation for this thesis.

1.2 The Problem of Combustion Instability

As introduced above, combustion instability is a spontaneous, self-sustained coupling between heat release from a flame and the natural acoustic modes of the combustion chamber. This phenomenon has been the focus of significant research efforts

over the past fifty years, and more recently has received a particular focus due to its frequent, detrimental occurrence in LPM combustion systems.

There is a large body of research and a number of review articles and books which examine combustion noise, combustion dynamics, and instability in detail, such as references [26-33]. The following discussion is intended to provide a general background and description of the controlling physics of combustion instability.

1.2.1 A Brief History of Combustion Instability

The first recorded observation (of which I am aware) that flames will produce pure tones in a semi-enclosed chamber occurred in 1777 when hydrogen (only recently discovered) flames in glass tubes were observed to produce 'singing flames' [34]. Later experiments with flames in glass tubes further investigated these curious flame-sound interactions and identified a remarkable number of phenomena important to the modern study of thermo-acoustic oscillations. For instance, John Tyndall discusses the relationship between the natural modes of the combustion chamber and sound produced by the flame, the ability to produce half-tones and over-tones of the natural acoustic modes, the dependence on the position of the flame in exciting these natural modes, and observations of triggering [34]. Similarly, observations of unconfined flames noted the pronounced effect of coherent versus incoherent noise (or vibrations) in eliciting a strong flame response with unconfined flames [35].

Perhaps the most significant contribution from this time period in understanding these combustion instabilities was made by Lord Rayleigh in 1878, who identified a critical relationship between the phase of the heat addition and the phase of the pressure oscillation in the production of sustained instability [36]. This relationship can be

understood as analogous to a simple harmonic oscillator, such as a pendulum. If a force is applied to a pendulum, in the direction the pendulum is moving, as it passes through its lowest point the amplitude of oscillation will be increased. Conversely, if the force is in the direction opposite to that of the pendulum, the amplitude of oscillation decreases.[i] In the case of a flame in an acoustic field, energy is transferred from the flame to the acoustic field when the addition of heat occurs in phase with acoustic pressure oscillations above the average pressure (i.e. when the gas is compressed) [36]. This criterion is now known as the Rayleigh criterion. If the energy added to the acoustic field exceeds or is equal to the dissipative losses, the energy in the acoustic field is sustained or grows in time, respectively [26].

An extended version of this criterion may be expressed mathematically as:

$$\iint_{VT} q'(x,t)p'(x,t)\,dtdV \geq \iint_{VT} \sum_i \mathcal{L}_i(x,t)\,dtdV\ . \tag{1.1}$$

Here, *p'* is the unsteady pressure oscillation, *q'* is the unsteady heat fluctuation, *x*, is the spatial location, *t* is the time, *V* is the volume of the domain, and *T* is the period of the harmonic oscillations. $\mathcal{L}_i$ are the losses associated with a given dissipative path, such as viscous dissipation, convection outside of the combustor environment, and sound emitted [26]. Note that the left hand side of Equation (1.1) is the mathematical expression of Rayleigh's criterion (i.e. energy transfer from the flame to the acoustic field), while the inequality and right hand side provide the necessary requirement for growth in the magnitude of the acoustic oscillations (i.e. energy transfer into the acoustic field must be greater than losses).

---

[i] This may be simply demonstrated using your pocket watch.

The issue of combustion instability moved from arcane if interesting observations of flames in tubes to one of practical necessity as the power of combustion devices increased. In addition to LPM gas turbine systems, combustion instability has been observed in liquid and solid rocket motors, jet engine afterburners, and various industrial burners [26].

One of the best known examples of combustion instability occurred in the famed F-1 liquid-fueled rocket engine, which powered the first stage of the Apollo moon rocket. This rocket engine experienced serious combustion instability problems. Lacking a detailed understanding of the combustion instability, engineers performed approximately 2000 full scale tests specifically to address the problem. Different combinations of fuel and oxygen injector arrangements and baffles added to the injector face were tried (see Figure 1.4), in an attempt to dampen velocity and pressure oscillations. In one configuration, pressure oscillations of 400% of the mean pressure were observed [37]. Needless to say, this type of appraoch is expensive and has motivated research in order to better understand and predict combustion instability during the design process.

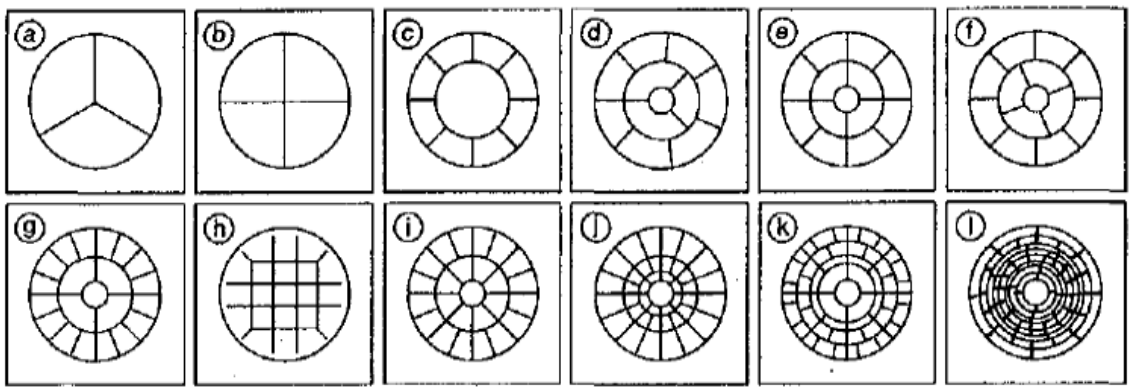

Figure 1.4. Various baffle arrangements tested in order to mitigate combustion instability during development of the F-1 engine, from [37].

Combustion instability has also been an ongoing problem for solid-fueled rocket motors, including the space shuttle rocket booster motor, the Sidewinder air to air missile, the third stage of the Minuteman ICBM, amongst many others. In some cases, the instability is small and may be ignored, but often this is not the case. For example, a 1 psi fluctuation for the space shuttle solid rocket booster results in a 33,000 lbf change in thrust [38].

Interestingly, a clear understanding and full description of the causes of the combustion instabilities observed in many of the solid-fueled rocket motors, as well as for the F-1, was never achieved. Instead, during this period, *ad hoc* methods, such as adding baffles or changing the grain of the solid propellant, often sufficed. Despite these past practical accomplishments, the susceptibility of LPM systems to combustion instability has driven a widespread effort to develop a deeper understanding of this problem, and the ability to predict and avoid combustion instability without performing thousands of full scale tests.

1.2.2 Overview of Combustion Instability Damping Mechanisms and Driving Pathways

Although Equation (1.1) provides a delightfully concise statement of the necessary condition for thermo-acoustic oscillation, a more complete picture of combustion instability requires understanding the mechanisms through which fluctuations in heat release rate and pressure are related. Two important features contained in Equation (1.1) (the extended Rayleigh criterion), which are perhaps not readily obvious, are 1) the necessity of alignment between the phases of the heat release and pressure fluctuations, and 2) the relative magnitude between additions to and losses from the acoustic field.

The alignment of heat release and pressure oscillations in phase space is of primary importance. Specifically, the absolute value difference between the phase of the pressure fluctuation and heat addition must be less than or equal to 90^{o}. Returning to the analogy of the pendulum, this is another way of saying that a driving force will increase the amplitude of the oscillation only when it is pushing in the direction of the pendulum's motion, rather than against it, in which case the amplitude will decrease.

The second feature of Equation (1.1) is that the energy added to the acoustic field must be greater than losses from it. Because combustion instability is composed of thermo-acoustic feedback which occurs at a discrete tone or tones, losses in this context imply the transfer of energy out of the discrete frequency of interest within the control volume [29].

Losses occur through three processes, as discussed in reference [26]. First, acoustic energy can bet transferred to entropy modes or into vorticity modes. This occurs where the acoustic pressure wave interacts with viscous boundaries, and the no-slip boundary condition causes the excitation of vortical disturbances. Additional viscous losses occur at points of sharp change in the geometry, similar to the head losses encountered with flow separation [39]. In addition, the essentially constant wall temperature of a combustor at steady state results in entropy fluctuations where the non-steady temperature fluctuation associated with the acoustic field impinges on the wall. Both of these processes result in a transfer of acoustic energy out of the acoustic field of interest and thus constitute a damping process [26].

Second, acoustic energy can move from one acoustic mode (i.e. a discrete frequency) to another acoustic mode. Although the acoustic energy is not strictly being

damped in such a process, the overall effect may be one of damping if the mode into which the acoustic energy is transferred is not one of the combustor's unstable or amplified modes, in which case it acts as an acoustic energy sink. Alternatively, flame flapping and turbulent eddies can transfer narrowband acoustic energy to broadband acoustic noise, where it is subsequently dissipated [40, 41].

Third, acoustic energy can leave the combustor by radiation out of the control volume, as is the case for emitted sound. Acoustic energy can also convect out of the control volume due to mean flow through the combustor, an effect that increases sharply with increasing Mach number. Moreover, end losses are particularly important, and may dominate over other types of losses, particularly in short ducts (e.g. combustors) [26, 39].

Based upon the above discussion, it may appear that description and prediction of combustion instability is straightforward: determine heat release and pressures oscillation phases and magnitudes and calculate expected losses. Yet, predicting the phasing and magnitude of the pressure and heat release oscillations requires detailed knowledge of the physical pathways which actually link the heat release and pressure fluctuations and vice-versa. To a large degree it is these dependencies which represent the thorniest aspects of combustion instability. The complexity of these interactions is further increased by the introduction of turbulence, which, even by itself, remains an unsolved problem. Despite these challenges, great progress has been made in understanding different the various sounds generation mechanisms and the effects of acoustic pressure oscillations on heat release.

The dominant source of noise in a gas turbine combustor, at low Mach number, is due to the dilation of fluid associated with the heat release during combustion, which acts

as a monopole (i.e. directionless) sound source at points along the flame. In unconfined flames, the sound produced is generally broadband [42, 43]. However, if the flame is confined, such as in a combustion chamber, the broadband noise, which contains significant low frequency content due to the effect of coherent structures, may excite the longitudinal, transverse, or azimuthal natural acoustic frequencies of the duct or convective modes [27, 29, 44].

Fluctuations in heat release ultimately are caused by fluctuations in flow velocity, and thermodynamic variables, such as temperature, density, and pressure. However, it is important to note that in general fluctuations in these variables can result from multiple sources. For example, a vorticity fluctuation will have components arising from acoustic, entropy (i.e. temperature and density), and vortical modes [29]. These different modal components are linearly independent. However, there are variety of ways in which they can couple and interact with one another. For example, in addition to the noise arising from the combustion itself, acoustic fluctuations can also arise when vorticity or entropy fluctuations pass through a flame, or when entropy fluctuations, also resulting from unsteady heat release, are accelerated through a nozzle (as is often the case in a combustor) [27, 29, 45].

In many combustion systems, the global flame length scale, l_F, is much smaller than the length scale of the acoustic disturbances, $\lambda_a = c / f$, where c is the speed of sound and f is the disturbance frequency. When this condition is true, the flame is acoustically compact, with respect to the discrete disturbance. Acoustic compactness greatly simplifies analysis of the flame because the monopole acoustic excitation associated with unsteady heat release is then essentially in phase. That is, the sound

generated by the flame losses its spatial dependence, at points far from the flame (i.e. at distances much greater than the acoustic wavelength). In contrast, if the flame is not acoustically compact, the resulting acoustic field varies spatially, in which case the acoustic waves may interfere constructively and destructively [27]. Furthermore, the coherent effect of acoustically compact pressure and velocity oscillations can increase their ability to modify the flame [28].

Figure 1.5 shows a simplified outline of the feedback pathways which give rise to combustion instabilities in premixed gas turbine systems. Combustion instabilities result from a coupling between driving processes which create acoustic oscillations (shown by the red arrow in Figure 1.5) and coupling processes, which link the fluctuations back to heat release (shown by the green, yellow, and blue arrows).

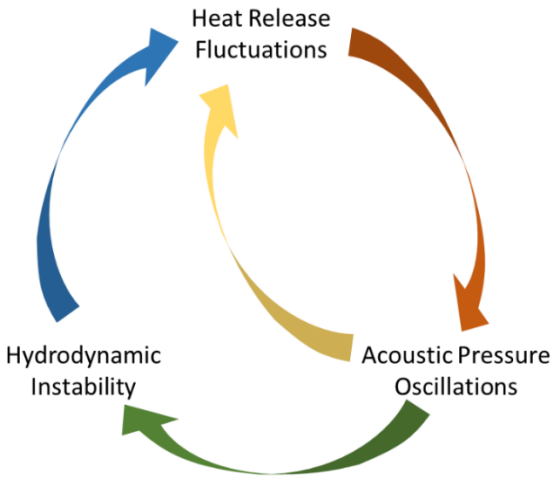

Figure 1.5. Simplified outline of feedback pathways leading to combustion instability.

It is important to note the generally large difference in time and length scales associated with acoustic and convective disturbances. Acoustic disturbances travel at a phase speed equal to the sum of the speed of sound and flow velocity in the direction of propagation, while convective disturbances propagate at approximately the speed of the

mean flow [27]. Because the convective disturbances do not propagate upstream, it is the acoustic field which generally closes the coupling path between convective disturbances and heat release. That is, the acoustic disturbance is able to propagate upstream and thereby trigger a convective disturbance from a heat release oscillation or, conversely, trigger a heat release oscillation from a convective disturbance downstream. Note also that the time delay between the point in time where a convective disturbance is excited to when it interacts with the flame is much longer than the delay associated with an acoustic disturbance [46].

Moreover, the convective length scale $\lambda_c = u / f$ is much shorter than the acoustic length scale, λ_a , such that even for acoustically compact flames, a convective disturbance can retain spatial dependence, with important implications in regard to the phase of heat release oscillations [27, 46].

Pressure and velocity fluctuations associated with the acoustic field alter the flame through two primary mechanisms: by changing the flame reaction rate or heat of reaction directly, or indirectly by changing the global geometry of the flame and thereby changing the surface area of the flame, which is proportional to heat release. The resulting fluctuations in heat release add to the acoustic field if the phase of the unsteady heat release and pressure oscillations are within 90 degrees of one another, as discussed previously.

These two primary pathways are furthermore composed of a variety of sub-pathways, describing specific, individual physical mechanisms. For example, direct changes in reaction rate occur when the acoustic wave passes through the flame zone because of the velocity, pressure, and temperature disturbances associated with the

acoustic oscillation. The temperature and pressure perturbations have a direct effect on the burning rate of the flame, and while the magnitude of this effect is small compared to that associated with velocity disturbances it is likely to satisfy Rayleigh's criterion and contribute to the acoustic field [27]. Thus, while the magnitude of energy transferred into the acoustic field per cycle may be quite small, repeated cycling can quickly amplify the disturbance [47].

Both velocity and density disturbances associated with the acoustic field alter the rate at which reactants are delivered to the flame zone, thereby generating heat release fluctuations. Similarly, convective vorticity disturbances can change the local flame speed due to the associated velocity disturbance. Wrinkles induced on the flame by these vorticity fluctuations also alter the local burning rate due to thermodiffusive stretch effects [27, 48] and discussed further in Section 2.1.3.

In addition to inducing local changes in the burning rate, disturbances associated with entropy, vorticity, and pressure fluctuations can have a secondary effect on the global flame shape by changing the total flame area and/or flame position. That is, changes in flame speed will change the orientation of the flame and the global surface area. Because the surface area is proportional to the heat release, these dependencies introduce a feedback pathway. Furthermore, flame flapping can contribute significantly to area variations, noise production, and heat release oscillations, (including production of disturbances at integer multiples of the forcing frequency), when the flame interacts with a wall [49].

To complicate things further, note that these effects are nonlocal, because changes in the flame position induced at an upstream point are convected downstream. In this

sense, the flame has a memory of earlier perturbations affecting flame speed and shape, and thus the flame response at a given location is the convolution of all upstream flame disturbances as well as any local disturbances [29].

Acoustic pressure oscillations and their associated velocity oscillations can also trigger hydrodynamic instabilities. These large scale coherent motions cause flame wrinkling and resultant heat release oscillations [42, 50]. Additionally, for dump combustors or combustors with bluff bodies, the roll-up of a vortex containing both unburned reactants and hot products may produce a surge in heat release when the vortex interacts with other vortices or walls and the large-scale structures collapses into finer scale turbulence. The frequency of vortex shedding is also affected by the acoustic field, which can cause the collective interaction of vortices, lowering the dominant vortex frequency [51].

Finally, acoustic pressure oscillations in the combustor environment can alter the ratio of fuel to oxidizer upstream, producing equivalence ratio perturbations [46]. When these equivalence ratio perturbations pass through the flame, they alter the heat release both directly and indirectly. Locally, equivalence ratio oscillations change the flame speed and heat of reaction, producing heat release perturbations. Additionally, due to the 'memory' feature of flames subjected to tangential velocity fields (discussed previously), these local perturbations indirectly contribute to heat release oscillations at points downstream on the flame by changing the flame shape [29, 46].

Figure 1.6, adapted from Lieuwen [29], shows a more complete picture of the coupling pathways which link perturbations in pressure, velocity, and equivalence ratio to heat release oscillations, as described above. Clearly, understanding combustion

instability is somewhat more difficult (and conceptually complicated) than simply determining the phase of heat release and pressure oscillations, their magnitude and phase, and their losses; the devil is in the details.

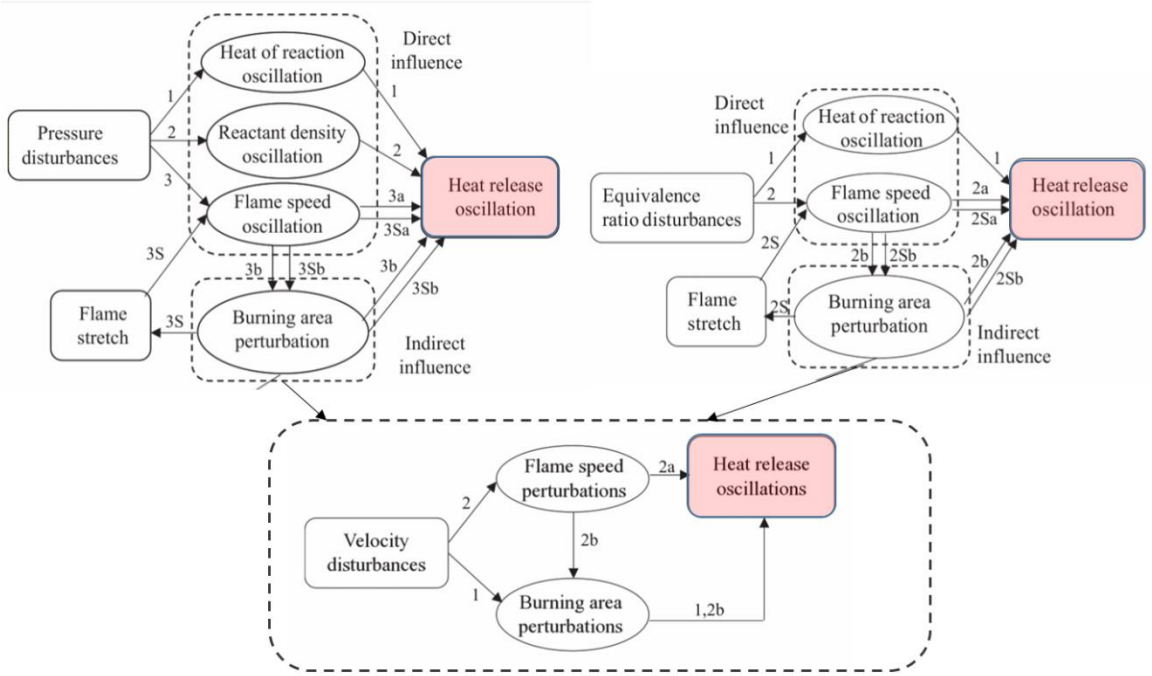

Figure 1.6. Combustion instability pathways showing the acoustic pressure coupling (top left), equivalence ratio coupling (top right), and velocity coupling mechanisms (bottom center), adapted from Lieuwen [29].

Many of the models developed to analyze explicit flame dynamics and heat release response (including some of the work presented in this thesis) assume small perturbation amplitudes so that governing equations can be linearized, greatly simplifying the analysis. However, while the use of the linear approximation makes models more analytically tractable, such models are not generally able to capture non-linear features, including limit cycle amplitudes and nonlinear modal coupling, which occur when disturbance amplitudes become non-infinitesimal. Together, these difficulties and the complexity of the feedback pathways give rise to a very challenging problem.

1.3 Current Work

The work presented in this thesis aims to improve understanding of the response of a premixed flame perturbed by both narrowband harmonic oscillations as well as broadband fluctuations associated with a turbulent flow field. As such, the flame response, both in terms of the spatio-temporal dynamics of flame itself as well as of the heat release dynamics is examined. Because the coherent flame response is obscured by the presence of fine scale turbulence, much of the work presented here makes use of what is termed an 'ensemble average', which is equivalent to the phase average, for harmonic functions.

Chapter 2 provides the background for the following analytical and experimental work, with a literature review of relevant background material. First, an overview of relevant premixed flame dynamics is given, which includes the laminar flame position and heat release response, discussion of the effects of stretch sensitivity, and the hydrodynamic flame instability. Next, premixed turbulent combustion regimes are reviewed in the context of the current work. Then, previous work examining the ensemble-averaged flame response is reviewed. Chapter 2 concludes with a review of turbulent flame speed closures, including the ensemble-averaged curvature dependent closure used throughout this thesis.

Chapter 3 begins with an introduction to the *G*-equation, the fundamental analytical tool used throughout the following work to model ensemble-averaged flame position dynamics, after which a model for heat release is then developed from the *G*-equation flame position model. The implications of the choice of coordinate system when integrating the flame to determine surface area are also discussed. A description of the numerical code used to simulate turbulent, premixed, flames perturbed by harmonic

oscillations of the flame attachment point follows. Numerical results regarding the ensemble-averaged, turbulent, flame position, displacement and consumption speeds, and their sensitivity to ensemble-averaged curvature is then presented.

The results of the numerical simulations are compared with those of a reduced order model derived from the *G*-equation. Several linearized reduced order models are also developed in Chapter 3. These models are also based on the *G*-equation, but unlike those derived in the first part of Chapter 3, assume small perturbation amplitudes, so that the *G*-equation may be linearized. Two models are developed, which examine different forms of harmonic forcing: a convecting, decaying vortex and an oscillating flame attachment point. These models provide closed form solutions for the linearized flame position and heat release fluctuations.

Chapter 4 provides a description of the novel experimental facility developed for this research. This facility produces a premixed, turbulent flame, anchored on an oscillating flame holder. Ensemble-averaged flame shape results are presented for different forcing frequencies and mean flow speeds. The flame shape and flow field results provide the required inputs for calculations of the turbulent displacement and consumption speeds, results of which are given. The dependence of the turbulent displacement and consumption speeds on forcing frequency and turbulence intensity is examined. A physical mechanism is proposed which explains the observed sensitivity.

Chapter 5 provides an investigation of the ensemble-averaged turbulent consumption speed, based on measurements of the flame surface area. A discussion of how the flame areas are extracted is followed by results which show the ensemble-

averaged consumption speed depends on the ensemble-averaged flame curvature similar to the displacement speed examined in Chapter 4.

Chapter 6 provides a summary of the analytical and experimental work and conclusions drawn from it, as well conclusions from this work as a whole. Lastly, some unanswered questions and directions for future research are discussed.

CHAPTER 2. BACKGROUND AND LITERATURE REVIEW

This chapter presents a literature review covering areas relevant to this thesis. First, concepts from premixed flames, including the laminar flame response to harmonic perturbations, and the laminar flame heat release response are reviewed. Following this, stretch effects are reviewed. Next, an introduction to turbulent premixed combustion is presented reviewing the different regimes of turbulent combustion. The modeling approach (i.e. for the ensemble-averaged flame) which provides the foundation for this thesis is then discussed, including previous work investigating the ensemble-averaged response of premixed turbulent flames, both in terms of spatio-temporal flame dynamics, as well as the heat release response. Finally, a review of turbulent flame speed models is given.

2.1 Overview of Relevant Flame Dynamics

2.1.1 Flame Position Response

A significant body or research has focused on understanding the spatio-temporal dynamics of laminar flames, and the key physics controlling the local space-time dynamics of the flame position [52-58] are well understood. A key parameter determining the response of flames to acoustic forcing is the ratio of time scales of the acoustic forcing and flame wrinkling convection times. This parameter is often denoted as a Strouhal (*St*) number, defined as $St = f_0 L_f / u_c$, where u_c is a characteristic convective speed on the order of the mean tangential flow velocity. For values of *St* much less than unity, the flame has sufficient time to respond globally to the acoustic forcing.

In this case, the flame response is equivalent to the flame response for a steady velocity field of the same magnitude, and the flame is said to be ‘quasi-steady’ [29].

For values of *St* greater than unity, there is *insufficient* time for flame wrinkles introduced by the flow disturbances to convect out of the domain, resulting in an increasingly wrinkled flame with increasing forcing frequency. In this case the flame is said to be ‘non-quasi-steady’. For flames subjected to forcing with *St* much greater than unity, significant flame wrinkling can result [55]. In the turbulent case, flames are also perturbed by turbulent flow disturbances with a continuum of times scales. However, the relationship between the acoustic and convective time scales remains fundamentally the same, although the flame length and convection speed may be changed by the introduction of turbulence. Because the focus of this thesis is the interaction of coherent / acoustic flame disturbances with turbulence, the work presented in this thesis is at conditions such that $St > 1$. Thus, the flames examined here are subject to non-quasi-steady effects.

For anchored, premixed flames in tangential flows, the flame response is governed by several factors. First, the fact that the flame is anchored prevents significant flame response in the nearfield. In this region, the response of the flame to a velocity perturbation grows monotonically downstream, and is proportional to the magnitude of the velocity disturbance [56].

Further downstream, the flame response becomes more complicated due to the fact that the flame retains a certain memory of disturbances which have occurred previously and upstream of the local point [52]. Because the phase speeds of the disturbances on the flame and convective flow disturbances may not be equal, the flame

response is subject to constructive and destructive interference effects between convective disturbances and flame wrinkles [54, 59]. As the convective disturbance decays downstream, the amplitude of the flame wrinkles may also decrease [56]. In addition, for a laminar or weakly turbulent flame, wrinkle growth or decay will be influenced by stretch effects [58, 60], as discussed in next Section 2.1.2.

Far downstream, the flame response is dominated by kinematic restoration, which is the smoothing effect caused by flame propagation normal to itself. As such, it is highly nonlinear [57]. This effect is illustrated in Figure 2.1, which shows a schematic of a flame at two instances of time, as well as the contour of constant displacement from the initial location.

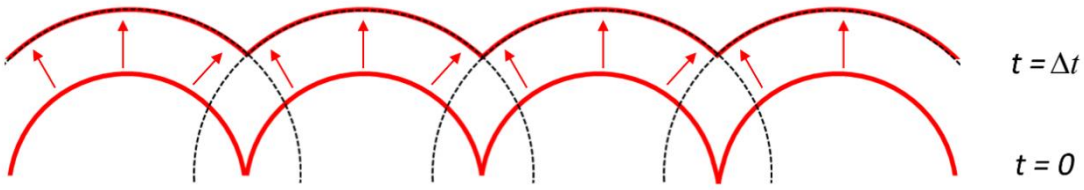

Figure 2.1. Illustration of the kinematic restoration effect, showing how an initially wrinkled flame becomes smoother due to propagation normal to itself. The dashed black lines indicate a position of constant displacement from the initial flame. The maxima (top) of these lines is the flame position.

At points where the flame is cusped towards the reactants, kinematic restoration causes an increase in interference of the flame with itself, annihilation of the flame surface, and a resulting reduction in the amplitude of flame wrinkles [56, 57]. These same processes are also present in turbulent premixed flames, but the situation is further complicated by the interaction between coherent velocity disturbances and stochastic disturbances due to the flow turbulence. The nature and effect of this interaction is the topic of this thesis and will be discussed further throughout the this work.

2.1.2 Laminar Heat Release Response

In addition to the spatio-temporal flame position dynamics, full characterization of the flame response also requires understanding the flames' heat release response [55, 60-65]. The magnitude and phase of the heat release in relation to the magnitude and phase of the incident velocity perturbation is particularly important. The input-output relation between the coherent forcing and the coherent fluctuations heat release is often measured or quantified using Equation (2.1), which denotes the global flame describing function (*FDF*) of a premixed flame. For example, the spatially integrated heat release of a flame forced by flow disturbances:

$$FDF\ \left(a,\omega_d\right)=\frac{\hat{Q}_1/Q_0}{\hat{u}_1/u_0} \tag{2.1}$$

where the $\hat{\ }$ denotes the Fourier transformed variable, $\left(\ \right)_1$ indicates a coherent fluctuation, $\left(\ \right)_0$ the mean value, a is the amplitude of coherent excitation, ω_d is the angular driving frequency, Q is the global heat release, u_1 is the coherent velocity fluctuation. In the linear, small forcing amplitude limit, the *FDF* is amplitude independent and denoted as the global flame transfer function, *FTF*.

As Equation (2.1) shows, the *FTF* or *FDF* is the ratio of the normalized heat release fluctuation, in the frequency domain, to the normalized velocity or other perturbation, where both the heat release and perturbation are normalized by a relevant mean or reference quantity. The *FTF* and/or *FDF* have been widely investigated for laminar flames. For example, Fleifil et al. [55] examined the flame response and laminar *FTF* of a flame in Poiseuille flow, modeling the flow using the level set *G*-Equation approach [66].

Figure 2.2 shows area ratio calculations from Fleifil et al. [55]. Note that if the density, heat of reaction per unit mass, and burning speed are assumed constant, these factors cancel out of the numerator of Equation (2.1), leaving the normalized area fluctuation, as shown in Figure 2.2. One of the key findings of this relatively early study is that the global heat release response has a low-pass filter characteristic. That is, the magnitude of the heat release response decreases with increasing frequency. This can be seen quite clearly in Figure 2.2, and results from the fact that for a fixed velocity, increasing the frequency results in decreasing displacement.

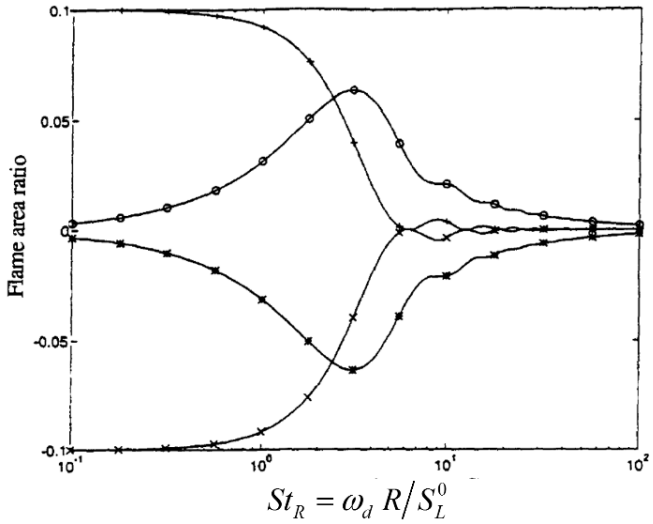

Figure 2.2. The flame area ratio (A_1/A_0) as a function of dimensionless frequency, St_R, reproduced from Fleifil et al. [55].

Numerous works have further developed the methods used by Fleifil et al. [55]. For example, later workers used a different method to solve for an explicit expression for the *FTF* and were able to incorporate larger flame angles[ii] [61]. Prediction of the phase characteristics was subsequently improved by considering a non-uniform, convecting

[ii] Fleifil et al. [55] assumed the flame angle to be very small in order to obtain an explicit expression for the flame position and *FTF*.

velocity disturbance [65]. The approach was then extended to include stretch effects, as discussed in Section 2.1.2, which were found to impact the *FTF* both through changes to the flame shape and area, as well as through direct contribution to the heat release due to flame speed changes at sufficiently high forcing frequency [60]. Santosh and Sujith kinematically coupled the acoustic velocity perturbation with the flame shape, resulting in a refinement of the low frequency response prediction [64].

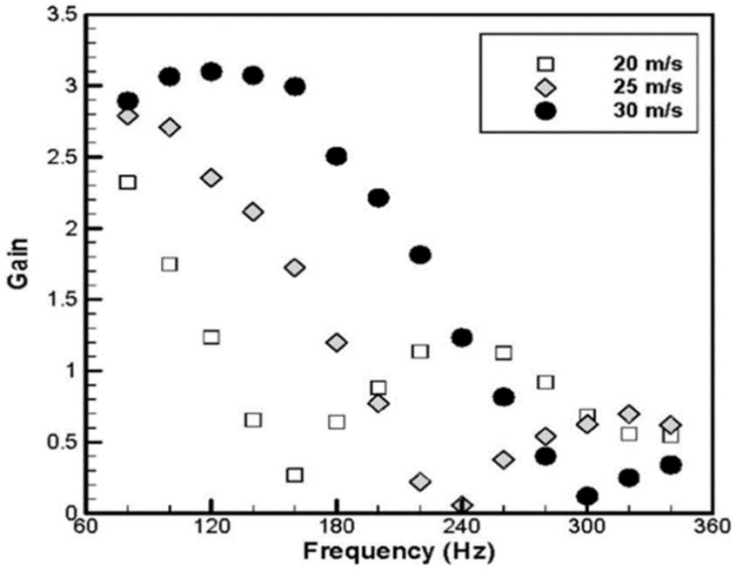

Figure 2.3. Experimentally determined *FDF* gain for a turbulent premixed, swirl-stabilized flame at three mean flow velocities, from Jones et al. [67].

In addition to these laminar studies, The *FTF* and/or *FDF* is what is measured in the numerous data now available on the response of premixed turbulent flames, such as shown in Figure 2.3, to harmonic forcing [31, 67-70]. The turbulent *FTF* is the focus of Sections 3.3.3 and 3.5.

2.1.3 Flame Stretch

Whether laminar or turbulent, premixed flames are subject to hydrodynamic stretch and curvature effects, which can change the local burning rates. Flame stretch

effects result either from changes in the flow velocity tangential to the flame or, if the flame is curved, from the flow and flame velocity normal to the flame. Together, hydrodynamic strain and curvature effects are described by the stretch rate, κ, for weakly stretched flames [29, 71].

$$\kappa = \nabla_t \cdot u_t + \left(\vec{v}_f \cdot \vec{n}\right)\left(\nabla \cdot \vec{n}\right) \tag{2.2}$$

Here, u_t is the flow velocity tangential to the flame, $\vec{v}_f$ is the velocity of the flame in the laboratory reference frame, and $\vec{n}$ is the normal vector on a point on the flame surface. Although termed 'stretch', the quantity described by Equation (2.2) can also be understood as a normalized rate of change in the local flame area. That is, $\kappa = \left(1/A\right) dA/dt$ in the Lagrangian framework. Thus, the first term in Equation (2.2) describes the proportional rate of change in flame area due to flow gradients along the flame, while the second term describes the rate of area change due to changes in the radius of curvature of wrinkled portions of the flame.

Stretch due to either hydrodynamic or curvature effects results in misalignment between convective and diffusive fluxes. The impact of this misalignment on the burning rate depends on the Lewis number, $Le = \alpha/\mathscr{D}$, where α is the molecular thermal diffusivity, and $\mathscr{D}$ is the mass diffusivity, typically of the deficient reactant. To illustrate this effect consider Figure 2.4, reproduced from Lieuwen [29], which shows examples of flame stretch due to curvature and flame stretch due flow strain.

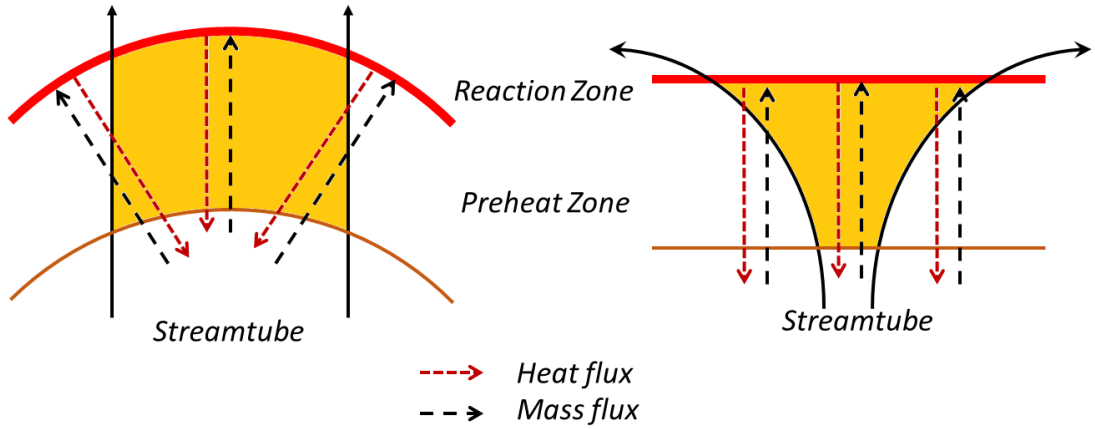

Figure 2.4. Effect of curvature (left) and hydrodynamic stretch (right) in creating misalignment between convective and diffusive fluxes. The black solid arrows indicate the edge of the streamtube, adapted from [29].

If thermal diffusivity is greater than molecular diffusivity (i.e. $Le > 1$) a negatively stretched flame (Figure 2.4, left) experiences a net positive flux of energy into the preheat zone and the reactants arriving at the flame, while a positively stretched flame (Figure 2.4, right) will experience a net loss of energy. This gain or loss of energy from the preheat zone results in a change in the flame temperature, which alters the flame speed. Note that the effects are reversed for a Lewis number less than unity.

The effect of stretch on the laminar flame speed is often modeled simply using either a Markstein length [58], denoted as $\mathscr{L}_M$, or Markstein number, σ_M, i.e.:

$$S_L = S_L^0 - \mathscr{L}_M \kappa \tag{2.3}$$

This equation is often recast in a non-dimensional form by dividing and multiplying the Markstein length and stretch rate by the flame thickness. The stretch rate, κ, is a flow time scale. Thus, this results in dependence on the Karlovitz number (*Ka*), discussed in Section 2.2, i.e.:

$$S_L = S_L^0 \left(1 - \frac{\mathscr{L}_M}{\ell_F} \frac{\ell_F \kappa}{S_L^0} \right) = S_L^0 \left(1 - \sigma_M Ka \right) \tag{2.4}$$

The Markstein number (or length) can be measured from experiments [72, 73] or computations [74]. In addition, analytical models for the Markstein number have been derived. For example, Groot et. al [74] expanded upon Chung and Law's [75] integral analysis, and split the Markstein number, for weakly stretched flames, into contributions due to stretch and curvature. They showed that while the total Markstein number and the curvature Markstein numbers are uniquely defined in terms of unstretched quantities, the strain Markstein number is not unique (i.e. it varies along the flame and with the specific combustion conditions and geometry). Other workers [76, 77] have examined stretch and curvature sensitivity of premixed flames using asymptotic analysis methods (i.e. assuming high activation energy kinetics), finding modification of the flame speed with flame stretch. DNS has been used to investigate unsteady effects on Markstein number [78].

Note also, that while the Markstein number provides a convenient approach to modeling stretch effects, it must be used with care because it depends on the iso-surface used to define the relevant quantities. Nonetheless, the simplicity of the Markstein length / number approach provides a convenient tool for analytical examination of stretch and curvature effects.

2.1.4 Additional Considerations in Turbulent, Premixed Flames

Because turbulent flames in the corrugated flamelets regime are subject to high curvatures and stretching, these thermo-diffusive effects can potentially alter the turbulent burning velocity [28, 79]. In fact, there is evidence that thermal-diffusive effects may be important even at moderate and high turbulence intensity $\left(u'/S_L^0\right)$ values

[79, 80], particularly in hydrogen fueled flames but also possibly for methane-air flames [79, 81, 82]. The interaction of turbulence and Lewis number effects is more pronounced in thermo-diffusively unstable flames where it leads to an increased flame surface area. Therefore, for the range of turbulence intensities and reactant composition (lean methane-air) in this work, thermo-diffusive effects are expected to have a small to negligible impact on the turbulent flame propagation speed and/or its response to curvature because lean methane-air flames have a positive Markstein number, as shown in Figure 2.5, (i.e. they are thermo-diffusively stable) [83, 84].

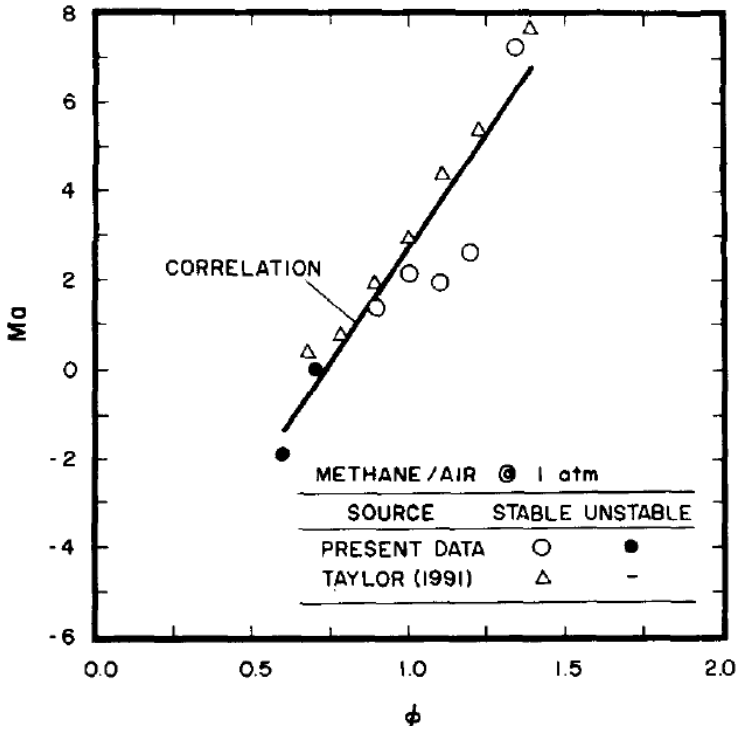

Figure 2.5. Laminar Markstein number for methane-air flames as a function of equivalence ratio, ϕ, at standard temperature and pressure. Reproduced from Tseng et al. [84].

However, because the degree to which these effects change turbulent flame properties, and particularly how they change the response of the ensemble-averaged

flame, remains unsettled in the former and unaddressed in the latter, this effect will be considered further in light of the experimental results given in Chapter 4.

In addition to its relevance in laminar flames, the concept of flame speed dependence on flame curvature can be extended to the ensemble-averaged turbulent displacement speed in turbulent flames. This extension is elaborated in Section 2.4.1.

Another potentially confounding effect is that of the Darrieus-Landau instability which is a hydrodynamic instability resulting from heat release which preferentially slows the flow in front of flame regions convex to the reactants and accelerates the flow in concave regions, resulting in disturbance amplification [85]. However, this effect is greatly reduced when the turbulence $u'/S_L^0 > O(1)$ [79], which is true for all cases examined in this work (See Appendix D). Furthermore, the Darrieus-Landau instability generally produces relatively large scale disturbances which may be on order of 10 cm for atmospheric flames, and this scale is much larger than the scale of flames considered in this work. The potential impact of the Darrieus-Landau instability is discussed further in regard to the experimental flame dynamic results, in Section 4.4.

2.2 Premixed Turbulent Combustion Regimes

Premixed flames are often specified as being either laminar or turbulent. Yet, it is inaccurate to treat all flames in turbulent flows as a well-defined group. This is because turbulence, as a continuum process in terms of length and time scales [86, 87], produces a range of effects on premixed flames. The nature of these effects depends on the relevant length and time scales of the flow and flame. Flames in very weak turbulence may have

more in common with laminar flames than with other turbulent flames in extremely strong turbulence.

One way to understand and delineate the various combustion regimes is through a plot (commonly called a turbulent combustion or Borghi diagram [88]), which compares the length and time sales of the flow to the length and time scales of the flame. Figure 2.6 shows a turbulent combustion diagram. The root mean square of the turbulent velocity fluctuation is u'. S_L^0 is the unstretched laminar burning speed, and L_{11}, ℓ_F, and ℓ_δ are the flow integral length scale, the total flame thickness, and the reaction zone thickness, respectively.

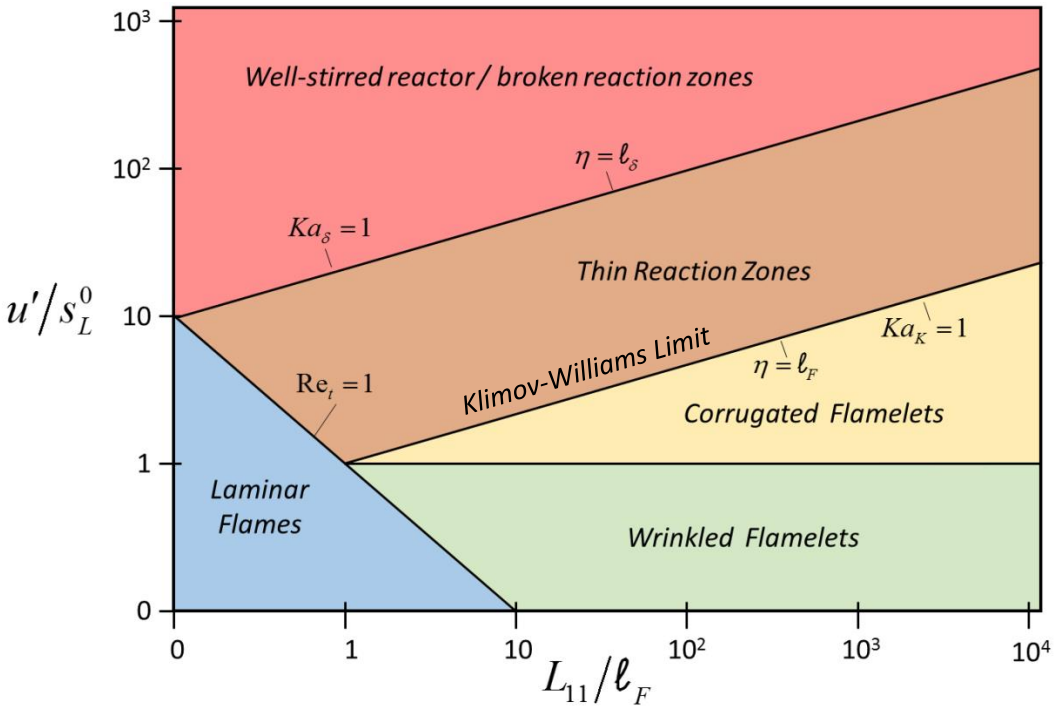

Figure 2.6. Turbulent combustion diagram showing the relation of the laminar and various turbulent combustion regimes to the length scale ratio (x-axis) and time scale ratio (y-axis) of the flow and flame [28, 89].

As shown in Figure 2.6, there are four turbulent combustion regimes, progressing from essentially laminar, but wrinkled flames, to flames subjected to such intense

turbulence that the turbulent time and length scales are both faster and smaller than those of the flame. Like a peach in a blender, the typical diffusive laminar processes are completely disrupted by the turbulence. In addition, Figure 2.6 shows the region (blue) in which laminar flames will exist.

In order to understand Figure 2.6, consider the following time and length scale ratios. First, the Karlovitz number (*Ka*) is ratio of the characteristic chemical time, τ_F, associated with the flame, to the characteristic (in this case turbulent) flow time, τ_t, i.e. $Ka = \tau_F / \tau_t$. Several Karlovitz numbers are shown in Figure 2.6, corresponding to different turbulent scales and flame thicknesses. Note that a similar ratio sometimes used in turbulent combustion diagrams, known as the Damköhler number (*Da*), is ratio of flow time to the characteristic flame time, i.e. $Da = \tau_t / \tau_F$. Thus, it is the inverse of the Karlovitz number.

In the wrinkled flamelets regime (green), the laminar flame speed is greater than the turbulent fluctuations, thus the flame is able to quickly dampen wrinkles introduced on its surface. This precludes large wrinkle formation and thus interactions of the flame with itself. In addition, the turbulent length scale is much larger than the length scale of the flame, and therefore the turbulent eddies are unable to disrupt internal flame processes.

In the corrugated flamelets regime (yellow), the turbulent velocity is greater than the laminar burning speed, while the turbulent length scale remains equal to or larger than all flame length scales. Thus, in this regime, the flame may become highly wrinkled and folded. Moreover, pockets of unburned reactants in the products (or vice-versa) may form due to flame interactions. Because the burning speed is less than the turbulence velocity,

flame wrinkles form faster than they can be smoothed by the flame. To illustrate this, compare the wrinkle formation time $\tau_{\xi,t} = \lambda_{\xi,t}/u'$ with a wrinkle destruction time, $\tau_{F,t} = \lambda_{\xi,t}/S_L^0$. Here, $\lambda_{\xi,t}$ is a turbulent flame disturbance length scale.

If $Da = \tau_{\xi,t}/\tau_{F,t} = S_L^0/u'$ is less than unity the smoothing process associated with flame speed is overwhelmed by turbulent fluctuations. However, because the turbulent eddies remain larger than the flame thickness, i.e. $L_{11}/\ell_F \geq 1$, the turbulent fluctuations are still unable to penetrate the interior of the flame, allowing the flame sheet, though corrugated, to function locally in a manner similar to a laminar flame. Quenching is also theoretically possible at this point due to hydrodynamic stretch effects [29].

The thickened, wrinkled flames regime (shown in brown) is bounded below by a Karlovitz number based on the Kolmogorov time scale and time scale associated with the overall flame, $Ka_K = \tau_F/\tau_K = 1$ line, and above by the Karlovitz number based on the Kolmogorov time scale and flame reaction zone time scale, $Ka_\delta = 1$. The $Ka_K = \tau_F/\tau_K$ ratio can be equivalently expressed in terms of length scales as: $Ka_K = \ell_F{}^2/\eta^2$, where η is the Kolmogorov length scale [86, 89]. Above this line the smallest turbulent length scale is on the order of (or smaller than) the total flame thickness. At this point, the turbulent eddies begin to change the internal structure of the flame directly, and the quasi-steady, laminar nature of flame surface elements is lost [90]. The highly wrinkled, possibly broken flame begins to thicken due to the strong turbulent stirring. However, the reaction zone, which is approximately 10% the thickness of the flame remains intact, as it is still smaller than the smallest turbulent eddies.

As shown in Figure 2.6, the $Ka_K = 1$, is also known as the Klimov-Williams limit. At this limit, steady, laminar flames are expected to extinguish. However, this not the case with turbulent flames, as eddies of this size do not effectively stretch the flame and are quickly dissipated by increased viscosity at the higher temperatures in the flame and reaction zone [29, 91].

The well-stirred reactor / broken reaction zone region is shown in red in Figure 2.6. In this region, the turbulent length and time scales are both smaller and faster than those of the flame. Thus, $Ka_\delta = \tau_\delta / \tau_K \geq 1$. This Karlovitz number is based on the Kolmogorov time scale and a time scale derived from the thickness of the flame reaction zone. Again, this ratio can be equivalently defined as: $Ka_\delta = \ell_\delta^2 / \eta^2$. The laminar flame structure is, in theory, overwhelmed by the turbulence such that the reaction approximates a well-stirred reactor.

Finally, the laminar regime occurs below and to the left of the Re_t=1 line. In this region, the turbulent fluctuations are damped by viscous diffusion. Note that, although the preceding discussion addresses these different regimes as well-defined zones, this is a simplification, and the boundaries shown in the diagram are only approximate. In reality, the thin flamelets regime extends to higher Karlovitz numbers than suggested by the Klimov-Williams limit [91, 92]. In addition, turbulent combustion diagrams assume frozen, isotropic turbulence, limiting the generality of their application. Such diagrams generally do not consider the lifetime of eddies, which on the Kolmogrov scale may be too short to adequately wrinkle the flame [28, 93], while other evidence suggests that quenching due to flame strain occurs prior to development of a distributed reaction regime [94].

The work presented in this thesis examines flames in the corrugated turbulent and thin reaction zones regimes. For numerical and analytical work, examination of flames in the wrinkled and corrugated regimes greatly simplifies analysis of the flame. For $Ka_K \ll 1$ $\left(Da_K \gg 1\right)$, the flame is thin compared to the all flow length scales, and is internally dominated by molecular diffusion rather than turbulent mixing. Thus, the flame essentially acts like a discontinuity in the flow. Furthermore, in the corrugated flamelets regime, order of magnitude analysis indicate that flame speed propagation tends to dominate over diffusive effects [90].

2.3 Ensemble-Averaged Flame Response

Having introduced the turbulent combustion regimes, the response of turbulent flames modelled and analyzed through ensemble-averaging is now addressed. As discussed above, a considerable amount of research has been focused on the response of laminar flames to harmonic flow disturbances, and the key physics controlling both the local space-time dynamics of the flame position [52-58] and spatially integrated heat release [61-64] are well understood. Yet, virtually all practical combustion devices operate in the turbulent regime. If acoustic and/or coherent disturbances are also present, then the flame is simultaneously disturbed by both spatio-temporally narrowband and broad-band turbulence fluctuations.

A large body of research has attempted to understand and predict averaged turbulent burning speeds as reviewed subsequently in Section 2.4 (See also [92]). On the other hand, investigations of the *interaction* between broad-band turbulence and narrowband harmonic disturbances are still relatively sparse, as reviewed below.

Moreover, the turbulent displacement speed is not constant in the presence of harmonic/coherent disturbances, and furthermore, because the flame dynamics are nonlinear, the influence of these disturbances on the flame cannot be treated additively [1, 95-97], but requires a turbulent flame speed model capable of capturing these dynamical effects.

This problem (i.e. the interaction between narrowband coherent disturbances and broadband turbulent disturbances) naturally arises in several applications, such as the general problem of turbulent flames in hydrodynamically unstable flow fields, where significant narrowband energy exists in large scale, organized vortices. Additionally, this problem naturally arises in confined systems which experience thermo-acoustic instabilities, as described in Section 1.2. One approach to studying this interaction is to identify the coherent content of turbulent flames and flow fields. This can be done through the use of the ensemble-average.

In the context of this work (i.e. in the presence of narrowband harmonic content) the ensemble-average is equivalent to a phase average. By sampling either computational or experimental data at specific points of phase during the harmonic cycle, and averaging these samples together, it is possible to recover the ensemble-average. An illustration of this process is shown in Figure 2.7, which plots instantaneous flame edges, determined through Mie scattering, from a turbulent flame at the same point of phase in the forcing cycle as well as an overlay of thirty edges together. The coherent flame wrinkles which are masked in the instantaneous snapshots become obvious when multiple images at the same point of phase are overlaid. That is, the use of the ensemble-average allows

recovery of the coherent content, which may otherwise be obscured by the presence of broadband turbulent fluctuations.

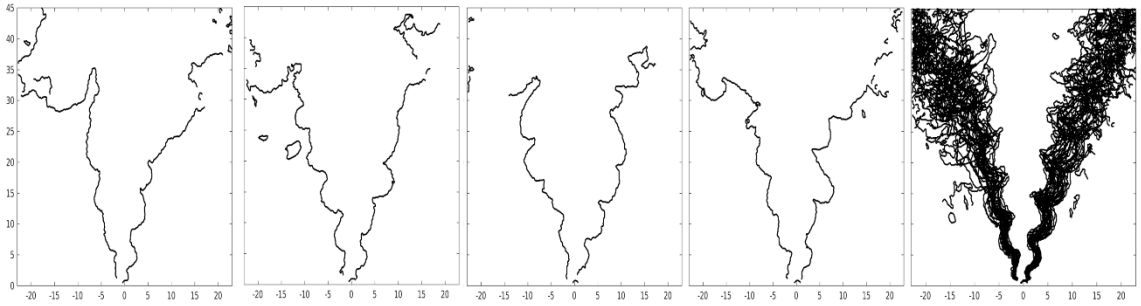

Figure 2.7. Four instantaneous flame edges from a turbulent V-flame, at the same point of phase and an overlay (right) of 30 flame edges from the same point of phase, f_0 = 750 Hz, $U_{x,0}$ = 5.0 m/s, $u'/u_{x,0}$ = 15.1%.

Hemchandra et al. [96] computationally investigated a turbulent, premixed flame perturbed by harmonic, travelling disturbances and presented ensemble-averaged results from these calculations. They found that kinematic restoration (i.e. the smoothing effect of flame propagation normal to itself) diminishes the amplitude of the wrinkles induced by harmonic forcing, and that this effect is enhanced with increasing turbulence, as shown in Figure 2.8. Furthermore, the interaction between the coherent wrinkles due to acoustic forcing and the turbulent fluctuations is not simply additive. That is, the ensemble-averaged flame position differs from the laminar flame position (even with a constant *local* burning speed, S_L). This indicates a non-linear interaction between the coherent and broadband perturbations on the flame. Because of the interaction between the coherent and broadband disturbances, the mean flame position (and flow field) are not equivalent to the nominal base / unforced conditions [95].

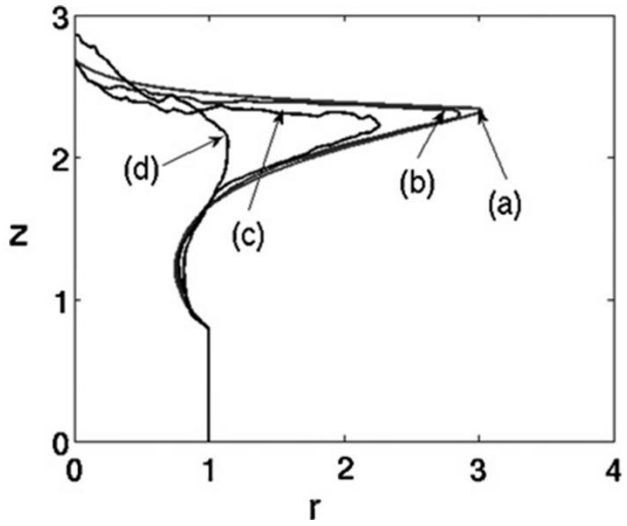

Figure 2.8. Ensemble-averaged flame wrinkle stabilized on a burner lip. The turbulence level increases from (*a*) laminar, to (*d*) $u'/S_L^0 = 2.0$, reproduced from Preetham and Lieuwen [96].

Following this work, Shin and Lieuwen [1] performed a numerical investigation of ensemble-averaged flame sheet dynamics for a turbulent, premixed isothermal flame anchored on a harmonically oscillating bluff body. They were able to further characterize several key effects of turbulence on the ensemble-averaged flame response. First, the introduction of turbulence, as with the study by Hemchandra et al. [96], smoothed the cusps which result from harmonic forcing and reduced the amplitude of coherent flames wrinkles relative to laminar flames.

In the near field, this smoothing is due to phase jitter and kinematic restoration associated with fine-scale turbulent wrinkles. In the far-field, the increase in turbulent flame speed accelerates the smoothing of the large-scale, harmonically induced flame wrinkles. As will be discussed further in Section 2.4.1, the increased rate of wrinkle destruction also has the effect of increasing the displacement speed of the ensemble-averaged flame. This effect can be seen in Figure 2.9, where the simulated turbulent flame is lifted as compared to a laminar flame.

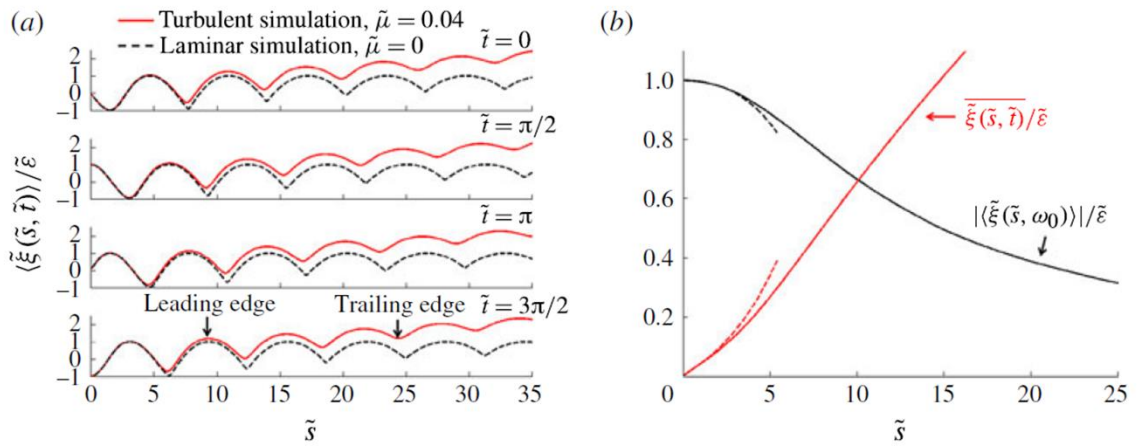

Figure 2.9. Ensemble-averaged flame wrinkles attached to an oscillating flame holder. (*a*) illustrates the smoothing effect of turbulence (b) illustrates the decrease in flame wrinkle amplitude and the simultaneous increased displacement of the mean flame location. $\tilde{\xi}$, $\tilde{\varepsilon}$, and $\tilde{s}$, are the non-dimensional ensemble-averaged flame fluctuation, harmonic excitation amplitude and flame coordinate, respectively. Figure reproduced from Shin and Lieuwen [1].

In addition to the flame position response, Preetham and Lieuwen [96] also examined the area ratio response. As noted previously for laminar flames, if the heat of reaction per unit mass and local burning speed are assumed constant, a ratio of flame areas is equivalent to the heat release ratio. The results of their study indicated that the introduction of turbulence reduced the area ratio response of the ensemble-averaged flame and also changed the phase response [96].

Subsequently, Hemchandra et al. [95] assessed the heat release response through an asymptotic analysis of turbulent and acoustic fluctuations. In support of the previous findings, they determined that the ensemble-averaged heat release response is affected by the introduction of turbulence, even to first order in turbulence intensity as compared to the laminar heat release response. They attributed this effect to kinematic coupling between the acoustic and turbulent fluctuations due to kinematic restoration [95].

In sum, these results show that when premixed flames are perturbed by both narrowband coherent and broadband turbulent disturbances the flames' response is

changed nonlinearly, both in terms of the flame position, as well as the area and heat release response.

2.4 Turbulent Flame Speed Models

In laminar, premixed flames, the displacement speed describes the rate at which an isosurface propagates, such as a temperature or species mass fraction contour, defined with respect to either the burned products or unburned reactants. This propagation velocity is a function of the balance between convective fluxes into the preheat zone, diffusive heat and species fluxes out of the reaction zone and heat release and chain branching reactions in the reaction zone [85]. The high temperature and radical concentrations result in strong gradients which drive diffusion toward the unburned reactants, igniting them and causing the flame to propagate. Due to the dependence on reaction rate and diffusion rate, this process depends on the temperature, pressure, flow field, and composition of reactants [9, 48].

Predictions of turbulent flame speed have long occupied a significant position in combustion research. A variety of models, some phenomenological, some empirical, and some theoretical, (as well as different combinations of these) have been proposed. The primary goal of these turbulent flame speed models has been to develop the tools to reliably predict turbulent flame dynamics and heat release. Although significant progress has been made in this area, a fully general model of turbulent combustion has yet to be developed; this is a formidable task.

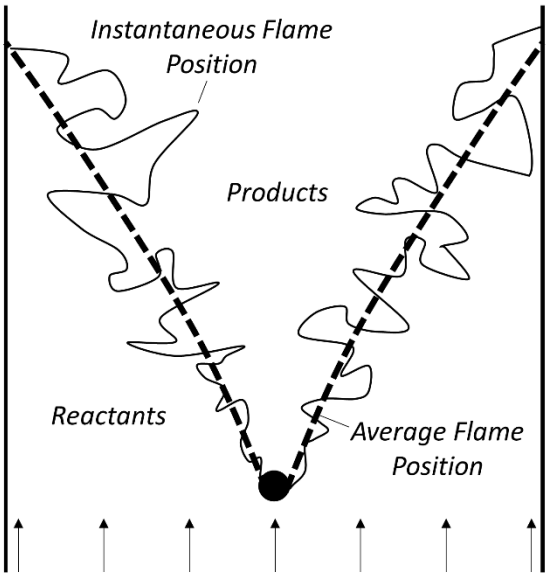

Figure 2.10. Schematic representation of the instantaneous and time averaged flame position of a confined, turbulent V-flame.

For flamelets in the wrinkled and corrugated regimes, the turbulent burning speed depends strongly on the total flame surface area. To see this, consider Figure 2.10 which shows a cartoon of the instantaneous and time averaged flame position for a turbulent V-flame spreading from its attachment point to the wall. Convecting downstream from the flame holder, the flame becomes progressively more wrinkled by turbulent fluctuations, greatly increasing the surface area. If the instantaneous flame propagates at a constant local speed, S_L, and the reactants are assumed to have a constant density, ρ^u, mass conservation provides the following global relationship, assuming the flame consumes all the reactants.

$$\dot{m} = \rho^u S_L A_{I,T} = \rho^u S_{T,GC} A_0 \tag{2.5}$$

Here, $\dot{m}$ is the mass flow rate through the flame, $A_{I,T}$ is the instantaneous turbulent flame area, $S_{T,GC}$ is the turbulent, global consumption speed, and A_0 is the area of the average flame. Equation (2.5) can be rearranged to provide a definition for the

normalized turbulent global consumption speed in terms of the mean and instantaneous flame areas, giving:

$$\frac{S_{T,GC}}{S_L} = \frac{A_{I,T}}{A_0} \tag{2.6}$$

Even if the assumptions in Equation (2.6) are relaxed (e.g. non-constant local burning velocity), the importance of the increase in flame area due to wrinkling clearly remains critical.

Recognizing this area dependence, Damköhler [98] proposed one of the first turbulent flame speed models for flames in the thin flamelet regime, based on the idea that the effect of turbulent eddies is predominantly kinematic and creates a series of conical flame elements, similar to the flame produced by a Meker burner. Thus, he related the ratio of the turbulent and laminar areas to the ratio of the velocity fluctuation and laminar flame speed, i.e.:

$$\frac{A_{I,T}}{A_0} = \frac{S_{T,GC}}{S_L} \propto \frac{u'}{S_L} \tag{2.7}$$

A number of workers have proposed refinements on this basic relationship, as discussed in references [9, 28, 89, 93, 99-101]. These improved relationships generally take the form [28]:

$$\frac{S_{T,GC}}{S_L^0} = 1 + \alpha \left(\frac{u'}{S_L^0} \right)^n \tag{2.8}$$

Here, α and n are empirical constants with values near unity. Other models of this type incorporate the turbulent length scale, burner geometry, or a Markstein length in order to make the correlation more robust.

Despite the large number of these type of models, and their wide use, they have not succeeded generally in accurately predicting the turbulent flame speed without adjustment of various coefficients, and there is wide scatter in the derived scaling exponents. Driscoll [92] argues that this shortcoming is due to an implicit assumption contained in this type of model, namely that the turbulent flame speed is a function of local quantities only, and primarily of *u'*. However, Verma and Lipatnikov [101] argue that the observed scatter does not necessarily completely undermine the concept of a well-defined turbulent flame speed, as measured turbulent flame speeds depend strongly on the measurement methods used in their determination.

The notion of a universal, well-defined flame speed is called into doubt because it takes a finite amount of time and/or distance for a flame to become wrinkled by turbulent fluctuations (as well as for wrinkles to decay). For example, the instantaneous turbulent flame area increases with distance from a flame holder for anchored flames and with time from initiation for spherically expanding flames.

This effect can be seen in Figure 2.11, which shows the results of a DNS computation for an anchored flamed. Because of this dependence the flame speed cannot depend only on local quantities. Moreover, for flames subject to tangential flow, the flame retains a 'memory' of events which occur upstream. That is, if the flame is perturbed at some upstream point, the resulting flame perturbation will convect downstream and alter the instantaneous turbulent area at a removed point and time, again casting doubt on flame speed correlations based purely on local properties.

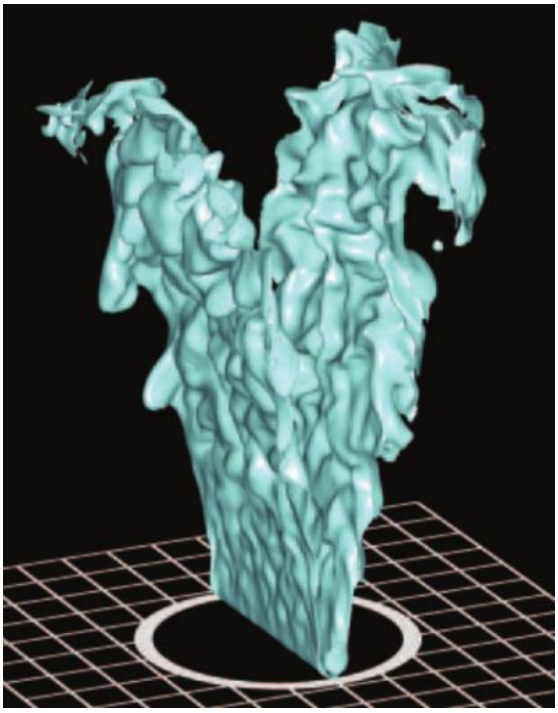

Figure 2.11. DNS visualization of a bluff-body anchored flame in a turbulent field, showing the increase in wrinkling which occurs with distance from the anchor point. The surface is determined from the local temperature gradient, from [102].

Similar correlations have also been adapted for use in the thin reaction zones regime to model the local effect small scale turbulent motions on the local flame consumption speed, $S_{T,LC}$. At the small scales the effect of turbulence is to increase the thermal diffusivity and thereby increase the reaction rate. For example, Zimont and Battaglia [103] assumed that the small scale wrinkles on the flame reach statistical equilibrium (analogous to turbulent equilibrium) and use the following model for sub-grid turbulent flame speed in a RANS/LES computation:

$$\frac{S_{T,LC}}{S_L^0} = \mathscr{A}\left(\frac{u'}{S_L^0}\right)^{1/2}\left(\frac{u' \cdot L_{11}}{\alpha^u}\right)^{1/4} \tag{2.9}$$

The constant $\mathscr{A}$ is adjustable here ($\mathscr{A}$ ~0.5), and α^u is the molecular thermal diffusivity of the reactants.

In this application, the flame speed model given in Equation (2.9) is used to model the dynamics of a Favre averaged progress variable field, i.e.:

$$\frac{\partial \bar{\rho}\breve{c}}{\partial t} + \nabla \cdot \left(\bar{\rho}\breve{c}\breve{\vec{u}} \right) = \underbrace{-\nabla \cdot \overline{\left(\rho c'' \vec{u}'' \right)} + \bar{\rho}\breve{W}}_{\text{Unclosed Terms}} = \underbrace{\nabla \cdot \left(\bar{\rho} D_t \nabla \breve{c} \right) + \rho^u S_{T,LC} \left| \nabla \breve{c} \right|}_{\text{Model Closure Terms}} \qquad (2.10)$$

where the $(\bar{})$ indicates a time average, $(')$ a fluctuating quantity, $\breve{c}$ is the Favre average progress variable, and W is the chemical source term. The first of the unclosed terms describes turbulent transport of the scalar progress variable, while the second is the chemical source term. In a separate but related paper, Zimont [104] points out that while many flame speed models assume some equilibrium balance between flame area creation and destruction, most practical combustors do not operate in this regime, but rather have continuously increasing flame brush thickness. That is, residence times are too short to allow this fully-developed equilibrium to occur. This implies, again, that the flame speed model needs to be non-local.

Note that this approach, (where the probability of mean temperature, density, and other conditional quantities are modeled in terms of a progress variable), derives from the well-known Bray-Moss-Libby (BML) formulation [105, 106] which has been widely used [28, 99, 106].

In addition to the correlation methods, and the BML approach, turbulent flame speeds have also been modeled using an approach known as flame surface density modeling. Marble and Broadwell [107] first introduced this method for diffusion flames in the fast chemistry limit (i.e. flamelet regime) for their work on Project Squid (a rocket engine development program). In this method, area increase due to turbulence and the reaction rate per unit area are treated essentially independently. The turbulent flame

speed can be determined from the turbulent flame area multiplied by the rate of reactant consumption per unit area.

One of the major advantages of the flame surface density approach is that it is not a fully local model. Instead, the flame surface density, $\sum$, which is the amount of flame area contained within a unit volume, is modeled using a partial differential conservation equation of the form [92, 107]:

$$\frac{\partial \sum}{\partial t} + u\frac{\partial \sum}{\partial x} + v\frac{\partial \sum}{\partial y} = \upsilon_T \frac{\partial^2 \sum}{\partial y^2} + \bar{\kappa}\sum - \bar{M} - \bar{Q}_e \tag{2.11}$$

The left-hand side describes convection of flame surface by the flow. In the first term on the right-hand side, υ_T is the turbulent viscosity, and the full term describes dissipation of flame surface area due to turbulence. The second term predicts creation of flame area due to stretching. The third term on the right hand side, $\bar{M}$, describes flame area destruction due to flame merging, and $\bar{Q}_e$ describes loss of flame surface area due to flame quenching [91]. Once the flame surface density is known, it can be multiplied by a stretch factor, I_0 [92, 108], which describes the enhancement of the burning rate due to stretch. The flame speed is recovered by integrating through the flame, i.e.:

$$S_{T,LC} = S_L^0 I_0 \int_{-\infty}^{\infty} \sum(\chi) d\chi \tag{2.12}$$

The flame surface density method also does not directly describe the propagation speed of an iso-contour. Rather, it describes the local turbulent consumption speed, or, when integrated, the global turbulent consumption speed.

Similarly, the turbulent flame speed may be estimated from measured experimental flame areas, similar to the model given in Equation (2.12). This approach is

adopted in Chapter 5, for an investigation of the ensemble-averaged turbulent consumption speed. Note that the preceding discussion of turbulent flame speed models is by no means comprehensive, but lays the groundwork for the following research presented in this thesis. Additional discussions of the turbulent flame speed may be found in references [28, 89, 92, 99] for example.

2.4.1 Turbulent Flame Speed Closure for the Ensemble-Averaged Turbulent Flame

Before continuing to the next chapter, a final flame speed model is introduced. The problem of combustion instability in turbulent combustors, discussed in Section 1.2, directly motivates the development of this model, which was proposed by Shin and Lieuwen [1]. This flame speed closure model is introduced here but will be further discussed in the following chapters.

It is important to point out that the flame speed models introduced above, with the exception of the flame surface density approach, are intended to predict an *average* turbulent flame speed based on relevant statistics of the flow. That is, these models represent an attempt to model the propagation speed of some average iso-contour, as shown in Figure 2.10. Furthermore, these models do not capture (or attempt to capture) any dynamical effects due to the spatio-temporal dynamics of the iso-contour on which they are based. In effect, they are largely independent of the flame.

Note that depending on how the flame surface generation, destruction, and merging terms in Equation (2.11) are modeled, it may be possible to capture some dynamical effects, as well as the convective nature arising from the terms on the left hand side of the equation. However, the flame surface density approach requires the solution to

the additional PDE (i.e. Equation (2.11)) as well as modeling the aforementioned flame surface area generation and destruction terms, increasing computational demands.

In contrast, Shin and Lieuwen's model [1] attempts to model the propagation of a time or phase *dependent* iso-contour, the speed of which depends not only on statistics of the flow but also on shape of the iso-contour itself, and does so using a simple reduced order model which does not require solution of any additional equations. This flame speed closure is intended to capture the interaction of the broadband, fine scale perturbations due turbulence and the narrowband perturbations resulting from harmonic disturbances of the flame or flow field, on the ensemble-averaged (i.e. phase averaged) flame surface.

This problem occurs in several applications, such as the general problem of turbulent flames in hydrodynamically unstable flow field and also arises in confined systems which experience thermo-acoustic instabilities, which can result from the self-excited feedback between heat-release and narrow-band acoustic oscillations [31-33], as discussed in Chapter 1.

The interaction between turbulent and harmonic perturbations is modeled through the use of a flame speed closure expression analogous to that of stretch sensitive laminar flames, i.e.:

$$S_{T,Disp}(s,t) = S^0_{T,Disp}(s)\left(1-\sigma_{T,D}(s)\left\langle C(s,t)\right\rangle\right) \tag{2.13}$$

Here, $S_{T,Disp}$ is the ensemble-averaged turbulent displacement speed, where the angle brackets henceforth indicate an ensemble-averaged quantity. This is the speed at which the ensemble-averaged flame propagates into the ensemble-averaged velocity field. The quantity $S^0_{T,Disp}$ is the unperturbed, ensemble-averaged turbulent displacement speed,

$\sigma_{T,D}$ is the turbulent Markstein length, which quantifies the dependence of the turbulent ensemble-averaged displacement speed on the curvature of the ensemble-averaged flame, $\langle C \rangle$. As discussed above, the turbulent Markstein number may vary as a function of the turbulent intensity, turbulent length scale, spatial location, or other statistics of the flow.

Lipatnikov and Chomiak [109] have previously introduced a similar concept, also denoted as a turbulent Markstein number, in their study of expanding spherical turbulent premixed flames. In this study they compared predicted and measured flame radii from [110], finding linear growth in the flame speed with time due to flame brush development and the average (i.e. global) stretch due to the flame curvature. For weakly globally stretched flames, they found a nearly linear dependence of the flame speed on the turbulent Markstein number [109].

The dependence of the ensemble-averaged turbulent displacement speed on the ensemble-averaged flame curvature is predicated on the annihilation of flame surface area which occurs when flamelets merge due to kinematic restoration, introduced for laminar flames in Section 2.1.1. The kinematic restoration effect is enhanced by the presence of turbulence [96]. To understand this more clearly, consider Figure 2.12 which shows a depiction of a turbulent flame subjected to positive, zero, and negative curvatures.

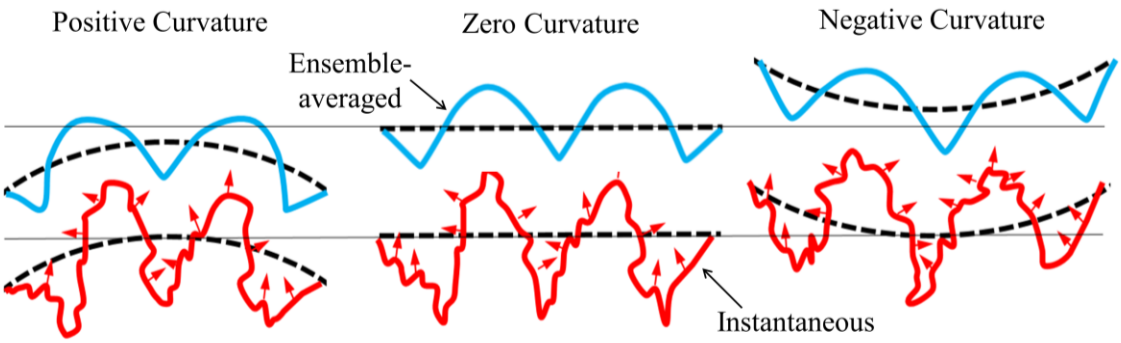

Figure 2.12. Schematic of the interaction of narrowband flame curvature with broadband turbulent wrinkling, following Shin and Lieuwen [1].

Large scale negative flame curvatures (i.e. *concave* towards the reactants) resulting from harmonic oscillations are expected to cause an increase in the turbulent burning speed because in these regions the flame is essentially facing itself and, due to the normal propagation of the flame surface it quickly intersects the opposing flame surface, wherein both flame surfaces are annihilated. In contrast, this effect is decreased in flat and positively curved flames. The overall result is that a negatively curved flame is excepted to propagate further into the reactants than a flat or positively curved flame. This model forms the basis of the following work presented in this thesis.

CHAPTER 3. MODELING THE RESPONSE OF TURBULENT FLAMES TO HARMONIC FORCING

As discussed in Chapters 1 and 2, thermo-acoustic oscillations are a key motivator for this work, as these self-excited oscillations involve the feedback of narrowband acoustic oscillations with vortices and the flame [26, 30, 42]. The least understood part of the internal feedback loop leading to these oscillations is how flames respond to these narrowband oscillations.

Chapter 2 introduced the laminar flame position and heat release response, and as discussed previously, a significant literature now exists on the response of laminar flames to harmonic flow disturbances. The key physics controlling both the local space-time dynamics of the flame position [52-54, 56, 57, 111] and spatially integrated heat release [55, 61, 62, 65] is well understood.

However, real flames, in most practical combustion systems, exist in a turbulent flow environment and so the flame is simultaneously disturbed by both spatio-temporally narrow and broadband disturbances. Because the flame dynamics are nonlinear, the influence of these disturbances on the flame cannot be treated additively [1, 95, 96].

This chapter describes an analysis of the ensemble-averaged flame position and heat release dynamics of harmonically forced, turbulent, premixed flames, and was presented in reference [112]. The chapter starts with the development of the *G*-equation, which is the basis for most of the analysis in this thesis. After this development, the problem of determining the global surface area of premixed flames is discussed. Specifically, a subtle, but important issue regarding the use of different coordinate

systems is explained and resolved. Next, a description of the ensemble-averaged flame position equation and its use in defining the ensemble-averaged turbulent flame speed are given. The problem geometry, introduced above, is then elaborated on, followed by a description of the numerical procedure, and an explanation of the calculation of the global heat release. Validation of the proposed flame speed closure and modeling approach is provided by a direct comparison of the flame shape and heat release between the numerical simulation and the analytical model in Section 3.4. The use of the flame speed closure is further examined with two model problems in Section 3.5: (1) the development of a linear model from the general analytical model presented in Section 3.4 and (2) application of these results to a flame perturbed by a convecting, decaying vortex. A discussion of the results is also given in Section 3.5, while Section 3.6 presents conclusions from this work.

3.1 Modeling Approach

3.1.1 The G-Equation

This section introduces the primary analytical tool, the *G*-Equation, used throughout this thesis to analyze the flamelet dynamics, flame area, and as the basis of the definition for the ensemble-averaged turbulent flame speed, discussed in Section 3.2.1.

This approach is commonly used in studies of flame kinematics [54, 55] and is well-developed [68, 113-116]. For high activation energy molecular kinetics, the flame becomes thin relative to the scales of the flow and can be treated as a flow discontinuity. Following the derivations given by Lieuwen [29] and Markstein [66], an implicit and explicit governing equation for premixed flames can be derived. In this approach, the

flame is defined as the location of the zero surface in a scalar variable field, denoted by G, i.e.:

$$G(\vec{x},t)=0 \tag{3.1}$$

This definition is shown schematically in Figure 3.1, where the value of G decreases towards the reactants.

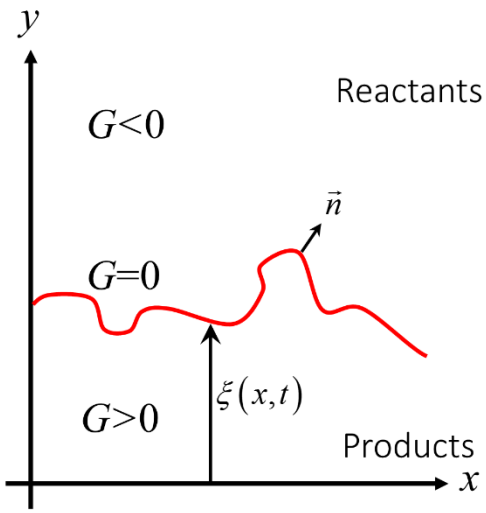

Figure 3.1. Schematic illustration of the variation of G and definition of the flame.

Because $G = 0$ at all locations on the flame by definition, if one follows a Lagrangian flame packet it can be seen that:

$$\frac{D}{Dt}G(\vec{x},t)\Big|_{Flame}=0 \tag{3.2}$$

This expression can be expanded in an Eulerian frame as:

$$\frac{\partial G(\vec{x},t)}{\partial t}+\underbrace{\left(\vec{\boldsymbol{u}}^{u}+S_L\bullet\vec{n}\right)}_{\vec{v}_f}\bullet\nabla G(\vec{x},t)=0 \tag{3.3}$$

where $\vec{\boldsymbol{u}}^{u}$ is the unburned flow velocity at the flame front and S_L denotes the *local* propagation front speed, with respect to the reactants, and $\vec{v}_f$ is the speed of the flame in

the laboratory frame. The unit vector normal to the flame, pointing towards the reactants, is $\vec{n}$. Equation (3.3) shows that *G* is not only convected by the flow, but also propagates at some velocity, S_L. The unit vector normal to the flame, $\vec{n}$, may be defined in relation to the gradient of the *G* field as:

$$\vec{n} = -\frac{\nabla G}{|\nabla G|} \tag{3.4}$$

Then, substituting Equation (3.4) into (3.3) and rearranging provides a useful form of the *G*-equation:

$$\frac{\partial G}{\partial t} + \vec{\boldsymbol{u}}^u \cdot \vec{\nabla} G = S_L \left| \vec{\nabla} G \right| \tag{3.5}$$

For a single valued flame position, this implicit equation can be further refined using a change of variables to obtain an explicit governing equation for the premixed flame position. Note, however, that the computational results shown later in this chapter, do not assume a single valued flame position. Defining $G \equiv \xi(x,z,t) - y$, and substituting into Equation (3.5), this equation can be written as:

$$\frac{\partial \xi}{\partial t} + u_x \frac{\partial \xi}{\partial x} - u_y + u_z \frac{\partial \xi}{\partial z} = S_L \left[1 + \left(\frac{\partial \xi}{\partial x} \right)^2 + \left(\frac{\partial \xi}{\partial z} \right)^2 \right]^{1/2} \tag{3.6}$$

Equation (3.6) provides an explicit governing equation for the instantaneous flame position. Here, the flame position equation is defined on a coordinate system oriented along the *x*, *y* coordinate system, but it is also possible to define the equation on a coordinate system based on the mean flame position. The left-hand side describes how the flame sheet is convected by the flow, while the right-hand side describes the flames propagation normal to itself towards the reactants. The strong nonlinearity inherent in

premixed flame dynamics derives from the kinematic restoration effect described by the right-hand side of Equation (3.6).

3.1.2 Coordinate Systems, Integration Limits, and End Corrections

Before continuing to a discussion of the calculation of the heat release response from the numerical results, a subtlety of integrating the surface area of confined flames and the appropriate resolution is examined. Specifically, this subsection describes the influence of coordinate systems and integration limits on global *FTF* calculations [63]. Here also, the front tracking approach (i.e. the *G*-Equation approach, as given in Equation (3.5)), forms the basis of the flame response modeling.

As shown in Figure 3.2, and discussed in the previous section, $G(\vec{x},t)$ can be written as an explicit flame position, ξ, by defining the location of the instantaneous flame sheet with respect to some coordinate system.

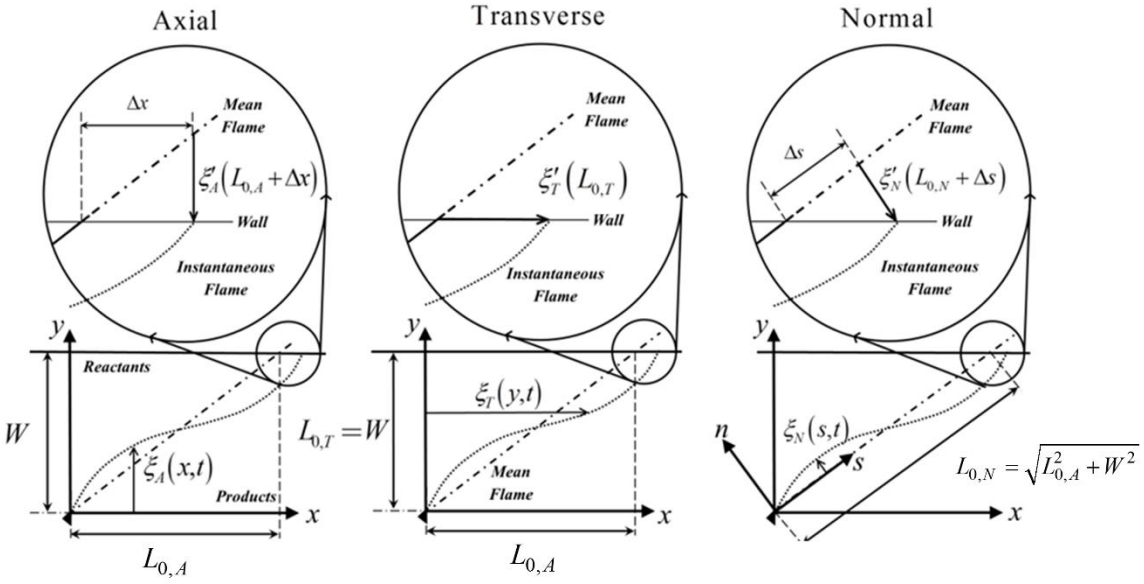

Figure 3.2. Schematic of coordinate systems, direction of flame dependence and end correction factor.

For example, past studies have defined the flame position with respect to the axial coordinate [56, 59], transverse coordinate [55, 117, 118] or in a coordinate system normal to the time averaged flame position [1, 53, 65]. To illustrate, the resulting expression written in the axial coordinate system is:

$$\frac{\partial \xi_A}{\partial t} + u_x \frac{\partial \xi_A}{\partial x} - u_y + u_z \frac{\partial \xi_A}{\partial z} = S_L \left[\left(\frac{\partial \xi_A}{\partial x} \right)^2 + \left(\frac{\partial \xi_A}{\partial z} \right)^2 + 1 \right]^{1/2} . \quad (3.7)$$

Here, $\xi_A \equiv \xi_A(x, z, t)$. The reasons for using different coordinate systems depend upon the particular focus of the study. The majority of studies have used a transverse coordinate system. However, Schuller *et al.* [65], Lieuwen [29], and Preetham *et al*. [53] used the normal coordinate system for their discussion of the local space-time dynamics of the flame sheet, as they are most naturally evident in that coordinate system. Shin *et al.* [59] and Shanbhogue *et al.* [56] used the axial coordinate system for their study of the growth and decay of the flame response, as the position of shallow angle flames remains a single valued function of the coordinate for much larger amplitudes in that coordinate system.

For linearized flame area dynamics, the flame area transfer function is defined as:

$$FTF(\omega_d) = \frac{\hat{A}_1(\omega_d)/A_0}{\hat{u}_{1,ref}/u_0}, \quad (3.8)$$

where $\hat{u}'_{ref}$ denotes the "reference" excitation velocity, such as the velocity at the flame base. The instantaneous flame area is given by:

$$A(t) = \int_0^{L(t)} dA(t) \quad (3.9)$$

The leading order perturbation to this flame area is given by:

$$A'(t) = A(t) - A_0 = \underbrace{\int_{L_0}^{L(t)} dA_0}_{\substack{\text{Length fluctuation} \\ \text{of unperturbed flame}}} + \underbrace{\int_0^{L_0} dA_1}_{\substack{\text{Area fluctuation due to} \\ \text{perturbations of base flame}}}, \tag{3.10}$$

whose frequency domain equivalent for a two-dimensional domain in the different coordinate systems is:

$$\hat{A}'_{Axial}(\omega_d) = \underbrace{\left[\frac{1}{\beta^2}+1\right]^{1/2}\Delta\hat{x}}_{\substack{\text{Length fluctuation} \\ \text{of unperturbed flame}}} + \underbrace{\left[1+\beta^2\right]^{-1/2}\int_0^{L_{0,A}} \frac{\partial \hat{\xi}'_A}{\partial x}dx}_{\substack{\text{Area fluctuation due to} \\ \text{perturbations of base flame}}}, \tag{3.11}$$

$$\hat{A}'_{Transverse}(\omega_d) = \underbrace{\frac{\beta}{\sqrt{\beta^2+1}}\int_0^{L_{0,T}} \frac{\partial \hat{\xi}'_T}{\partial y}dy}_{\substack{\text{Area fluctuation due to} \\ \text{perturbation of base flame}}}, \tag{3.12}$$

$$\hat{A}'_{Normal}(\omega_d) = \underbrace{\Delta\hat{s}}_{\substack{\text{Length fluctuation} \\ \text{of unperturbed flame}}}. \tag{3.13}$$

where $\beta = L_{0,A}/W$, and Δx and Δs are shown in Figure 3.2. The differences between Equations (3.11), (3.12), and (3.13) reflect the way first order area fluctuations manifest in the different coordinate systems. In the axial coordinate system, first order area fluctuations occur over the length of the base flame *and* in the oscillating integration limit. In the transverse coordinate system, there is no variation in integration limit; first order area fluctuations manifest entirely along the base flame. In the normal coordinate system there is no variation in base flame position with downstream coordinate. That is, $\partial\xi_{N,0}/\partial s = 0$, eliminating area fluctuation contributions along the base flame; area fluctuations are manifest entirely in the oscillating integration limit.

It seems intuitive that a global quantity such as flame area should be invariant of the coordinate system. *However, the solution to these expressions are completely*

different, depending upon integration limits. For example, if the integration limits are assumed to be constants, and equal to a fixed axial distance, $L_{0,A}$ (the flame height), transverse distance, *W* (flame width), or flame length, $\sqrt{L_{0,A}^2+W^2}$, then three different answers are obtained for the *FTF*. To illustrate, consider the solution of eqn. (3.8) using these fixed integration limits for a two dimensional geometry, and the excitation of the flame by bulk axial forcing, a problem originally solved by Fleifil *et al.* [55] in the transverse coordinate system:

$$FTF_{Axial} = -\frac{2}{St_A}\frac{1}{\left(\beta^2+1\right)}\sin\left(\frac{St_A}{2}\frac{\beta^2+1}{\beta^2}\right)e^{i\frac{St_A}{2}\frac{\beta^2+1}{\beta^2}} \tag{3.14}$$

$$FTF_{Transverse} = \frac{2}{St_A}\frac{\beta^2}{\left(\beta^2+1\right)}\sin\left(\frac{St_A}{2}\frac{\beta^2+1}{\beta^2}\right)e^{i\frac{St_A}{2}\frac{\beta^2+1}{\beta^2}} \tag{3.15}$$

$$FTF_{Normal} = 0 \tag{3.16}$$

where $St_A = \omega_d L_{0,A}/u_0$. Note that the transverse and axial *FTFs* differ by a factor of $\left(-\beta^2\right)$, while the *FTF* is identically zero for the normal coordinate system (the area contribution arising at higher order). For this reason, Schuller *et al.* [65] and Preetham *et al*. [53] worked in a normal coordinate system when analyzing the local space time flame dynamics, but reverted to a transverse coordinate system for finding the flame area.

It is important to recognize that all of these solutions are correct within the approximations of the fixed integration limits; *the fact that they are different arises from the fact that they are all solutions to different problems*. For example, a problem where the transverse integration limit is fixed necessarily involves an oscillatory flame length in the other two integration limits, as shown in Figure 3.2.

Probably the most physically relevant problem for confined flame problems is the situation where the integration limit is transversely fixed. This represents a problem where an oscillatory flame spreads to the wall and the edge of the approach flow reactants, with an oscillatory flame height and length. In order to analyze this case in the normal or axial coordinate systems requires the solution of Equation (3.8) with a time varying integration limit. The time varying integration limit corrections for the axial and normal coordinate systems were determined by expanding the frequency domain fluctuating flame position functions to first order in a Taylor series and solving for the end correction using the geometric relations shown in Figure 3.2. They are given by:

$$\Delta\hat{x} = 2\frac{u_{ref}}{\omega_d}\sin\left(\frac{St_A}{2}\frac{\beta^2+1}{\beta^2}\right)e^{i\frac{St_A}{2}\frac{\beta^2+1}{\beta^2}} \tag{3.17}$$

$$\Delta\hat{s} = 2\frac{u_{ref}}{\omega_d}\frac{\beta}{\sqrt{1+\beta^2}}\sin\left(\frac{St_A}{2}\frac{\beta^2+1}{\beta}\right)e^{i\frac{St_A}{2}\frac{\beta^2+1}{\beta}} \tag{3.18}$$

Substituting these expressions into Equations (3.11) and (3.13) yields the expression shown in Equation (3.15) for all three coordinate systems, as must be the case.

The key takeaway from this subsection is the significance of the integration limit when evaluating global *FTF*'s – very different answers are obtained for different assumptions on the integration surface. These differences in the global flame area and their resolution are applied in the following sections in order to determine both the analytical and numerical heat release response.

3.2 Problem Definition

Having introduced the *G*-Equation, explicit flame position equation, integrated flame surface area, and flame transfer function, I now continue with the current problem:

modeling the response of *turbulent* flames to harmonic forcing. To set up the problem, consider Figure 3.3 which shows a flame spreading from a stabilization point. Again, if the flame is weakly wrinkled, it is possible to define its instantaneous location by the single valued function ξ.

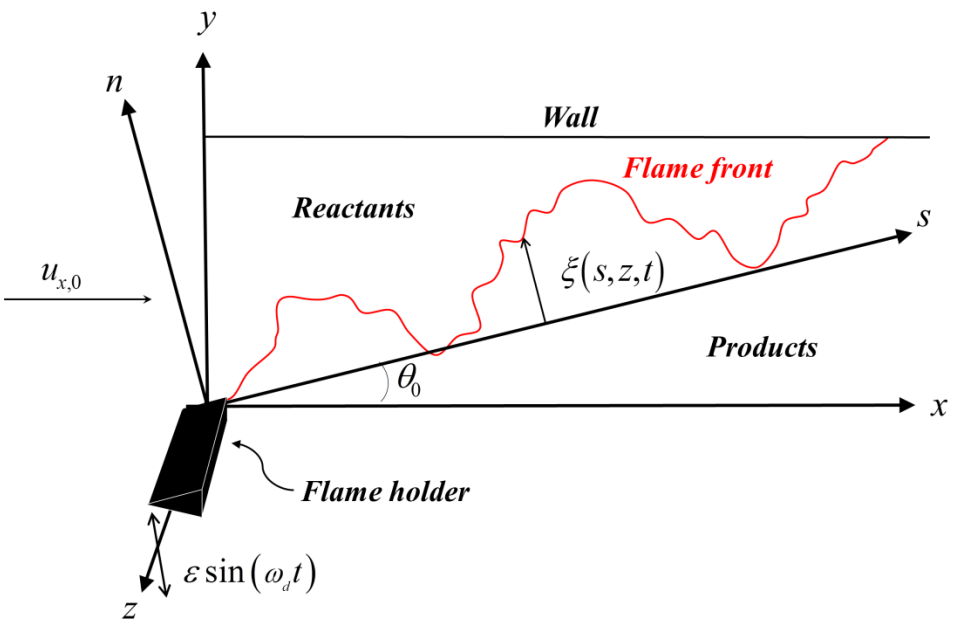

Figure 3.3. Schematic of flame geometry and coordinate system

In addition, we can define the spatially integrated heat release as *Q*. As discussed in the Section 3.1.2, and noted in Humphrey et al. [63], multiple definitions for the spatially integrated heat release exist, depending upon one's assumptions of the potentially oscillating integration limits. Here, I assume that flames are confined and spread to the wall and so the transverse integration limits are fixed, implying that the axial integration limits oscillate.

We can write each of the relevant variables, $\vec{u}, \xi, Q$, as the following triple decomposition, shown here for flow velocity:

$$\vec{\boldsymbol{u}}(\vec{\boldsymbol{s}},t) = \vec{\boldsymbol{u}}_0(\vec{\boldsymbol{s}}) + \vec{\boldsymbol{u}}_1(\vec{\boldsymbol{s}},t) + \vec{\boldsymbol{u}}_2(\vec{\boldsymbol{s}},t) \tag{3.19}$$

where $(\ )_0$ is the time-averaged quantity, defined as:

$$\vec{u}_0(\vec{s}) = \frac{1}{T}\int_0^T \vec{u}(\vec{s},t)\,dt \tag{3.20}$$

The second quantity, $(\ )_1$, is the coherent fluctuation and is defined using the ensemble average, denoted by the operator $\langle\ \rangle$, as:

$$\vec{u}_1(\vec{s},t) = \left\langle \vec{u}(\vec{s},t) - \vec{u}_0(\vec{s}) \right\rangle. \tag{3.21}$$

And, the random fluctuation, $(\ )_2$ is then:

$$\vec{u}_2(\vec{s},t) = \vec{u}(\vec{s},t) - \vec{u}_0(\vec{s}) - \vec{u}_1(\vec{s},t) \tag{3.22}$$

Note that $(\vec{u}_1)_0 = (\vec{u}_2)_0 = 0$, $\langle \vec{u}_2 \rangle = 0$, but $\langle \vec{u}_1 \rangle \neq 0$.

The key problem of interest in this chapter is the input-output relation between the coherent velocity forcing and the coherent fluctuations in flame position and heat release; e.g., for the spatially integrated heat release of a flame forced by flow disturbances:

$$FDF\ (a,\omega_d) = \frac{\langle \hat{Q}_1 \rangle / Q_0}{\langle \hat{u}_1 \rangle / u_0} \tag{3.23}$$

where, in contrast to Equation (2.1), the quantities of interest are now determined by ensemble-averaging, as indicated by the $\langle\ \rangle$ brackets. Equation (3.23) denotes the global flame describing function (*FDF*) of the *turbulent*, premixed flame.

This problem - i.e., the input-output relation between the coherent velocity forcing and the coherent fluctuations in flame position and heat release of turbulent flames- has been previously addressed both implicitly and explicitly. Hemchandra et al. [96] appears to be the first study which explicitly considered the ensemble-averaged response of a flame forced by simultaneous broadband and narrowband disturbances. A related follow

on study was also reported by Hemchandra et al. [95]. The first of these studies demonstrates that one of the key effects of the broadband disturbances, $\vec{u}_2$, on $\langle Q \rangle$ is through its influence on the time-averaged flame shape. This particular effect can be modeled by treating the flame as laminar and considering its response to harmonic forcing, but using the time-averaged turbulent flame properties as inputs to the flame shape – this is referred to as a "quasi-laminar" approach below.[iii] In addition, flame wrinkles induced by the random fluctuations increase the destruction rate of the coherent wrinkles due to harmonic forcing, such as shown in Figure 3.7. Thus, the effects of turbulence and harmonic forcing are not simply additive but are nonlinearly coupled. Shin and Lieuwen [1] subsequently analyzed the explicit dynamic influences of turbulence on the ensemble-averaged flame dynamics and showed that, for flames with constant *local* laminar burning velocities, background broadband forcing leads to an effect on the ensemble-averaged flame position that is equivalent to a modulation in turbulent burning velocity, proportional to the local ensemble-averaged curvature. In other words, to reiterate the flame speed closure discussed in Section 2.4.1:

$$S_{T,Disp}(s,t) = S^0_{T,Disp}(s)\left(1-\sigma_{T,D}(s)\langle C(s,t)\rangle\right) \tag{2.13}$$

where $S_{T,Disp}$ is the ensemble-averaged turbulent displacement speed (defined in Equation (3.26)), and $\langle C \rangle$ is the ensemble-averaged flame curvature. Due to its analogy with the

---

[iii] Note that an analogous approach is sometimes used in the hydrodynamic stability literature, where the time averaged velocity profile of a turbulent flow is used as an input to a stability calculation to determine the growth rate of a harmonic space/time disturbance; see discussion of this approach in, e.g., references [119-121]

stretch sensitivity of laminar flames, $\sigma_{T,D}$ is denoted as the turbulent displacement Markstein length (although the local, instantaneous burning velocity is stretch independent in this calculation). Note that this modulation of the ensemble-averaged turbulent burning velocity is not captured by quasi-laminar approaches.

In addition, several experimental studies have used measured velocity fields as inputs to the level-set equation to predict flame position [69] and *FDF's* [70]. These *FDF's* were also directly measured and compared to the predictions. These approaches used the measured ensemble-averaged velocity field as inputs to the level-set equation, and the mean turbulent flame position as parameters. As noted above, this quasi-laminar approach accounts for turbulent background effects on time-averaged flame properties and ensemble-averaged fluctuating quantities, but does not incorporate any dynamical effects. These analyses showed quite good agreement with the predictions and measurements, suggesting that the key impact of the turbulent background is on the time-averaged flame/flow properties.

The objective of this chapter is to analytically consider this problem further. The spatially integrated heat release, $\langle Q(t) \rangle$, of a turbulent, premixed flame, is examined by modeling the ensemble-averaged flame response, using Shin and Lieuwen's [1] ensemble-averaged turbulent flame speed closure, Equation (2.13), discussed above.

Both the numerical and analytical analysis here is restricted to isothermal flames. For real flames, heat release, and the resulting density change, alters the approach flow, and there is a significant body of work which discusses this effect [113, 116, 122, 123].

Realistically, flames generally have non-zero heat release, density, and temperature jumps. However, it should be noted that the isothermal limit is interesting for

its own sake, as there are practical applications such as vitiated flow or highly compressed flows with small temperature and density jumps. A non-zero density jump introduces an important effect, the Darrieus-Landau flame instability, resulting from changes in the approach flow which cause flame wrinkle amplification [113]. In addition, heat release for a ducted flame causes acceleration of the flow, causing the velocity field to vary spatially along the flame.

As the focus of this chapter is on the influence of the stochastic flame wrinkling induced by turbulent velocity fluctuations upon the coherent wrinkles induced by the harmonic flow disturbances, this assumption enable us to focus on the flame dynamics problem, without the added complication of the modifications of the flow field induced by the moving flame. However, Chapters 4 and 5 address the flame speed closure from an experimental (i.e. non-isothermal) perspective.

3.2.1 Ensemble-averaged Flame Position Equation

This section presents a discussion of the ensemble-averaged flame position equation, which is based on the explicit flame position equation (Equation (3.6)) introduced in Section 3.1.1. The ensemble-averaged flame position equation is used both in the following theoretical and numerical analysis as well as the experimental work presented in Chapter 4, and is the primary analytical tool of this study.

In order to derive a model equation-for the ensemble-averaged flame, one could start from Equation (3.6). However, ensemble-averaging this equation leads to:

$$\frac{\partial\langle\xi\rangle}{\partial t}+\left\langle u_s\frac{\partial\xi}{\partial s}\right\rangle-\langle u_n\rangle+\left\langle u_z\frac{\partial\xi}{\partial z}\right\rangle=\left\langle S_L\left[1+\left(\frac{\partial\xi}{\partial z}\right)^2+\left(\frac{\partial\xi}{\partial s}\right)^2\right]^{1/2}\right\rangle \tag{3.24}$$

Note that analyzing the ensemble-averaged flame position, $\langle \xi \rangle$, as shown in Equation (3.24), leads to the same "closure" problem as found in most nonlinear problems, such as in the Reynolds-Averaged Navier-Stokes (RANS) equations. As such, Shin and Lieuwen [1] computationally solved the *G*-equation, Equation (3.5) (i.e., they did not assume that the flame was instantaneously single valued) for a flame with constant laminar burning velocity, S_L, and post-processed the ensemble-averaged results. In analogy with Equation (3.6), above, they wrote the following equation relating ensemble-averaged flame position to the ensemble-averaged disturbance field:

$$\frac{\partial \langle \xi \rangle}{\partial t} + \langle u_s \rangle \frac{\partial \langle \xi \rangle}{\partial s} - \langle u_n \rangle + \langle u_z \rangle \frac{\partial \langle \xi \rangle}{\partial z} = S_{T,D}(s,z,t) \left[1 + \left(\frac{\partial \langle \xi \rangle}{\partial z} \right)^2 + \left(\frac{\partial \langle \xi \rangle}{\partial s} \right)^2 \right]^{1/2} \tag{3.25}$$

There are no assumptions in this equation; rather it *defines* the turbulent displacement speed, $S_{T,Disp}$, which can be seen by rearranging the above as:

$$S_{T,Disp}(s,z,t) \equiv \frac{\frac{\partial \langle \xi \rangle}{\partial t} + \langle u_s \rangle \frac{\partial \langle \xi \rangle}{\partial s} - \langle u_n \rangle + \langle u_z \rangle \frac{\partial \langle \xi \rangle}{\partial z}}{\left[1 + \left(\partial \langle \xi \rangle / \partial z \right)^2 + \left(\partial \langle \xi \rangle / \partial s \right)^2 \right]^{1/2}} \tag{3.26}$$

where $\langle \xi \rangle$ is the ensemble-averaged flame position, and *s* is the downstream coordinate for a coordinate system aligned with the unforced flame position, and *z* is the transverse coordinate, parallel with the flame holder, as shown in Figure 3.3. The use of Equations (3.25) and (3.26) requires the ensemble-averaged flame to remain single-valued, which introduces an upper limit on harmonic forcing amplitude, but does not require the instantaneous flame to remain single-valued, as shown in Figure 3.4.

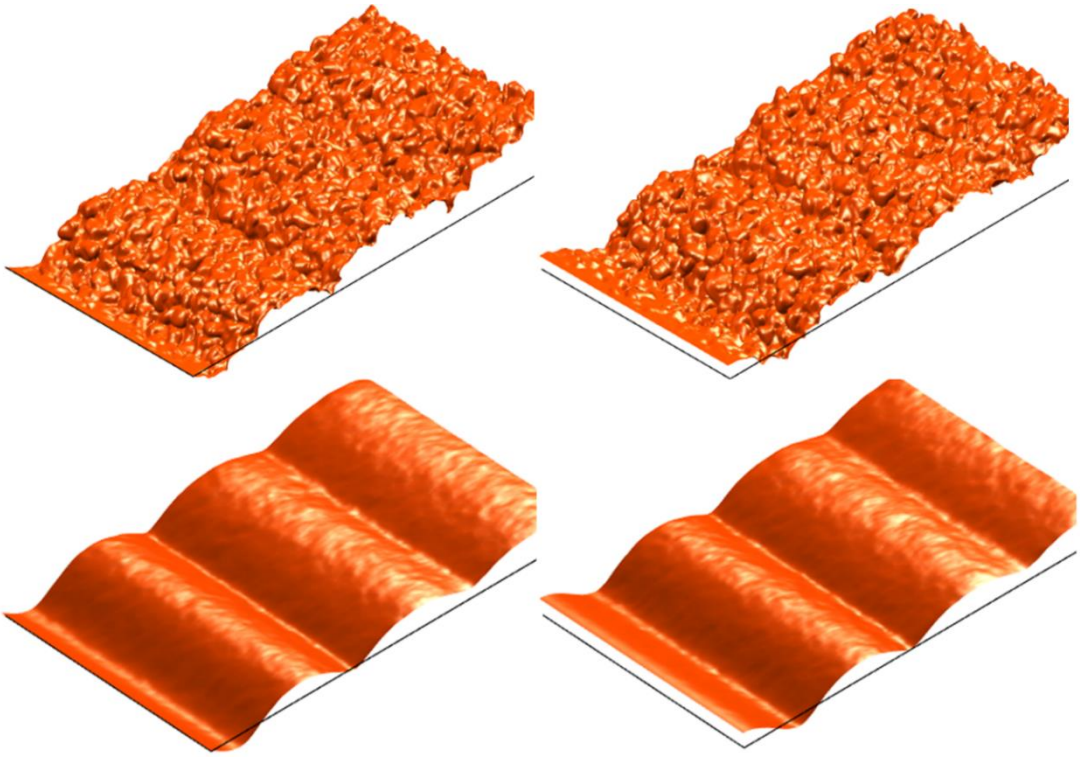

Figure 3.4. Snapshots of the instantaneous flame surface (top) and ensemble-averaged result (bottom) at two time instances, $t \cdot \omega_d = 0$ (left) and $t \cdot \omega_d = \pi/2$ (right). Data shown for a turbulent field with $L_{11}/\varepsilon = 0.5$, $\varepsilon/(u_{S,0}/\omega_d) = 0.65$, $u'/u_{s,0} = 0.082$.

Empirical post-processing of their computational results led Shin and Lieuwen [1] to the model equation for $S_{T,D}$ shown in Equation (2.13). Related equations for the phase or ensemble-averaged flow dynamics have also been developed for work on the hydrodynamic instability of shear flows in the presence of background turbulence; e.g., see Tammisola and Juniper [124]. Some of these results from Shin and Lieuwen [1] are reproduced in Figure 3.6 and discussed further in Section 3.3.4.

Having considered the flame position, I next consider its heat release. The ensemble-averaged, spatially integrated heat release is given by the expression:

$$Q(t) = \left\langle \int_{s_I(t)}^{s_W(t)} \rho \Delta h_r S_L dA \right\rangle \tag{3.27}$$

where ρ is the unburned gas density, Δh_R is the heat of combustion per unit mass, and dA is the instantaneous flame area element. The integration limits, $s_I(t)$ and $s_W(t)$ are time dependent, reflecting the potential motion of both the flame stabilization point and flame length. Assuming constant density and heat of reaction, I *define* the turbulent consumption speed, $S_{T,C}$ through the following relation:

$$\int_{\langle s_I(t)\rangle}^{\langle s_W(t)\rangle} S_{T,C}(t,s)\,dA_1 \equiv \left\langle \int_{s_I(t)}^{s_W(t)} S_L\,dA \right\rangle \tag{3.28}$$

Although $S_{T,C}$ was not analyzed by Shin and Lieuwen [1], results presented in Section 3.3.4 show that it exhibits a similar sensitivity to ensemble-averaged flame curvature, $\langle C\rangle$, although the proportionality constant is not exactly equal to $\sigma_{T,D}$. In addition, $S_{T,C}$ is examined experimentally in Chapter 5.

3.3 Numerical Calculations – Oscillating Flame Holder

3.3.1 Geometry

Following Shin and Lieuwen [1], I consider first the problem of an oscillating flame holder [52, 125, 126]. This is an important canonical problem for understanding flame response physics, because the oscillating flame holder is the only flame wrinkle excitation source, and leads to a traveling wave that convects down the flame. The magnitude of this flame wrinkling traveling wave is constant when considering a constant density, constant burning velocity, linear analysis. A number of studies have investigated *FDFs* where forcing is induced by velocity fluctuations [53, 60]. In this case, the flame is excited simultaneously over its entire length and the resulting flame wrinkle amplitude

exhibits spatial interference patterns, as discussed in Section 2.1.1. These interference patterns complicate the analysis of flame wrinkle destruction behavior; multiple processes can lead to reduction in flame wrinkling amplitude. Thus, the simplification afforded by use of flame anchor excitation facilitates identification of key problem variables. The more physically interesting velocity forced flame problem is considered in Section 3.5.2.

Consider the geometry shown in Figure 3.3, where a flame is attached to a harmonically oscillating bluff-body, and spreads to the wall. Figure 3.4 shows two snapshots of the instantaneous, multi-valued flame, and the corresponding ensemble-averaged result at that same phase of the harmonic forcing cycle. Note that at high turbulence intensities, the instantaneous flame may become highly multi-valued and is three-dimensional. In this case, the ensemble-averaged result remains single-valued (but not necessarily in general) and is two-dimensional.

As discussed in Section 3.1.1, the area integration is taken over a fixed width (rather than fixed length, or fixed axial distance), which is the most physically relevant problem for confined combustion problems. The inclusion of end correction factors accounts for flame area fluctuations which occur as a wrinkled flame intersects a wall. The unforced burning area is based on the two-dimensional area of the flame, equal to the flame length. It is calculated as the time-averaged length of the mean flame, integrated between the oscillating end points:

$$L_f = \left[\int_{s_I(t)}^{s_W(t)} \left(\left(\frac{\partial \xi_0}{\partial s} \right)^2 + 1 \right)^{1/2} ds \right]_0 \tag{3.29}$$

This flame length is used to calculate the Strouhal number, $St_{Lf} = \left(L_f \cdot \omega_d \right) / u_{s,0}$.

3.3.2 Numerical Procedure

This section describes the numerical approach used to compute the space-time dynamics of the flame position and heat release. Analysis of the ensemble-averaged space-time dynamics of the flame position, $\langle \xi \rangle$, was previously presented by Shin and Lieuwen [1]; here I consider also the heat release. The key assumptions for this analysis are that (1) S_L is constant (2) the flame remains attached to the harmonically oscillating flame holder (3) isothermal flow field, as discussed in Section 3.2.

As described by Shin [97] and Shin and Lieuwen [1], the level-set equation is solved with a semi-Lagrangian Courant-Isaacson-Rees (CIR) scheme, using the back-and-forth error correction and compensation (BFECC) method [127]. The computational domain size is 201 x 201 x 801, and the time step is 1/(1000 f_0), where f_0 is the forcing frequency. The spatial resolution is greater than $\left(u_{s,0}/f_0\right)/100$, $L_{11}/10$. The scheme provides fifth-order accuracy where the solution has smooth spatial derivatives, and is third-order accuracy in regions where spatial gradients are discontinuous.

The attachment condition at the oscillation flame holder is specified by enforcing values of the *G* field as positive in the products and negative in the reactants. At time points where the flame holder exists between grid points, the adjacent values of the *G* field are determined by bilinear interpolation. In calculating the *G* field, a local level-set approach is adopted. In this approach, the *G*-field is solved only in a small region adjacent to the $G = 0$ level-set, which reduces computational expense. Outside of the local level-set region, the values of the *G*-field have no physical meaning, and thus are not solved for. In order to improve numerical stability, a re-distancing procedure is used,

wherein the values of the *G*-field are periodically reset by solving a signed distance function [127]. Periodic boundary conditions are used at the transverse (side) boundaries, and a non-reflecting boundary condition is used at the domain outlet. The non-reflecting boundary is implemented using a fully upwind differencing scheme [97].

Grid convergence was determined for several cases; for a laminar baseline case, less than 1% difference in flame position was obtained with a factor-of-ten increase in grid density at $s/\left(u_{s,0}/\omega_d\right)=25$. A second case was conducted with a turbulence intensity of $u'/u_{s,0}=0.04$, and a factor-of-two increase in grid density, showed a 3% difference in the ensemble-averaged flame position at $s/\left(u_{s,0}/\omega_d\right)=15$.

As discussed in Shin and Lieuwen [1], different approaches have been used in the past to determine ensemble-averaged flame positions. One approach is to binarize the *G*-fields between products and reactants and then average these fields. The averaged field is then associated with a progress variable (e.g. $\bar{C}$), and the ensemble-averaged flame position defined at some progress variable value, such as $\bar{C}=0.5$. However, this approach results in a progress variable which defines a median rather than mean value of the flame position. This difference is discussed further in Chapter 4 and Appendix B. As this creates some complications when comparing with analytical results, I extract the instantaneous flame position coordinates and define the flame position as the average transverse value at each axial location. The ensemble-averaged flame position results from ensemble averaging over 160 forcing cycles.

For the oscillating flame holder problem, the flow field consists of the superposition of a spatially uniform field with a stochastic component, but with no coherent component; i.e.

$$\vec{\boldsymbol{u}}\left(\vec{\boldsymbol{s}},t\right)=\vec{\boldsymbol{u}}_0\left(\vec{\boldsymbol{s}}\right)+\vec{\boldsymbol{u}}_2\left(\vec{\boldsymbol{s}},t\right) \tag{3.30}$$

The stochastic velocity fluctuations are isotropic, incompressible, and Gaussian distributed with spatial correlation lengths that decay exponentially over a longitudinal, integral length scale; i.e.

$$\frac{\left\langle u_{x,2}\left(x,n,z,t\right)u_{x,2}\left(x+r,n,z,t\right)\right\rangle}{\left\langle u_{x,2}^2\right\rangle}=\exp\left(-\frac{\pi}{4}\left(\frac{r}{L_{11}}\right)^2\right) \tag{3.31}$$

The flow convects these disturbances with the mean flow velocity as-per Taylor's hypothesis, and so the integral time and length scales are directly related through the mean flow velocity. As such, while these disturbances are stochastic, the fact that they are single length/time scale implies that they do not describe Navier-Stokes turbulence. However, this general structure of the correlation function is used routinely in the turbulence literature, e.g., see [87] and [128]. These flow disturbances are used as inputs to solve Equation (3.5)– note that the fact that the flow field is imposed upon the flame, as opposed to being simultaneously solved with the flame implies negligible gas expansion across the flame, as discussed above. Additional discussion of the numerical method and turbulence field are given in Shin and Lieuwen [1]. The outputs of these calculations are instantaneous flame positions and areas.

3.3.3 Numerical Heat Release Calculations

Because the numerical calculations all assume constant local burning velocity, S_L, and mixture composition, heat release is directly proportional to instantaneous flame surface area. To calculate the numerical flame area, the instantaneous flame position and area (with area data extracted from the multi-valued numerical simulation) are averaged

in the transverse direction. Because the discretization of the flame position and area along the *s*-coordinate does not generally align with a desired integration point on the *y*-axis, the flame position is interpolated between adjacent *s*-locations where it crosses the integration limits. The area fluctuation is determined by taking the Fourier transform of the entire area time signal. This area is then normalized by L_f, the two-dimensional unforced area, which again is proportional to the burning rate.

The maximum area fluctuation occurs when out of phase wrinkle anti-nodes exist at the integration limits, at a given instant in phase time, as illustrated in Figure 3.5.

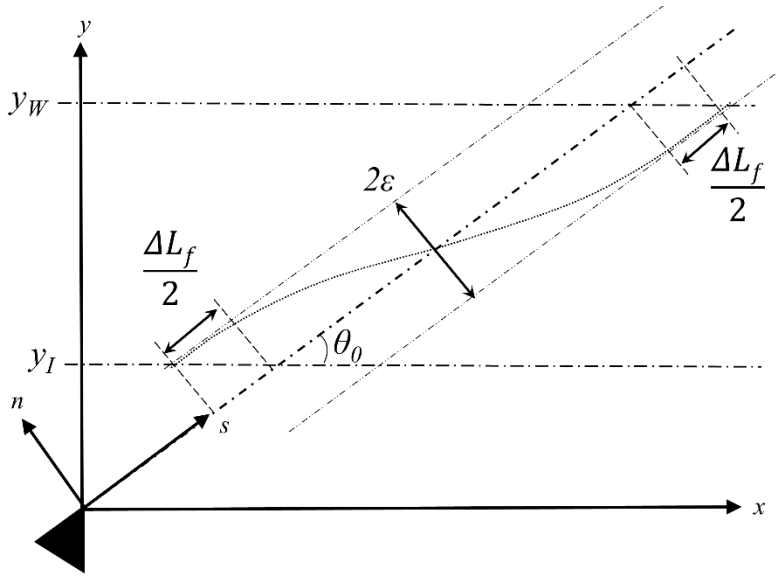

Figure 3.5. Illustration of flame length fluctuation.

This maximum flame length fluctuation, normalized by the flame length, L_f is:

$$\frac{\Delta L_f}{L_f} = \frac{2\varepsilon}{L_f \cdot \tan(\theta_0)} \tag{3.32}$$

Equation (3.32) is equal to the denominator of the *FDF*, which is defined as:

$$FDF = \frac{\hat{Q}_1 / Q_0}{\hat{\varepsilon}_{ref} / l_0} \tag{3.33}$$

where ε_{ref} denotes the amplitude of displacement of the flame holder in the flame normal direction. Note that setting Equation (3.32) equal to the denominator in Equation (3.33), and solving for l_0, provides the appropriate reference length scale.

$$l_0 = \frac{L_f \tan(\theta_0)}{2} \tag{3.34}$$

3.3.4 Numerical Calculation of Turbulent Parameters

As discussed above in the context of Equation (2.13), in the far-field, $S_{T,Disp}$ shows curvature dependence analogous to that of stretch sensitive laminar flames with positive Markstein lengths [1]. This section briefly shows several illustrative calculations demonstrating this dependency.

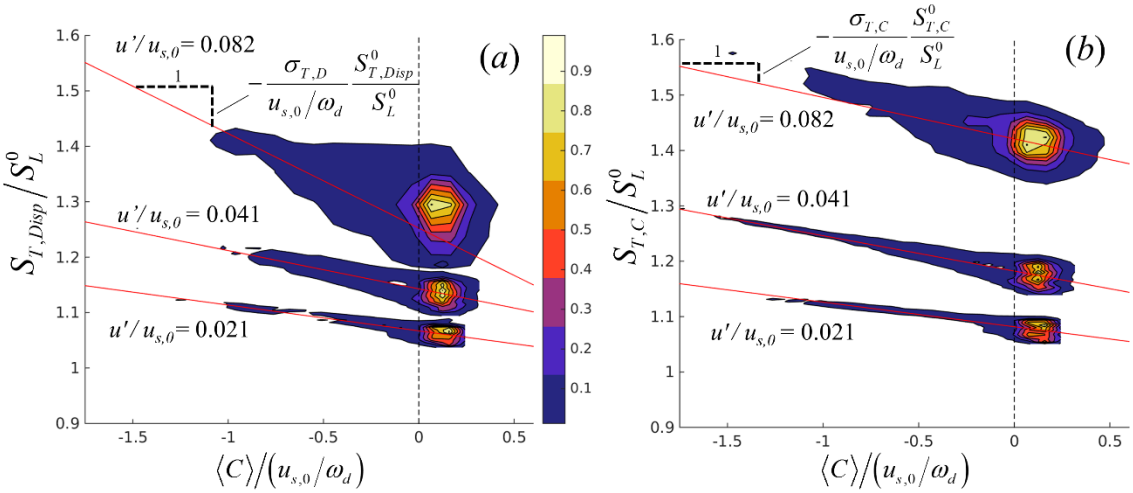

Figure 3.6. Joint probability density function plots showing the normalized, non-dimensional (*a*) effective turbulent displacement speed and (*b*) effective turbulent consumption speed versus ensemble-averaged flame curvature extracted from numerical computations of the level set equation. The turbulent Markstein lengths are derived from the slope of the linear regressions. Data shown for a turbulent field with $L_{11}/\varepsilon = 0.5$, $\varepsilon/(u_{S,0}/\omega_d) = 0.65$.

Figure 3.6 shows illustrative calculations, plotting the joint probability density functions of the turbulent flame speed and ensemble-averaged curvature, $\langle C \rangle$. Results are shown for both $S_{T,Disp}$ and $S_{T,C}$ for the locations $s/(u_{s,0}/\omega_d) \cong 10.2 - 35.3$ at which $S_{T,Disp}$ and $S_{T,C}$ approach a constant value (near the flame holder, both the burning velocities and turbulent Markstein lengths change substantially). This result demonstrates the clear correlation between the instantaneous flame speed and ensemble-averaged curvature. The line is a least-squares best fit through the simulation results. The simulations show that $S_{T,Disp}$ and $S_{T,C}$ (and therefore $\sigma_{T,D}$ and $\sigma_{T,C}$) have similar dependencies on turbulence intensity and instantaneous curvature, with $S_{T,C}$ greater than or equal to $S_{T,Disp}$ by about 10-45%, depending on turbulent intensity. Note that the figure uses data from multiple spatial locations, while the parameters used for the calculations described in Section 3.4 are calculated locally, at each spatial location. These results show that the consumption speed, like the displacement speed, demonstrates an approximately linear sensitivity to ensemble-averaged curvature and can be modeled as:

$$S_{T,C}(s,t) = S_{T,C}^0(s)\left(1 - \sigma_{T,C}(s)\langle C(s,t)\rangle\right) \tag{3.35}$$

where $\sigma_{T,C}$ is the turbulent consumption speed length, and $S_{T,C}^0$ is the uncurved consumption speed.

From these results, the value of $S_{T,Disp}^0$ in Equation (2.13) is determined by extrapolating $S_{T,Disp}$ to zero curvature. At each spatial location, the turbulent displacement Markstein length, $\sigma_{T,D}$ and turbulent consumption Markstein length $\sigma_{T,C}$ are calculated by determining the slope of the regression between $S_{T,Disp}$ (or $S_{T,C}$) and the

ensemble-averaged curvature, $\langle C \rangle$, and then dividing by the value of $S^0_{T,Disp}$ or $S^0_{T,C}$, for the displacement or consumption Markstein length, respectively. These extracted local values of $S^0_{T,Disp}$, $S^0_{T,C}$, $\sigma_{T,D}$ and $\sigma_{T,C}$ are used in the reduced order model discussions in the next sections. Additional results and discussion of these trends, as well as a physical explanation of why this correlation occurs, is described in [1] and also in Chapters 4 and 5, and so I do not go into further details here.

3.4 Analytical Model Development and Validation

This section describes the development of a reduced order model for $\langle Q \rangle$, utilizing the turbulent flame speed models described above. The results of this model are compared to computed results for flame position and $\langle Q \rangle$ in Section 3.4.2 and 3.4.3, respectively.

3.4.1 Formulation

We can use the equations for the ensemble-averaged flame position, Equation (3.25), and heat release Equations (3.27) and (3.28) along with the closures for the turbulent displacement and consumption speeds to solve for the *FDF*. In other words, the flame position is solved from the following expression, derived from Equations (2.13) and (3.25):

$$\frac{\partial \langle \xi \rangle}{\partial t} + \langle u_{s,eff} \rangle \frac{\partial \langle \xi \rangle}{\partial s} - \langle u_n \rangle + \langle u_z \rangle \frac{\partial \langle \xi \rangle}{\partial z} =$$
$$S^0_{T,Disp}(s) \left(1 + \sigma_{T,D}(s) \frac{\partial^2 \langle \xi \rangle / \partial s^2}{\left[1 + \left(\partial \langle \xi \rangle / \partial s \right)^2 \right]^{3/2}} \right) \left[1 + \left(\frac{\partial \langle \xi \rangle}{\partial z} \right)^2 + \left(\frac{\partial \langle \xi \rangle}{\partial s} \right)^2 \right]^{1/2} \quad (3.36)$$

where $u_{s,eff}$ indicates the effective tangential velocity of the wrinkle (i.e. $u_{s,eff}$ is the slope of the phase of the ensemble-averaged flame wrinkle), which accounts for correlations between turbulent and harmonic fluctuations. This effect was not accounted for in the original publication of Shin and Lieuwen [1]. The correction is quite small but its effect compounds with distance from the flame holder. Also, note the definition of ensemble-averaged curvature, $\langle C \rangle$, so that flames oriented convex to the reactants have positive curvature, as typically defined for flamelets :

$$\langle C \rangle = -\frac{\partial^2 \langle \xi(s,t) \rangle / \partial s^2}{\left[1+\left(\partial \langle \xi(s,t) \rangle / \partial s\right)^2\right]^{3/2}} \tag{3.37}$$

This equation can be solved for a given disturbance field, and axial distribution of $S^0_{T,Disp}$ and $\sigma_{T,D}$. Then, having solved for $\langle \xi(s,t) \rangle$, the heat release can then be solved from the expression

$$Q(t) = \int_{\langle s_I(t) \rangle}^{\langle s_W(t) \rangle} \rho \Delta h_r S^0_{T,C}(s) \left(1+\sigma_{T,C}(s)\frac{\partial^2 \langle \xi \rangle / \partial s^2}{\left[1+\left(\partial \langle \xi \rangle / \partial s\right)^2\right]^{3/2}}\right)\left(\left(\frac{\partial \langle \xi \rangle}{\partial s}\right)^2+1\right)^{1/2} ds \tag{3.38}$$

where I assume constant ρ and Δh_R. The *FDF* result then follows from inserting the computed heat release into Equation (3.33). In order to evaluate the validity of the flame speed closures for the turbulent displacement and consumption speeds, the flame position and heat release response were compared to the numerical results, as shown in the following two subsections.

3.4.2 Model Evaluation: Flame Position

The turbulent flame speed closure was evaluated by integrating Equation (3.36) for a two-dimensional geometry.

$$\frac{\partial\langle\xi\rangle}{\partial t}+\langle u_{s,eff}\rangle\frac{\partial\langle\xi\rangle}{\partial s}-\langle u_n\rangle=$$
$$S_{T,Disp}^{0}(s)\left(1+\sigma_{T,D}(s)\frac{\partial^2\langle\xi\rangle/\partial s^2}{\left[1+\left(\partial\langle\xi\rangle/\partial s\right)^2\right]^{3/2}}\right)\left[1+\left(\frac{\partial\langle\xi\rangle}{\partial s}\right)^2\right]^{1/2} \tag{3.39}$$

This equation was solved using a total variation diminishing (TVD) Runge-Kutta scheme, employing weighted, essentially non-oscillatory (WENO) derivatives and local Lax-Friedrichs flux [129]. Values of $S_{T,Disp}^{0}$ and $\sigma_{T,D}$ at each spatial location, *s*, were extracted from the computed results, as described at the end of Section 3.3.4. Similarly, the effective tangential velocity is calculated by extracting the wrinkle phase speed from the phase of the ensemble-averaged result.

Figure 3.7 shows a comparison between the flame fluctuation determined from ensemble-averaging of the numerical solution to the *G*-equation (solid line; discussed in Section 3.3) and the predicted flame fluctuation determined from the analytical model (i.e. from integration of Equation (3.39), dotted line), as well as the quasi-laminar result (dashed line, discussed below). The figure shows that the ensemble-averaged flame shape predicted from the analytical model agrees very well with the ensemble-averaged results directly extracted from the computations. For the two lower turbulence cases, the predicted flame shape is virtually identical. For the two higher turbulence intensity cases, there is some difference between the analytical and numerical predictions, the difference increasing with the flame coordinate, *s*.

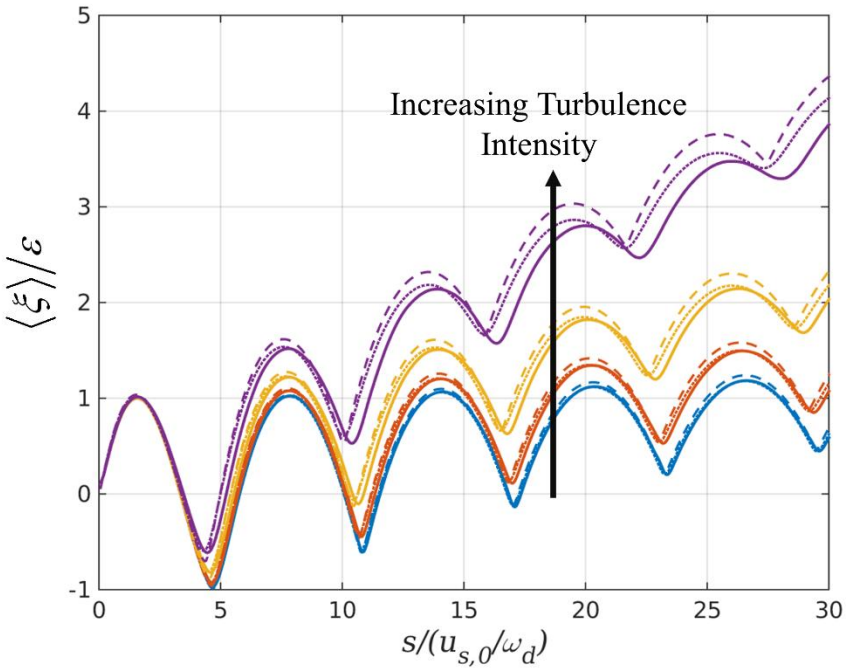

Figure 3.7. Ensemble-averaged flame position calculated from numerical solution of the *G*-equation (solid lines), integration of Equation (3.39) (dotted lines), and "quasi-laminar" result (dashed lines). Data shown for a turbulent field with L_{11}/ε = 0.5, $\varepsilon/(u_{S,0}/\omega_d)$ = 0.65, $t\cdot\omega_d = \pi$, and $u'/u_{s,0}$ = 0.010, 0.021, 0.041, 0.082.

The quasi-laminar results shown in Figure 3.7 incorporate the spatial variation in $S^0_{T,Disp}$ but have no dynamical flame speed closure model (equivalent to setting $\sigma_{T,D} = 0$). The turbulent flame speed closure clearly improves the accuracy of the predicted flame position, even for the lowest turbulence intensity. These comparisons, therefore, demonstrate the validity of the turbulent Markstein length displacement speed closure, Equation (2.13) discussed previously, for low to moderate turbulence intensities.

3.4.3 Model Evaluation: Heat Release

Further validation of the turbulent displacement speed closure, as well as of the turbulent consumption speed closure, which is closely related to heat release, is given by comparing the heat release characteristics of the numerical solution of the *G*-equation to those predicted by the analytical model. The numerical heat release is determined by

integrating the instantaneous flame surface area over the integration domain, and finding the response at the forcing frequency using the Fourier transform of the area time signal. The flame area integration of the non-linear analytical model is accomplished using a trapezoidal integration method. The values of $\sigma_{T,D}$, $\sigma_{T,C}$, $S^0_{T,Disp}$, and $S^0_{T,C}$ used in the analytical model correspond to those calculated from numerical data simulated with the specified values L_{11}, u' and harmonic forcing amplitude. The response at the forcing frequency is determined using the Fourier transform of the burning-rate weighted area time signal.

Figure 3.8 shows the gain and phase of the numerical (solid lines), analytical (dotted lines), and quasi-laminar (dashed lines) *FDFs*. Before discussing these results, it is important to explain how the laminar, constant flame speed flame holder forced response differs from the velocity forced one. The velocity forced *FTF* asymptotes to a value of unity as frequency tends to zero. This result can be understood from quasi-steady considerations – an increase in flow velocity of a fixed composition mixture causes a proportional increase in heat release rate. In contrast, the *FTF* of the flame holder forced flame asymptotes to zero as frequency tends toward zero, since the quasi-steady heat release is invariant to flame holder position.

Similarly, the gain of the velocity forced *FTF*, while exhibiting some interference patterns, has a general low pass filter character, decaying as *1/St*, as discussed in Section 2.1.2. This occurs because the magnitude of particle displacement, and consequent flame wrinkling scales as u_1/f, and so doubling the frequency at a fixed velocity disturbance magnitude halves the magnitude of displacement fluctuations. In contrast, the *displacement* is forced for the oscillating flame holder problem, and so the magnitude of

flame wrinkling does not roll off with frequency when normalized by displacement amplitude. Similar to the velocity forced case, the gain of the laminar *FTF* is modulated due to phase cancellation effects associated with integration.

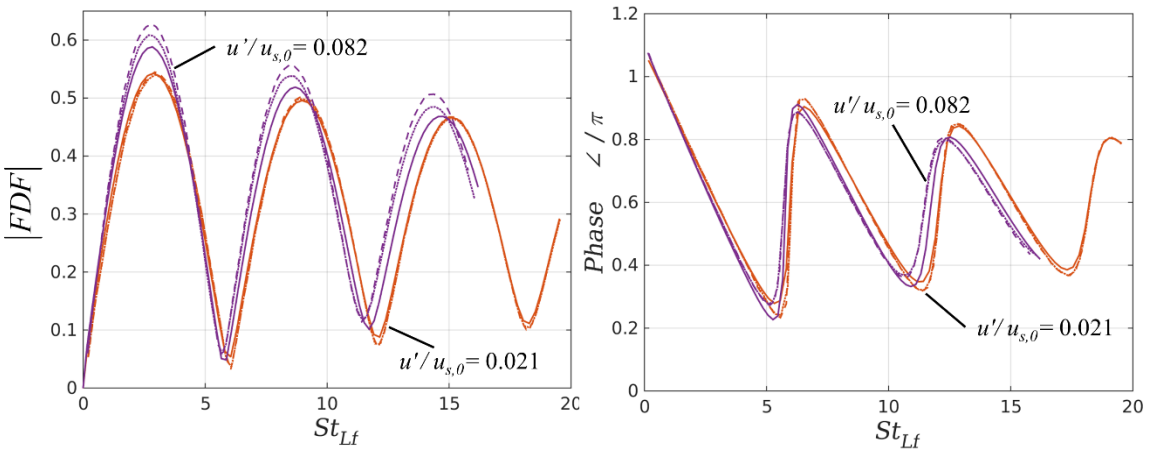

Figure 3.8. Flame describing function gain (left) and phase (right) calculated from the numerical solution of the *G*-equation (solid lines), integration of Equation (3.38) (dotted lines), and quasi-laminar result (dashed lines). Data shown for a turbulent field with L_{11}/ε = 0.5, $\varepsilon/(u_{s,0}/\omega_d)$ = 0.65, at two turbulence intensities.

The analytical model correctly predicts the shape of the numerical *FDF*. Both the numerical solution and analytical model clearly indicate the role of phase cancellation effects in controlling the gain, and the gain maxima and minima are well-aligned in Strouhal space. In addition, Figure 3.8 shows that the model predicts two key qualitative effects of stochastic fluctuations: (1) a progressively decreasing maximum, and increasing minimum, of the *FDF* with increasing Strouhal number, and (2) a slight shift in the position of the node and anti-node locations in Strouhal space, associated with higher turbulence intensity. These effects are also present in the simulations, and are discussed further in the context of the linearized model problem presented in Section 3.5.1

The phase results also are quite similar between the model and the computations - namely, the linearly increasing phase with frequency, the jump in phase across the gain minima, and the smoothing effect of the stochastic fluctuations on this phase jump.

In addition to the analytical and numerical results, Figure 3.8 shows the results from the quasi-laminar approach, which are nearly identical to those of the analytical model, for $u'/u_{s,0} = 0.021$. However, the model shows a significant improvement in prediction of gain maxima over those of the quasi-laminar approach with respect to the numerical results, at $u'/u_{s,0} = 0.082$. Nonetheless, this close concurrence between the quasi-laminar result and the analytical model result suggests why quasi-laminar approaches have been so successful in comparisons of experimental data and models. Apparently, the "averaging" inherent in calculation of a global quantity, such as heat release, minimizes the importance of this turbulent flame speed modulation induced by turbulent fluctuations.

3.5 Results: Model Problems

The purpose of the prior section was to evaluate the closures presented in Equations (2.13) and (3.35) in terms of predicting the phase-averaged flame position and heat release response obtained from phase averaging the full computations. The purpose of this section is to analyze two model problems and to obtain analytical solutions that explicitly illustrate turbulence impacts on the *FTF*. Such explicit solutions are not possible in general, such as for the comparison shown in the prior section, because the equations to be solved are nonlinear and have non-constant coefficients. This section considers the linearized problem with constant coefficients in order to obtain explicit

solutions that show the form of the solution. The first problem is the linear analysis of the oscillating flame holder problem, addressed in the previous section. The second problem is the case of a velocity forced flame with a convecting, decaying velocity disturbance, and a stationary attachment point, a problem previously investigated for laminar flames [60, 130, 131].

3.5.1 Model Problem: Flame Perturbed by an Oscillating Flame Holder

While the preceding general analysis (Section 3.4) required the use of numerical solutions to determine the spatio-temporal flame and heat release characteristics, here I simplify the above expressions in order to obtain explicit analytical results. The key additional assumptions for this model problem are that (4) $S_{T,Disp}^{0}$, $\sigma_{T,D}$, and $S_{T,C}$ are spatially constant, and (5) small amplitude disturbances so that results can be linearized. As in the prior section, for this oscillating flame holder problem, ensemble-average properties are two-dimensional and $\vec{\boldsymbol{u}}_1 = 0$. Applying the additional assumptions (4) and (5) to Equation (3.36), leads to:

$$\frac{\partial \langle \xi_1 \rangle}{\partial t} + u_{s,eff} \frac{\partial \langle \xi_1 \rangle}{\partial s} = S_{T,Disp}^{0} \sigma_{T,D} \frac{\partial^2 \langle \xi_1 \rangle}{\partial s^2} \tag{3.40}$$

Here, the $\langle\ \rangle$ are shown to again emphasize that this is the ensemble-averaged problem, but are not included for the following development. The problem is transformed to Fourier space using a definition for the fluctuating quantities as:

$$\xi_1(s,t) = \text{Real}\left\{ \hat{\xi}_1'(s)\, \varepsilon e^{-i\omega_d t} \right\}. \tag{3.41}$$where

$\hat{\xi}_1'$ is the fluctuating Fourier-space ensemble-averaged flame position, and ε is a non-

dimensional excitation amplitude. This equation is solved subject to the boundary condition:

$$\xi_1(s=0,t) = \text{Real}\left\{\varepsilon e^{-i\omega_d t}\right\}, \tag{3.42}$$

which stipulates that the flame remains attached to the moving flame holder at s = 0. The second boundary condition is that no disturbances flow from the end of the flame upstream – it will be described further below. The general solution is given by:

$$\hat{\xi}_1'(s) = Ae^{sR_1} + Be^{sR_2} \tag{3.43}$$

where

$$R_1, R_2 = \frac{u_{s,eff} \mp \left(u_{s,eff}{}^2 - 4i\omega_d S^0_{T,Disp}\sigma_{T,D}\right)^{1/2}}{2S^0_{T,Disp}\sigma_{T,D}} \tag{3.44}$$

Here, $u_{s,eff}$ is the flow velocity tangential to the unforced flame. The R_1 term corresponds to the solution with a wave moving downstream, while the term R_2 is associated with the wave moving upstream. This latter term is nonphysical and so the coefficient B that multiplies terms containing R_2 is set to zero. In the small $\sigma_{T,D}$ limit, the R_1 term can be expanded as:

$$R_1 = \frac{i\cdot\omega_d}{u_{s,eff}} - \frac{\sigma_{T,D}S^0_{T,Disp}\omega_d{}^2}{u_{s,eff}{}^3} + O(\sigma_{T,D})^2 \tag{3.45}$$

Hence the solution is as follows:

$$\hat{\xi}_1(s) = \varepsilon \exp\left[s\left(\frac{i\cdot\omega_d}{u_{s,eff}} - \frac{\sigma_{T,D}S^0_{T,Disp}\omega_d{}^2}{u_{s,eff}{}^3}\right)\right] \tag{3.46}$$

Thus, the solution for ξ_1 shows that a wrinkle present on the flame front convects in the s-direction at a velocity of $u_{s,eff}$ and decays exponentially at a rate proportional to $\sigma_{T,D}$.

Consider the heat release next which, when linearized, is given by:

$$Q(t) = \int_{s_{I,1}(t)}^{s_{W,1}(t)} \rho \Delta h_r S_{T,C}^0(s) \left(1 + \sigma_{T,C}(s) \frac{\partial^2 \xi_1}{\partial s^2} \right) ds \tag{3.47}$$

The limits of integration oscillate due to wrinkles on the flame, and it is therefore necessary to introduce start and end corrections to the limits of integration, as discussed previously in Section 3.1.1, and Reference [63]. The start and end corrections equal:

$$\Delta \hat{s}_{I,1} = -\frac{\varepsilon}{\tan(\theta_0)} e^{s_I R_1} \tag{3.48}$$

$$\Delta \hat{s}_{W,1} = -\frac{\varepsilon}{\tan(\theta_0)} e^{s_W R_1} \tag{3.49}$$

Assuming spatially constant $S_{T,C}^0$ and $\sigma_{T,C}$, integration of Equation (3.47) yields:

$$\hat{Q}_1(\omega_d) = \rho \Delta h_r S_{T,C}^0 \left(\underbrace{\Delta \hat{s}_{W,1}(\omega_d) - \Delta \hat{s}_{I,1}(\omega_d)}_{\hat{Q}_{A,1}} + \underbrace{\sigma_{T,C} \frac{\partial \hat{\xi}_1}{\partial s}\Big|_{\hat{s}_{I,1}(\omega_d)}^{\hat{s}_{W,1}(\omega_d)}}_{\hat{Q}_{S,1}} \right) \tag{3.50}$$

where I have decomposed the contributions of flame area and turbulent burning velocity fluctuations to the ensemble-averaged heat release. Normalizing these terms by the mean flame heat release, and ε / l_0 (see Equation (3.33)), leads to the following flame area and turbulent burning velocity transfer functions:

$$FTF_A(\omega_d) = \frac{1}{2}(e^{s_I R_1} - e^{s_W R_1}) = \frac{1}{2} e^{s_I R_1}(1 - e^{L_f R_1}) \tag{3.51}$$

$$FTF_S(\omega_d) = \frac{1}{2}\tan(\theta_0)\sigma_{T,C} R_1 \left(e^{s_W R_1} - e^{s_I R_1} \right) = -\frac{1}{2} e^{s_I R_1} \left(1 - e^{L_f R_1} \right) \tan(\theta_0) \sigma_{T,C} R_1 \tag{3.52}$$

The total analytical linear transfer function is simply the sum of these two components.

$$FTF_{Tot}\left(\omega_d\right)=\frac{1}{2}e^{s_I R_1}\left(1-e^{L_f R_1}\right)\left(1-\tan\left(\theta_0\right)\sigma_{T,C}R_1\right) \tag{3.53}$$

Using the small σ expansion derived in Equation (3.45), this expression becomes:

$$FTF_{Tot}\left(\omega_d\right)= \frac{1}{2}\exp\left[s_I\left(\frac{i\omega_d}{u_{s,eff}}-\sigma_{T,D}\frac{S^0_{T,Disp}\omega_d{}^2}{u_{s,eff}{}^3}\right)\right]\left(1-\exp\left[L_f\left(\frac{i\omega_d}{u_{s,eff}}-\sigma_{T,D}\frac{S^0_{T,Disp}\omega_d{}^2}{u_{s,eff}{}^3}\right)\right]\right)\left(1-\tan\left(\theta_0\right)\frac{i\omega_d\sigma_{T,C}}{u_{s,eff}}\right) \tag{3.54}$$

This equation is then non-dimensionalized per the following scheme.

$$\begin{aligned}\tilde{s}&=s/\left(u_{s,eff}/\omega_d\right)\\ \tilde{\sigma}_T&=\sigma_T/\left(u_{s,eff}/\omega_d\right)\\ \tilde{S}_{T,Disp}&=S_{T,Disp}/u_{s,eff}\\ \tilde{c}&=c\cdot\left(u_{s,eff}/\omega_d\right)\end{aligned} \tag{3.55}$$

where all lengths are non-dimensionalized by $\left(u_{s,eff}/\omega_d\right)$, and all velocities by $u_{s,eff}$. Non-dimensional spatial lengths along the *s*-axis are denoted as Strouhal numbers, as described previously. The transfer function is then given by:

$$FTF_{Tot}\left(\omega_d\right)=\frac{1}{2}e^{St_I\left(i-\tilde{S}^0_{T,Disp}\tilde{\sigma}_{T,D}\right)}\left(1-e^{St_{Lf}\left(i-\tilde{S}^0_{T,Disp}\tilde{\sigma}_{T,D}\right)}\right)\left(1-i\tan\left(\theta_0\right)\tilde{\sigma}_{T,C}\right) \tag{3.56}$$

Equation (3.53) and (3.56) are key products of this chapter – they show the explicit dynamical influence of stochastic background fluctuations on the ensemble-averaged heat release oscillations.

Figure 3.9 plots the magnitude and phase of FTF_{Tot} from Equation (3.53). Also, $S^0_{T,C}$ is assumed equal to $S^0_{T,Disp}$ for these calculations. Note that Figure 3.9, which illustrates the linearized flame response, cannot be directly compared to Figure 3.8, which also includes nonlinear effects (leading to harmonics in the flame wrinkling

spectrum and kinematic restoration) and is included to demonstrate the validity of the flame speed closure.

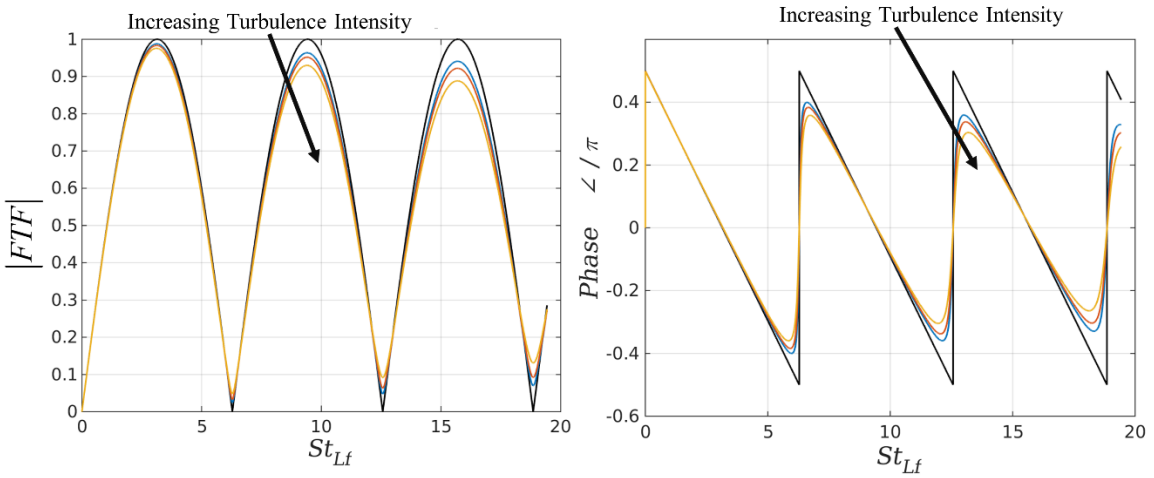

Figure 3.9. Analytical *FTF* gain (left), and phase (right) as a function of St_{Lf}, for a turbulent field with L_{11}/ε = 0.5, $\varepsilon/(u_{S,0}/\omega_d)$ = 0.65, $\sigma_{T,D}/(u_{S,0}/\omega_d)$ = 0.0, 0.0313, 0.0408, and 0.0568, for the turbulence intensities from $u'/u_{S,0}$= 0 to 0.041, respectively.

The key dynamical effect of stochastic background disturbances enters through the turbulent Markstein length terms. Their influence on the model problem gain results can be seen most easily by working from the expansion in Equation (3.54). The magnitude of the small σ expansion is:

$$\left|FTF_{Tot}\left(\omega_d\right)\right| = \frac{1}{2} e^{-St_I \tilde{S}^0_{T,Disp} \tilde{\sigma}_{T,D}} \left(1 - \cos\left(St_{Lf}\right) e^{-St_{Lf} \tilde{S}^0_{T,Disp} \tilde{\sigma}_{T,D}}\right) \qquad (3.57)$$

This expression shows two influences of $\sigma_{T,D}$. First, it causes a general decay in the gain through the term $\exp\left[-St_I \tilde{S}^0_{T,Disp} \tilde{\sigma}_{T,D}\right]$. This decay in gain values at a fixed Strouhal number with increasing turbulence intensity is clearly evident in Figure 3.9.[iv]

[iv] Note, however, that the numerical results and non-linear analytical integration (see Figure 3.8) show that the *FDF* gain can increase with turbulence if the mean flame speed and flame slope changes with downstream distance.

The second effect of stochastic fluctuations is to reduce the influence of the interference term, $1-\cos\left(St_{Lf}\right)\exp\left[-St_{Lf}\tilde{S}^{0}_{T,Disp}\tilde{\sigma}_{T,D}\right]$; thus, increasing $\sigma_{T,D}$ causes the turbulent flame *FTF* to reduce its peak values, but also to increase the gain minima. Again, both of these effects are evident in Figure 3.9. For example, the calculation results in the figure show that the first maximum drops from a value of 1 to about 0.91 at the highest turbulence intensity cases. The Strouhal number exerts a similar influence, as it multiplies $\sigma_{T,D}$, and is therefore responsible for the drop in magnitude of the local maxima with increasing frequency. For example, the highest turbulence intensity case gain has values of 0.91, 0.87, and 0.83 for the first three local maxima.

There are also competing effects in area and burning rate terms. Consider Equation (3.56): the magnitude of the third term, representing fluctuations due to burning rate increases with increasing turbulent Markstein lengths, while the first term, representing area changes decreases. That is, increasing the turbulent displacement Markstein length increases the rate of wrinkle destruction, which reduces the integration limit corrections and therefore the area fluctuations arising from those corrections.

This point can be seen from Figure 3.10, which shows the magnitude of the individual contributions to the *FTF*, where the contribution from the downstream integration limit correction is denoted $FTF_{W,}$ and the upstream integration limit correction is denoted FTF_I; collectively these two contributions are equal to FTF_A. Note that the magnitude of FTF_I stays constant, while the magnitude of FTF_W decreases with increasing Strouhal number. This reflects the fact that at higher St_{Lf} there is more time / distance for flame wrinkles to decay downstream and consequently the area fluctuation and contribution to the *FTF* are reduced.

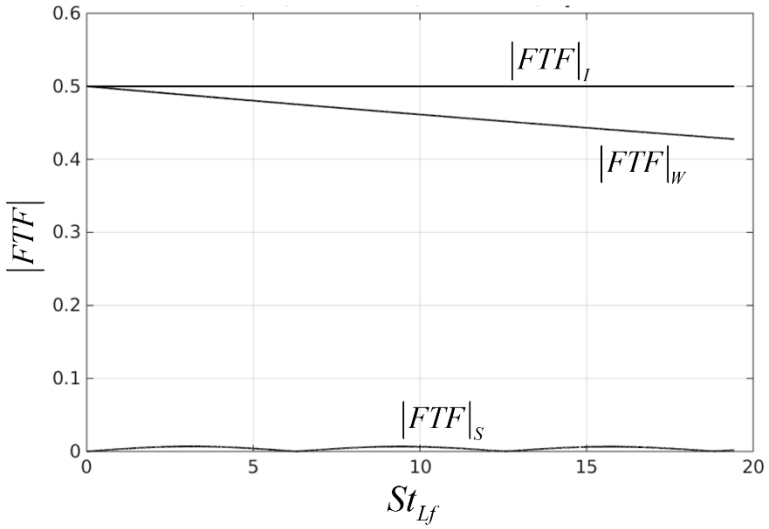

Figure 3.10. Individual contributions to the analytical *FTF*, for a turbulent field with $L_{11}/\varepsilon = 0.5$, $\varepsilon/(u_{S,0}/\omega_d) = 0.65$, $u'/u_{S,0} = 0.01$. FTF_I, FTF_W, and FTF_S are the contributions due to the start correction, wall correction, and consumption speed, respectively.

Additionally, Figure 3.10 shows the contribution due to the non-constant consumption speed, FTF_S, given in Equation (3.52). Clearly, area fluctuations dominate the *FTF*, rather than the consumption speed correction. Ultimately, the small contribution due to the consumption speed correction reflects the fact that the consumption speed differs little from $S^0_{T,Disp}$ for this linear analysis. This is not to say, however, that the effect of $\sigma_{T,D}$ is insignificant. On the contrary, $\sigma_{T,D}$ has a large effect on the *FTF*, but that effect occurs through changes to the flame *area*, rather than the flame *speed*. The right side of Figure 3.9 shows the phase of the analytical *FTFs.* For increasing values of $\sigma_{T,D}$, the phase change across the gain minima becomes smoother.

Comparing the analytical results in Figure 3.9 to the numerical simulation results presented in Figure 3.8, it is clear that this model problem correctly predicts the general qualitative shape of the numerical *FDF* – specifically, the progressive decrease of *FTF* gain maxima, and increase of gain minima, with increasing Strouhal number.

The qualitative features of the phase are also predicted by the model. The phase increases linearly with increasing Strouhal number, jumping across the gain minima. In addition, the stochastic fluctuations smooth the gain jumps, similar to the numerical simulation. Finally, the linear, analytical model clearly displays higher gain maxima values. This difference results from nonlinear effects which spread the heat release response spectral energy over higher harmonics of the forcing frequency, and in turn decrease the amplitude of the *FDF* at the forcing frequency.

3.5.2 Model Problem: Flame Perturbed by Convecting, Decaying Vortex

As described earlier, the oscillating flame holder problem is an important one from a pedagogical perspective. In this section, I consider a problem that has additional complexities, but is of significant interest as a practical problem. Specifically, this section considers the response of a flame to a convecting disturbance, generalizing the laminar *FTF* work previously presented in several studies [53, 65, 131]. While a fully general treatment of this problem requires numerical treatment as in Section 3.4, I consider here a V-flame model problem which is quite similar to several of the prior laminar studies. I retain the same assumptions as in Section 3.5.1, except here the flame holder is fixed and there is a harmonically oscillating flow disturbance, whose component normal to the nominal flame position is given by:

$$u_{n,1} = \text{Real}\left\{ \varepsilon \cdot u_{s,eff} \cdot e^{-\gamma \frac{\omega_d \cdot s}{2\pi u_{s,eff}}} \cdot e^{i \frac{\omega_d \cdot s}{u_C}} \cdot e^{-i\omega_d t} \right\} \tag{3.58}$$

where ε is a non-dimensional velocity perturbation amplitude, γ is a non-dimensional decay rate, and u_c is the velocity disturbance phase speed along the flame coordinate.

The derivation of the flame position and *FTF* are given in Appendix A. The resulting Fourier space fluctuating flame position is:

$$\left\langle \hat{\xi}'\left(\omega_d, s\right)\right\rangle = \frac{e^{sR_1} - e^{s\frac{\omega_d}{u_{s,eff}}P}}{\frac{S^0_{T,Disp}\sigma_{T,D}}{u_{s,eff}}\left(\frac{\omega_d}{u_{s,eff}}\right)^2 P^2 - \frac{\omega_d}{u_{s,eff}}P + i\frac{\omega_d}{u_{s,eff}}}, \qquad P = \left(i\frac{u_{s,eff}}{u_C} - \frac{\gamma}{2\pi}\right) \tag{3.59}$$

This solution can be expanded around small σ values as:

$$\left\langle \hat{\xi}'\left(\omega_d, s\right)\right\rangle = \frac{\exp\left[s\left(\frac{i\omega_d}{u_{s,eff}} - \frac{\omega_d^2 S^0_{T,Disp}\sigma_{T,D}}{u_{s,eff}^{\ 3}}\right)\right] - \exp\left[s\frac{\omega_d}{u_{s,eff}}\left(i\frac{u_{s,eff}}{u_C} - \frac{\gamma}{2\pi}\right)\right]}{\frac{\omega_d}{u_{s,eff}}\left(i - P\right)}\left(1 - \sigma_{T,D}\frac{S^0_{T,Disp}\omega_d P^2}{u_{s,eff}^{\ 2}\left(i-P\right)}\right) \tag{3.60}$$

Non-dimensionalizing the *FTF*, according to the scheme given in Equation (3.55), gives:

$$FTF_{Tot}\left(\omega_d\right) = \frac{e^{St_{L_f}\tilde{P}} - e^{St_{L_f}\tilde{R}_1} + \tan\left(\theta_0\right)\tilde{\sigma}_{T,C}\left[\tilde{R}_1\left(e^{St_{L_f}\tilde{R}_1} - 1\right) + \tilde{P}\left(1 - e^{St_{L_f}\tilde{P}}\right)\right]}{St_{L_f}\left(\tilde{S}^0_{T,Disp}\tilde{\sigma}_{T,D}\tilde{P}^2 - \tilde{P} + i\right)} \tag{3.61}$$

Additionally, Equation (3.61) can be expanded for small turbulent Markstein lengths as:

$$FTF_{Tot}\left(\omega_d\right) = \frac{\left(e^{St_{L_f}\tilde{P}} - e^{St_{L_f}\left(i - \tilde{S}^0_{T,Disp}\tilde{\sigma}_{T,D}\right)}\right)\left(1 - \frac{\tilde{S}^0_{T,Disp}\tilde{P}^2}{\left(i-\tilde{P}\right)}\tilde{\sigma}_{T,D}\right) + \tan\left(\theta_0\right)\tilde{\sigma}_{T,C}\left[i\left(e^{St_{L_f}\left(i - \tilde{S}^0_{T,Disp}\tilde{\sigma}_{T,D}\right)} - 1\right) + \tilde{P}\left(1 - e^{St_{L_f}\tilde{P}}\right)\right]}{St_{Lf}\left(i - \tilde{P}\right)} \tag{3.62}$$

Figure 3.11 shows the *FTF* gain and phase for the convecting, decaying velocity disturbance perturbed V-flame. For comparison to the oscillating flame holder model problem, the same values of $S^0_{T,Disp}$, $\sigma_{T,D}$, and $\sigma_{T,C}$ are used.

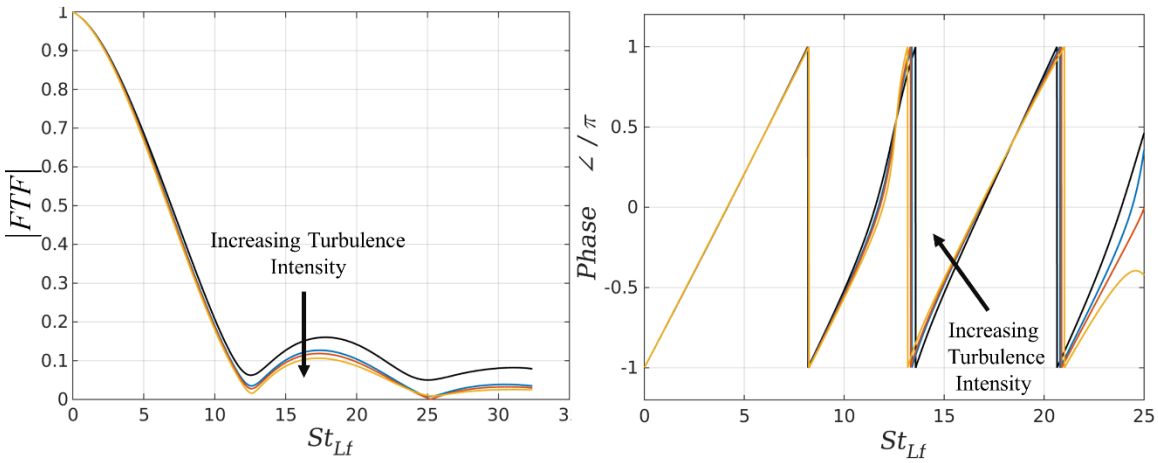

Figure 3.11. Analytical *FTF* gain (left), and phase (right) for a V-flame perturbed by a convecting, decaying velocity perturbation, $u_{S,0}/u_c$ = 0.5, γ = 0.25, as a function of St_{Lf}, for a turbulent field with L_{11}/ε = 0.5, $\varepsilon/(u_{S,0}/\omega_d)$ = 0.65, $\sigma_{T,D}/(u_{S,0}/\omega_d)$ = 0.0, 0.0313, 0.0408, and 0.0568, for the turbulence intensities from $u'/u_{S,0}$ = 0 to 0.041, respectively.

The gain of the *FTF* shows the characteristic magnitude roll-off with increasing Strouhal number. In the bulk forcing case (i.e., $u_{s,eff}/u_c = 0$), with no disturbance velocity decay $(\gamma = 0)$, the turbulent, ensemble-averaged *FTF* reverts to the same as that previously derived for a stretch-sensitive, bulk-forced laminar flame [60, 131]. The effect of increasing turbulence, with a resultant increase in the turbulent Markstein length, is less pronounced for the convecting, decaying velocity disturbance than for the oscillating flame holder model problem, but still results in a similar effect; increasing turbulence decreases the *FTF* gain maxima. The phase plot of the *FTF* shown in Figure 3.11 shows the influence of the convecting velocity disturbance. Note the near linear dependence of the phase with Strouhal number for low Strouhal values, implying that the flame can be described by a lumped, fixed time delay model in this region.

The close correspondence between the *FTFs* at different turbulence intensities indicates why the quasi-laminar approach has been successful for prediction of turbulent flame response to harmonic disturbances. The *FTF* of the convecting, decaying vortex

problem is not as strongly dependent on turbulence intensity, because the presence of the convecting disturbance continuously excites the flame response.

3.6 Conclusions on Reduced Order Turbulent Flame Modeling

This chapter examines the global heat release response of turbulent, premixed, flames subjected to harmonic forcing of the flame holder. The position of the ensemble-averaged flame is determined by application of a definition for the effective turbulent flame speed, given by Shin and Lieuwen [1]. The curvature sensitivity of the ensemble-averaged flame is accounted for by inclusion of a curvature dependent flame speed, which is a function of the turbulent Markstein length. Validation for the closure model is provided by comparison to a numerically simulated flame. For low to moderate turbulence intensities, the model predicts a nearly identical flame shape and closely approximates the gain and phase of *FDF*. Furthermore, these results demonstrate that a key qualitative trend predicted by the burning velocity closure – the progressive decrease in maxima and increase in minima with Strouhal number – is also observed in the ensemble-averaged computational results.

Together, these results show that it is possible to model the response of a turbulent flame perturbed by both narrowband harmonic oscillations and broadband turbulence though analysis of the ensemble-averaged flame, for low to moderate stochastic amplitudes. Furthermore, this approach captures some of the nonlinear effects of turbulence (i.e. kinematic restoration) even in a linearized model. This approach is analogous to that used with laminar flames, and uses a modified flame position equation, as well as an ensemble-averaged flame speed closure with a Markstein like dependence on the ensemble-averaged flame curvature.

Two linear model problems are also presented. The first derives the *FTF* for the oscillating flame holder problem. These linear models show that it is possible to capture several of the key effects of stochastic disturbances on the *FTF*. Specifically, the linear model predicts increasing Strouhal number simultaneously decreases gain maxima and increases gain minima. *FTF* phase trends also qualitatively match the numerical results. The second model problem investigates a flame attached to a stationary flame holder, but perturbed by a convecting decaying velocity fluctuation. Similar to the first model problem, increasing turbulence decreases the gain maxima.

CHAPTER 4. EXPERIMENTAL INVESTIGATION OF TURBULENT, HARMONICALLY FORCED, PREMIXED FLAMES

Chapter 3 demonstrated that the use of the ensemble-averaged flame speed closure, Equation (2.13), improves predictions of both the spatio-temporal flame position and heat release dynamics. Furthermore, it was shown that the use of this closure model captures some of the non-linear effects due to kinematic restoration even in linear, reduced order models. Thus, this flame speed closure shows promise in modeling ensemble-averaged turbulent flame dynamics. So far, however, the justification for its use is predicated entirely on isothermal numerical simulations and theoretical investigations. The purpose of this chapter is to investigate the spatio-temporal dynamics of the ensemble-averaged flame and flame speed closure through *experimental* investigations.

The rest of this chapter is organized as follows. First, a description of the experimental facility is given, describing the burner configuration and the method of harmonic forcing. The following subsections describe the image processing steps necessary for determining the ensemble-averaged flame position and ensemble-averaged velocity fields. Then, results and discussion of the ensemble-averaged flame position and burning speed are presented in Section 4.3. Lastly, Section 4.5 provides conclusions from this experimental work.

4.1 Experimental Methods

Because this chapter examines the *experimentally* determined ensemble-averaged turbulent flame position and turbulent displacement speed, the isothermal assumption is

clearly inapplicable. As a result, the flow field can no longer be considered to be decoupled from the flame dynamics. For a confined, anchored flame, the products will accelerate due to dilatation associated with the flame's heat release. In recognition of this difference, a slight modification of Equation (3.26) is used in calculating the ensemble-averaged turbulent displacement speed, $S_{T,Disp}$.

$$S_{T,Disp}\left(s,z,\hat{t}\right) \equiv \frac{\frac{\partial\left\langle \xi\left(s,\hat{t}\right)\right\rangle}{\partial\hat{t}} + \left\langle \underset{\sim}{u}_s\left(s,\hat{t}\right)\right\rangle \frac{\partial\left\langle \xi\left(s,\hat{t}\right)\right\rangle}{\partial s} - \left\langle \underset{\sim}{u}_n\left(s,\hat{t}\right)\right\rangle}{\left[1+\left(\partial\left\langle \xi\left(s,\hat{t}\right)\right\rangle / \partial s\right)^2\right]^{1/2}} \tag{4.1}$$

where, $\hat{t}$ is the phase time (i.e. the time associated with a specific point of phase in the forcing cycle, and used to differentiate from instantaneous quantities), and $\underset{\sim}{u}$ indicates the reactant conditioned ensemble-averaged velocity field. Formally, this definition for $S_{T,Disp}$ is identical to the two-dimensional version of the definition given in Equation (3.26), because in the isothermal case, the reactant conditioned velocity field is equal to the non-conditioned velocity field. This modified nomenclature is introduced here for specificity, as well as to clarify the definition for future work.

4.1.1 Experimental Setup

Like the isothermal work discussed in Chapter 3, the experimental work presented here examines a turbulent, premixed flame attached to an oscillating flame holder. The experiment is conducted in an atmospheric, premixed methane-air facility. The equivalence ratio, calculated laminar flame speed and thickness are given in below in Table 4.1, for the various mean flow velocities and blockage ratios (discussed below). The laminar flame speed, S_L^0, is based on a Chemkin [132] PREMIX calculation using

the GRIMech 3.0 mechanism [133]. The flame thickness is determined from the reactant and product temperature and maximum gradient, i.e. $\ell_F = \left(T^b - T^u\right) \big/ \max(dT/dx)$.

Table 4.1. Equivalence ratio and calculated unstretched laminar flame speed and flame thickness at each experimental flow condition.

$U_{x,0}$	Blockage Ratio (%)	Equiv. Ratio	S_L^0 (m/s)	ℓ_F (mm)
5 m/s	0	0.95	0.36	0.44
	69	0.97	0.37	0.44
	94	0.98	0.37	0.44
	97	0.97	0.37	0.44
8 m/s	0	0.91	0.34	0.46
	69	0.92	0.35	0.45
	94	0.91	0.34	0.46
	97	0.91	0.34	0.46

A schematic of the experimental setup is shown in Figure 4.1. The burner test section consists of a circular jet with an exit diameter of 27.4 mm, surrounded by a velocity-matched, annular co-flow, with a diameter of 36.3 mm. The mean flow, $U_{x,0}$, is from bottom to top. The bluff body is held approximately 10 mm above the exit plane, bisecting the jet. The bluff body is a 20 AWG (0.81 mm) nichrome wire.

The wire is heated by application of a 6-12 V AC current. The nichrome wire oscillates transverse to the mean jet flow, driven harmonically at the forcing frequency by two modified 90 W Goldwood speakers (see Figure 4.1). The speakers are connected in parallel to the fixture which holds the oscillating flame holder. The driving signal is created by a function generator and amplified using two linear amplifiers, one for each speaker.

Fuel and air enter the burner at its base through four inlet ports. The flow then passes through a metal screen which mixes the fuel-air mixture and supports a bed of ball-bearings above the screen. After the ball-bearing bed, the fuel-air mix continues

through a settling plenum before passing through the variable turbulence generation plates. The turbulence generator consists of two plates with several pie-shaped slots cut through them and is detailed in Marshall et al. [134].

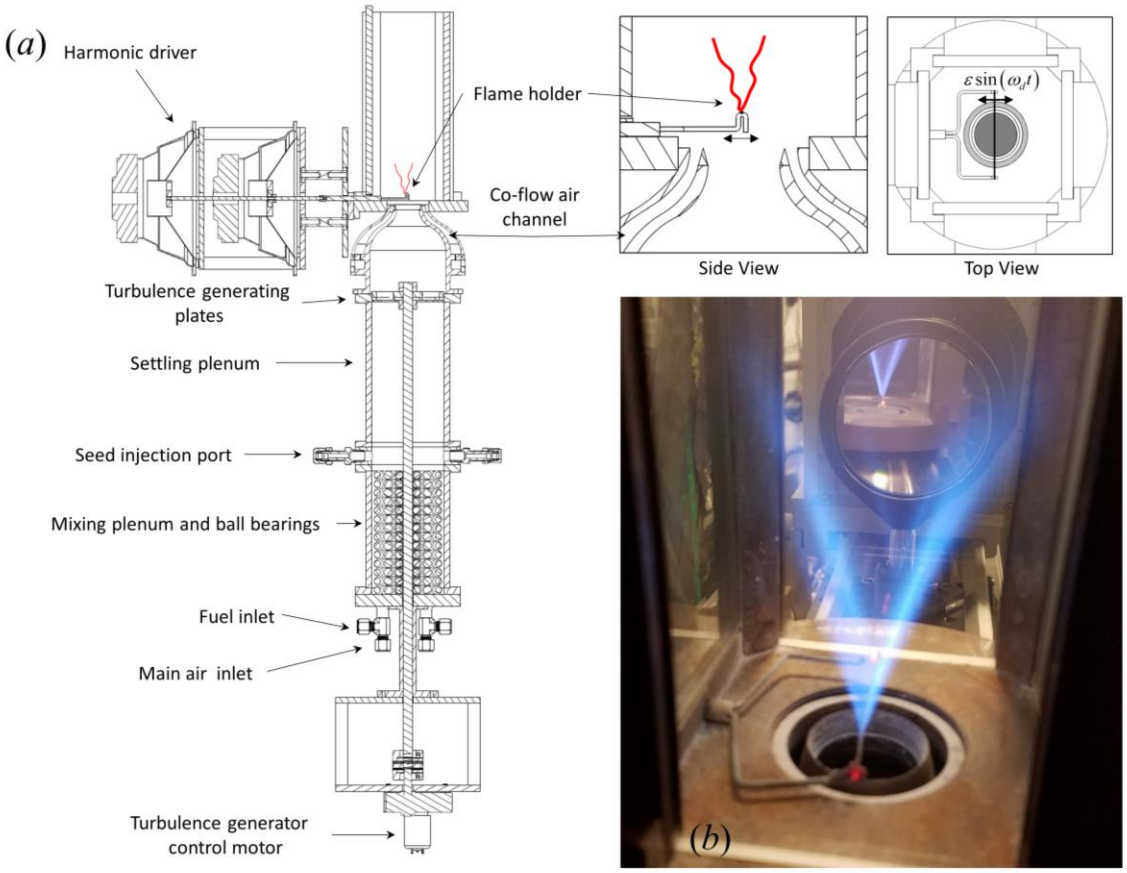

Figure 4.1. (*a*) A schematic of the experimental facility, showing major burner components, and (*b*) an image of the experimental facility in use, showing the V-flame and oscillating flame holder.

The bottom plate is fixed, while the top plate can rotate over a 28^{o} range. By changing the relative angle between the top and bottom plates, the blockage ratio can be varied from 69-97%. The plate angle is measured from a compass, with an uncertainty of ±0.25^{o}. This turbulence generation system allows the independent variation of the mean flow velocity and turbulence level. For the lowest turbulence case, the plates are removed entirely. However, even in this case the flow has a low turbulence level. After the

turbulent generation plates, the flow passes through a contoured nozzle, designed to create a uniform top-hat velocity profile at the plane of the jet exit.

The main air supply is metered using an Aalborg GFC-67, 0-500 L/min mass flow controller, while the fuel is metered using an Omega FMA-5428, 0-50 L/min mass flow controller. Co-flow air is metered using an Omega FMA-1843 gas flow meter and manual needle valve. The main air and fuel mass flow controllers are controlled using LabVIEW. The co-flow air is adjusted to match the main jet velocity.

Mie scattering is used both to detect the flame edge and quantify the velocity field using particle image velocimetry (PIV). Images are taken using a Photron Fastcam SA5 high speed video camera with a Nikon Micro-Nikkor f=55m f/2.8 lens, set to a resolution of 768 x 848 pixels for the 200 Hz and 750 Hz cases and 640 x 848 pixels for the 1250 Hz case. A bandpass filter is used to minimize off-frequency light. The camera is triggered by a timing box tied to the laser pulse from a dual head, frequency doubled Litron Nd:YLF, 527 nm laser. The laser is formed into a vertical sheet, approximately 6 cm high and 1 mm thick. The laser and optical setup are shown in Figure 4.2.

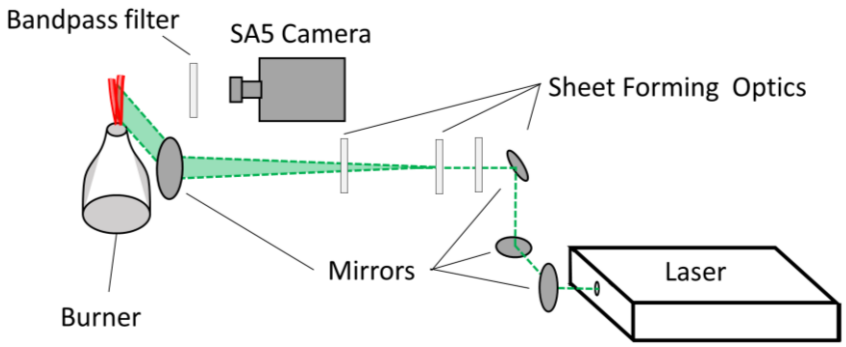

Figure 4.2. Schematic of laser and camera setup.

Titanium oxide (TiO_2) seed particles, with a nominal diameter of 1 micron are added to the flow by diverting a portion of the main air (prior to mixing with the fuel)

through a small cyclone seeder. The seeded flow re-enters the main flow upstream of the settling plenum and prior to the turbulence generator. Cold flow tests show the seed to be well-mixed with the main flow. The co-flow is unseeded.

Three forcing frequencies (200 Hz, 750 Hz, and 1250 Hz) are investigated at two nominal mean, axial flow velocities (5 m/s and 8 m/s), denoted as $U_{x,0}$, and four turbulence intensities each ($u'/u_{x,0} \approx 8-32\%$), where u' is the root mean square of the turbulent velocity fluctuations, and $u_{x,0}$ is the mean measured axial flow velocity. For the 200 Hz cases, pairs of images are recorded at 2000 Hz. For the 750 Hz and 1250 Hz cases, a sequence of images is taken at 7500 Hz and 12500 Hz, respectively. These acquisition rates result in 10 samples per forcing cycle for all conditions and, by virtue of being a nearly exact integer multiple of the forcing frequency, virtually eliminate spectral leakage bias errors in spectral estimation. The total number of image pairs is 8790, 17580, and 21095, for the 200 Hz, 750 Hz, and 1250 Hz cases, respectively.

PIV processing is accomplished with LaVision DaVis PIV software [135], using a multipass algorithm. The first pass uses a 48 x 48-pixel interrogation window, with 25% overlap between windows, while two subsequent passes use an 8 x 8-pixel window, with a 25% overlap. This yields a resolution 6 pixels (~0.46 mm) between vectors. However, note that due to the window overlap, adjacent velocity vectors are not completely independent. The uncertainty of these measurements and calculations is discussed in Section 4.2.3.

4.2 Image and Data Processing

4.2.1 Image Processing Procedure

This section details the steps used to extract ensemble-averaged flame edge and flow field data. The raw images collected during the experimental run are first de-warped using LaVision's DaVis PIV processing software [135]. This step corrects image distortion due to the presence of the quartz window and provides physical reference coordinates for the images. Figure 4.3 shows four representative images of the flame at different conditions, at this stage of processing.

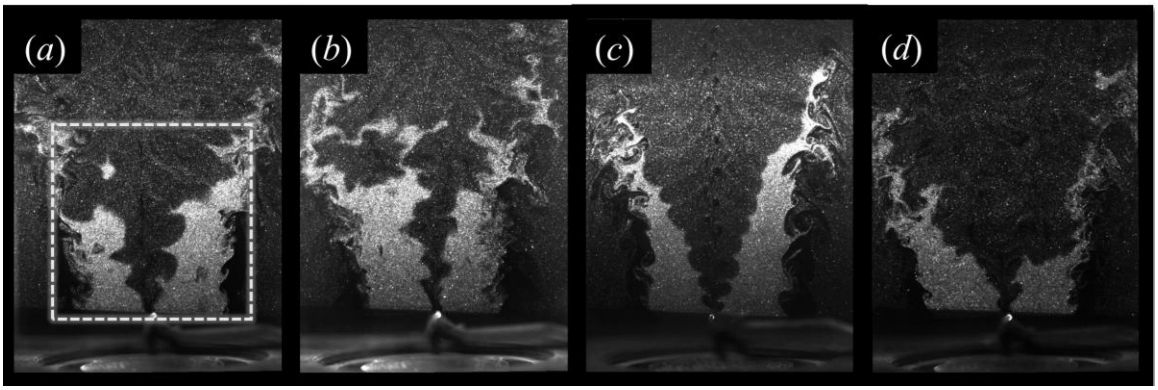

Figure 4.3. Four representative instantaneous flame images, at (*a*) f_0 = 750 Hz, $u_{x,0}$ = 4.2 m/s, $u' / u_{x,0}$ = 26.8%, (*b*) f_0 = 750 Hz, $u_{x,0}$ = 7.1 m/s, $u' / u_{x,0}$ = 25.5%, (*c*) f_0 = 1250 Hz, $u_{x,0}$ = 4.2 m/s, $u' / u_{x,0}$ = 12.2%, (*c*) f_0 = 1250 Hz, $u_{x,0}$ = 6.7 m/s, $u' / u_{x,0}$ = 28.0%. Image (*a*) shows the cropped region.

If necessary, the strength of unwanted reflections is reduced using a sliding minimum subtraction method. This algorithm subtracts a weighted minimum intensity value (determined over a set number of images at a given point of phase) at each pixel, effectively removing persistently bright pixels. However, for most cases this step was not required. Next, axial (i.e. flow direction) variation in the image brightness, resulting from laser sheet intensity variation, is normalized. This normalization uses the average

brightness of a region with recirculating seed and illuminated by the laser, but beyond the edge of the jet as a reference. The normalization is accomplished by dividing each row in the image by the corresponding row in the intensity reference multiplied by a weighting factor. After normalizing the images, they are filtered using a Gaussian filter, which removes high frequency noise, and then filtered with an edge-preserving bilateral filter.

The images are cropped to a region containing the flame, reactants, and the region downstream of the co-flow, as the flame expands into this region due to flow divergence around the flame, as shown in Figure 4.3 and Figure 4.4. The cropped images are binarized using a weighted threshold based on Otsu's method [136]. This produces a series of instantaneous, binary flame images, an example of which is shown in Figure 4.4.

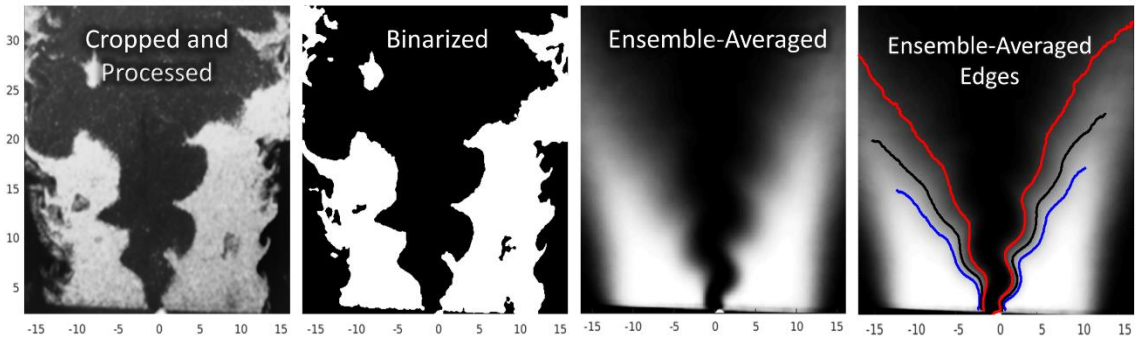

Figure 4.4. Identification of ensemble-averaged flame edges from instantaneous flame images, at $u_{x,0}$ = 4.2 m/s, $u'/u_{x,0}$ = 26.5%, and f_0 = 750 Hz. Ensemble-averaged edge shown at $\bar{C}$ = 0.2 (blue), $\bar{C}$ = 0.5 (black), and $\bar{C}$ = 0.8 (red). Dimensions shown are in mm.

In order to determine the ensemble-averaged flame edge, the set of instantaneous binary images at a given phase in the forcing cycle are averaged together. This produces an ensemble-averaged progress variable field, which varies from zero in the reactants to unity in the products. The ensemble-averaged flame edge associated with some reference progress variable contour is then extracted, as shown in the fourth image in Figure 4.4. Note that the coherent harmonic wrinkle, initially obscured by the turbulent fluctuations,

becomes evident after ensemble-averaging. The result of these processing steps is the physical location of the ensemble-averaged flame edge, at each phase in the forcing cycle. Note that because flame locations are determined by averaging a series of binary images, the resulting flame positions reflect the *median* location of the flames rather than the arithmetic *mean* of the flame locations. This difference is discussed further in Appendix B, and also in reference [1].

4.2.2 Ensemble-Averaged Flame and Flow Field

Figure 4.5 shows a simple schematic of the flame geometry, and the coordinate systems used in defining the ensemble-averaged flame wrinkles. The *s*-coordinate is defined as the mean flame position. Although the mean flame position is not exactly a straight line, it is nearly so: linear regressions on the full mean flame yield an average correlation coefficient (R^2) value of 0.97, with the lowest observed $R^2 = 0.91$.

Determination of the fluctuating, ensemble-averaged flame position, and reduction of noise inherent in the experimental data, requires several processing steps. These processing steps are needed because the edge data extracted from the ensemble-averaged progress variable fields is subject to spatial aliasing. In order to remove noise in the extracted data, the ensemble-averaged flame edge is fit with a smoothing spline curve. Only minimal smoothing is necessary, and the interpolated flame edges fit the original edge data well, with $R^2 > 0.99$ for all cases.

The ensemble-averaged, fluctuating flame position as a function of the *s* coordinate, $\xi_1\left(s,\hat{t}\right)$, is extracted from the ensemble-averaged flame edge data (see Figure 4.5) by determining the perpendicular distance from the mean flame to the ensemble-

averaged flame (using a normal vector defined from a linear regression with a sliding stencil on the mean flame), at each *s* location on the mean flame, and at each phase. The flame position is defined as positive towards the reactants, regardless of whether it is the left or right flame edge, as shown in Figure 4.5.

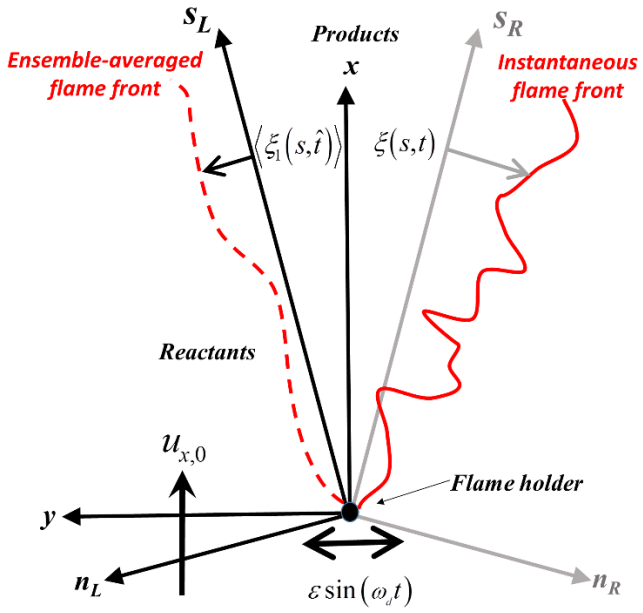

Figure 4.5. Schematic of the coordinate system, ensemble-averaged turbulent flame (dashed), and instantaneous flame (solid). The excitation amplitude is ε, ω_d is the radial driving frequency.

The result of these processing steps are ensemble-averaged, fluctuating flame positions, as shown in Figure 4.8, which is discussed further in the next section. While the instantaneous flame may be highly corrugated, the ensemble-averaged flame is relatively smooth. In fact, the ensemble-averaged flame actually becomes smoother with increasing turbulence intensity due to the kinematic restoration effect discussed earlier, even while the instantaneous flame becomes more wrinkled.

The velocity field is determined using PIV measurements, as described previously in Section 4.1.1. Representative instantaneous flow results, with the instantaneous and

ensemble-averaged flame position are shown in Figure 4.6. The velocity fields are ensemble-averaged by averaging the instantaneous, reactant conditioned, velocity fields at a given phase of the forcing cycle. Reactant conditioning is carried out by only including velocity values from the reactants, upstream of the instantaneous flame. This averaging procedure produces ensemble-averaged, reactant-conditioned velocity fields, $\underset{\frown}{u}$, which are a function of spatial location and phase.

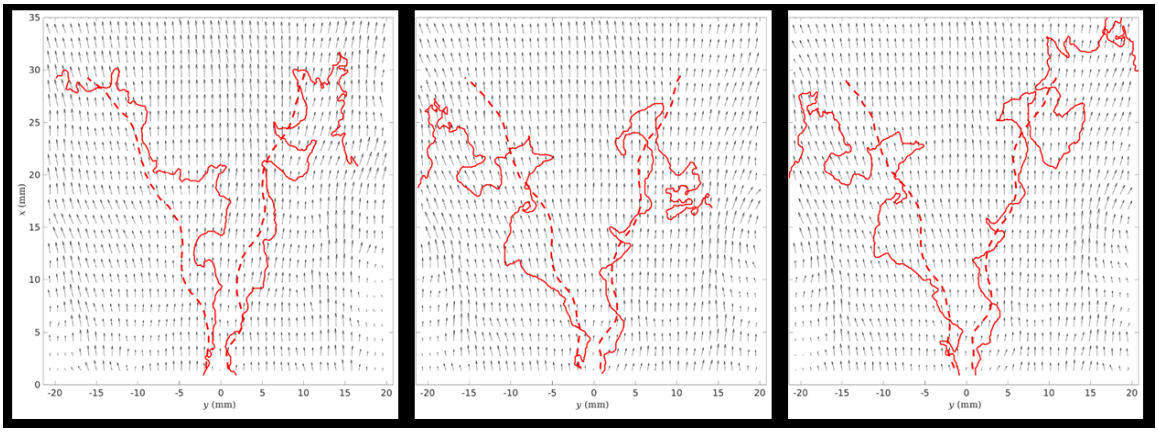

Figure 4.6. Representative instantaneous flow field and flame edge (solid) and ensemble-averaged flame edge (dashed), at $u_{x,0}$ = 7.2 m/s, $u'/u_{x,0}$ = 25.6%, and f_0 = 750 Hz. Phase increases from left to right, in increments of $\Delta\hat{t}/T$ = 0.10, where T is the cycle period.

In addition to the ensemble-averaged velocity field, calculation of the ensemble-averaged turbulent burning speed, $S_{T,Disp}$, (defined in Equation (4.1)) requires the first derivative of the flame with respect to s. This is computed by fitting a spline to the ensemble-averaged flame fluctuation. The first (and second) derivatives can then be calculated from the spline fit. Note that the second derivative is required for calculation of the ensemble-averaged flame curvature. This fitting procedure is used in order to minimize the amplification of noise which otherwise occurs when finding finite difference approximations to derivatives.

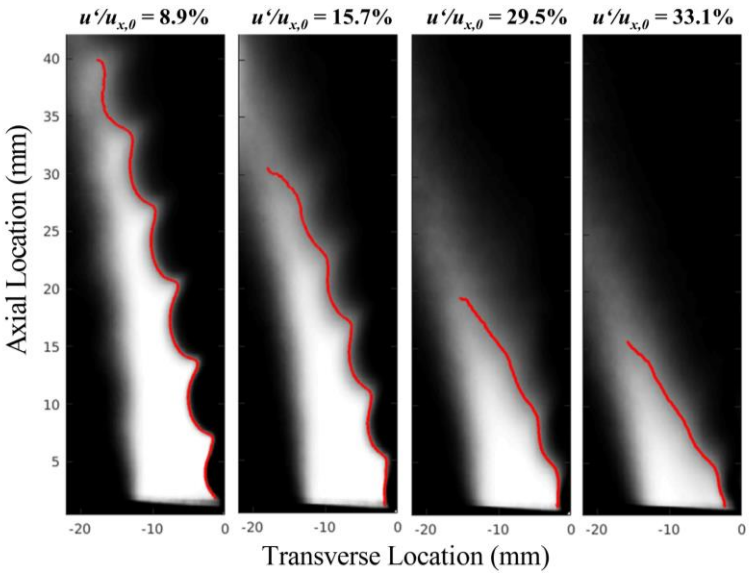

Figure 4.7. Ensemble-averaged flame at $\bar{C} = 0.5$ and progress variable field showing the decrease in wrinkling amplitude and degree of cusping with increasing turbulence intensity, f_0 = 750 Hz, $u_{x,0}$ = 4.9, 4.7, 4.1, and 3.8 m/s, from left to right.

Derivatives in the phase domain are computed using a weighted essentially non-oscillatory (WENO) derivative algorithm [129]. This is necessary because the change of flame position in time can be discontinuous as a result of strong cusp formation. These strong cusps are particularly evident at the lowest turbulence intensities, while increasing turbulence intensity significantly decreases their magnitude, as shown in Figure 4.7. The WENO derivative is designed to accurately measure the derivative of a function with such discontinuous derivatives.

4.2.3 Uncertainty Analysis

Uncertainty in flame position is determined by comparison of raw, instantaneous flame images with the algorithmically determined instantaneous flame edge. The thickness of the flame edge is manually adjusted until it overlaps the apparent flame edge based on the raw image. The thickness is recorded, and this procedure is repeated for 55 images for each data set. A one-sided, 95% confidence interval is calculated for each set

of thickness values, and this measurement is taken to be the uncertainty in instantaneous flame position.

In order to determine the uncertainty of the calculated ensemble-averaged turbulent flame speeds, the ensemble-averaged flame edge uncertainty is calculated from the instantaneous flame edge uncertainty, using standard propagation of uncertainty techniques [137]. However, because of the complexity of the processing algorithms used to extract the ensemble-averaged flame and flow fields used in the calculation of the ensemble-averaged turbulent burning speed, $S_{T,Disp}$, a Monte-Carlo approach is adopted in order to determine flame speed uncertainty.

This is accomplished by first creating a synthetic progress variable field which is qualitatively similar to the actual data, but based on a known analytical function. The analytical function has the same number of phase points, and the same approximate shape, wrinkle magnitude, and convection speed as the experimental data. Gaussian noise with a specified mean and standard deviation, determined from the ensemble-averaged flame position data (discussed above), is introduced. Similarly, synthetic velocity fields with the same mean axial velocity are created. Noise is introduced in this synthetic velocity data based on the mean axial velocity, frame position, time delay between PIV image pairs, number of velocity data points included in each phase average, pixel size, and uncertainty in the calibration plate used for PIV analysis, as discussed further below.

The synthetic data is processed using the same algorithm as that used for the actual experimental data. Uncertainty is determined by comparison of relevant quantities (i.e. derivatives of flame position and velocity) with the known, analytical function on which the synthetic data is based. For each quantity, a one-sided, 95% confidence interval

is determined and this value is used to find the relative uncertainty in a given quantity. Finally, the uncertainty of an actual specific ensemble-averaged flame speed data point is determined using standard error propagation techniques, which provides final uncertainty estimates that vary depending on the magnitude of measured quantities (i.e. an uncertainty is found for each data point). Uncertainties in averaged quantities are again determined using standard uncertainty propagation techniques.

The turbulent Markstein length, $\sigma_{T,D}$, and uncurved turbulent flame speed, $S^0_{T,Disp}$, are calculated from the slope and intercept of an orthogonal regression between the $S_{T,Disp}$ and $\langle C \rangle$ values, as discussed in Section 4.4. To characterize the uncertainty in $\sigma_{T,D}$ and $S^0_{T,Disp}$ a Monte Carlo approach is also used. Synthetic data is created by drawing from a normal distribution with a mean equal to the calculated experimental data value and a standard deviation equal to one half the same data point's uncertainty. These synthetic data are generated in each flame curvature bin, as shown in Figure 4.16. Estimates of $\sigma_{T,D}$ and $S^0_{T,Disp}$ are determined from 1000 independently generated realizations. A 95%, two-sided confidence interval based on these 1000 synthetic values of $\sigma_{T,D}$ and $S^0_{T,Disp}$ provides the uncertainty estimate.

Uncertainty estimates of the instantaneous PIV flow field measurements are based on four factors: out of plane particle movement, particle aliasing due to pixel resolution, calibration error due to pixel resolution, and the manufacturing tolerance of the calibration plate. The effect of out of plane particle movement increases from zero at the center of the image to approximately 20% at the edges of the image. The uncertainty in the particle position due to finite resolution is estimated as 10% of the pixel size.

Similarly, the uncertainty of the calibration due to finite pixel resolution is estimated as 10% of the pixel size. The manufacturing tolerance of the calibration plate is 0.02 mm. The uncertainties resulting from these factors are treated additively. Because these uncertainty estimates depend both on the mean flow velocity and the time delay between images, the uncertainty due to a given factor and the overall uncertainty vary from case to case. Uncertainties due to out of plane motion and particle location are treated as random uncertainties, while the uncertainties resulting from calibration error are treated as bias errors. The resulting PIV uncertainty varies significantly with position for a given case (due to out of plane particle motion) and between cases, due to differences in mean velocity and different time delays between image pairs.

The largest uncertainties in instantaneous, ensemble-averaged, and time averaged velocities are approximately 17%, 6%, and 5%, respectively. The largest uncertainty of the ensemble-averaged velocity fields used for calculation of the ensemble-averaged turbulent displacement speed is approximately 6%.

4.3 Experimental Results and Discussion

This section presents results for the ensemble-averaged flame position and $S_{T,Disp}$. Figure 4.8 shows the ensemble-averaged flame position fluctuation at two forcing frequencies and four turbulence intensities. Each line is the ensemble-averaged flame edge at given phase. Note that harmonic wrinkling is not necessarily evident on the instantaneous flame, but can be seen much more readily by the ensemble-averaging process. Clear harmonic wrinkling of the flame is observed in all cases. In addition, the downstream convection of these flame wrinkles is also evident by the axial translation of the wrinkles at subsequent phases.

At the lowest turbulence intensity and a forcing frequency of 750 Hz, approximately five full spatial periods of oscillation are present on the flame, while at 1250 Hz, there are approximately eight full periods of oscillation, reflecting the reduced convective length scale at 1250 Hz. Representative results from the 750 Hz and 1250 Hz cases are examined in the following discussion and results.

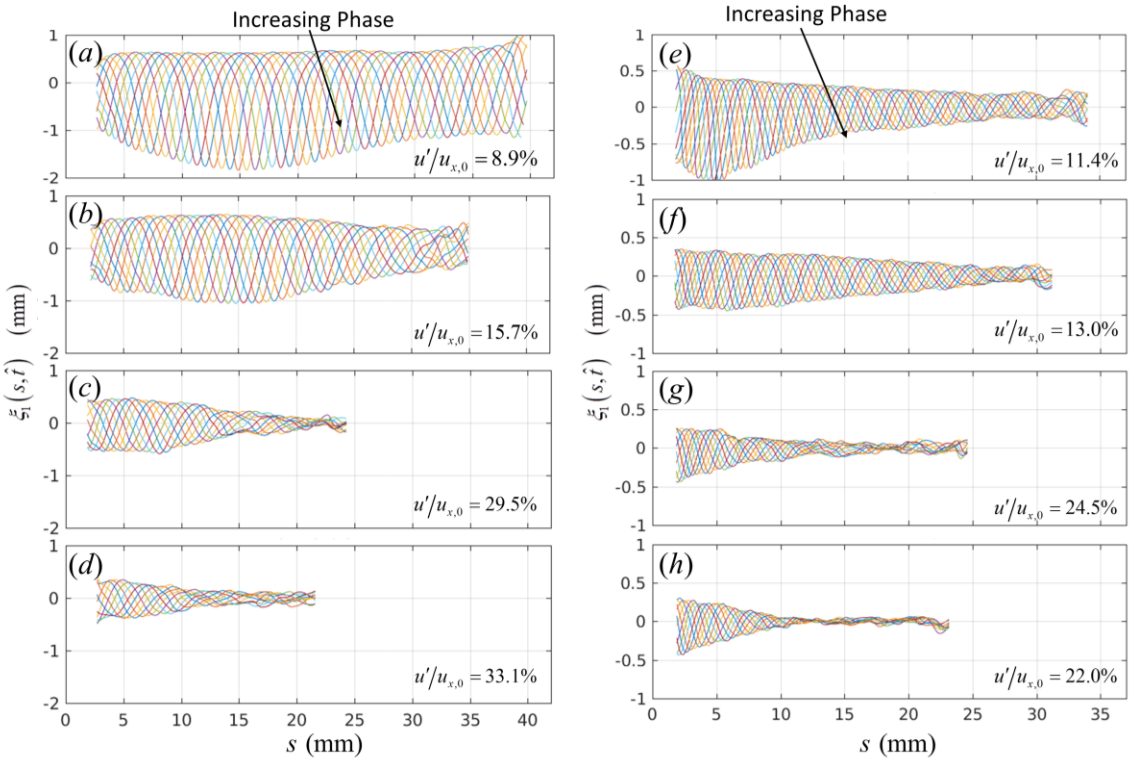

Figure 4.8. Ensemble-averaged flame position fluctuations with increasing turbulence intensity from the left flame edge at f_0 = 750 Hz, $u_{x,0}$ = 4.9, 4.7, 4.1, and 3.8 m/s (*a*-*d*), and for a right flame edge at f_0 = 1250 Hz, $u_{x,0}$ = 4.5, 4.6, 4.3, and 4.4 m/s (*e*-*h*).

As introduced in Section 4.2, the flame positions are the median rather than the arithmetic mean of the flame position. This is most pronounced in the low turbulence intensity cases Figure 4.8(*a*,*e*), where the flame is clearly asymmetrically distributed around the zero location. This effect decreases with increasing turbulence due to the

decrease in the magnitude of the flame position fluctuations, as the median does not reflect the magnitude of outlying events.

One of the most prominent observations from these data is the smoothing effect of turbulent fluctuations on the harmonic flame wrinkle. In the low turbulence cases (Figure 4.8*a,e*) the harmonic flame wrinkles persist beyond the experimentally observable window, while for the high turbulence intensity cases (Figure 4.8*c,d,g,h*) the harmonic wrinkles are damped out to within the measurement tolerance, after approximately 10-20 mm downstream from the flame holder. This smoothing effect increases monotonically with turbulence intensity. This result is consistent with conclusions reached in prior *isothermal* computations from Shin and Lieuwen [1] and Hemchandra et al. [96]. Thus, these results clearly show that turbulent flow disturbances dissipate the magnitude of wrinkles introduced on the flame by acoustic disturbances and/or quasi-coherent large scale vortical structures.

Figure 4.8 also provides an indication of the importance of thermo-diffusive effects on the ensemble-averaged flame response. For lean, methane-air flames, the laminar Markstein length is positive. That is, these flames are thermo-diffusively stable, and therefore the effect of thermo-diffusive effects should act to smooth flame wrinkles. Moreover, because the importance of these effects decreases with increasing turbulence, the most pronounced dependence of the flame on thermo-diffusive effects is expected to occur at the lower turbulence intensities, as discussed previously in Section 2.1.4. However, as shown in Figure 4.8, the largest wrinkle amplitude and even wrinkle *growth* is observed at the lowest turbulence intensities. This is inconsistent with a thermo-

diffusively controlled flame response and indicates that for the mixture composition investigated in this work, these effects are likely to be insignificant.

Isothermal calculations and modeling results suggest that the wrinkle amplitude should decay exponentially with distance downstream. These data clearly show that this is not the case. Rather, the growth/decay in flame wrinkle amplitude is non-monotonic for the two lower turbulence cases at 750 Hz, and the lowest turbulence case at 1250 Hz. For the two lowest turbulence intensities, flame wrinkle amplitude first grows up to an axial position of ~17 mm, in Figure 4.8(*a*) before decreasing further downstream. This non-monotonic behavior is likely due to gas expansion effects which induce phase-coherent velocity disturbances, as discussed next.

Detailed analysis of Figure 4.8 shows the effect of an additional convecting disturbance, for the low and moderate turbulence intensity cases. This disturbance likely results from vortex shedding from the flame. Note that a significant difference between the current work and the previous computational studies is that only an isothermal flame was considered by Shin and Lieuwen [1] and Hemchandra et al. [96], effectively removing the influence of the flame on the flow field. An important effect of heat release (i.e., non-isothermal effects) is that the coherent flame wrinkles modulate the approach flow velocity, also introducing an additional source for coherent wrinkles on the flame.

This coherent velocity disturbance can be seen clearly in the data in Figure 4.9(*a*), which shows the normal component of the reactant conditioned, ensemble-averaged velocity. The figure shows a propagating disturbance on the velocity beyond about $s = 5$ mm. Again, this velocity disturbance is not directly excited in the experiment (only flame

base motion and turbulent flow disturbances are directly excited) – rather, it is an indirect effect due to vortex shedding and gas expansion-induced motion.

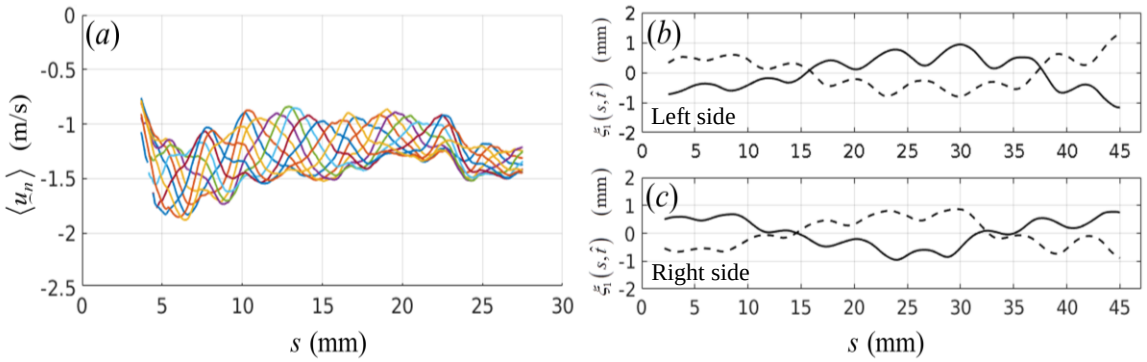

Figure 4.9. (*a*) Ensemble-averaged normal velocity along the right mean flame position (average over all phases), at f_0 = 750 Hz, $u_{x,0}$ = 4.8 m/s, $u'/u_{x,0}$ = 9.3%, (*b*, *c*) Ensemble average flame position, showing the effect of the convecting vortex at two points of phase, $\Delta\hat{t}/T$ = 0 (solid) and $\Delta\hat{t}/T$ = 0.5 (dashed) for (*b*) f_0 = 200 Hz, $u_{x,0}$ = 8.1 m/s, $u'/u_{x,0}$ = 8.8%, and (*c*) f_0 = 200 Hz, $u_{x,0}$ = 8.1 m/s, $u'/u_{x,0}$ = 8.4%.

This harmonic modulation of the disturbance velocity provides an indicator of how important non-isothermal effects are in understanding these interactions. For the result in Figure 4.9(*a*), it shows that the induced disturbance in velocity is about 18% of the mean velocity. This convecting flow disturbance can also be seen in Figure 4.9(*b*,*c*), which plots the ensemble-averaged flame at two points of phase at the lowest frequency for which data were obtained. For this low frequency (f_0 = 200 Hz) case, only approximately three-quarters of the convective wavelength due to the harmonic flame holder movement appears on the flame, enabling more clear separation in scales of the flame wrinkling induced by flame holder motion and convecting velocity disturbances. The smaller scale undulations are the result of a velocity disturbance.

4.4 Turbulent Ensemble-Averaged Burning Velocity

Although the flame position is important in its own right, the ensemble-averaged burning speed, $S_{T,Disp}$, provides insight into how it is temporally modulated by the harmonic disturbances. Values of $S_{T,Disp}$ are determined from the ensemble-averaged velocity and flame edge data, using Equation (4.1). As discussed above, the ensemble-averaged flame develops small-scale wrinkles which are not directly due to harmonic flame holder motion, and these regions are not included in the flame speed calculations as they add significant noise to the calculation of derivatives. For example, in Figure 4.8(*b*) the included region corresponds to s = 4-30 mm.

Note that $S_{T,Disp}$ is a function of both time (or, more precisely, the phase) and space, as opposed to the more familiar turbulent displacement speed which is taken as a time average and, consequently, is only a function of space. The average of $S_{T,Disp}$ over all phases, denoted as $\overline{S}_{T,Disp}$, provides a measure of the spatial dependence of $S_{T,Disp}$, as shown in Figure 4.10. Note that $\overline{S}_{T,Disp}$ is a function of both harmonic disturbance amplitude and turbulence intensity, so all results are shown for constant $\varepsilon \approx 0.32$ mm (Figure 4.10*a*) and $\varepsilon \approx 0.27$ mm (Figure 4.10*b*).

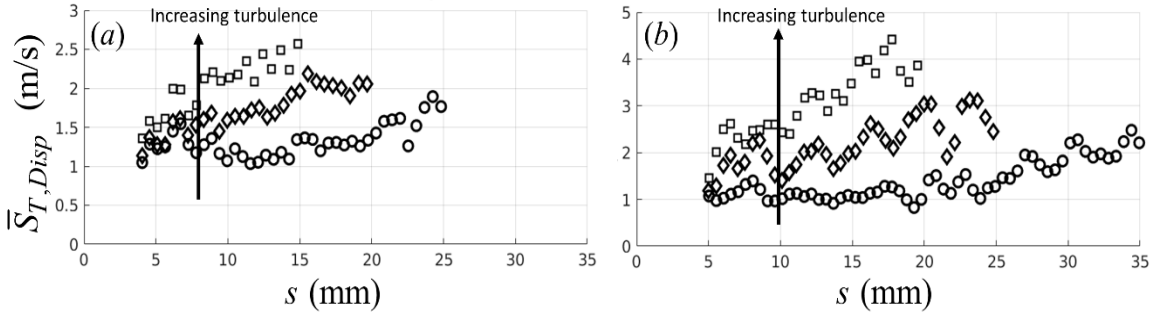

Figure 4.10. Ensemble-averaged turbulent burning speed, averaged over all phases, $\bar{S}_{T,Disp}$, for (a) right flame edge, f_0 = 750 Hz, $u_{x,0}$ = 4.6, 4.3, and 4.4 m/s, and $u'/u_{x,0}$ = 14.6%, 24.4%, and 26.4%, (b) right flame edge, f_0 = 200 Hz, $u_{x,0}$ = 7.8 m/s, 7.2, and 7.1 m/s, and $u'/u_{x,0}$ = 13.1%, 25.5%, and 26.7%, in order of circles, diamonds, and squares, respectively for both cases.

The average ensemble-averaged turbulent burning speed increases in a roughly monotonic fashion with increasing downstream distance. This is a familiar result in anchored flames [138]. In general, $\bar{S}_{T,Disp}$ also increases with increasing turbulence intensity. The value of $\bar{S}_{T,Disp}$ at the higher turbulence intensities is approximately 1.5-4 times greater than at the lowest turbulence intensities, for both forcing frequencies shown. A complete set of average flame speed plots for all cases and turbulence intensities is given in Appendix F.

Consider next the axial dependence of the phase-dependent burning speed, $S_{T,Disp}$. Both the 750 Hz (Figure 4.11) and 1250 Hz (Figure 4.12) cases show significant variations in $S_{T,Disp}$ with the flame coordinate. Several trends are evident - of particular interest are changes in $S_{T,Disp}$ which correspond with the curvature of the ensemble-averaged flame. For instance, Figure 4.11(*a*) shows a series of peaks in the flame speed with the magnitude of the peaks diminishing with the *s* coordinate. In the flame wrinkle plot (Figure 4.11*b*), these peaks generally correspond to regions of negative flame curvature. For example, consider Figure 4.11(*a*) at $s \approx 7$, 11, 13, 17, and 21 mm. The

temporal maxima in flame speed is also noticeable for the higher turbulence intensity Figure 4.11(*c*). However, the maxima are not as sharp, a reflection of the fact that the ensemble-averaged flame is smoother for the higher turbulence intensity case. In other words, $\langle C \rangle$ varies more smoothly at higher turbulence (at increasing *s*) than at the lower turbulence intensity case, where the flame is composed of broad regions of positive curvature, punctuated by relatively narrow regions of strongly negative curvature.

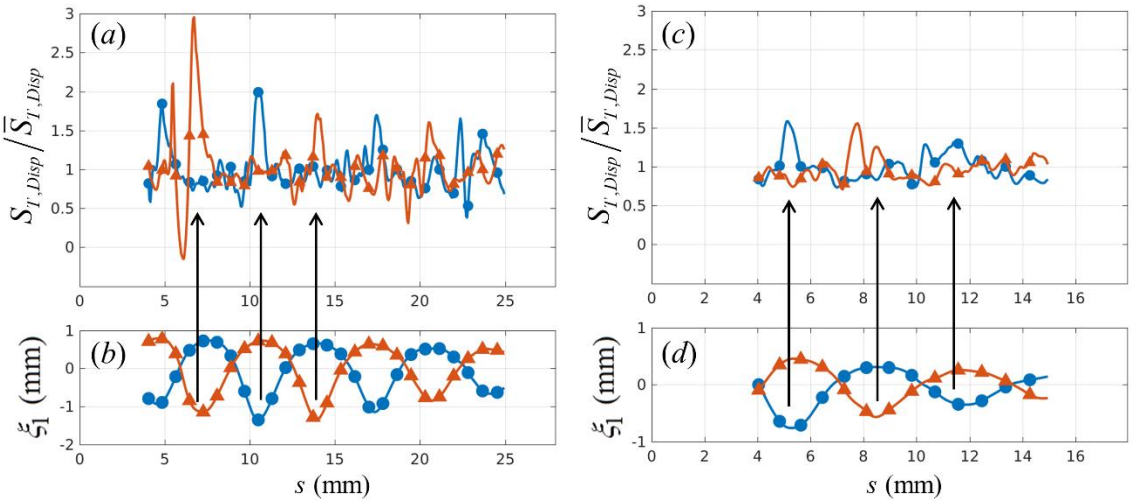

Figure 4.11. Normalized ensemble-averaged turbulent displacement speed (*a,c*) and flame fluctuation (*b, d*) as a function of the flame coordinate, for the right edge at f_0 = 750 Hz, (*a, b*) $u_{x,0}$ = 4.6 m/s, $u'/u_{x,0}$ = 14.6%, and (*c, d*), the right edge at $u_{x,0}$ = 4.4 m/s, $u'/u_{x,0}$ = 26.4% at two phases, $\Delta\hat{t}/T$ = 0 (circles) and $\Delta\hat{t}/T$ = 0.5 (triangles).

This same modulation of $S_{T,Disp}$ is also clear in Figure 4.12, which plots the ensemble-averaged turbulent displacement speed for a 1250 Hz case. Again, there is a distinct correspondence between points of negative curvature and local peaks in the ensemble-averaged turbulent flame speed, for both points of phase shown.

For the lower turbulence intensity case (Figure 4.12*a,b*) the peaks are sharper than for the higher turbulence intensity case (Figure 4.12*c,d*). Again, increased turbulence intensity smooths the flame wrinkles, decreasing the magnitude of ensemble-averaged

flame curvature. Thus, the areas of increased flame speed are also broadened and of lower magnitude. Like the 750 Hz cases (Figure 4.11) the 1250 Hz cases shown in Figure 4.12 also demonstrate diminishing flame speed modulation with downstream distance. As the flame wrinkles decay, so too do the modulations in ensemble-averaged turbulent flame speed. Additionally, the magnitude of flame speed modulation appears reduced at 1250 Hz as compared to the 750 Hz case, due to the somewhat reduced flame wrinkle size, as seen in Figure 4.8.

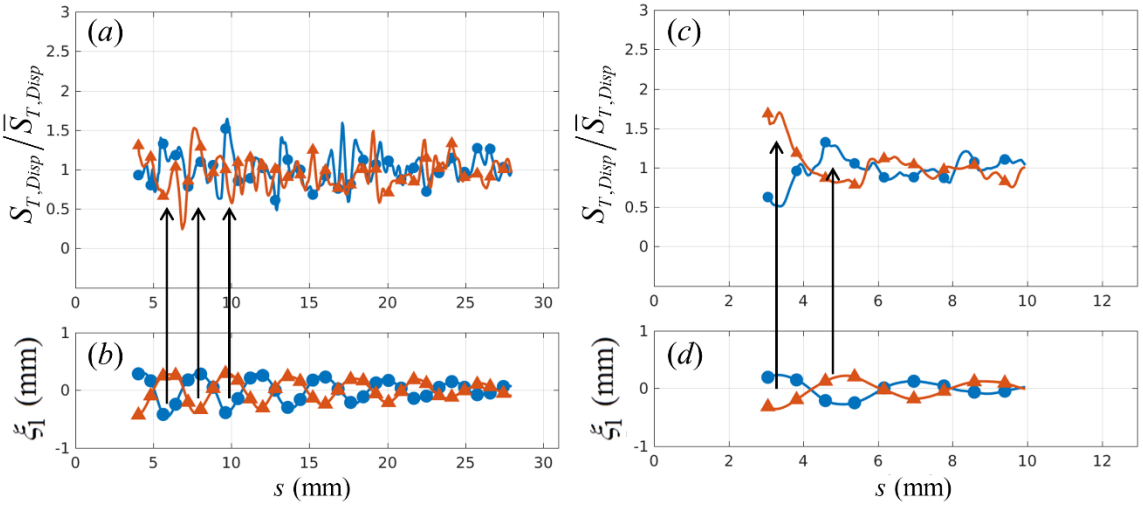

Figure 4.12. Ensemble-averaged turbulent displacement speed (*a, c*) and flame fluctuation (*b, d*) as a function of the flame coordinate, for the right edge at f_0 = 1250 Hz, (*a, b*) $u_{x,0}$ = 4.6 m/s, $u'/u_{x,0}$ = 13.0%, (*c, d*) $u_{x,0}$ = 4.4 m/s, $u'/u_{x,0}$ = 22.0%, at two phases, $\Delta\hat{t}/T$ = 0 (circles) and $\Delta\hat{t}/T$ = 0.5 (triangles).

To further examine modulation of $S_{T,Disp}$, Figure 4.13 shows a PDF plot of the normalized ensemble-averaged displacement speed plotted against the normalized ensemble-averaged curvature. The best fit line in Figure 4.13 and those used in determining the turbulent Markstein lengths shown later are determined by orthogonal linear regression (i.e. a procedure that minimizes the *orthogonal* distance from the best fit line to the data, rather than minimizing either the x or the y distance). The orthogonal

linear regression is the appropriate regression tool when there is uncertainty in both the regression variable and the regressor [139], in this case the experimentally determined ensemble-averaged flame curvature.

Figure 4.13 shows that $S_{T,Disp}$ correlates with $\langle C \rangle$. Specifically, $S_{T,Disp}$ increases with negative ensemble-averaged flame curvature. This point was previously inferred from the analysis of Figure 4.11 and Figure 4.12, but can be seen more directly here.

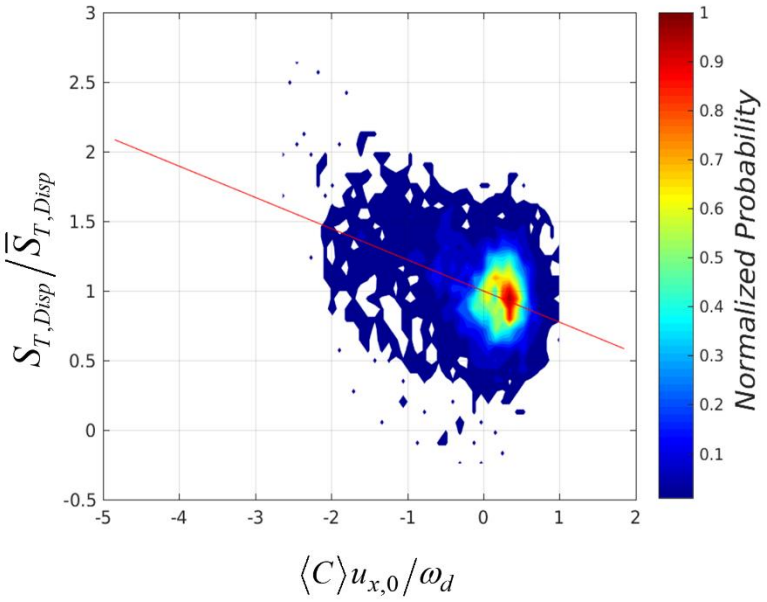

Figure 4.13. PDF plot of the ensemble-averaged turbulent displacement speed versus normalized ensemble-averaged flame curvature for the left edge at f_0 = 750 Hz, $u_{x,0}$ = 4.7 m/s, $u'/u_{x,0}$ = 15.7%. The red line is determined by orthogonal linear regression.

However, while Figure 4.13 provides evidence for this relationship, the relationship between $S_{T,Disp}$ and $\langle C \rangle$ cannot be determined using a straightforward regression analysis, as this leads to significant bias errors because the data is not uniformly distributed in curvature space. Figure 4.13 clearly shows a clustering of data for ensemble-averaged curvatures between zero and unity, which has the effect of biasing

any regression between the two variables towards values in a relatively narrow, positive curvature range. This analysis is concerned with the effect of flame curvature not only at these most probable, positive curvature locations but also for relatively improbable events at large negative flame curvature. Therefore, an additional processing step is utilized to minimize bias error effects due to the nonuniform sampling in curvature space. First, the data is divided into bins for sub-ranges of curvature values. Then, a conditional median value for $S_{T,Disp}$ is determined in each curvature bin where there are at least five data points. The median, rather than a mean, is used so that the value for a given bin is not skewed by outlying data points. Several representative results of this procedure are shown in Figure 4.14 and Figure 4.16.

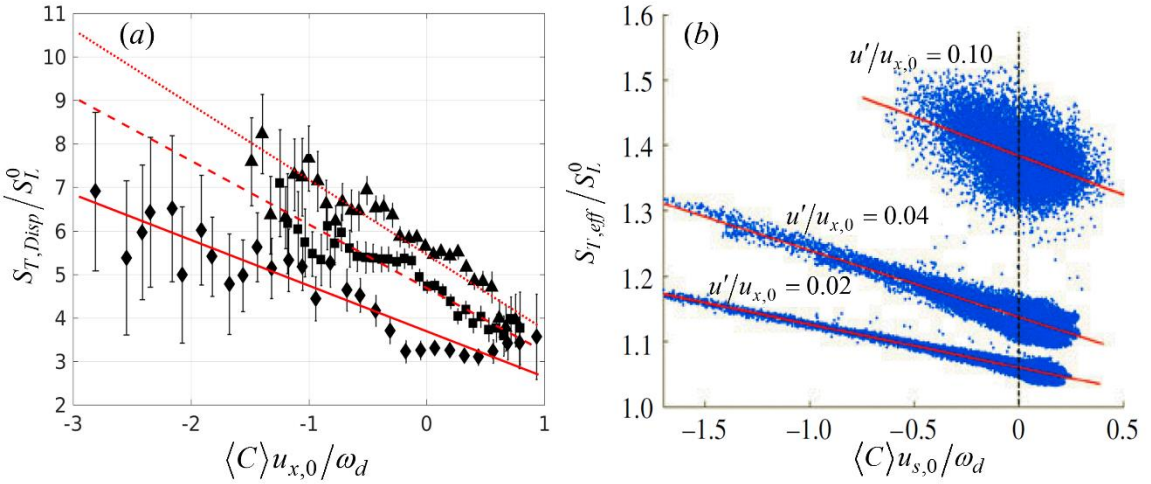

Figure 4.14. (*a*) Dependence of the ensemble-averaged turbulent displacement speed upon ensemble-averaged curvature for the right edge at f_0 = 750 Hz, $U_{x,0}$ = 5.0 m/s, $\bar{C} = 0.5$, for three turbulence intensities, $u_{x,0}$ = 4.7 m/s, $u'/u_{x,0}$ = 15.7% (solid line, diamonds), $u_{x,0}$ = 4.1 m/s, $u'/u_{x,0}$ = 29.5% (dashed line, squares), and $u_{x,0}$ = 3.8 m/s, $u'/u_{x,0}$ = 33.1% (dotted line, triangles), (*b*) Numerical results reproduced from Shin and Lieuwen [1].

These data are the most significant result from this chapter, and clearly show the relationship between curvature and turbulent displacement speed. In particular, they show

the approximately linear rise in $S_{T,Disp}$ with curvature. Note the use of a slightly different non-dimensionalization for curvature in Figure 4.14(*b*). $S_{T,Disp}$ and $S_{T,eff}$ are both defined from Equation (4.1), however, the $S_{T,eff}$ calculation used an ensemble-averaged flame based on the mean, rather than the median, flame location. Figure 4.14(*a*) also shows that, for this case, the uncurved ensemble-averaged turbulent displacement speed, $S^0_{T,Disp}$, (i.e. the intercept of the regression line at zero curvature) and the slope of the regression demonstrate similar sensitivities to increasing turbulence. That is, the uncurved turbulent displacement speed increases with increasing turbulence, and the sensitivity of the flame speed to curvature (as characterized by the slope of the regression line) increases. However, in general the dependence of slope and intercept is not a monotonic function of turbulence intensity, as discussed later. For reference, Figure 4.14(*b*) reproduces a result from Shin and Lieuwen [1], which shows a scatterplot of calculated $S_{T,Disp}$ values (i.e., the data is not averaged in curvature bins as in Figure 4.14(*a*)), also demonstrating an approximately montonic relationship between the ensemble-averaged flame curvature and flame speed. Both results are consistent with the closure in Equation (2.13), previously proposed by Shin and Lieuwen [1].

The dependence of $S_{T,Disp}$ on $\langle C \rangle$ shown in Figure 4.14 and Figure 4.16 results from the interaction between the large-scale, narrowband disturbances due to the harmonic forcing and the small-scale, broadband disturbances due to turbulence. Figure 4.15, reproduced from Section 2.4.1 for reference, illustrates this effect.

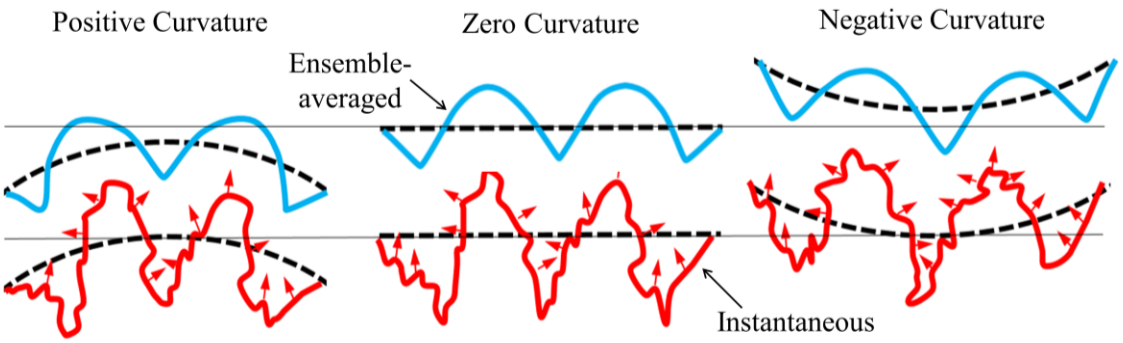

Figure 4.15. Schematic of the interaction of narrowband flame curvature with broadband turbulent wrinkling, following Shin and Lieuwen [1].

For a flame with coherent negative curvature, as shown on the right-hand side of the figure, the distance between opposing flame surfaces will on average be decreased, particularly at the trailing edge of the flame [1]. In turn, this increases the rate at which opposing faces will interact and annihilate one another through kinematic restoration (i.e. the propagation of the flame normal to itself). The net result is that the average flame surface propagates further in the negatively curved case than for positive or neutral curvature over a given time increment.

Similar relationships between $S_{T,Disp}$ and $\langle C \rangle$ were observed for all 750 Hz and 1250 Hz cases, and most 200 Hz cases, as illustrated in Figure 4.16. A full set of the experimental correlations is provided in Appendix G. In these results, $S_{T,Disp}$ is normalized by the *local* average value, $\overline{S}_{T,Disp}$, and denote this quantity as $\tilde{S}_T$, which somewhat reduces the sensitivity of the plots to turbulence intensity and helps identify the spatio-temporal modulation of the phase dependent flame speed. Figure 4.16(*c*) illustrates the relationship of the normalized uncurved turbulent flame speed values, $\tilde{S}_T^0$, and the "normalized turbulent Markstein length," $\mathcal{M}_{T,D}$ to the intercept and slope of the regression line. Note that while $\mathcal{M}_{T,D}$ describes the same fundamental curvature

sensitivity as $\sigma_{T,D}$, because $\sigma_{T,D}$ cannot be recovered from values of $\mathscr{M}_{T,D}$, and vice-versa, $\mathscr{M}_{T,D}$ is not directly proportional to the definition given in Equation (2.13). These normalized values are also non-dimensional.

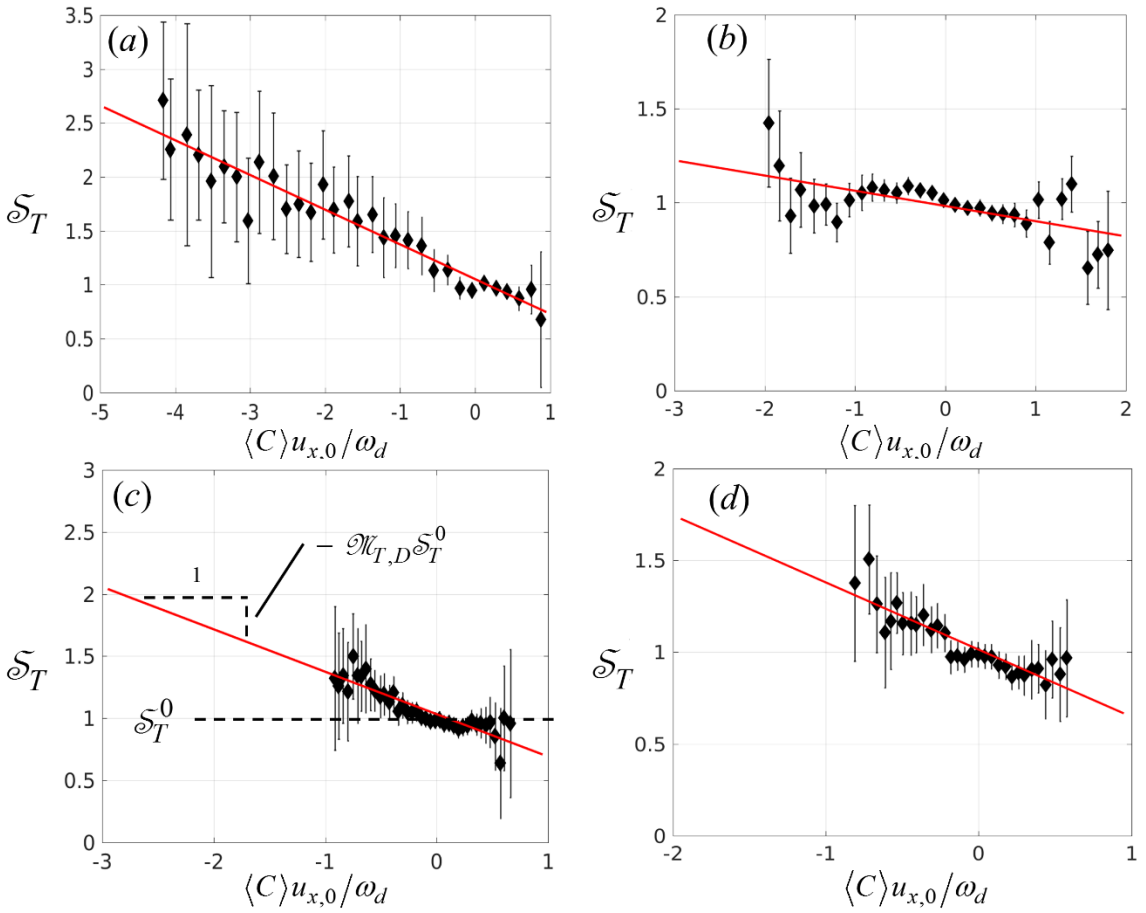

Figure 4.16. Dependence of the normalized ensemble-averaged turbulent displacement speed upon ensemble-averaged curvature at four representative conditions, (*a*) left edge, f_0 = 750 Hz, $u_{x,0}$ = 4.8 m/s, $u'/u_{x,0}$ = 9.3%, $\bar{C} = 0.5$, (*b*) left edge, f_0 = 750 Hz, $u_{x,0}$ = 7.0 m/s, $u'/u_{x,0}$ = 27.3%, $\bar{C} = 0.5$, (*c*) left edge, f_0 = 1250 Hz, $u_{x,0}$ = 4.7 m/s, $u'/u_{x,0}$ = 14.5%, $\bar{C} = 0.5$ (*d*) left edge, f_0 = 1250 Hz, $u_{x,0}$ = 6.2 m/s, $u'/u_{x,0}$ = 32.1%.

Note the consistent flattening of $\mathscr{S}_T$ between approximately zero and unity curvature. This behavior is evident in Figure 4.16(*a*), but also occurs at other conditions and appears to approximately coincide with the region of higher data realizations (see

Figure 4.13). There are two possible explanations: (1) this flattening trend may be a bias error associated with non-uniform sampling of the curvature space. In other words, uncertainty in the curvature causes errors in estimation of the curvature in the high probability data region, (2) this flattening may reflect a real change in the sensitivity of the flame speed to curvature for positive curvature values. As shown in Figure 4.16 (as well as in the full set of results in Appendix G), this flattening trend is a common feature for many of the examined experimental conditions.

If the flattening is a real result, this indicates that for positive curvatures the relationship between curvature and flame speed changes. That is, the turbulent Markstein number may itself be a function of the curvature, demonstrating different values at positive and negative curvatures. As discussed in Section 2.1.4, there are several features of premixed flames which can impact the flame response, including thermo-diffusive effects and the Darrieus-Landau instability. It is unlikely that the thermo-diffusive effect could account for this flattening. That is, for the thermo-diffusively stable reactant mixture examined in this work, this effect should further decrease the flame speed in the positive curvature regions rather than increase (and therefore flatten) the trend.

A second possibility is that this flattening reflects the effect of the Darrieus-Landau instability. This explanation appears more likely as the hydrodynamic instability should cause wrinkle growth and thus would amplify wrinkles with positive curvature. Moreover, as shown in Appendix G, the most pronounced flattening at positive curvatures generally occurs for low and moderate turbulence intensity, where the hydrodynamic is expected to be most significant. Note also that this flattening occurs for

other progress variables, both higher and lower, and is not unique to the choice of the $\bar{C} = 0.5$ definition for the ensemble-averaged flame, as discussed further in Appendix C.

An interesting result of negative $S_{T,Disp}$ values is observed at the lowest turbulence intensities in some cases. Figure 4.17 shows a PDF illustrating the occurrence of some realizations of negative ensemble-averaged turbulent displacement speeds. In these cases, (particularly the 200 Hz, $U_{x,0}$ = 8 m/s cases) negative $S_{T,Disp}$ values were observed at points near flame cusps (See Appendix G for additional results). In most cases the negative flame speeds constitute only a small fraction of the overall realizations (such as shown in Figure 4.13), and these instances fall within the absolute uncertainty of the measurements and calculations. However, the fact that this phenomenon is observed repeatedly (1) at the lowest turbulence intensity, and (2) at locations of strong cusping suggests it is not simply an error. Moreover, it is well known that laminar and turbulent *displacement speeds* can become negative. This occurs when the reference isocontour moves in the same direction as the flow; in contrast, consumption- based flame speed definitions are always positive. For example, in locally laminar flames, negative displacement speeds occur for strongly stretched and curved flames [29, 81, 140, 141]. Of course, it is important to note that the presence of these negative ensemble-averaged turbulent flame speeds is a function of the definition and does not imply that instantaneous flame speeds are negative.

4.4.1 Turbulent Displacement Markstein Numbers

These results, such as those shown in Figure 4.16, can also be used to quantify the sensitivity of the flame speed modulation to curvature. Figure 4.19 shows the results for

the 750 Hz case, while Figure 4.20 shows the results for all cases. The value of $\mathscr{M}_{T,D}$ is estimated separately from both sides of the flame. Because this estimate of $\mathscr{M}_{T,D}$ is prone to noise induced from estimation of derivatives, cases (which differ between the left and right sides of the flame) where there are significant convecting velocity disturbance amplitudes are excluded because this convecting disturbance introduces short length scale flame wrinkles which significantly complicate estimates of flame position derivatives (i.e., see discussion in context of Figure 4.9). This is done by only including cases where the maximum normal velocity perturbation magnitude, averaged over all phases, $\max\left(\bar{u}_{n,1}\right) < 0.55\ S_L^0$.

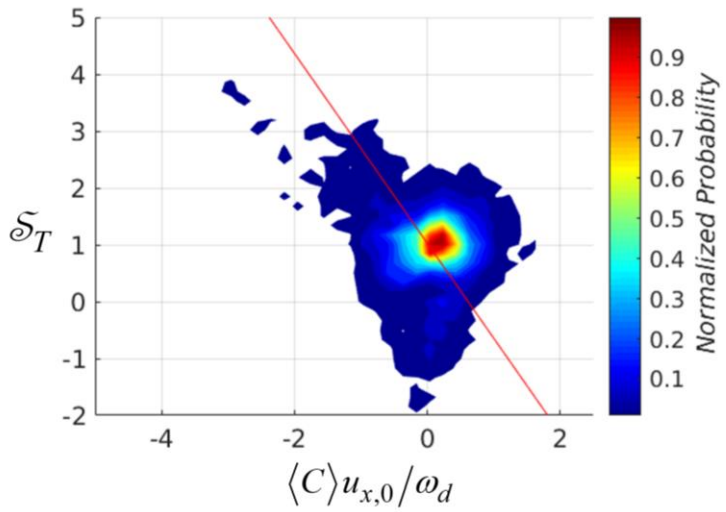

Figure 4.17. PDF plot of ensemble-averaged displacement speed versus ensemble-averaged curvature for a case showing realizations of negative flame speeds for the left edge at f_0 = 750 Hz, $u_{x,0}$ = 7.9 m/s, $u'/u_{x,0}$ = 9.8%.

Figure 4.19(*a*) plots results for the 750 Hz, 5 m/s case. It shows that the non-dimensional turbulent Markstein length is largely insensitive to the turbulence intensity. This is somewhat surprising as earlier isothermal work [1] indicated increasing sensitivity of the ensemble-averaged turbulent displacement speed with turbulence intensity; i.e.,

that $\mathscr{M}_{T,D}$ increases with *u'*. Thus, while Figure 4.19(*a*) and above results confirm the sensitivity of the ensemble-averaged turbulent displacement speed to ensemble-averaged flame curvature, it indicates that this this sensitivity does not increase with increasing turbulence. A potential resolution between these results is that that the turbulence intensity examined in this work is significantly higher than that examined by Shin and Lieuwen [1]. In fact, the *highest* turbulence intensity examined by Shin and Lieuwen [1] is approximately equal to the *lowest* turbulence intensity examined in the current work (e.g. $u'/u_{x,0} \approx 0.10$, $u'/S_L^0 \approx 0.40$). Thus, one possibility is that the increase in sensitivity observed previously occurs at relatively low turbulence intensity but saturates at higher turbulence levels.

Indeed, there is good physical reason to expect such saturation; i.e., if the sensitivity of the ensemble-averaged flame speed to curvature occurs due to mutual interaction and annihilation of opposing flame faces in negatively curved regions, as proposed by Shin and Lieuwen [1] and discussed above in relation to Figure 4.15, it seems likely that this mechanism would saturate at stronger turbulence, because once the flame faces interact, the mechanism of interaction is eliminated.

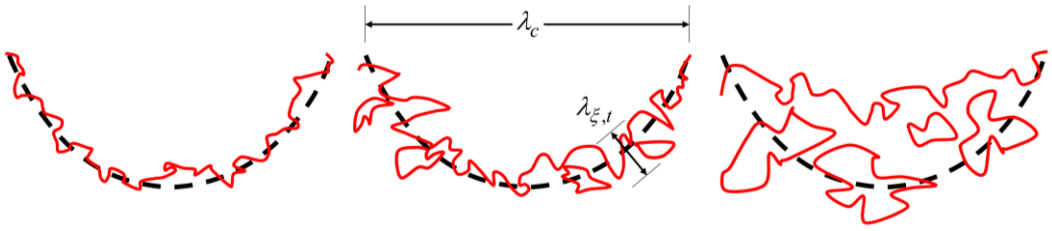

Figure 4.18. Schematic illustration of curvature sensitivity saturation with increasing turbulence intensity. The center figure illustrates the convective, λ_c, and turbulent flame, $\lambda_{\xi,t}$, length scales.

This point is illustrated pictorially in Figure 4.18; at low turbulence intensities where the magnitude of turbulence induced flame wrinkling is small relative to the coherent flame wrinkle wavelength, these small-scale wrinkles increase the rate of coherent wrinkle destruction. In contrast, once the magnitude of these turbulence-induced wrinkles approaches the coherent wrinkling wavelength, the effect will saturate with increasing turbulent wrinkling amplitude.

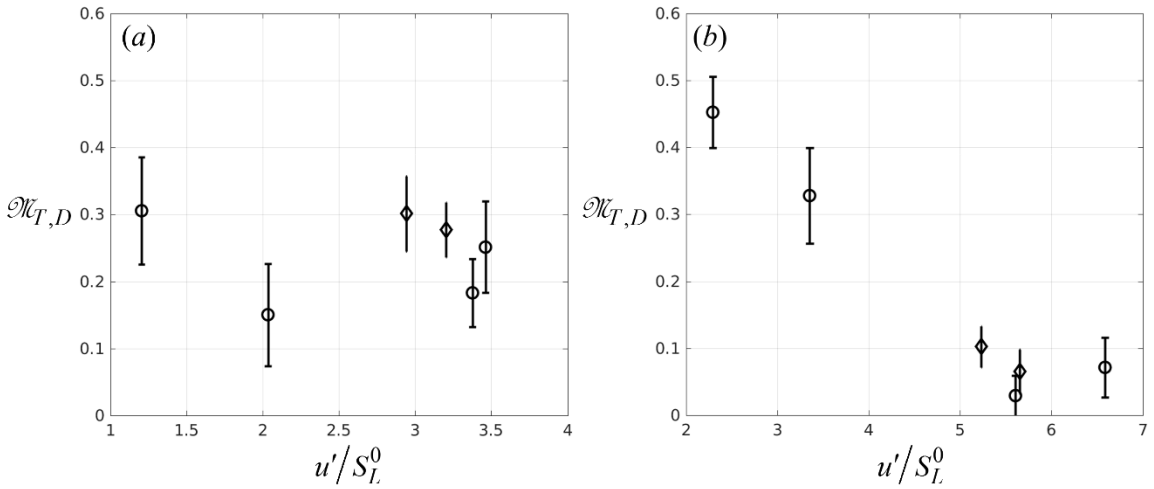

Figure 4.19. Calculated non-dimensional turbulent Markstein lengths at f_0 = 750Hz, (*a*) for a nominal mean flow velocity $U_{x,0}$ = 5 m/s, (*b*) for a nominal mean flow velocity $U_{x,0}$ = 8 m/s. Circles indicate values determined from left side of the flame while diamonds indicate the right side of the flame.

Some support for this interpretation can be obtained from Figure 4.19(*b*), obtained at a 60% higher mean flow velocity, and therefore a longer convective wavelength ($\lambda_c = u_{x,0}/f_0$) than the lower mean flow results. Following the above argument, increasing the convective wavelength would delay saturation to higher turbulence intensities. Indeed, as Figure 4.19(*b*) shows, $\mathscr{M}_{T,D}$ appears more sensitive to turbulence intensity at lower values of u'/S_L^0 . Specifically, $\mathscr{M}_{T,D}$ is decreasing with turbulence

intensity before reaching a nearly constant value of $\mathscr{M}_{T,D} \approx 0.075$ at the higher u'/S_L^0 values.

Figure 4.20 summarizes results from all cases where accurate $\mathscr{M}_{T,D}$ estimates can be obtained. As suggested by the discussion above, $\mathscr{M}_{T,D}$ is plotted as a function of the ratio of turbulent flame wrinkling amplitude, $\lambda_{\xi,t}$, normalized by the coherent flame wrinkle wavelength, $\lambda_c = u_{x,0}/f_0$. In this case, $\lambda_{\xi,t} \propto u'\tau_{\text{int}}$, and τ_{int} denotes the integral turbulence time scale, estimated as $D/u_{x,0}$, where D is the jet diameter.

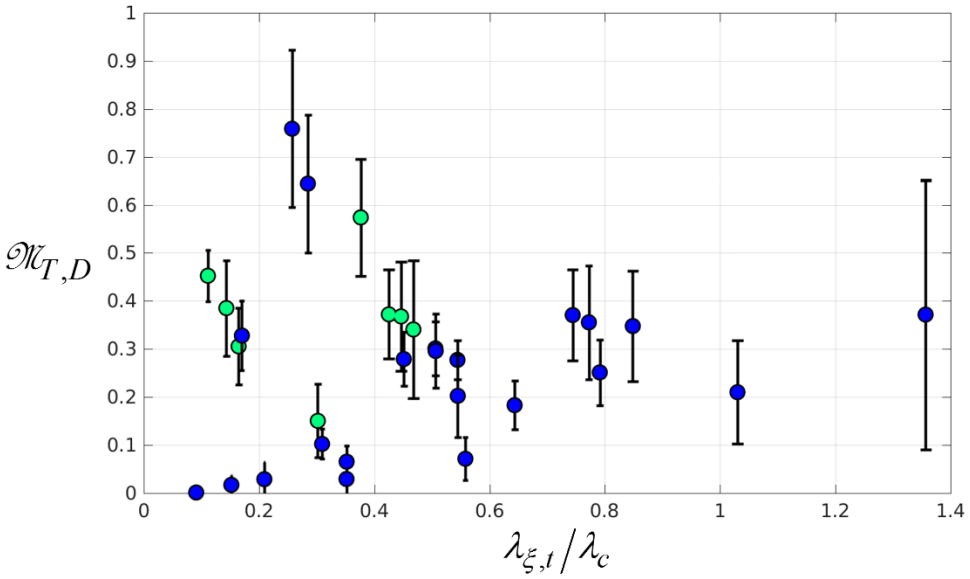

Figure 4.20. Calculated non-dimensional turbulent Markstein numbers plotted as a function of the ratio of a turbulent $\lambda_{\xi,t} = u'D/u_{x,0}$ to convective length scale, λ_c. The color indicates whether $u'/S_L^0 \leq 2.5$ (green) or $u'/S_L^0 > 2.5$ (blue).

The results in Figure 4.20 suggest that the $\mathscr{M}_{T,D} = f\left(\lambda_{\xi,t}/\lambda_c\right)$ scaling captures some, but not all, of the sensitivity to turbulence intensity. Specifically, it suggests that $\mathscr{M}_{T,D}$ is independent of turbulence intensity for $\lambda_{\xi,t}/\lambda_c \sim O(1)$ (specifically $\lambda_{\xi,t}/\lambda_c >$ ~0.75), with a value around 0.3. As discussed above, this may indicate that the global

response saturates at higher $\lambda_{\xi,t}/\lambda_c$ values, although, due to the limited number of data points at the higher wrinkle ratios it is not possible to conclude this with certainty. The two colors shown in Figure 4.20 indicate whether the given data point has $u'/S_L^0 \leq 2.5$ (green) or $u'/S_L^0 > 2.5$ (blue). Although the grouping is not completely homogeneous, it is evident that points in the higher u'/S_L^0 regime follow a different trend than for those with the lower $u'/S_L^0 \leq 2.5$ values. To see this more clearly, Figure 4.21 shows these two groupings in individual plots.

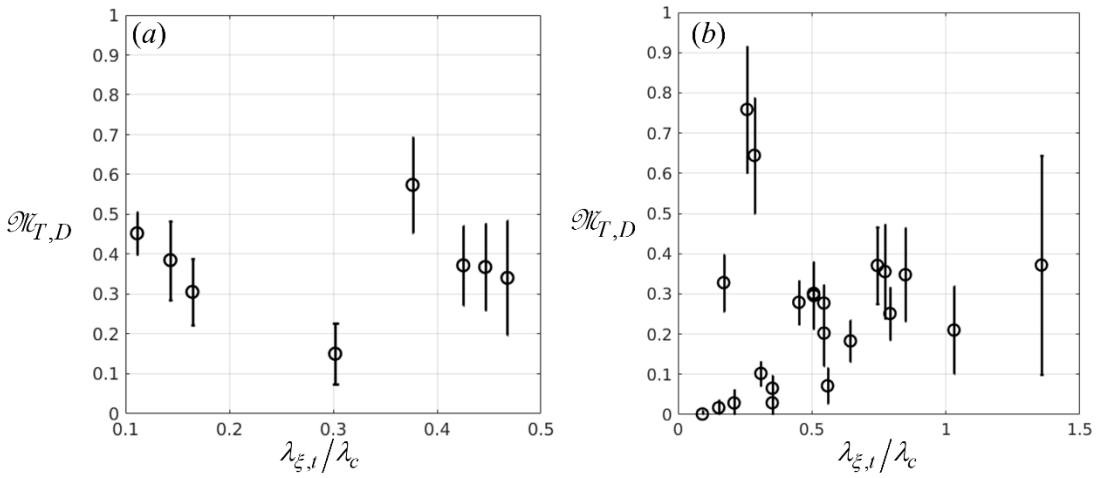

Figure 4.21. Normalized turbulent Markstein values for (*a*) data points with $u'/S_L^0 \leq$ 2.5, and (*b*) u'/S_L^0 >2.5 as a function of the ratio of turbulent flame wrinkling length to the coherent wrinkle length.

For the low u'/S_L^0 cases, Figure 4.21(*a*), the normalized turbulent Markstein length appears generally insensitive to the ratio of turbulent and coherent length scales. On the other hand, for values of $u'/S_L^0 > 2.5$, as shown in Figure 4.21(*b*), there is an approximately monotonic increase in the value of $\mathscr{M}_{T,D}$ with increasing wrinkling length scale ratio. The different frequencies and flow velocities are distributed between both groupings; e.g., it is not that the 5 m/s velocity data falls into one set and the 8 m/s fall

into the other (although because the grouping is based on u'/S_L^0, the higher values generally come from the 8 m/s cases).

Returning to the discussion introduced in Section 2.1.4, regarding the effect of the Darrieus-Landau instability on the ensemble-averaged flame response, the results shown in Figure 4.20 and Figure 4.21 indicate the approximate point at which turbulence effects come to dominate the flame response over this instability mechanism. For values of $u'/S_L^0 > 2.5$, the ensemble-averaged flame response appears to be largely controlled by the effect of kinematic restoration, resulting in the montonic trend observed in Figure 4.21(*b*). Moreover, the value of $u'/S_L^0 = 2.5$ as a cutoff between these two regimes is in line with research which suggests that the Darrieus-Landau instability is greatly diminished for values of $u'/S_L^0 > O(1)$ [79]. In their work on turbulent, expanding spherical flames and global stretch, Lipatnikov and Chomiak [109] also suggest that the hydrodynamic instability is negligible for $u'/S_L^0 > 3.6$. Other work [142] suggests that even for low turbulence intensity, $u'/S_L^0 < 1$, density ratio effects by themselves do not appear to strongly alter average turbulent flame speeds, at least in expanding spherical flames. In addition to the Darrieus-Landau instability, other factors also likely affect the results in the low $u'/S_L^0 \leq 2.5$ regime. For example, even after filtering the results to remove cases with unusably large convecting disturbances, the low turbulence cases generally still contained the largest remaining disturbances.

There are also several outlying values which occur for lower values of the length scale ratio in the $u'/S_L^0 > 2.5$ regime. The two largest values in Figure 4.21(*b*), at $\mathscr{M}_{T,D} \approx 0.65$ and $\mathscr{M}_{T,D} \approx 0.75$, are the result from a specific case ($f_0 = 1250$ Hz, $U_{x,0}$=8.0

m/s, $u'/u_{x,0} \approx 14.0\%$), and it is possible that there is an unknown confounding variable in this case. Furthermore, consider that while the grouping used in Figure 4.21 appears to separate the two groups quite well, the exact point of division is not obvious and these values may potentially fall into the other category, due to the various complicating effects discussed above. If these two outlying data points are neglected, the monotonic increase in $\mathscr{M}_{T,D}$ with increasing wrinkling length scale ratio, up to $\lambda_{\xi,t}/\lambda_c \approx 0.8$ is unmistakable, as shown in shown in Figure 4.21(*b*).

The preceding discussion shows that in the low turbulence regime (i.e. $u'/S_L^0 < 2.5-3.0$) the ensemble-averaged results are potentially affected by the presence of hydrodynamic instabilities, and high probability of convecting disturbances. Thus, in the low u'/S_L^0 the effect of turbulence on the ensemble-averaged turbulent displacement speed and its dependence on curvature is unclear.

On the other hand, for $u'/S_L^0 \gtrsim 2.5$ a distinct trend emerges, with the value of $\mathscr{M}_{T,D}$ increasing with the ratio of the wrinkling length scales, $\lambda_{\xi,t}/\lambda_c$ before possibly saturating at values above $\lambda_{\xi,t}/\lambda_c \approx O(1)$. This result suggests that this $\lambda_{\xi,t}/\lambda_c$ parameter captures the sensitivity of $\mathscr{M}_{T,D}$ to turbulence intensity at higher u'/S_L^0 values, but that the grouping definitions are not complete, while at lower values of u'/S_L^0 laminar-like flame instabilities and other factors come to dominate.

4.5 Conclusions on Ensemble-averaged Experimental Flame Position and Speed

This chapter presented experimental results showing the interaction of turbulent flow disturbances with harmonic flame wrinkles. Harmonic perturbations are introduced

on the flame using an oscillating flame holder. Turbulence is introduced in the flow with the use of a variable turbulence generation system. Simultaneous Mie scattering and high speed PIV provide instantaneous flame edges and the instantaneous flow fields. The flame edges and flow fields are ensemble-averaged to determine the ensemble-averaged flame wrinkle dynamics and flow field.

The key contribution of this chapter is showing that interactions between turbulent flow disturbances with harmonic flame wrinkling significantly alter the ensemble-averaged flame dynamics. Specifically, the flame shape results show that increasing turbulence causes a decrease in amplitude of the harmonic flame wrinkles. These flame shape results are similar to those found in some previous isothermal computational studies.

Using the ensemble-averaged flame shape data and flow field, the ensemble-averaged, turbulent burning speed is calculated using a definition proposed by Shin and Lieuwen [1]. The ensemble-averaged turbulent burning speed, when averaged over all points of phase, increases approximately montonically with the flame coordinate. Furthermore, the phase-dependent turbulent burning speed shows dependence on the shape of the ensemble-averaged flame. Specifically, the flame speed increases where the ensemble-averaged flame curvature is negative. At low turbulence, and high mean flow velocity conditions, the strong wrinkling of the ensemble-averaged flame speed produces negative ensemble-averaged flame speeds, using the definition given in Equation (4.1).

The sensitivity of the ensemble-averaged turbulent burning speed is quantified by calculation of the turbulent Markstein length. The results provide confirmation of the curvature sensitivity of ensemble-averaged flame speeds. It is suggested that the turbulent

Markstein length is controlled by the ratio of the turbulent flame wrinkling amplitude, and the coherent flame wrinkling wavelength for values of $u'/S_L^0 \tilde{>} 2.5-3$.

Several additional studies are recommended as follow-ons. First, while it is well known quasi-coherent velocity disturbances are present in shear driven, high turbulence flows, these data clearly show the nonlinear interaction between the multi-scale turbulent disturbances and the more narrowband disturbances associated with coherent structures. In other words, conceptual models of controlling physics in combustors with shear driven turbulence must account for the fundamentally different effects of spectrally distributed turbulent disturbances and more narrowband, quasi-coherent disturbances. Future work should consider the effects of additional superposed velocity disturbances, such as two superposed coherent frequencies that are and are not integer multiples.

Finally, guiding theories are clearly needed for interpreting the results. Due to the inherent noisiness of the results, a result of taking second derivatives of data, and also the potential presence of confounding effects at low turbulence levels, several trends are confirmed but interpretation would benefit from a guiding theory.

CHAPTER 5. EXPERIMENTAL INVESTIGATION OF ENSEMBLE-AVERAGED TURBULENT FLAME AREA AND CONSUMPTION SPEED

The previous chapters showed that the ensemble-averaged flame position can be modeled using the ensemble-averaged flame position equation, Equation (3.25), with the flame speed closure, Equation (2.13), proposed by Shin and Lieuwen [1]. Chapter 3 demonstrated that this modeling approach improves predictions of the ensemble-averaged flame position and heat release and more closely matches high fidelity simulations than quasi-laminar models which do not incorporate the dynamical flame speed closure. In fact, this modeling approach is even able to capture some nonlinear effects of kinematic restoration in linearized models.

Chapter 4 demonstrated experimentally that the ensemble-averaged flame speed shows the predicted curvature sensitivity even in the more complex case of a real, non-isothermal flame. In addition, Chapter 4 examined the ensemble-averaged turbulent flame position, the mean ensemble-averaged turbulent displacement speed, and the local curvature dependence.

However, by themselves, these studies of the ensemble-averaged flame position and $S_{T,Disp}$ remain in some ways incomplete. While knowledge of $S_{T,Disp}$ and its sensitivity to curvature are important for modeling the ensemble-averaged flame, it does not provide direct information about the rate of conversion of reactants to products. For instance, the observed negative values of $S_{T,Disp}$ obviously do not imply negative heat release. Thus, to better understand the ensemble-averaged and particularly the heat

release, this chapter examines the turbulent flame surface area, which is approximately proportional to the heat release rate. The turbulent flame heat release rate is an important parameter in understanding the thermo-acoustic feedback loop. The heat release rate and turbulent consumption speed concept were introduced in the context of the numerical and theoretical investigations presented in Chapter 3.

This chapter presents an investigation of the turbulent flame area and the closely related ensemble-averaged turbulent consumption speed, $S_{T,C}$. The chapter is organized as follows. First, a discussion of the definition for the ensemble-averaged turbulent consumption speed is given. Next, I explain the procedure used to extract the local and ensemble-averaged turbulent flame areas. Results are presented in Section 5.3 showing the spatial development of the ensemble-averaged turbulent consumption speed, $S_{T,C}$, the consumption speed modulation with ensemble-averaged flame shape, and the sensitivity of $S_{T,C}$ to ensemble-averaged flame curvature. Finally, conclusions from this work are given in Section 5.4.

5.1 The Ensemble-Averaged Turbulent Consumption Speed

In order to relate the measured flame areas to the consumption speed, a definition for the ensemble-averaged, turbulent consumption speed, $S_{T,C}$ is developed here. Recall that the ensemble-averaged, spatially integrated heat release rate is given by the expression:

$$Q(t) = \left\langle \int_{s_I(t)}^{s_W(t)} \rho \Delta h_r S_L dA \right\rangle \tag{5.1}$$

where ρ is the unburned gas density, Δh_R is the heat of combustion per unit mass, and dA is the instantaneous area element. In order to quantify *local* degree of flame wrinkling, this concept is extended to a local element of the flame surface.

Following the discussion presented in Chapter 3, with the assumption of constant density and heat of reaction, the ensemble-averaged turbulent consumption speed, $S_{T,C}$ is defined through the following relation:

$$S_{T,C}(t,s)\Delta A_1(t,s) \equiv S_L^0 \left\langle \Delta A(t,s) \right\rangle \tag{5.2}$$

Here, ΔA is the area element determined within an incremental band which encompasses a slice of the local flame, as illustrated in Figure 5.1. Fundamentally, Equation (5.2) states that the turbulent consumption speed is proportional to the ratio of flame areas between the instantaneous flame and a reference surface. For this work, as for that presented in Chapter 3, the reference surface is chosen to be the area of the ensemble-averaged flame.

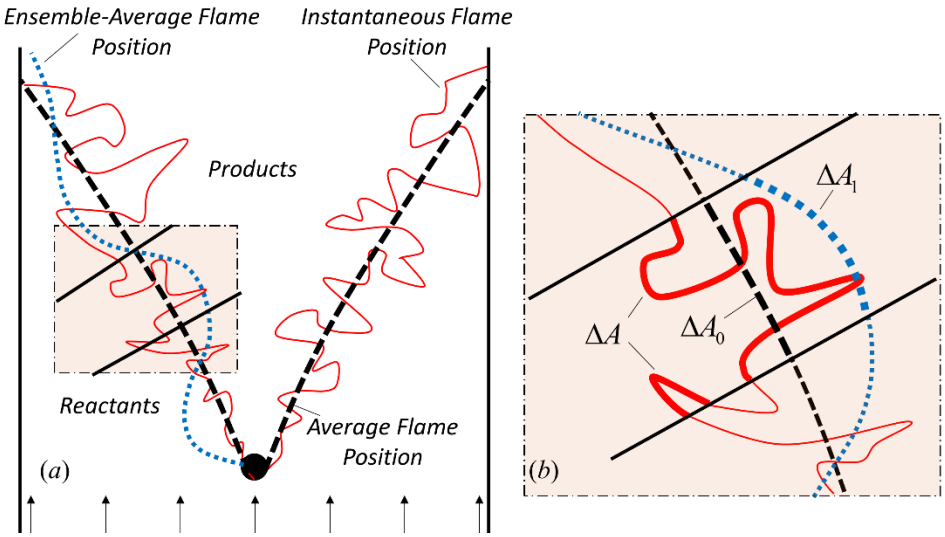

Figure 5.1. Schematic illustration of the instantaneous (red, solid), ensemble-averaged (blue, dotted), and time mean flame (black, dashed) area differential elements, showing the global flame (*a*) and local enlargement showing how areas/lengths are calculated (*b*).

Rearranging Equation (5.2) provides a definition for the ensemble-averaged turbulent consumption speed.

$$S_{T,C}(t,s) \equiv S_L^0 \frac{\langle \Delta A(t,s) \rangle}{\Delta A_1(t,s)} \tag{5.3}$$

In order to further clarify these definitions, Figure 5.1 shows a schematic illustration of the different surface areas.

This definition can also be understood as an extension of the flame speed term defined for the flame surface density modeling approach (see Chapter 2), but for an ensemble-averaged flame in two dimensions. Recall that the flame surface density, Σ, describes the flame surface area per unit volume. Multiplying the flame surface density by a stretch factor, I_0 [92, 108], which models the enhancement of the burning rate due to stretch, and integrating through the flame brush provides a definition for the local turbulent consumption speed. That is:

$$S_{T,LC} = S_L^0 I_0 \int_{-\infty}^{\infty} \Sigma(\chi) d\chi \tag{5.4}$$

For the experimental results presented here, it is not possible to identify the differential flame surface area but a similar quantity may be defined by determining a ratio of surface areas, as with the definition given in Equation (5.3). Thus, the flame integrated area ratio is estimated as:

$$\int_{-\infty}^{\infty} \Sigma(\chi) d\chi \approx \frac{\Delta A}{\Delta A_1} \tag{5.5}$$

As discussed in Section 2.1.3, for the range of turbulence intensities and reactant composition (lean methane-air) examined here, thermo-diffusive effects are expected to have a small to negligible impact on the turbulent flame propagation [83, 84]. Therefore,

the stretch factor is assumed unity, i.e. $I_0 = 1$. If these definitions are substituted in into Equation (5.4), the definition for the local, instantaneous turbulent consumption speed is recovered.

$$S_{T,LC} = S_L^0 \frac{\Delta A}{\Delta A_1} \tag{5.6}$$

Ensemble-averaging Equation (5.6) returns us to the definition given in Equation (5.3). Equations (5.6) and (5.3) describe the local, ensemble-averaged consumption speed, which depends on a ratio of the ensemble-averaged instantaneous flame surface areas to the ensemble-averaged flame reference area. An analogous definition could be created using the time mean surface area, ΔA_0 (rather than the ensemble-averaged surface area, ΔA_1), and doing so would provide information on the relation of the mean flame area and time varying ensemble-averaged area. However, the present work is concerned with developing a more complete understanding of the ensemble-averaged flame dynamics. Thus, the focus here is on the relationship between the ensemble-averaged and ensemble-averaged instantaneous flame surfaces, rather than the relationship between the time mean and ensemble-averaged instantaneous flames. Therefore, the definition given in Equation (5.6) is used in the following work.

In order to examine the curvature dependence of $S_{T,C}$, a turbulent ensemble-averaged consumption speed closure similar to that introduced in Section 3.3.4 is used to determine the turbulent consumption Markstein number. For this closure, the consumption speed is assumed to have a linear dependence on the ensemble-averaged flame curvature, analogous to the flame displacement speed closure, i.e:

$$S_{T,C}(s,\hat{t}) = S_{T,C}^0(s)\left(1 - \sigma_{T,C}(s)\left\langle C(s,\hat{t})\right\rangle\right) \tag{5.7}$$

For the results presented in this chapter, the flame speed is normalized by the local average value of the flame speed in order to better identify flame speed modulation associated specifically with the interaction of turbulent and coherent disturbances. This normalized flame speed is defined and denoted as $\mathcal{S}_{T,C}\left(\hat{t},s\right)=S_{T,C}\left(\hat{t},s\right)\big/\overline{S}_{T,C}\left(s\right)$, where $\overline{S}_{T,C}\left(s\right)$ is the local flame speed averaged over all phases. This normalization is analogous to that used in the investigation of $S_{T,Disp}$ in in Chapter 4. With this normalization the flame speed closure becomes:

$$\mathcal{S}_{T,C}(s,\hat{t})=\mathcal{S}^{0}_{T,C}(s)\left(1-\mathcal{M}_{T,C}(s)\left\langle C(s,\hat{t})\right\rangle\right) \tag{5.8}$$

Although values of $S_{T,C}$ cannot be recovered from $\mathcal{S}_{T,C}$ and vice-versa, they demonstrate the same fundamental sensitivity to curvature. Because the normalized values produce much clearer trends they are used for the work presented in this chapter.

5.2 Turbulent Flame Area Extraction Method

Turbulent flame areas are extracted from the same set of data described in Chapter 4. The pre-processing steps used to prepare the instantaneous flame images (normalization, image filtering and cropping, and binarization) are the same as those described in Section 4.2.1. The instantaneous flame areas are extracted directly from each instantaneous binary image.

The area of the ensemble-averaged flame, A_1, is extracted from the ensemble-averaged flame, which is determined according to the procedure described in Section 4.2.2. The method of determining both the instantaneous and ensemble-averaged flame is discussed next.

5.2.1 Determination of Included Edges

To determine the flame area, each instantaneous image was first divided into left and right side portions. This was done by determining the centroid of each reactant region in a binary image. Recall that the white regions indicate the reactants, for instance as shown in Figure 5.2. If the *x*-coordinate of a centroid is less than zero (in the coordinate system defined with the origin at the average location of the flame holder), then that reactant region is included in the left-hand side. If the centroid of the region is greater than zero, the region is included in the right-hand side of the flame. Examples of these divided flames are shown in Figure 5.2, where either the right side flame (*a*-*c*) or the left side flame (*d*) is shown.

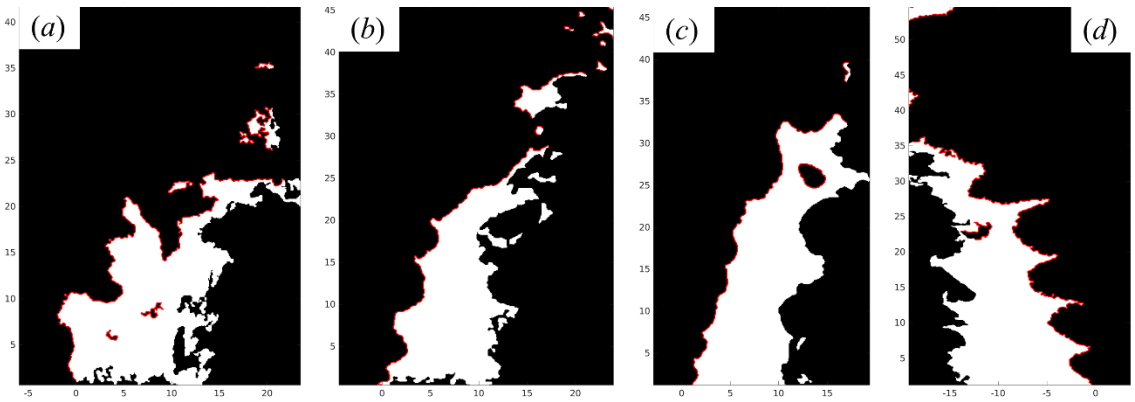

Figure 5.2. Examples of included edges used for determining the flame surface area (*a*) f_0 =200 Hz, $u'/u_{x,0}$ = 25.5%, $u_{x,0}$ = 7.2 m/s, (*b*) f_0 =750 Hz, $u'/u_{x,0}$ = 14.6%, $u_{x,0}$ = 4.6 m/s, (*c*) f_0 =1250 Hz, $u'/u_{x,0}$ = 13.0%, $u_{x,0}$ = 4.6 m/s, (*d*) f_0 =1250 Hz, $u'/u_{x,0}$ = 14.8, $u_{x,0}$ = 7.8 m/s. Dimensions are in millimeters.

A primary challenge in determining instantaneous flame surface areas for non-envelope flames, or for highly turbulent flames, is including flame edges which can reasonably be expected to indicate the flame interface while excluding those which are not expected to indicate the flame. Figure 5.2 shows four examples of instantaneous

flames and the edges which were included (indicated in red) in calculating the instantaneous flame surface area.

In the region immediately downstream of the flame holder, the flame can reasonably be assumed to exist at all times, as was observed during operation of the experiment. Furthermore, the outer edge and the bottom edge of the reactant pockets can be safely assumed to never represent the flame. However, at points downstream (particularly at higher turbulence intensities) it is not always clear whether the reactant edge is or is not a flame. Therefore, it is necessary to create and apply a series of logical rules to determine which edges to include or exclude.

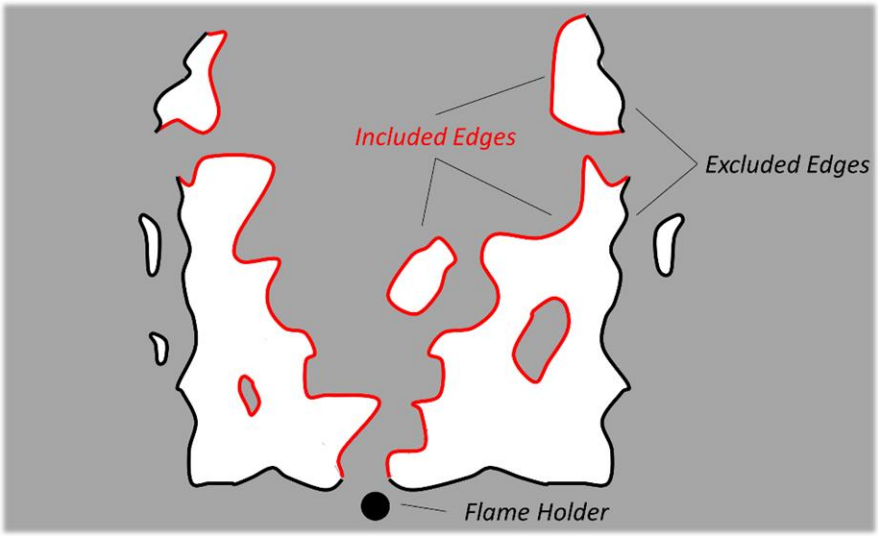

Figure 5.3. Schematic illustrating included and excluded flame edges. Red edges indicate inclusion during area calculation. Black edges indicate exclusion.

The rational used to create the edge determining algorithm is principally based on including region edges which face the interior (flame side) of the reactant field while excluding those edges that face towards the outside of the jet. The start and endpoints of an edge are determined by finding points which are both furthest towards the outer edge and also either the lowest (starting point) or the highest (ending point). Pockets which

occurred outside the main jet are excluded, while pockets which occur towards the interior of the primary flame edge are included completely (i.e. they are assumed to be burning on all the way around). Finally, holes within a reactant pocket were included. These rules are illustrated schematically in Figure 5.3, while Figure 5.2 shows several examples from the experimental data set.

5.2.2 Instantaneous and Ensemble-Averaged Flame Area

After determining which edges to include, the instantaneous area is calculated as a function of the mean flame coordinate. This is done by projecting two normal vectors from the mean flame. The distance between the vectors is approximately 0.15 mm. Then, the arc length of both the instantaneous flame and of the ensemble-averaged flame contained within the band is calculated. This is accomplished by finding all intersections between the instantaneous flame and normal vectors and finding all the edge points which fall between the intersections. The algorithm is written so that the flame area from multiple individual flame elements is included in the area for a given increment. This is illustrated schematically in Figure 5.1 and shown below in Figure 5.4. For the increment shown in Figure 5.4(a,*b*) six instantaneous individual flame elements (indicated in cyan) are included in the local area summation.

The area is determined by finding the sum of the length of all local flame elements. For this two-dimensional data, the arc length of flame elements is assumed proportional to the surface area (i.e. assuming a unit depth in the *z*-direction). Similarly, the area of the ensemble-averaged flame is also determined by finding the arc length of the ensemble-averaged flame element. The results of these summations are the local area

of the ensemble-averaged flame and the ensemble-averaged instantaneous flame area at each *s*-location for each point of phase.

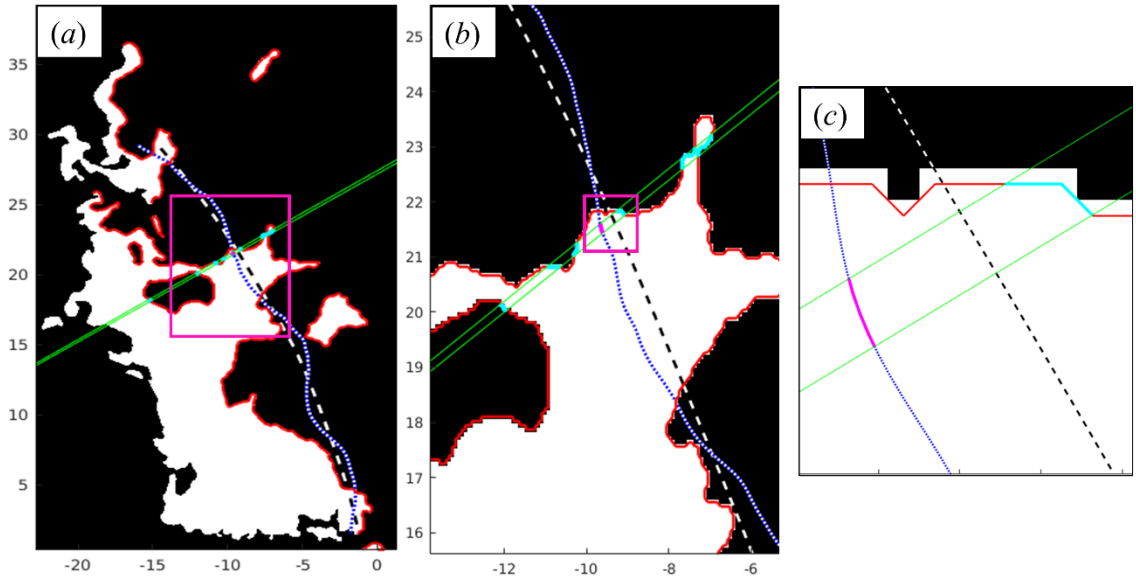

Figure 5.4. Illustration of the flame area extraction method, showing the instantaneous flame (red), the ensemble-averaged flame (white/blue), and the mean flame (white/black), the normal vectors defining the local increment (green), the included instantaneous flame elements (cyan), and the ensemble-averaged flame element (magenta). The magenta boxes indicate the enlarged region shown in the subsequent image. Dimensions are in millimeters.

The instantaneous area calculations produce a time series of local areas (integrated through the flame brush), at each location along the mean flame. The time series is composed of approximately 9,000 data points at each *s* location for the 200 Hz cases, 17,500 for the 750 Hz cases, and 21,000 for the 1250 Hz cases. The ensemble-average of the instantaneous areas is determined by averaging all points which occur at given point of phase at each *s* location. Finally, the ensemble-averaged turbulent consumption speed is calculated according to Equation (5.3).

Estimates of uncertainty for $S_{T,C}$ are computed from the standard error of the mean of the instantaneous time series of $S_{T,LC}$ at each *s* location. The value of the

standard error is multiplied by two to obtain a 95% confidence estimate of the standard error of the mean. The turbulent normalized consumption Markstein length, $\mathscr{M}_{T,C}$, and uncurved turbulent consumption flame speed, $\mathscr{S}_{T,C}^{0}$, are calculated from the slope and intercept of an orthogonal regression between the $\mathscr{S}_{T,C}$ and $\langle C \rangle$ values. A Monte Carlo approach is used to characterize the uncertainty in $\mathscr{M}_{T,C}$ and $\mathscr{S}_{T,C}^{0}$. This uncertainty characterization approach is identical to that described for the displacement Markstein length in Section 4.2.3. That is, synthetic data is created by drawing from a normal distribution with a mean equal to the calculated experimental data value and a standard deviation equal to one half the same data point's uncertainty. These synthetic data are generated in each flame curvature bin. Estimates of $\mathscr{M}_{T,C}$ and $\mathscr{S}_{T,C}^{0}$ are determined from 1000 independently generated realizations. A 95%, two-sided confidence interval based on these 1000 synthetic values of $\mathscr{M}_{T,C}$ and $\mathscr{S}_{T,C}^{0}$ provides the uncertainty estimate. However, note that the uncertainty values associated with these ensemble-averaged area calculations are much smaller than those associated with $S_{T,Disp}$, because the area calculations do not require velocity inputs or computing derivatives which amplify uncertainties.

5.3 Experimental Area and Consumption Speed Results

This section presents results from the experimentally determined flame ensemble-averaged turbulent consumption speed, $S_{T,C}$. First, results for $S_{T,C}$ when averaged over all phases, $\overline{S}_{T,C}$, are examined. Next, results showing the modulation of $S_{T,C}$ with ensemble-averaged flame shape are presented.

5.3.1 The Average Ensemble-Averaged Consumption Speed

In Chapter 4 an approximately linear increase in the ensemble-averaged turbulent displacement speed with downstream distance is identified and the increase attributed to an increase in flame area. This conclusion is further supported by the results of this flame area investigation. Figure 5.5 shows the ensemble-averaged turbulent consumption speed, averaged over all phases, $\overline{S}_{T,C}$, calculated according to Equation (5.3).

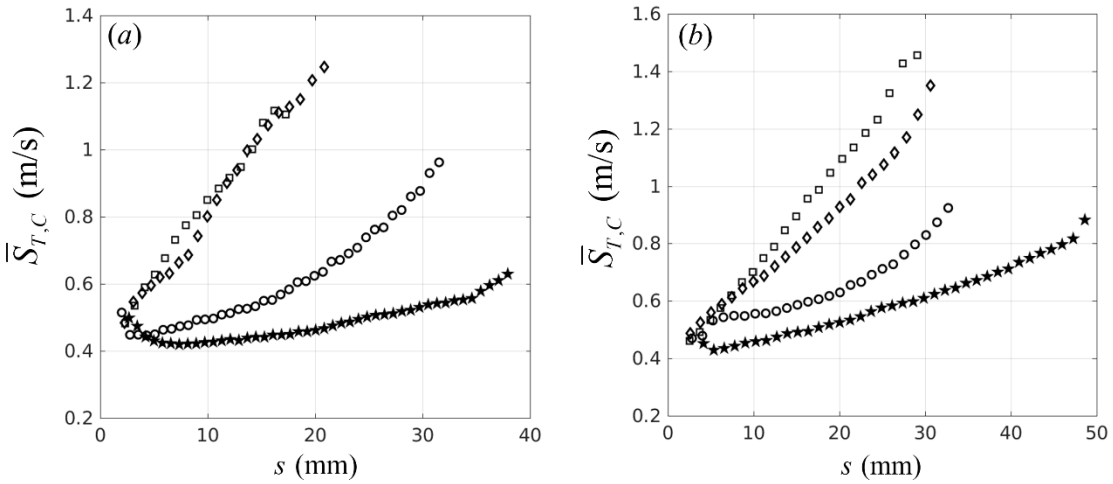

Figure 5.5. Average ensemble-averaged turbulent consumption speeds at (*a)* left side, f_0 = 200 Hz (*a, stars*) $u'/u_{x,0}$ = 8.4%, $u_{x,0}$ = 4.8 m/s; (*a, circles*) $u'/u_{x,0}$ = 16.2%, $u_{x,0}$ = 4.7 m/s; (*a, diamonds*) $u'/u_{x,0}$ = 29.6%, $u_{x,0}$ = 4.0 m/s; (*a, squares*) $u'/u_{x,0}$ = 32.9%, $u_{x,0}$ = 3.8 m/s; and (*b)* right side, f_0 = 750 Hz (*b, stars*) $u'/u_{x,0}$ = 8.0%, $u_{x,0}$ = 7.8 m/s; (*b, circles*) $u'/u_{x,0}$ = 14.2%, $u_{x,0}$ = 7.7 m/s; (*b, diamonds*) $u'/u_{x,0}$ = 24.7%, $u_{x,0}$ = 7.2 m/s; (*b, squares*) $u'/u_{x,0}$ = 27.4%, $u_{x,0}$ = 7.0 m/s.

For all cases, there is a clear increase in $\overline{S}_{T,C}$ with downstream distance, as shown in Figure 5.5. The results for all cases are given in Appendix H. Moreover, the increase with distance is generally monotonic and nearly linear for all cases. In comparison to the ensemble-averaged turbulent displacement speed, $\overline{S}_{T,Disp}$, results presented in Section 4.3 and Appendix F, the average consumption speed is much less noisy. As discussed

previously calculation of $S_{T,Disp}$ requires numerical approximations of sometimes noisy experimental data, a procedure which further amplifies that noise. The differences between the $\overline{S}_{T,Disp}$ and $\overline{S}_{T,C}$ results provide an indication of the degree of noise in the former. Note also that $\overline{S}_{T,C}$ generally appears to converge towards a common value (slightly greater than the laminar flame speed, $S_L^0 \approx 0.36$ m/s) near the flame holder. The increase over the laminar value is likely attributable to the coherent flame surface wrinkling.

In addition, Figure 5.5 shows that the higher nominal mean velocity produces slightly higher values of $\overline{S}_{T,C}$. Note that the Figure 5.5(*a*), with a lower mean velocity, has a slightly different *y*-axis scaling than the Figure 5.5(*b*). This result is consistent with higher turbulent flame speeds at higher values of u'/S_L^0, as discussed in Chapter 2. The turbulence level, in terms of u'/S_L^0 increases with increasing mean velocity, for a fixed value of $u'/u_{s,0}$.

It is also interesting to note a clear relationship between the coherent flame wrinkling amplitude and $\overline{S}_{T,C}$. In cases where the ensemble-averaged flame wrinkle increases in amplitude before decreasing further downstream, non-monotonic variation is observed in $\overline{S}_{T,C}$, as shown in Figure 5.6 where the *y*-axis scale is adjusted to allow examination of this relatively minor trend.

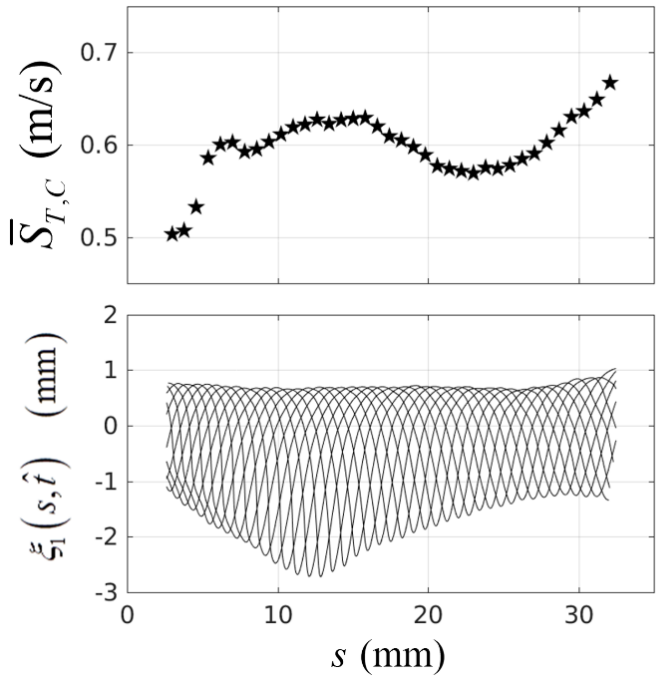

Figure 5.6. Variation of the ensemble-averaged turbulent consumption speed (top) with magnitude of the ensemble-averaged flame wrinkle (bottom) for the right edge, at f_0 = 750 Hz, $u'/u_{x,0}$ = 9.3%, $u_{x,0}$ = 4.8 m/s.

The non-monotonic variation of $\overline{S}_{T,C}$ shown in Figure 5.6 reflects the fact that the consumption speed is a function not only of turbulent forcing but also of harmonic forcing. For the case shown in Figure 5.6 growth in $\overline{S}_{T,C}$ is observed up to approximately s = 13 mm, coincident with the peak ensemble-averaged flame wrinkle amplitude. Further downstream the coherent wrinkles decay. However, $\overline{S}_{T,C}$ first decreases before subsequently increasing again. The second increase is likely due to the increase in flame area associated with increasingly wrinkled flame due to turbulent wrinkles while the first peak in $\overline{S}_{T,C}$ reflects the increase in flame area associated with the coherent flame wrinkles.

5.3.2 Turbulent Ensemble-Averaged Consumption Speed Modulation

Having examined the spatial variation of the ensemble-averaged consumption speed averaged over all phases, $\bar{S}_{T,C}$, we can now examine the phase dependent behavior of $S_{T,C}\left(\hat{t},s\right)$. Figure 5.7 shows the normalized ensemble-averaged consumption speed, $\mathcal{S}_{T,C}$. Like the results for $\mathcal{S}_{T,Disp}$ presented in Section 4.4, $\mathcal{S}_{T,C}$ clearly modulates with the shape of the ensemble-averaged flame. In fact, the modulation of $\mathcal{S}_{T,C}$ is, if anything, more distinct than the modulation of $\mathcal{S}_{T,Disp}$, as shown in Figure 5.7.

At lower turbulence intensity, as shown in Figure 5.7(*c*,*d*), where the instantaneous flame is only moderately wrinkled by turbulent fluctuations, $\mathcal{S}_{T,C}$ shows strong modulation with the ensemble-averaged flame. Because the area included in a local increment increases along the vertical edge of the coherent wrinkles (i.e. on either side of a flame cusps), the consumption speed also increases before decreasing slightly at the local flame position minima. This behavior is evident in both plots in Figure 5.7, but is more pronounced in Figure 5.7(*b*). These local $\mathcal{S}_{T,C}$ minima are not as apparent at higher turbulence, as shown in Figure 5.7(*a*). This decrease may result from increased phase jitter at higher turbulence as well as smoother flame area modulation.

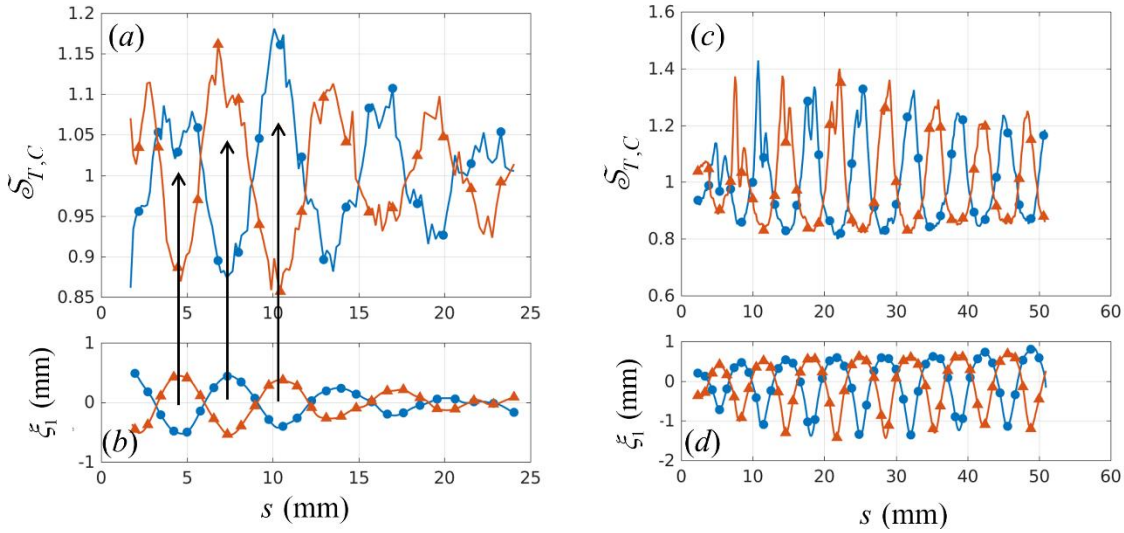

Figure 5.7. Normalized ensemble-averaged turbulent consumption speed (*a,c*) and flame fluctuation (*b, d*) as a function of the flame coordinate, at (*a, b*) left edge, f_0 = 750 Hz, $u_{x,0}$ = 4.1 m/s, $u'/u_{x,0}$ = 29.5%, (*c, d*), left edge, f_0 = 1250 Hz, $u_{x,0}$ = 8.0 m/s, $u'/u_{x,0}$ = 7.6% at two phases, $\Delta\hat{t}/T$ = 0 (circles) and $\Delta\hat{t}/T$ = 0.5 (triangles).

At higher turbulence intensity, the modulation of $\mathcal{S}_{T,C}$ is somewhat diminished in magnitude, but remains closely aligned with the curvature of the ensemble-averaged flame. As was the case with the ensemble-averaged turbulent displacement speed, higher turbulence smooths the ensemble-averaged flame, as well as introducing increased phase jitter in the ensemble-averaged instantaneous flame area. Together, the result is a reduction of the magnitude of the curvature and broadening of coherent instantaneous flame area modulations, in turn reducing the magnitude of $\mathcal{S}_{T,C}$ modulation, as shown in Figure 5.7(*a*). Similarly, as the ensemble-averaged flame wrinkle amplitude decays downstream, the amplitude of $\mathcal{S}_{T,C}$ modulation also decreases.

These results indicate that the ensemble-averaged turbulent consumption speed modulates in a manner very similar to that of the ensemble-averaged displacement speed. Specifically, $S_{T,C}$ increases in regions where the ensemble-averaged flame is concave to the reactants (i.e. negative curvature) and decreases where the ensemble-averaged

curvature is positive. The amplitude and length scale of modulation reflect the amplitude and length scale of the variation in curvature along the ensemble-averaged flame.

To illustrate the relationship between the consumption speed and curvature more clearly, Figure 5.8, shows several representative PDF plots of the normalized ensemble-averaged turbulence consumption speed, $\tilde{S}_{T,C}$, as a function of the normalized ensemble-averaged flame curvature. Additional results are provided in Appendix I. Again, note that this normalization is equivalent to that used in for the previous investigation of $S_{T,Disp}$, presented in Chapter 4.

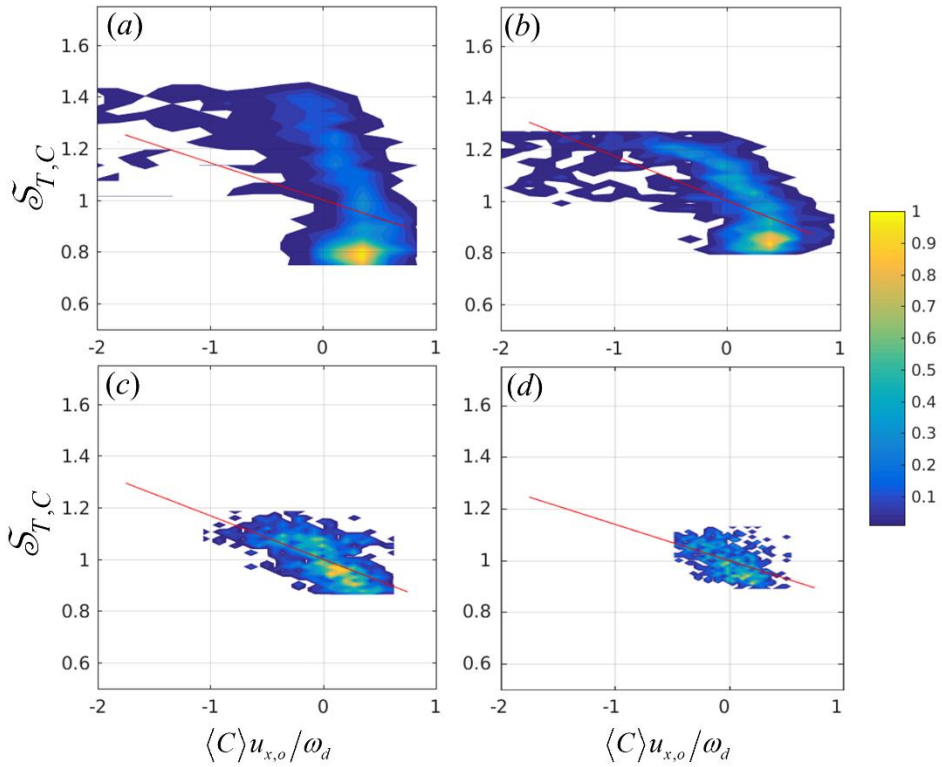

Figure 5.8. PDF plots of the normalized ensemble-averaged turbulent consumption speed versus normalized ensemble-averaged flame curvature for left edge, at f_0 = 750 Hz, (*a-d*) $u_{x,0}$ = 4.9, 4.7, 4.1, and 3.8 m/s, and (*a-d*) $u' / u_{x,0}$ = 8.9, 15.7, 29.5, and 33.1%. The red line is determined by orthogonal linear regression. The color bar indicates the normalized density of data points.

Figure 5.8 shows that, in general, $\mathcal{S}_{T,C}$ increases where the ensemble-averaged flame curvature is negative, supporting the curvature sensitivity discussed above and illustrated in Figure 5.7. However, the sensitivity at the lower two turbulence levels does not appear to follow a monotonic trend. Instead, $\mathcal{S}_{T,C}$ appears to decrease quite strongly for positive values of curvature before flattening at large negative curvature values. Thus, the variation of the consumption speed with ensemble-averaged curvature is less clear at low turbulence intensity, but approaches a more nearly linear trend at higher turbulence levels.

Next, the normalized flame speed data are binned based on curvature values, in the same way as was done for the displacement speed data discussed in Chapter 4. Figure 5.8 shows the same clustering of data for ensemble-averaged curvatures between zero and unity as was observed previously, in regard to $S_{T,Disp}$. Again, this has the effect of biasing any regression between the two variables towards values in a relatively narrow, positive curvature range, which has the effect of biasing any regression towards these positive values. Therefore, an additional processing step is utilized to minimize these bias error effects. First, the data is divided into bins for sub-ranges of curvature values. Then, a conditional median value for $\mathcal{S}_{T,C}$ is determined in each curvature bin where there are at least ten data points. The median, rather than a mean, is used so that the value for a given bin is not skewed by outlying data points.

Figure 5.9 shows the deweighted, normalized ensemble-averaged consumption speed as a function of the normalized ensemble-averaged curvature. Several trends are immediately obvious. First, for the low turbulence case shown in Figure 5.9(*a*), it is clear that a simple orthogonal linear regression does not provide an adequate description of the

variation in $\mathcal{S}_{T,C}$ with $\langle C \rangle$. For this case, (as well as several other low turbulence cases shown in Appendix I), at positive curvature, $\mathcal{S}_{T,C}$ has nearly constant value less then unity ($\mathcal{S}_{T,C} \approx 0.85$). Then, almost exactly at the point of zero curvature, $\mathcal{S}_{T,C}$ transitions discontinuously to a nearly constant value greater than unity ($\mathcal{S}_{T,C} \approx 1.3$).

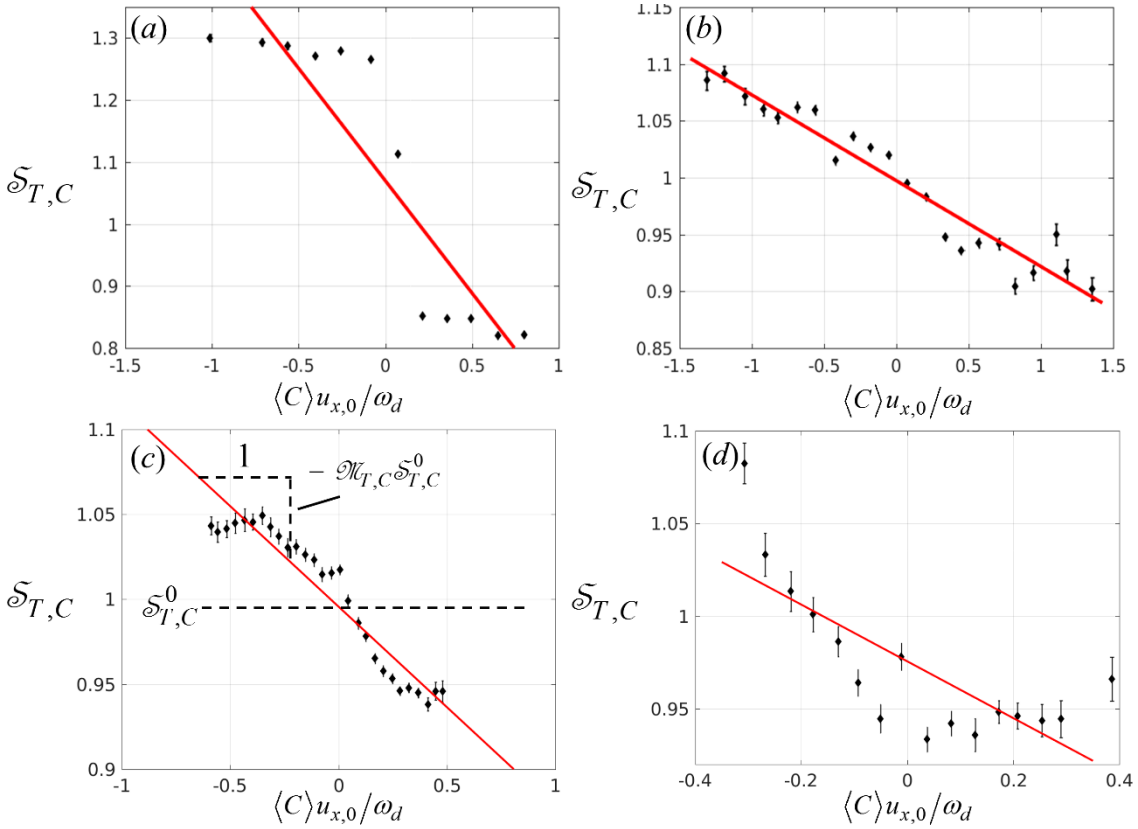

Figure 5.9. Dependence of the normalized ensemble-averaged turbulent consumption speed on ensemble-averaged curvature at four representative conditions, (*a*) left edge, f_0 = 750 Hz, $u_{x,0}$ = 4.8 m/s, $u'/u_{x,0}$ = 9.3%, $\bar{C} = 0.5$, (*b*) right edge, f_0 = 750 Hz, $u_{x,0}$ = 7.0 m/s, $u'/u_{x,0}$ = 27.3%, $\bar{C} = 0.5$, (*c*) left edge, f_0 = 1250 Hz, $u_{x,0}$ = 4.7 m/s, $u'/u_{x,0}$ = 14.5%, $\bar{C} = 0.5$ (*d*) left edge, f_0 = 1250 Hz, $u_{x,0}$ = 6.2 m/s, $u'/u_{x,0}$ = 32.1%.

This flattening trend is also similar to the flattening that is observed in Chapter 4 with respect to the displacement speed. The fact that similar flattening is observed for both the displacement and consumption speeds at positive curvature values provides

further evidence that this is a real trend. The physical reason for this flattening in the consumption speed is discussed further below.

The discontinuous flame speed curvature sensitivity implies that there are two relatively constant area ratios associated with either positive or negative curvature in this regime. Note that his behavior is also observed in Figure 5.8(*a*,*b*). In this low turbulence regime, the flame is only weakly wrinkled by turbulence. Therefore, the variation in $\mathcal{S}_{T,C}$ derives primarily from the coherent wrinkling of the instantaneous flame. Recall that the definition of $S_{T,C}$ is functionally a ratio of the ensemble-averaged instantaneous flame area to the area of the ensemble-averaged flame. However, these two areas are not generally equal, even in the low turbulence case.

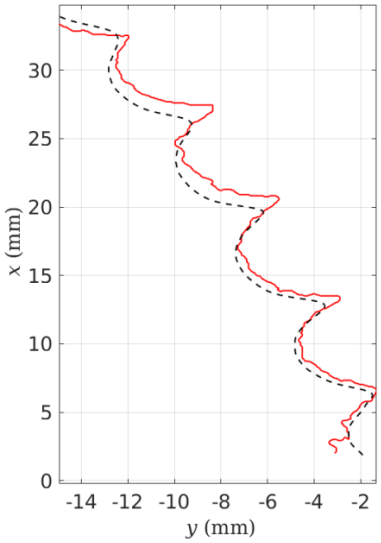

Figure 5.10. Ensemble-averaged (black dashed) and instantaneous (red solid) flames at f_0 = 750 Hz, $u_{x,0}$ = 4.8 m/s, $u'/u_{x,0}$ = 9.3%.

Consider Figure 5.10, which shows an ensemble-averaged and an instantaneous flame at the same point of phase for the case shown in Figure 5.9(*a*). The ensemble-averaged flame is generally smoother and of lower amplitude than the instantaneous

flame. Thus, the nearly constant values of $\mathcal{S}_{T,C}$ at positive and negative curvature reflects the fact that there are nearly constant area ratios obtained between the instantaneous and ensemble-averaged flames at a given curvature.

As the turbulence level increases the consumption speed curvature sensitivity appears to transition smoothly between the discontinuous, nonlinear trend shown in Figure 5.9(*a*) and the clearly linear trend shown in Figure 5.9(*b*). Figure 5.9(*c*) shows an example of an intermediate case where $\mathcal{S}_{T,C}$ appears to asymptote at both low and high curvatures, but transitions smoothly between these extremes and does not display a discontinuous jump. In general, the trend is linear at high turbulence intensity. However, the results also become progressively noisier, as illustrated in Figure 5.9(*d*).

Having discussed these local dynamics, we can now examine the dependence of the normalized turbulent consumption Markstein number, $\mathcal{M}_{T,C}$, with the ratio of turbulent to coherent wrinkling amplitude, discussed in Section 4.4. The flame wrinkling amplitude, $\lambda_{\xi,t}$, is normalized by the coherent flame wrinkle wavelength, $\lambda_c = u_{x,0}/f_0$. In this case, $\lambda_{\xi,t} \propto u'\tau_{\text{int}}$, and τ_{int} denotes the integral turbulence time scale, estimated as $D/u_{x,0}$, where *D* is the jet diameter.

This approach is again used here because the same fundamental dependence on turbulent and coherent length scales is expected to control the sensitivity of the consumption speed. For $\lambda_{\xi,t}/\lambda_c < O(1)$, increasing this length scale ratio increases the probability that a given increment will contain more flame surface in negatively curved regions (producing the curvature sensitivity). At the same time, for $\lambda_{\xi,t}/\lambda_c \approx O(1)$, it is reasonable to expect a saturation in the curvature sensitivity because of kinematic

restoration and resulting flame surface annihilation, which will increasingly reduce the relative increase of area and thus $S_{T,C}$ in negatively curved regions.

This concept is illustrated schematically in Figure 5.11, where the green regions indicate the incremental region for calculation of the flame surface area. Note that for the $\lambda_{\xi,t}/\lambda_c \approx O(1)$ case interaction of opposing flame faces results in a diminished increase in surface area in the negative curvature regions; the stronger turbulence causes destruction of the coherent instantaneous flame surface area fluctuations, thus reducing the curvature sensitivity.

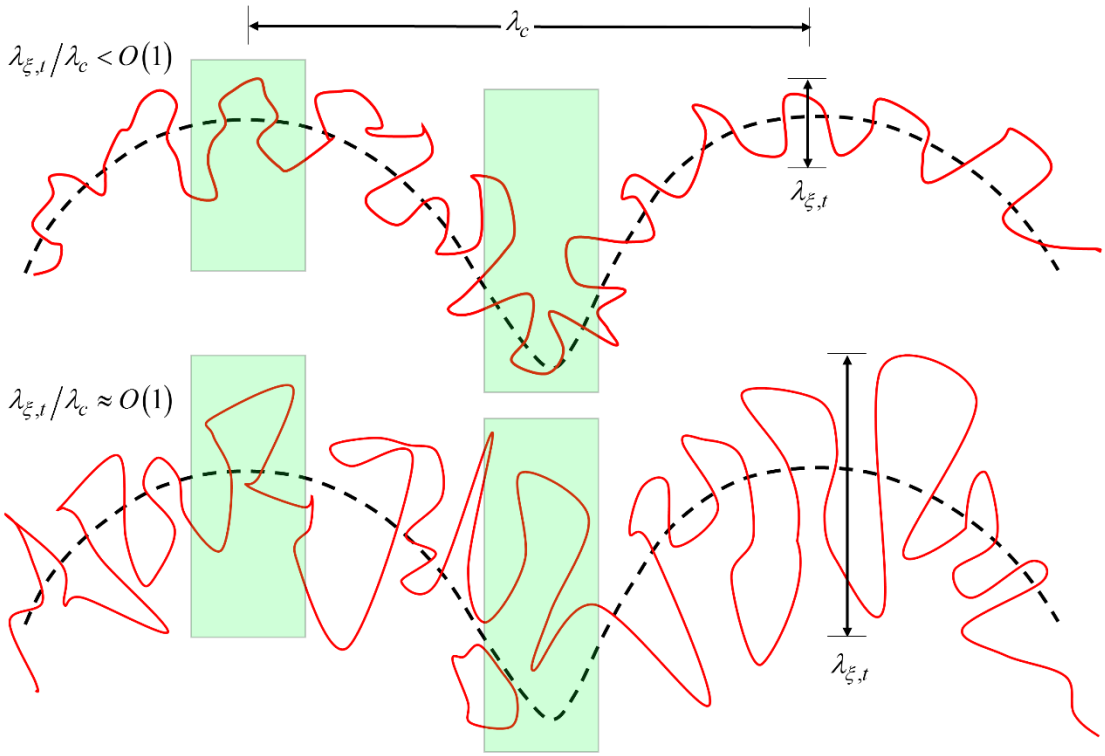

Figure 5.11. Schematic illustration of flame surface area curvature dependence for a $\lambda_{\xi,t}/\lambda_c < O(1)$ case (top) and a $\lambda_{\xi,t}/\lambda_c \approx O(1)$ case (bottom). The green regions indicate an increment of included flame.

This idea is supported by Figure 5.12 which summarizes results from all cases where accurate $\mathscr{M}_{T,C}$ estimates can be obtained. The data points are filtered to remove

cases where the flame was simultaneously disturbed by a strong convective disturbance. Thus, only cases where $\max\left(\bar{u}_{n,1}\right) < 0.55\ S_L^0$ are included, following the same filtering process as used for the displacement speed investigation. As suggested by the discussion above, $\mathscr{M}_{T,C}$ is plotted as a function of the length scale ratio of turbulent flame perturbations to convective disturbances.

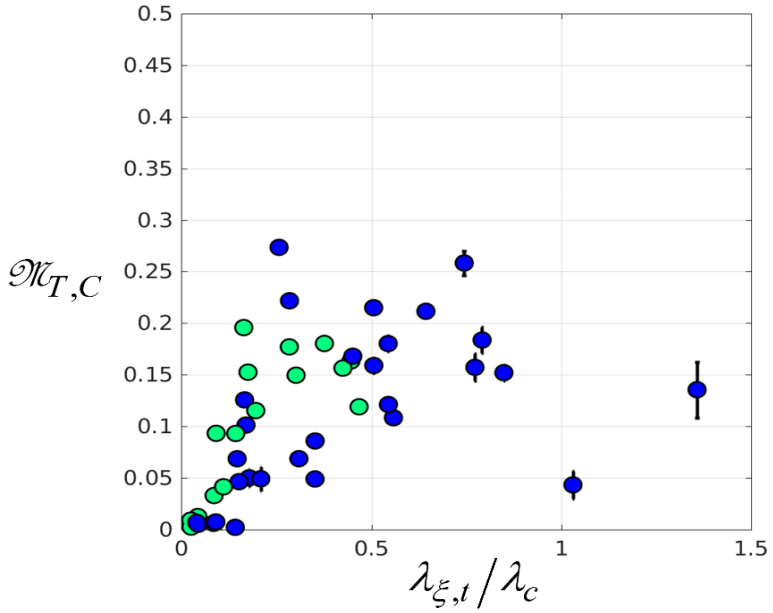

Figure 5.12. Calculated non-dimensional turbulent consumption Markstein numbers plotted as a function of the ratio of a turbulent $\lambda_{\xi,t} = u'D/u_{x,0}$ to convective length scale, λ_c. The color indicates whether $u'/S_L^0 \le 2.5$ (green) or $u'/S_L^0 > 2.5$ (blue).

Figure 5.12 shows results for $\mathscr{M}_{T,C}$ as a function of flame wrinkling length scale ratio. The data are again plotted in two groups, determined by the magnitude of u'/S_L^0, following the displacement speed data presented in Chapter 4. Unlike the results for $\mathscr{M}_{T,D}$, however, here the low u'/S_L^0 group is less distinct, and there is significant overlap between the low and high u'/S_L^0 regimes. For both groups of data $\mathscr{M}_{T,C}$ increases with $\lambda_{\xi,t}/\lambda_c$, apart from a few outlying data points beyond $\lambda_{\xi,t}/\lambda_c > 1$, where the increasing

curvature sensitivity may saturate. Again, the two values outlying values at $\lambda_{\xi,t}/\lambda_c$ = 0.25 are associated with the same case (i.e. they are from the left and right sides of the flame at $f_0 = 1250$ Hz, $U_{x,0}$=8.0 m/s, $u'/u_{x,0} \approx 14.0\%$).

Figure 5.13 shows the low and high u'/S_L^0 groupings plotted separately. The trend shown in Figure 5.13(*b*) is largely unchanged from the overall trend shown in Figure 5.12. However, the low u'/S_L^0 appears to saturate at $\lambda_{\xi,t}/\lambda_c \approx 0.2$. For $u'/S_L^0 > 2.5$ it is not clear whether there is a saturation, because there are only two data points beyond $\lambda_{\xi,t}/\lambda_c \approx 0.8$, although the two rightmost points suggest this.

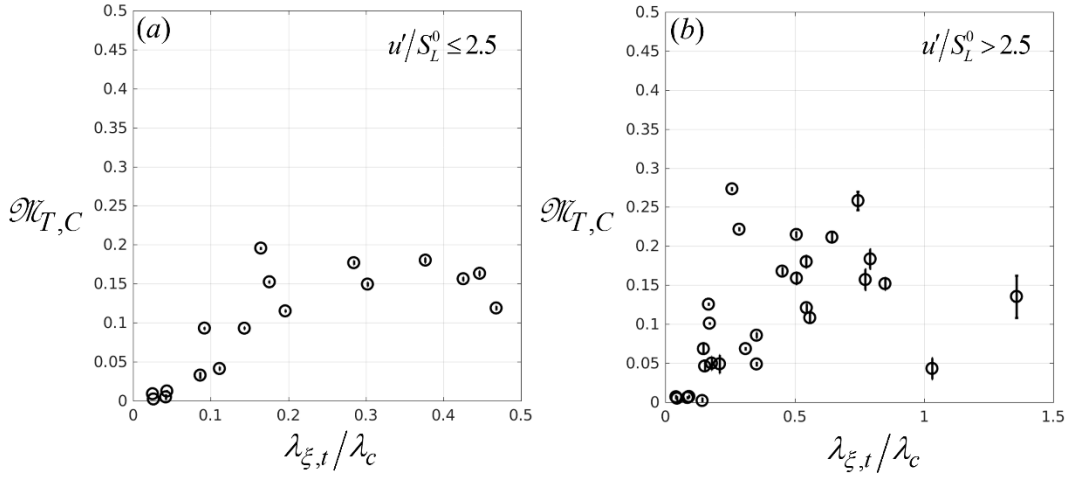

Figure 5.13. Normalized turbulent consumption Markstein number (a) data points with $u'/S_L^0 \leq$ 2.5, and (*b*) u'/S_L^0 >2.5 as a function of the ratio of turbulent flame wrinkling length to the coherent wrinkle length.

Figure 5.13(*a*) shows, for $u'/S_L^0 \leq 2.5$, $\mathscr{M}_{T,C}$ increases linearly from $\lambda_{\xi,t}/\lambda_c = 0$ to $\lambda_{\xi,t}/\lambda_c = 0.2$, before saturating at $\mathscr{M}_{T,C} \approx 0.17$. This result differs from the displacement speed results. Recall that $\mathscr{M}_{T,D}$ appears insensitive to wrinkling length scale ratio at $u'/S_L^0 \leq 2.5$. The earlier discussion regarding the expected curvature sensitivity

explains these low turbulence results well, although it is also worth noting that $\mathscr{M}_{T,C}$ in this turbulence range is more difficult to interpret due to the discontinuous behavior discussed above, in relation to Figure 5.9(*a*).

The results for $u'/S_L^0 > 2.5$ show that $\mathscr{M}_{T,C}$ continues to increase beyond $\lambda_{\xi,t}/\lambda_c = 0.2$. One possibility is that in the low turbulence regime the amount of local wrinkling is limited due to laminar-like flamelet propagation, so that the flame never becomes highly multi-valued, thus limiting the range of local area ratios. At high turbulence intensity, the local wrinkling is perhaps strong enough to cause the flame to become multivalued, which at points near flame cusps would result in significantly increased flame areas and consumption speeds.

Despite some minor differences, the general results shown in Figure 5.12 and Figure 5.13 for $\mathscr{M}_{T,C}$ are remarkably similar, both in general trend as well as magnitude, to the results for $\mathscr{M}_{T,D}$ shown in Figure 4.20 and Figure 4.21 in Chapter 4. For example, $\mathscr{M}_{T,C}$ and $\mathscr{M}_{T,D}$ both increase for $\lambda_{\xi,t}/\lambda_c \approx 0.8$ before reaching a possible saturation. Furthermore, the value of $\mathscr{M}_{T,D}$ at $\lambda_{\xi,t}/\lambda_c \approx 0.8$ is approximately 0.35 while that of $\mathscr{M}_{T,C}$ is approximately 0.2.

The close correspondence between these two sets of results is significant in itself. Consider that the flame speed values are determined through entirely different methodologies, excluding the early image processing. The displacement speed is calculated through ensemble-averaging instantaneous flames to determine the ensemble-averaged flame and ensemble-averaging instantaneous flow fields to determine the ensemble-averaged velocity field. Temporal and spatial derivatives are calculated and

these along with the velocity information are used as inputs to Equation (4.1). The consumption speed, on the other hand, is extracted directly from instantaneous flame areas, normalized by the area of the ensemble-averaged flame. The determination of $S_{T,C}$ requires no velocity field data at all, nor does it require any estimation of spatial or temporal derivatives[v]. The concurrence from these two sets of results provide strong mutual support for the flame speed closures given in Equation (2.13) and Equation (5.7); the turbulent flame speed is a function of the ensemble-averaged flame curvature.

5.4 Conclusions on Ensemble-Averaged Flame Area and Consumption Speed

This chapter presented experimental results examining the local ratio of the ensemble-averaged area of the instantaneous flame to the area of the ensemble-averaged flame. The consumption speed is calculated as the ratio of the ensemble-averaged instantaneous area to the ensemble-averaged flame area, multiplied by the unstretched laminar flame speed.

Coherent disturbances are imposed on the flame using an oscillating flame holder, and turbulent flow disturbances are introduced with a turbulence generation system, as described in Chapter 4. The instantaneous flame position is determined from two dimensional Mie-scattering images. This information is used to determine both the ensemble-averaged flame position and to determine the instantaneous flame location. The instantaneous area is determined by measuring the instantaneous flame arc length within a small band projected perpendicularly from the position of the mean flame. Care is taken

---

[v] However, note that ensemble-averaged flame curvature does require calculation of spatial derivatives.

to only include flame edges which are likely to represent the flame rather than simply the interface between reactants and co-flow air. The area of the ensemble-averaged flame is determined analogously, but using the position of the ensemble-averaged flame.

The main finding of this chapter is that the ensemble-averaged turbulent consumption speed demonstrates sensitivity to the ensemble-averaged flame curvature which is very similar to the sensitivity of the ensemble-averaged displacement speed. This finding is significant because the method used to calculate the displacement and consumption speeds share no common methodology beyond the initial image processing and filtering and the use of the ensemble-averaged flame area as the numerator of the consumption speed definition.

The ensemble-averaged turbulent consumption speed, when averaged over all points of phase, generally increases with the flame coordinate, and demonstrates a clear dependence on both turbulence intensity and coherent flame wrinkle amplitude. In some low turbulence cases, non-monotonic behavior is observed due to coherent wrinkle growth and decay. The results from the consumption speed are much less noisy than for the displacement speed. Moreover, near the flame holder the average consumption speed converges to an approximately common value, on the order of the laminar flame speed.

The phase-dependent turbulent consumption speed shows a dependence on the shape of the ensemble-averaged flame, similar to that of the displacement speed. Specifically, the flame speed increases where the ensemble-averaged flame curvature is negative. At low turbulence intensities, $S_{T,C}$ often modulates discontinuously with the ensemble-averaged flame curvature. For positive curvatures, the normalized consumption speed is less than unity while for negative curvatures it is greater than unity.

Following the analysis of Chapter 4, the sensitivity of the ensemble-averaged consumption speed is quantified by calculation of the normalized turbulent Markstein number. The general results closely follow the trend and magnitude of the displacement speed results and provide mutual validation of the curvature sensitivity of turbulent flame speeds.

The turbulent consumption Markstein number, like the turbulent displacement Markstein number, is controlled by the ratio of the turbulent flame wrinkling amplitude, and the coherent flame wrinkling. For values of $u'/S_L^0 < 2.5$ the Markstein number increases and then saturates, while for $u'/S_L^0 > 2.5$ the Markstein number continues to increase at higher values of the flame wrinkling length scale ratio and does not clearly reach a constant value.

CHAPTER 6. CONCLUSIONS AND FUTURE WORK

This chapter provides a summary of the results and key findings presented in this thesis. In addition, some suggestions for future avenues of research building on these thesis results are given. The need to improve predictions of turbulent flame spatio-temporal position and heat release dynamics provides the fundamental motivation for the work presented in this thesis. As is typically the case in realistic combustion environments [26], flames are perturbed not only by narrowband acoustic and/or hydrodynamic disturbances but also broadband turbulent fluctuations. Therefore, this work has focused on developing a modeling approach and validating that approach against numerically simulated and experimental data.

6.1 Summary of Work

This thesis concentrates on identifying, understanding, and modeling the interaction between narrowband quasi-coherent hydrodynamic and/or acoustic disturbances and broadband disturbances associated with turbulence in premixed flames. To address these issues, two corresponding primary avenues of research were followed. In the first, theoretical reduced-order models of the turbulent flame position and heat release response were developed and validated against numerical simulations. Second, because all previous work on this subject was based on isothermal simulations, a novel experimental facility was developed with the capability to subject premixed flames to simultaneous broadband turbulent fluctuations and narrowband coherent fluctuations introduced on the flame with an oscillating flame holder. This experimental work is further composed of analysis of the ensemble-averaged flame dynamics, the ensemble-

averaged turbulent displacement speed, the local ensemble-averaged area and consumption speed, and the dependence of both the displacement and consumption speed on the ensemble-averaged flame curvature. Finally, the flame speed sensitivity to curvature is quantified through calculation of the normalized turbulent Markstein displacement and consumption numbers. These findings were presented in Chapters 3 through 5.

Chapter 3 developed and validated the fundamental modeling and data analysis approach used throughout this thesis. The turbulent modeling method is based on the *G*-equation approach used in laminar flame position and heat release studies. In order to apply this approach to flame area and heat release analysis, an inconsistency which arises when determining the heat release response in different coordinate systems was first addressed. To correctly determine the flame surface area of a premixed flame, it is necessary to include time varying corrections to the limits of integration depending on the way first order area fluctuations manifest in the different coordinate systems.

The *G*-equation approach was then extended to turbulent flames through development of the ensemble-averaged turbulent flame position equation, where the turbulent flame speed closure proposed by Shin and Lieuwen [1] is used. In this closure, the turbulent flame speed is modeled as a function of the ensemble-averaged flame curvature, and the sensitivity to curvature quantified by the turbulent Markstein number. This approach is analogous to stretch dependent laminar flame speed models. Results from the reduced-order ensemble-averaged turbulent flame governing equation were compared with results from numerical simulations of the same flame configuration. The modeling approach predicted many of the dynamical features found in the numerical

simulation. Moreover, the modeling results were improved by the use of the flame speed model. This approach was further extended by assuming small perturbation amplitudes, allowing development of fully analytical expression for the flame position and heat release. These linearized models captured important nonlinear features of the numerical simulations.

A significant limitation of the work presented in Chapter 3, as well as previous investigations of ensemble-averaged flame dynamics [1, 96, 97], is the use of the isothermal assumption, necessary for analytical and numerical tractability. To overcome this limitation Chapter 4, examines the ensemble-averaged flame position and speed response experimentally. The development of an experimental facility which allows investigations of premixed, turbulent flames perturbed by harmonic oscillations of the flame holder is detailed. This facility is capable independent variation of mean flow velocity, turbulence intensity, harmonic forcing frequency, and equivalence ratio. High speed Mie scattering images are used to identify both the instantaneous flame edge position and for use in PIV flow field measurements. Together, this data provides the inputs for the flame speed equation, equivalent to the ensemble-averaged flame governing equation.

The amplitude of coherent flame wrinkles was generally observed to decrease with both downstream distance and with increasing turbulence intensity, providing the first experimental validation of the previous isothermal results. At low turbulence intensity, the presence of convective disturbances (due to vortex shedding from the flame holder and heat release effects from the wrinkled flame) resulted in fine scale coherent wrinkles which complicated subsequent analysis. Analysis of the ensemble-averaged

displacement speed when averaged over all points of phase indicated that the average displacement speed increases downstream and with increasing turbulence intensity. Moreover, investigation of the phase dependent, ensemble-averaged displacement speed demonstrated clear modulation with the shape of the ensemble-averaged flame. Specifically, the displacement speed increases in regions of negative curvature. The magnitude of the curvature sensitivity appears to depend largely on turbulent intensity (u'/S_L^0) and on the ratio of the turbulent flame length scale to coherent flame length scale. At low u'/S_L^0, the turbulent Markstein number appears insensitive to changes in length scale ratio. In this regime, the results are subject to convecting disturbances and the possible influence of the Darrieus-Landau instability. For higher u'/S_L^0, the magnitude of the normalized turbulent displacement Markstein length increases with the wrinkling length scale ratio. This dependence is attributed to the increase in kinematic restoration associated with the introduction of turbulence on a globally curved flame.

Lastly, Chapter 5 extended the analysis of the experimental data to a study of the instantaneous, local flame surface area and the ensemble-averaged turbulent consumption speed derived therefrom. The ensemble-averaged turbulent consumption speed is defined as the ratio of the ensemble-averaged instantaneous local flame area to the area of the local ensemble-averaged flame, multiplied by the laminar burning speed. Like the displacement speed, the consumption speed, averaged all points of phase increases with turbulence intensity and downstream distance. The results from the consumption speed are much less noisy than those of the displacement speed because the consumption speed does not require estimating temporal or spatial derivatives. In addition to turbulence

intensity and downstream location, the consumption speed also depends on the coherent wrinkle amplitude, although to a lesser degree than turbulence and downstream distance.

The phase-dependent consumption speed modulates with the ensemble-averaged flame shape similar to the modulation observed with the ensemble-averaged displacement speed. That is, the consumption speed increases in regions of negative ensemble-averaged flame curvature and also decreases in regions of positive curvature. As such, the consumption speed results generally validate the flame curvature sensitivity. However, at low turbulence intensity the modulation of flame speed with curvature does not display a linear relationship with curvature but instead is often discontinuous, with nearly constant increased values in negative curvature regions and decreased values in positive curvature regions.

Finally, the curvature sensitivity of the consumption speed is quantified by calculation of the turbulent consumption speed Markstein number. The results are remarkably similar to those for the displacement speed. This finding is notable because the methodologies for determining these flame speeds are essentially independent from one another. The turbulent consumption Markstein number appears to increase with the ratio of wrinkling length scales, following the trend observed with the turbulent displacement Markstein number. One notable difference is that a clear trend is observed at low u'/S_L^0 values, in contrast to the results for the displacement Markstein number.

6.2 Key Findings

This section summarizes the key findings from the body of work presented in this thesis. The first key finding is that it is possible to model a turbulent flame using the ensemble-averaged flame position equation, and that by incorporating the flame speed

closure model suggested by Shin and Lieuwen [1], the agreement with a simulated turbulent flame is improved. Secondly, this approach captures some of the nonlinear effects of turbulence (i.e. kinematic restoration) even in linearized models. Another important insight from this thesis is the necessity of accounting for oscillating integration limits when determining the global flame surface area. This point is particularly important when working with a coordinate system oriented on the mean flame, as the linearized area fluctuations in this system result entirely from the time-varying end corrections to the area integral.

The second key finding from this work is that experimentally generated ensemble-averaged flame wrinkles are affected by the presence of turbulence, supporting conclusions drawn previously from observations in isothermal simulations. That is, there is a nonlinear interaction between broadband turbulence and quasi-coherent flame disturbances which change the average properties of the flame. Moreover, the curvature sensitivity previously observed in isothermal computations of turbulent premixed flames is also observed in experimental investigations of turbulent premixed flames. This finding implies that development of more accurate, reduced-order turbulent flame models requires accounting for the dynamical effect of the ensemble-averaged flame shape on the displacement and consumption speeds. In addition, it was found that the turbulent displacement Markstein number varies with the ratio of turbulent flame length scale to the coherent flame wrinkle length scale. This work is particularly important for predicting thermo-acoustic combustion instabilities because the flame wrinkle amplitude and decay rate strongly influence the coherent heat release response.

The last key findings from this work come from the investigation of the local flame surface area, presented in Chapter 5. The ensemble-averaged consumption speed modulates with curvature comparable to the ensemble-averaged displacement speed modulation. That is, the consumption speed increases in negative curvature regions and decreases in positive curvature regions. Moreover, the sensitivity of the consumption speed to flame curvature follows very a very similar trend, as demonstrated by the variation of the turbulent consumption Markstein number with wrinkling length scale ratio. The turbulent consumption Markstein number increases with increasing length scale ratio.

Taken together, these key findings point to the utility of the ensemble-averaged turbulent flame modeling approach. The position of the ensemble-averaged flame can be modeled using the ensemble-average flame position equation with the flame speed closure, where measured experimental or numerical data provide turbulent displacement Markstein numbers and uncurved flame speeds. Once the flame position is known, heat release information can be determined using the consumption flame speed model with experimentally or numerically computed flame consumption speed information.

The ensemble-averaged modeling approach provides a new method of modeling turbulent flames in the presence of coherent forcing. Because of the relatively simplicity of this method, significant reductions in computational expense or even fully analytical expressions for turbulent heat release are possible. This capability, in turn, allows more rapid prediction of possible combustion instability, and thus helping to increase the reliability, reduce maintenance expenses, and avoid catastrophic failure in low NOx, lean, premixed gas turbine combustion systems.

6.3 Suggested Future Work

The work presented here suggests several future studies. First, an obvious next step is to determine the heat release from an experimentally investigated flame or from a high fidelity numerical simulation, such as DNS. This information could be compared with predictions from the reduced order models to further validate the modeling approach presented in Chapter 3.

The results presented in Chapter 4 provide an initial foray into analysis of the turbulent Markstein number. However, given the need to separate the data into two groups based on turbulence intensity and the relative noisiness of the results, additional work should focus on further identifying the physical mechanisms driving the curvature sensitivity, with the goal of improving understanding of the underlying controlling principles.

It is suggested that the Darrieus-Landau instability may play a role in changing the turbulent flame speed curvature sensitivity, particularly at low values of u'/S_L^0. The importance of this effect could be investigated by preheating the reactants (i.e. using a vitiated flow) to minimize the density ratio across the flame and thereby reduce the strength of the hydrodynamic instability. Similarly, the generality of these results could be extended to other pressures through modification of the experimental facility to pressures above atmospheric, which would impact the local flame speed and flame thickness and local, flamelet stretch sensitivity.

Future work should also examine the ensemble-averaged hydrodynamic stretch which is likely to also impact the ensemble-averaged flame response and could potentially resolve the ambiguities associated with the presence of strong convecting

disturbances. Significant clarification on this issue may also be gained by performing high fidelity simulations which account for heat release and flame generated vorticity. These issues are particularly relevant as the analysis of the experimental data was significantly complicated by the presence of convective velocity disturbances due to vortex shedding from the flame holder and the oscillating density gradient associated with the flame.

Additional analysis should also be directed towards examining the dependence of the Markstein number and uncurved flame speeds with additional turbulent and forcing parameters, such as the integral length scale and oscillation amplitude of the flame holder.

In addition, the generality of the results presented in this thesis should be extended to other geometries, as all results presented in here are based on the unusual configuration of an oscillating flame anchor. Given the difficulties associated with the convecting disturbances, discussed in Chapter 4, it is possible - though perhaps unlikely - that the interaction between the coherent and turbulent fluctuations which gives rise to the flame speed curvature sensitivity is altered by velocity disturbances. Thus, a first step in determining the generality of this sensitivity would be to extend these results to the canonical geometry of a Bunsen flame, forced not with an oscillating flame holder but with the more typical velocity forcing. If the flame speed sensitivities observed in the present work are observed in other geometries, this would provide strong evidence of the generality of the flame speed curvature sensitivity.

Finally, the local, time resolved area data presented in Chapter 5 provides the opportunity for interesting additional investigations beyond the scope of this thesis. For

instance, it would be interesting to examine the frequency content of the area signal both in terms of spatial and modal development, as the development of higher frequency content could impact the heat release response. It would also be quite interesting to see how the instantaneous area fluctuations correlate with instantaneous velocity fluctuations. Such an investigation could provide useful insight into the validity of the correlational turbulent flame speed models discussed in Chapter 2, or provide insight for their improvement.

APPENDIX A. DERIVATION OF CONVECTING VORTEX MODEL PROBLEM

Application of the given assumptions to Equation (3.36) leads to the following ordinary partial differential equation for the Fourier transformed flame position:

$$\frac{\partial^2\left\langle\hat{\xi}'(s)\right\rangle}{\partial s^2}-\frac{\partial\left\langle\hat{\xi}'(s)\right\rangle}{\partial s}\frac{\left\langle u_{s,eff}\right\rangle}{S_{T,Disp}^0\sigma_{T,D}}+\left\langle\hat{\xi}'(s)\right\rangle\frac{i\omega_d}{S_{T,Disp}^0\sigma_{T,D}}+\frac{u_{s,eff}}{S_{T,Disp}^0\sigma_{T,D}}\exp\left[s\frac{\omega_d}{u_{s,eff}}\left(i\frac{u_{s,eff}}{u_C}-\frac{\gamma}{2\pi}\right)\right]=0 \tag{A.1}$$

This equation has the same homogeneous solution as Equation (3.40), but a different particular solution due to the nature of the harmonic forcing. The solution of the Fourier space flame fluctuation is given by:

$$\hat{\xi}'(\omega_d,s)=Ae^{sR_1}+Be^{sR_2}-\frac{u_{s,eff}\exp\left[s\frac{\omega_d}{u_{s,eff}}\left(i\frac{u_{s,eff}}{u_C}-\frac{\gamma}{2\pi}\right)\right]}{S_{T,Disp}^0\sigma_{T,D}\left(\frac{\omega_d}{u_{s,eff}}\right)^2\left(i\frac{u_{s,eff}}{u_C}-\frac{\gamma}{2\pi}\right)^2-\omega_d\left(i\frac{u_{s,eff}}{u_C}-\frac{\gamma}{2\pi}\right)+i\omega_d} \tag{A.2}$$

where $R_{1,2}$ are defined according to Equation (3.44). This equation is solved subject to the stationary flame-attachment boundary condition:

$$\xi_1(s=0,t)=0 \tag{A.3}$$

As with the oscillating flame holder model problem, the second boundary condition stipulates that no information propagates upstream. Therefore, the *B* coefficient is set to zero. The resulting Fourier space fluctuating flame position is:

$$\left\langle \hat{\xi}'\left(\omega_d, s\right)\right\rangle = \frac{e^{sR_1} - e^{s\frac{\omega_d}{u_{s,eff}}P}}{\frac{S^0_{T,Disp}\sigma_{T,D}}{u_{s,eff}}\left(\frac{\omega_d}{u_{s,eff}}\right)^2 P^2 - \frac{\omega_d}{u_{s,eff}}P + i\frac{\omega_d}{u_{s,eff}}}, \qquad P = \left(i\frac{u_{s,eff}}{u_C} - \frac{\gamma}{2\pi}\right) \tag{A.4}$$

This solution can be expanded around small σ values as:

$$\left\langle \hat{\xi}'\left(\omega_d, s\right)\right\rangle = \frac{\exp\left[s\left(\frac{i\omega_0}{u_{s,eff}} - \frac{\omega_0^2 S^0_{T,Disp}\sigma_{T,D}}{{u_{s,eff}}^3}\right)\right] - \exp\left[s\frac{\omega_d}{u_{s,eff}}\left(i\frac{u_{s,eff}}{u_C} - \frac{\gamma}{2\pi}\right)\right]}{\frac{\omega_d}{u_{s,eff}}\left(i - P\right)}\left[1 - \sigma_{T,D}\frac{S^0_{T,Disp}\omega_d P^2}{{u_{s,eff}}^2\left(i-P\right)}\right] \tag{A.5}$$

Unlike the oscillating flame holder problem, with the velocity forced case only a downstream integration limit correction is required, because the flame attachment point is stationary. This end correction, determined in the same manner as described in Section 3.5.1 is:

$$\Delta\hat{s}_{W,1} = \frac{-\varepsilon}{\tan\left(\theta\right)}\frac{e^{s_W R_1} - e^{s_W\frac{\omega_d}{u_{s,eff}}P}}{\frac{S^0_{T,Disp}\sigma_{T,D}}{u_{s,eff}}\left(\frac{\omega_d}{u_{s,eff}}\right)^2 P^2 - \frac{\omega_d}{u_{s,eff}}P + i\frac{\omega_d}{u_{s,eff}}} \tag{A.6}$$

The general form of the heat release, after linearization, is given below.

$$Q\left(t\right) = \int_0^{s_{W,1}(t)} \rho\Delta h_r S^0_{T,C}\left(s\right)\left(1 + \sigma_{T,C}\left(s\right)\frac{\partial^2\xi_1}{\partial s^2}\right)ds \tag{A.7}$$

Assuming spatially constant $S^0_{T,C}$ and $\sigma_{T,C}$, integration of Equation (A.7) yields:

$$\hat{Q}(\omega_d) = \rho \Delta h_r S_{T,C}^0 \varepsilon \left\{ \frac{\sigma_{T,C}\left[R_1\left(e^{L_f R_1}-1\right) + P\frac{\omega_d}{u_{s,eff}}\left(1-e^{L_f \frac{\omega_d}{u_{s,eff}} P}\right)\right] - \frac{1}{\tan(\theta)}\left(e^{L_f R_1} - e^{L_f \frac{\omega_d}{u_{s,eff}} P}\right)}{\frac{S_{T,Disp}^0 \sigma_{T,D}}{u_{s,eff}}\left(\frac{\omega_d}{u_{s,eff}}\right)^2 P^2 - \frac{\omega_d}{u_{s,eff}} P + i\frac{\omega_d}{u_{s,eff}}} \right\} \quad \text{(A.8)}$$

The normal component of the coherent velocity fluctuation at the flame anchor provides the reference flow disturbance.

$$u'_{n,ref} = \hat{u}_{n,1}(s=0) = \varepsilon \cdot u_{s,eff} \quad \text{(A.9)}$$

This velocity disturbance, after normalization by $u_{n,0}$, becomes:

$$\frac{\hat{u}'_{n,ref}}{u_{n,0}} = \frac{\varepsilon}{\tan(\theta)} \quad \text{(A.10)}$$

Then, the resulting *FTF* according to Equation (3.23) is

$$FTF_{Tot}(\omega_d) = \frac{e^{L_f \frac{\omega_d}{u_{s,eff}} P} - e^{L_f R_1} + \tan(\theta_0)\sigma_{T,C}\left[R_1\left(e^{L_f R_1}-1\right) + \frac{\omega_d}{u_{s,eff}} P\left(1-e^{L_f \frac{\omega_d}{u_{s,eff}} P}\right)\right]}{St_{L_f}\left(\frac{S_{T,Disp}^0 \sigma_{T,D}}{u_{s,eff}}\left(\frac{\omega_d}{u_{s,eff}}\right) P^2 - P + i\right)} \quad \text{(A.11)}$$

This expression can be non-dimensionalized according to the scheme given in Equation (3.55) as:

$$FTF_{Tot}(\omega_d) = \frac{e^{St_{L_f}\tilde{P}} - e^{St_{L_f}\tilde{R}_1} + \tan(\theta_0)\tilde{\sigma}_{T,C}\left[\tilde{R}_1\left(e^{St_{L_f}\tilde{R}_1}-1\right) + \tilde{P}\left(1-e^{St_{L_f}\tilde{P}}\right)\right]}{St_{L_f}\left(\tilde{S}_{T,Disp}^0 \tilde{\sigma}_{T,D}\tilde{P}^2 - \tilde{P} + i\right)} \quad \text{(A.12)}$$

Equation (3.61) can be expanded for small turbulent Markstein lengths as:

$$FTF_{Tot}\left(\omega_d\right) =$$

$$\frac{\left(e^{St_{L_f}\tilde{P}} - e^{St_{L_f}\left(i-\tilde{S}^0_{T,Disp}\tilde{\sigma}_{T,D}\right)}\right)\left(1-\frac{\tilde{S}^0_{T,Disp}\tilde{P}^2}{\left(i-\tilde{P}\right)}\tilde{\sigma}_{T,D}\right)+\tan\left(\theta_0\right)\tilde{\sigma}_{T,C}\left[i\left(e^{St_{L_f}\left(i-\tilde{S}^0_{T,Disp}\tilde{\sigma}_{T,D}\right)}-1\right)+\tilde{P}\left(1-e^{St_{L_f}\tilde{P}}\right)\right]}{St_{L_f}\left(i-\tilde{P}\right)}$$

(A.13)

APPENDIX B. EFFECT OF ENSEMBLE-AVERAGED FLAME POSITION: MEDIAN VERSUS MEAN

As discussed in Section 4.2.2, the experimentally determined ensemble-averaged flame position is determined by creating a phase dependent progress variable field at each point of phase in the forcing cycle. This progress variable field is found by averaging binarized instantaneous images at a given point of phase. The ensemble-averaged flame results from extracting a progress variable iso-contour at a chosen progress variable contour.

Alternatively, the ensemble-averaged flame position could, in theory, be determined as an arithmetic mean of instantaneous flame positions. In which case, the instantaneous flame positions as a function the *x*, *y*, or *s* coordinate system would be required. However, this approach is problematic for a multivalued flame, as it is not clear how to consistently define the flame position once disconnected pockets or multivalued corrugations appear. On the other hand, an ensemble-averaged flame position based on the rebinarization approach provides a consistent and computationally inexpensive way to deal with instantaneous flame positions which in many cases are multi-valued.

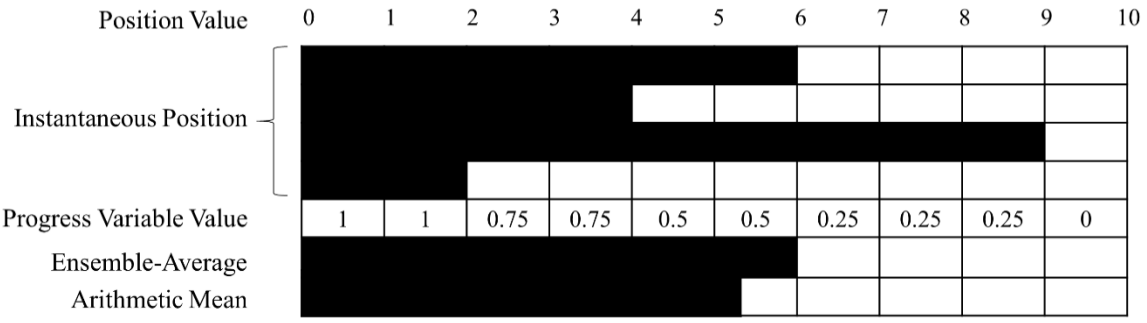

Figure B.1. Illustration of the effect of using binarization to determine the ensemble-averaged flame position.

Figure B.1 shows an illustration of why the binarization procedure produces a median rather than an arithmetic mean flame position. The top four rows illustrate several instantaneous flame positions. The fourth row shows the resulting progress variable field value determined by averaging the binary values from the top four rows. The fifth row shows the ensemble-averaged flame position, based on the $\bar{C} = 0.5$ contour. The iso-contour is defined by rebinarizing for values of $\bar{C} \geq 0.5$. Thus, the contour lies at the interface between 0.5 and 0.25.

Note that the position of the ensemble-averaged flame will not be affected by changing any of the instantaneous flame positions as long as that change does not alter the values in the cells adjacent to the ensemble-averaged flame position. For example, the instantaneous flame position shown in row two could be changed from four to three without changing the ensemble-averaged flame position. On the other hand, changing the value in row one will always alter the ensemble-averaged flame position. Thus, it is clear that the ensemble-averaged flame position reflects the median value. At the same time, any change in the instantaneous flame positions will alter the arithmetic mean flame position, shown in row five.

APPENDIX C. PROGRESS VARIABLE CONTOUR DEPENDENCE

The results shown in this thesis are generally defined based on a progress variable contour definition for the ensemble-averaged flame of $\bar{C} = 0.5$. Here, the generality of the results for a flame definition at two other progress variable contours is briefly considered in terms of changes in the regression between normalized curvature and the Markstein number dependence.

First, Figure C.1 shows two regressions for the same experimental case, but with the ensemble-averaged flame defined on two different progress variable iso-contours. The regressions are very similar in terms of slope and intercept. Figure C.1(*b*) shows increased noise, however.

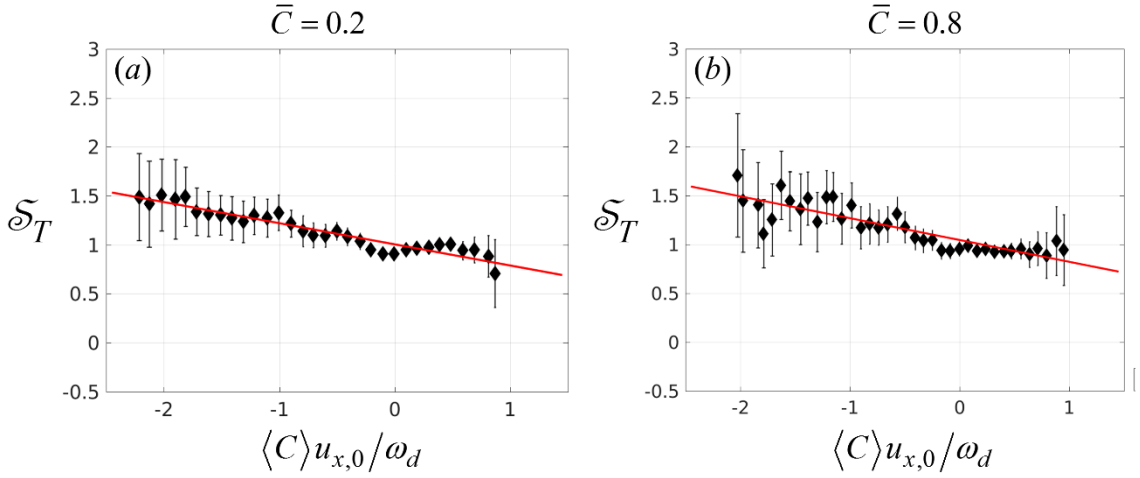

Figure C.1. Regression for, left edge, f_0 = 750 Hz, $u'/u_{x,0}$ = 15.7%, $u_{x,0}$ = 4.7 m/s based on ensemble-averaged flames defined at the (*a*) $\bar{C} = 0.2$ and (*b*) $\bar{C} = 0.8$ progress variable iso-contours.

In addition, Figure C.1 shows that, for both cases, there is a flattening of the slope between approximately zero and unity curvature values. In fact, Figure C.1(*a*) shows a

slightly increasing value of the normalized displacement speed for positive curvatures before again decreasing. The fact that this flattening is observed at multiple progress variable contours may indicates that this is real trend, rather than result of uncertainty in the curvature estimates.

Turning now to the Markstein number, the results shown in Figure 4.19 and Figure 4.20 are determined using an ensemble-averaged flame based on the $\overline{C} = 0.5$ progress variable contour.

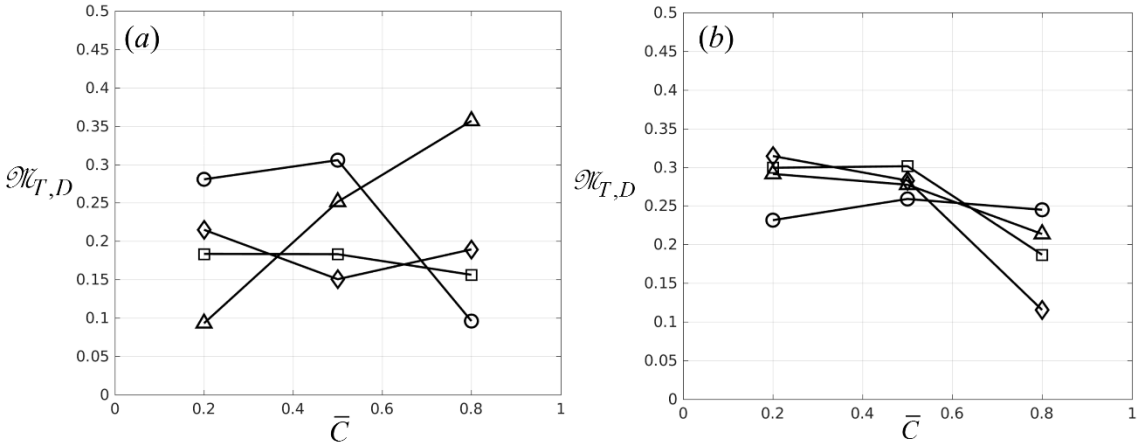

Figure C.2. Calculated non-dimensional turbulent Markstein numbers at f_0 = 750 Hz, based on (*a*) the left and (*b*) the right side of the flame, as a function of progress variable contour at four turbulence intensities, increasing in order of circles, diamonds, squares, and triangles, respectively.

Figure C.2 clearly shows that the choice of progress variable, upon which the ensemble-averaged flame is defined, affects the calculated turbulent Markstein number. Changing the definition of the ensemble-averaged flame changes both the shape of the surface as well as the surface position. In turn, this changes the ensemble-averaged velocity seen by the surface. Moving towards the products, the reactant-conditioned velocity field begins to approach that of the products because pockets and peninsulas of reactants are included in the ensemble-averaging and will therefore affect the result.

Secondly, the shape of the flame and therefore derivatives of flame change the calculated ensemble-averaged displacement speeds. Still, the variation due to progress variable choice is similar to the variation occurring within a given case between the left and right side of the flame. Interestingly, much larger variations with progress variable contour are observed for figure Figure C.2(*a*) than for Figure C.2(*b*), where the trend remains largely unchanged. Furthermore, Figure C.2 shows that the progress variable choice does not appear to change the sign of $\mathscr{M}_{T,D}$.

APPENDIX D. MEASURED EXPERIMENTAL CONDITIONS

This appendix provides a summary of the measured conditions at each test condition. The mean flow velocity and *u'* are measured separately for both the left and right sides of the flame. The oscillation amplitude, ε, is determined from the magnitude of a fast Fourier transform (FFT) of the flame holder position oscillation.

Table D.1. Nominal and measured conditions at each experimental test condition.

f_0 (Hz)	$U_{x,0}$ (m/s)	Flame Side	$u_{x,0}$ (m/s)	u' (m/s)	$u'/u_{x,0}$	u'/S_L^0	ε (mm)
200	5.0	Left	4.83	0.41	0.084	1.13	0.47
200	5.0	Left	4.71	0.76	0.162	2.07	0.50
200	5.0	Left	3.98	1.18	0.296	3.17	0.48
200	5.0	Left	3.78	1.25	0.329	3.38	0.47
200	5.0	Right	4.75	0.41	0.086	1.13	0.47
200	5.0	Right	4.62	0.77	0.166	2.09	0.50
200	5.0	Right	4.30	1.13	0.263	3.05	0.48
200	5.0	Right	4.35	1.19	0.275	3.24	0.47
200	8.0	Left	8.14	0.72	0.088	2.11	0.45
200	8.0	Left	7.82	1.13	0.145	3.26	0.51
200	8.0	Left	6.80	1.98	0.292	5.81	0.48
200	8.0	Left	6.06	2.17	0.359	6.39	0.42
200	8.0	Right	8.07	0.68	0.084	1.99	0.45
200	8.0	Right	7.75	1.02	0.131	2.93	0.51
200	8.0	Right	7.21	1.84	0.255	5.39	0.48
200	8.0	Right	7.06	1.89	0.267	5.54	0.42
750	5.0	Left	4.87	0.43	0.089	1.20	0.42
750	5.0	Left	4.67	0.73	0.157	1.99	0.31
750	5.0	Left	4.12	1.22	0.295	3.27	0.32
750	5.0	Left	3.76	1.25	0.331	3.38	0.32
750	5.0	Right	4.78	0.45	0.093	1.24	0.42
750	5.0	Right	4.61	0.67	0.146	1.83	0.31
750	5.0	Right	4.34	1.06	0.244	2.85	0.32
750	5.0	Right	4.37	1.15	0.264	3.13	0.32
750	8.0	Left	7.94	0.78	0.098	2.29	0.36
750	8.0	Left	7.76	1.14	0.147	3.28	0.32
750	8.0	Left	6.98	1.91	0.273	5.58	0.32
750	8.0	Left	6.01	2.24	0.373	6.57	0.35

750	8.0	Right	7.83	0.63	0.080	1.84	0.36
750	8.0	Right	7.67	1.09	0.142	3.13	0.32
750	8.0	Right	7.19	1.78	0.247	5.20	0.32
750	8.0	Right	7.01	1.92	0.274	5.64	0.35
1250	5.0	Left	4.69	0.65	0.139	1.82	0.55
1250	5.0	Left	4.65	0.67	0.145	1.83	0.28
1250	5.0	Left	4.14	1.18	0.284	3.17	0.26
1250	5.0	Left	3.70	1.24	0.335	3.36	0.28
1250	5.0	Right	4.54	0.52	0.114	1.44	0.55
1250	5.0	Right	4.60	0.60	0.130	1.63	0.28
1250	5.0	Right	4.33	1.06	0.245	2.86	0.26
1250	5.0	Right	4.43	0.98	0.220	2.65	0.28
1250	8.0	Left	8.01	0.61	0.076	1.80	0.22
1250	8.0	Left	7.79	1.15	0.148	3.31	0.35
1250	8.0	Left	7.11	1.84	0.258	5.37	0.23
1250	8.0	Left	6.24	2.01	0.321	5.89	0.21
1250	8.0	Right	7.97	0.83	0.104	2.44	0.22
1250	8.0	Right	7.69	1.01	0.132	2.92	0.35
1250	8.0	Right	7.31	1.61	0.220	4.70	0.23
1250	8.0	Right	7.21	1.75	0.243	5.15	0.21

APPENDIX E. ENSEMBLE AVERAGED FLAME POSITIONS

This appendix presents a full set of results from the experimental investigation of the ensemble-averaged flame position.

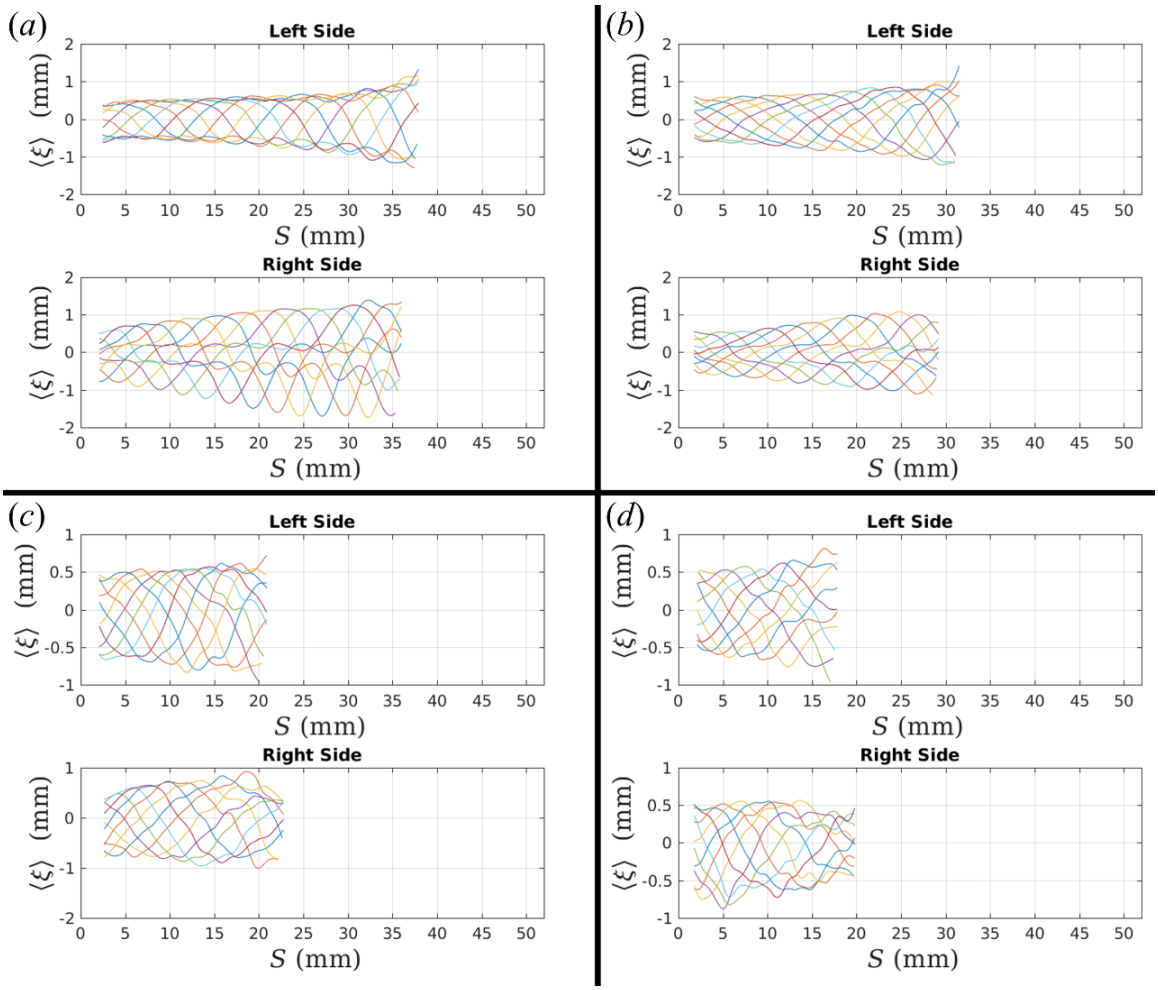

Figure E.1. Ensemble-averaged flame position fluctuations at f_0 = 200 Hz at (*a, top*) $u'/u_{x,0}$ = 8.4%, $u_{x,0}$ = 4.8 m/s; (*a, bottom*) $u'/u_{x,0}$ = 8.6%, $u_{x,0}$ = 4.8 m/s; (*b, top*) $u'/u_{x,0}$ = 16.2%, $u_{x,0}$ = 4.7 m/s; (*b, bottom*) $u'/u_{x,0}$ = 16.6%, $u_{x,0}$ = 4.6 m/s; (*c, top*) $u'/u_{x,0}$ = 29.6%, $u_{x,0}$ = 4.0 m/s; (*c, bottom*) $u'/u_{x,0}$ = 26.3%, $u_{x,0}$ = 4.3 m/s; (*d, top*) $u'/u_{x,0}$ = 32.9%, $u_{x,0}$ = 3.8 m/s; (*d, bottom*) $u'/u_{x,0}$ = 27.4%, $u_{x,0}$ = 4.3 m/s.

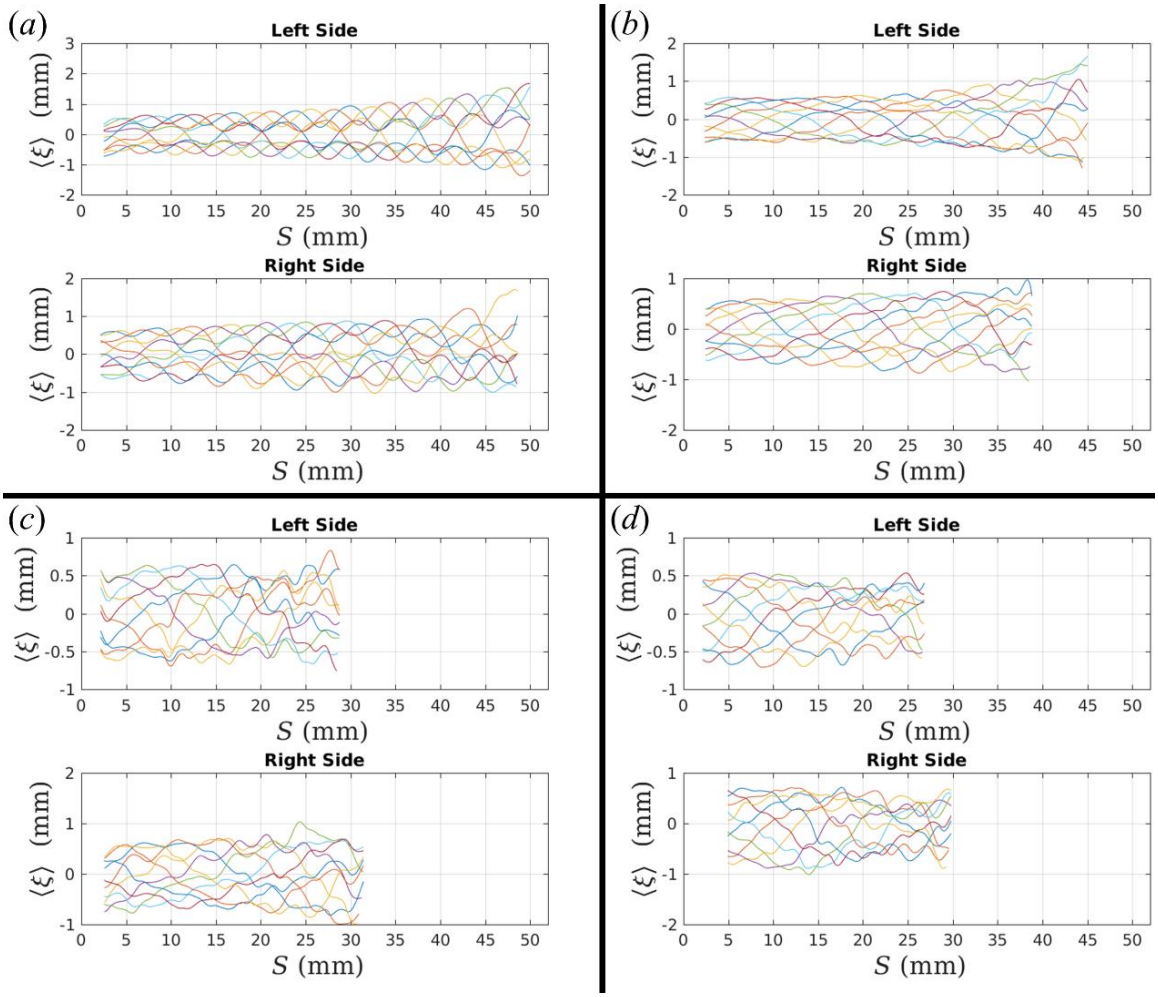

Figure E.2. Ensemble-averaged flame position fluctuations at f_0 = 200 Hz at (*a, top*) $u'/u_{x,0}$ = 8.8%, $u_{x,0}$ = 8.14 m/s; (*a, bottom*) $u'/u_{x,0}$ = 8.4%, $u_{x,0}$ = 8.1 m/s; (*b, top*) $u'/u_{x,0}$ = 14.5%, $u_{x,0}$ = 7.8 m/s; (*b, bottom*) $u'/u_{x,0}$ = 13.1%, $u_{x,0}$ = 7.8 m/s; (*c, top*) $u'/u_{x,0}$ = 29.2%, $u_{x,0}$ = 6.8 m/s; (*c, bottom*) $u'/u_{x,0}$ = 25.5%, $u_{x,0}$ = 7.2 m/s; (*d, top*) $u'/u_{x,0}$ = 35.9%, $u_{x,0}$ = 6.1 m/s; (*d, bottom*) $u'/u_{x,0}$ = 26.7%, $u_{x,0}$ = 7.1 m/s.

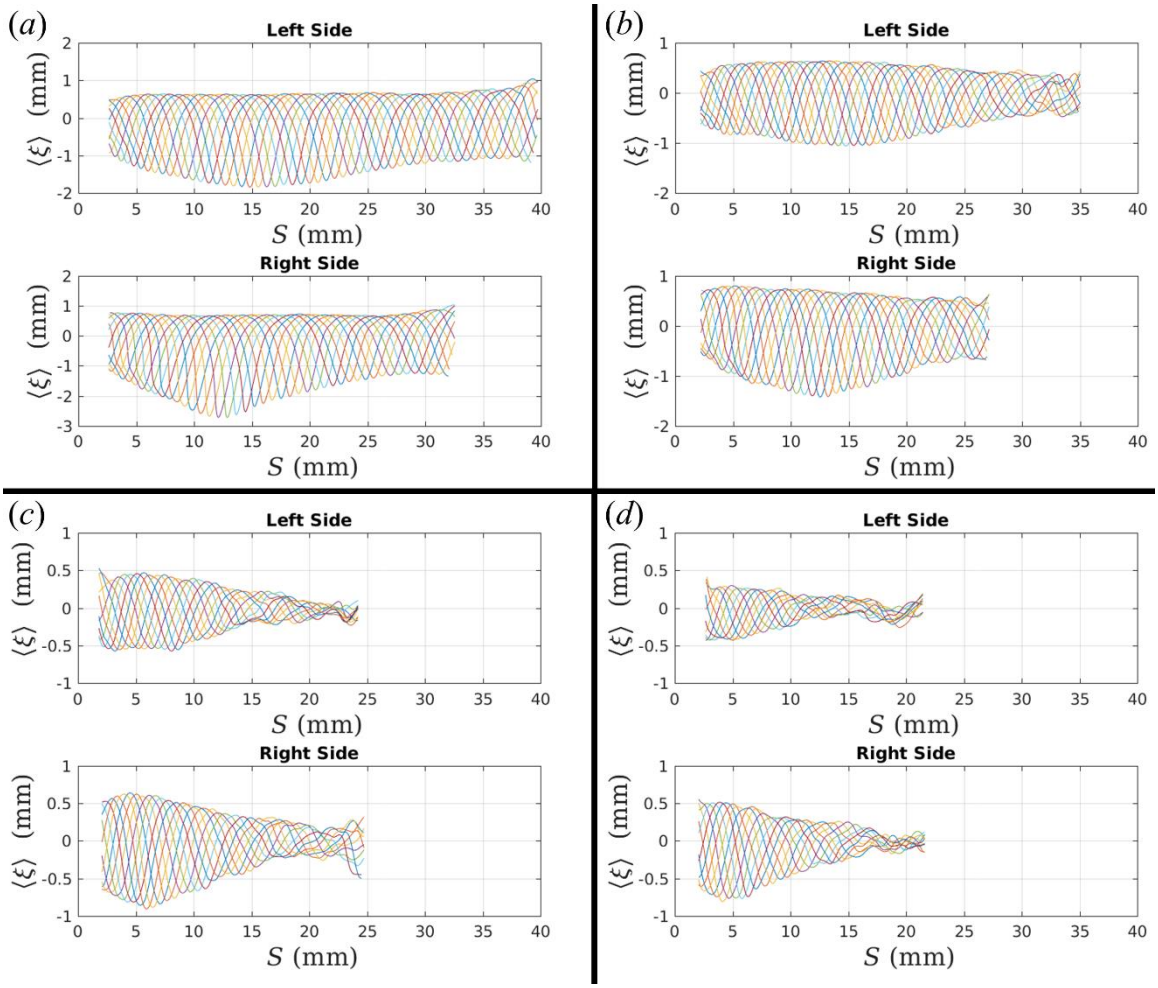

Figure E.3. Ensemble-averaged flame position fluctuations at f_0 = 750 Hz at (*a, top*) $u'/u_{x,0}$ = 8.9%, $u_{x,0}$ = 4.9 m/s; (*a, bottom*) $u'/u_{x,0}$ = 9.3%, $u_{x,0}$ = 4.8 m/s; (*b, top*) $u'/u_{x,0}$ = 15.7%, $u_{x,0}$ = 4.7 m/s; (*b, bottom*) $u'/u_{x,0}$ = 14.6%, $u_{x,0}$ = 4.6 m/s; (*c, top*) $u'/u_{x,0}$ = 29.5%, $u_{x,0}$ = 4.1 m/s; (*c, bottom*) $u'/u_{x,0}$ = 24.4%, $u_{x,0}$ = 4.3 m/s; (*d, top*) $u'/u_{x,0}$ = 33.1%, $u_{x,0}$ = 3.8 m/s; (*d, bottom*) $u'/u_{x,0}$ = 26.4%, $u_{x,0}$ = 4.4 m/s.

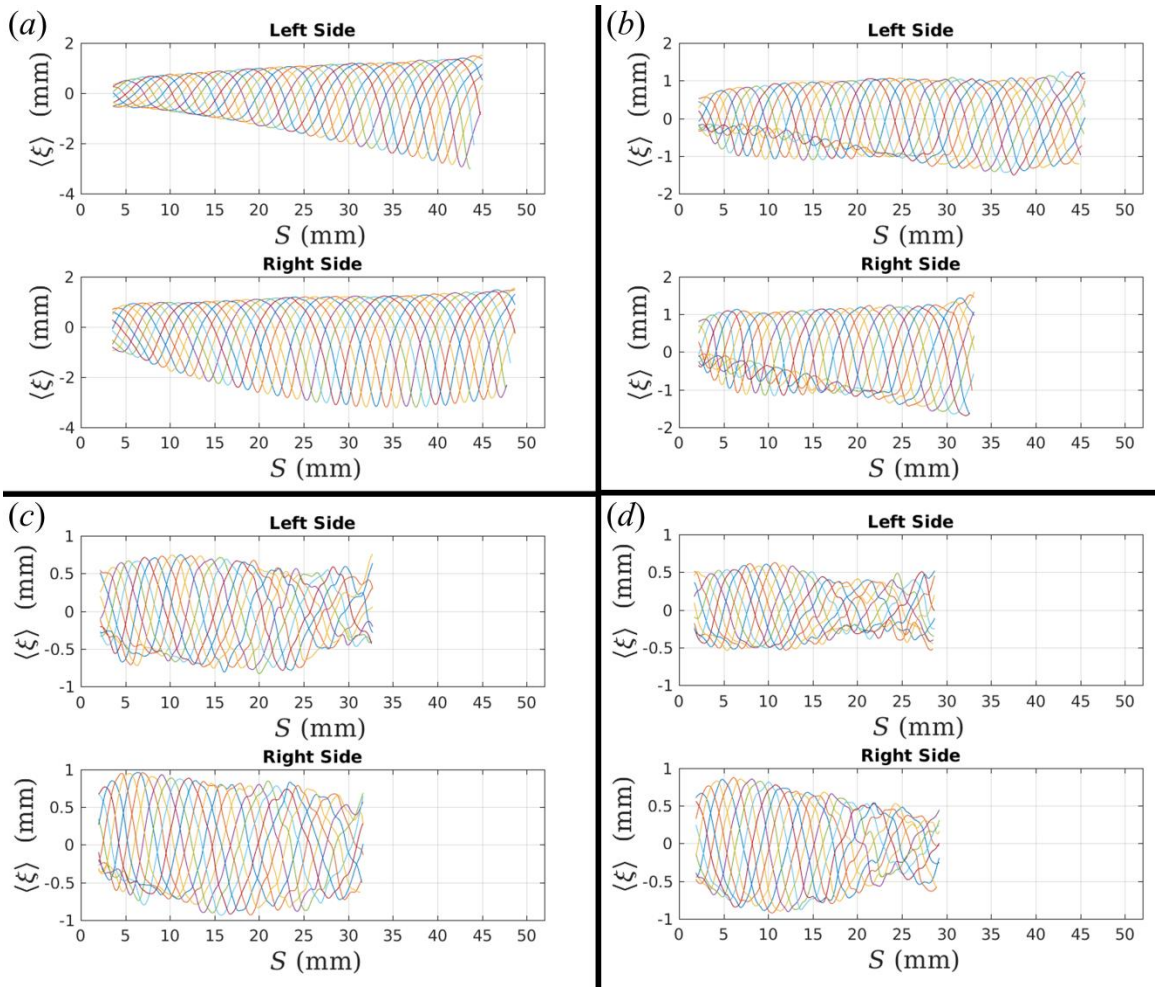

Figure E.4. Ensemble-averaged flame position fluctuations at f_0 = 750 Hz at (*a, top*) $u'/u_{x,0}$ = 9.8%, $u_{x,0}$ = 7.94 m/s; (*a, bottom*) $u'/u_{x,0}$ = 8.0%, $u_{x,0}$ = 7.8 m/s; (*b, top*) $u'/u_{x,0}$ = 14.7%, $u_{x,0}$ = 7.8 m/s; (*b, bottom*) $u'/u_{x,0}$ = 14.2%, $u_{x,0}$ = 7.7 m/s; (*c, top*) $u'/u_{x,0}$ = 27.3%, $u_{x,0}$ = 7.0 m/s; (*c, bottom*) $u'/u_{x,0}$ = 24.7%, $u_{x,0}$ = 7.2 m/s; (*d, top*) $u'/u_{x,0}$ = 37.3%, $u_{x,0}$ = 6.0 m/s; (*d, bottom*) $u'/u_{x,0}$ = 27.4%, $u_{x,0}$ = 7.0 m/s.

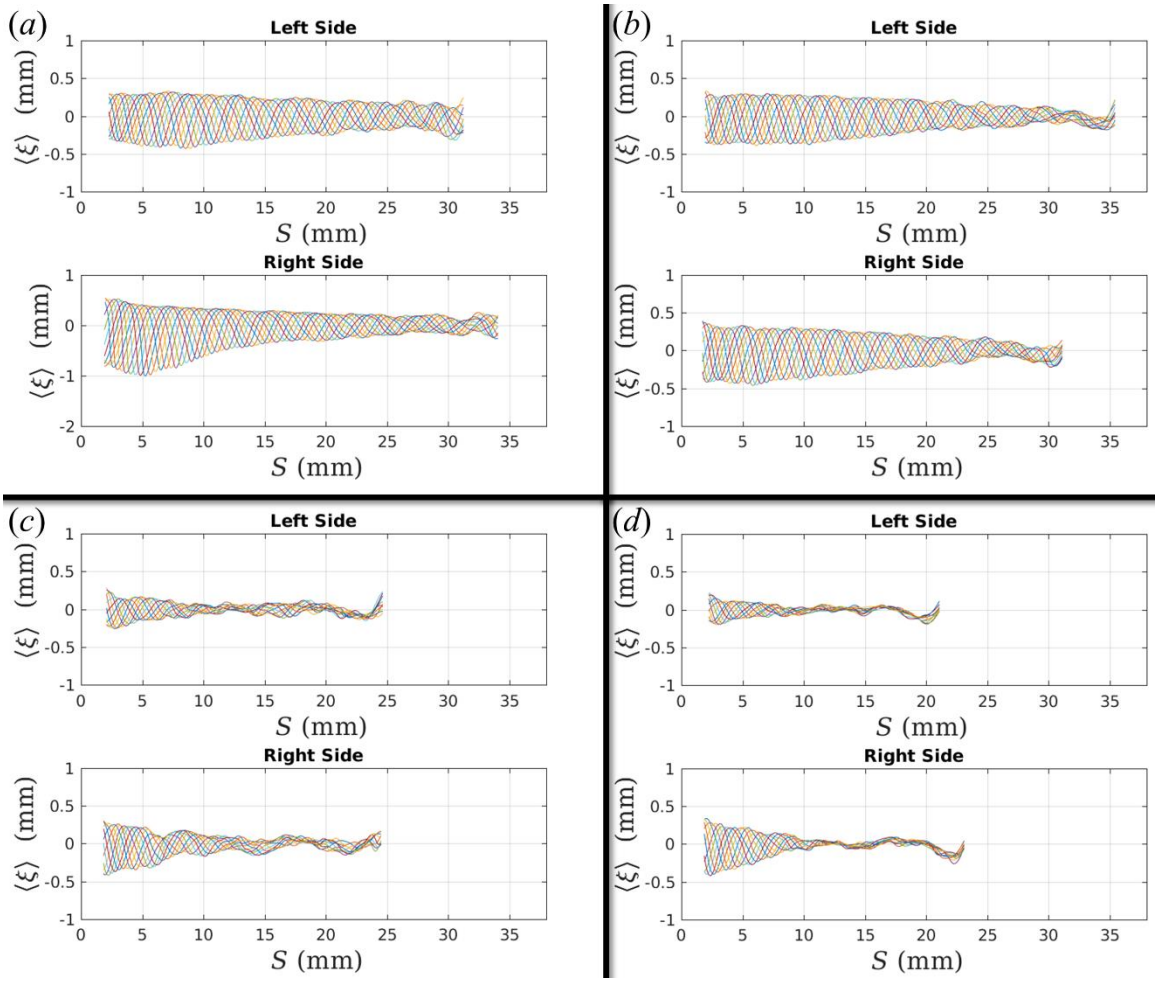

Figure E.5. Ensemble-averaged flame position fluctuations at f_0 = 1250 Hz at (*a, top*) $u'/u_{x,0}$ = 13.9%, $u_{x,0}$ = 4.7 m/s; (*a, bottom*) $u'/u_{x,0}$ = 11.4%, $u_{x,0}$ = 4.5 m/s; (*b, top*) $u'/u_{x,0}$ = 14.5%, $u_{x,0}$ = 4.6 m/s; (*b, bottom*) $u'/u_{x,0}$ = 13.0%, $u_{x,0}$ = 4.6 m/s; (*c, top*) $u'/u_{x,0}$ = 28.4%, $u_{x,0}$ = 4.1 m/s; (*c, bottom*) $u'/u_{x,0}$ = 24.5%, $u_{x,0}$ = 4.3 m/s; (*d, top*) $u'/u_{x,0}$ = 33.5%, $u_{x,0}$ = 3.7 m/s; (*d, bottom*) $u'/u_{x,0}$ = 22.0%, $u_{x,0}$ = 4.4 m/s.

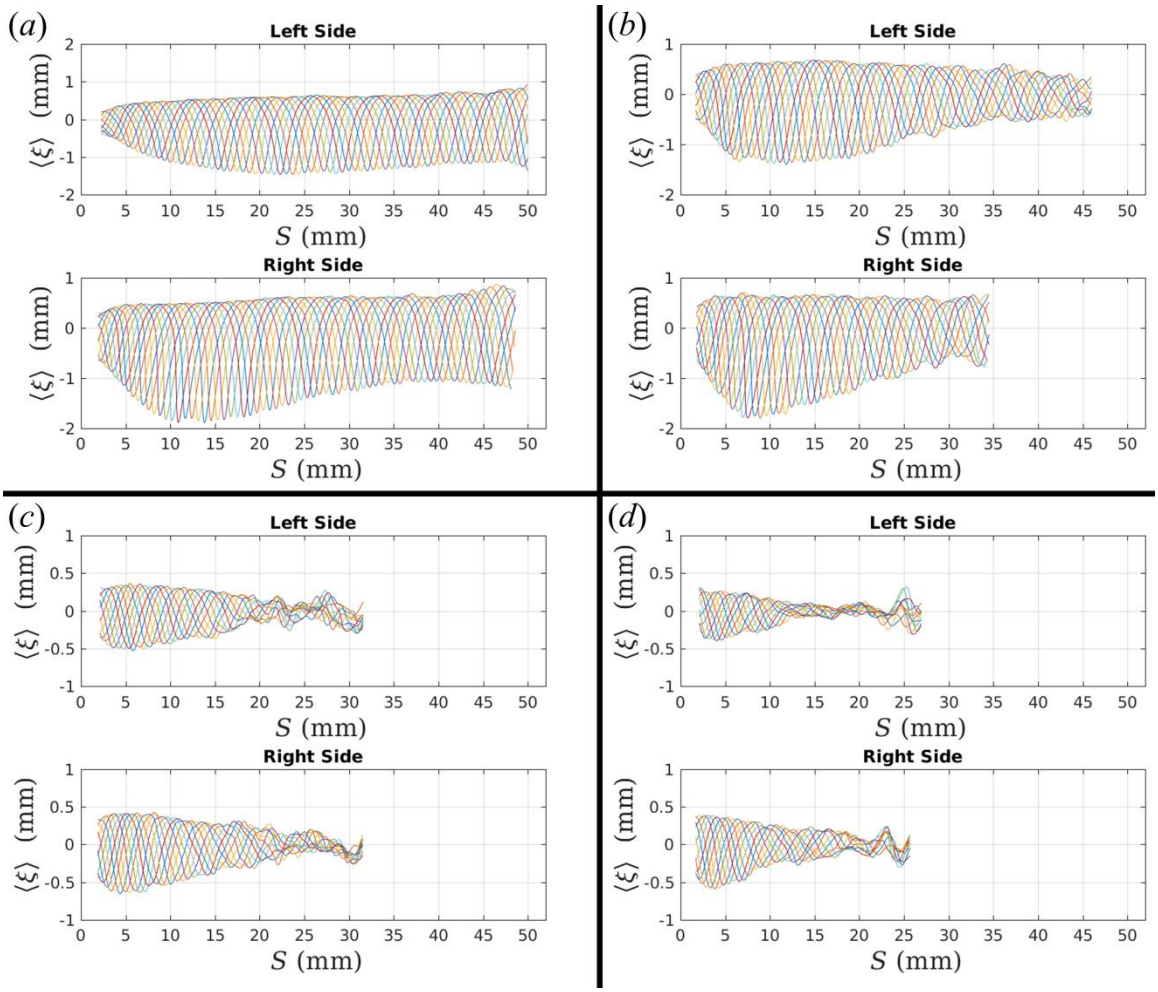

Figure E.6. Ensemble-averaged flame position fluctuations at f_0 = 1250 Hz at (*a, top*) $u'/u_{x,0}$ = 7.6%, $u_{x,0}$ = 8.0 m/s; (*a, bottom*) $u'/u_{x,0}$ = 10.4%, $u_{x,0}$ = 8.0 m/s; (*b, top*) $u'/u_{x,0}$ = 14.8%, $u_{x,0}$ = 7.8 m/s; (*b, bottom*) $u'/u_{x,0}$ = 13.2%, $u_{x,0}$ = 7.7 m/s; (*c, top*) $u'/u_{x,0}$ = 25.8%, $u_{x,0}$ = 7.1 m/s; (*c, bottom*) $u'/u_{x,0}$ = 22.0%, $u_{x,0}$ = 7.3 m/s; (*d, top*) $u'/u_{x,0}$ = 32.1%, $u_{x,0}$ = 6.2 m/s; (*d, bottom*) $u'/u_{x,0}$ = 24.3%, $u_{x,0}$ = 7.2 m/s.

APPENDIX F. AVERAGE DISPLACEMENT SPEEDS

This appendix provides plots of the average ensemble-averaged turbulent displacement speed as a function of the flame coordinate for all cases. Turbulence level generally increases in order of stars, circles, diamonds, to squares. Data from the left side of the flame are shown in subplots (*a*) and (*c*), while data from the right side of the flame are shown in subplots (*b*) and (*d*).

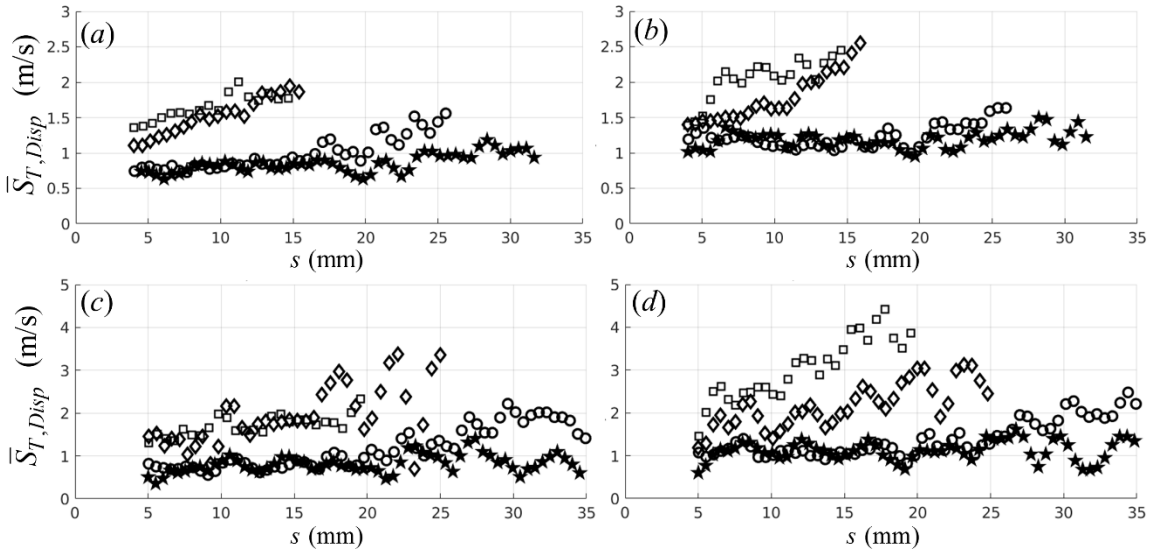

Figure F.1. Average ensemble-averaged turbulent displacement speed at f_0 = 200 Hz (*a, stars*) $u'/u_{x,0}$ = 8.4%, $u_{x,0}$ = 4.8 m/s; (*a, circles*) $u'/u_{x,0}$ = 16.2%, $u_{x,0}$ = 4.7 m/s; (*a, diamonds*) $u'/u_{x,0}$ = 29.6%, $u_{x,0}$ = 4.0 m/s; (*a, squares*) $u'/u_{x,0}$ = 32.9%, $u_{x,0}$ = 3.8 m/s; (*b, stars*) $u'/u_{x,0}$ = 8.6%, $u_{x,0}$ = 4.75 m/s; (*b, circles*) $u'/u_{x,0}$ = 16.6%, $u_{x,0}$ = 4.62 m/s; (*b, diamonds*) $u'/u_{x,0}$ = 26.3%, $u_{x,0}$ = 4.3 m/s; (*b, squares*) $u'/u_{x,0}$ =27.5%, $u_{x,0}$ = 4.35 m/s; (*c, stars*) $u'/u_{x,0}$ = 8.8%, $u_{x,0}$ = 8.14 m/s; (*c, circles*) $u'/u_{x,0}$ = 14.5%, $u_{x,0}$ = 7.8 m/s; (*c, diamonds*) $u'/u_{x,0}$ = 29.2%, $u_{x,0}$ = 6.8 m/s; (*c, squares*) $u'/u_{x,0}$ = 35.9%, $u_{x,0}$ = 6.1 m/s; (*d, stars*) $u'/u_{x,0}$ = 8.4%, $u_{x,0}$ = 8.1 m/s; (*d, circles*) $u'/u_{x,0}$ = 13.1%, $u_{x,0}$ = 7.8 m/s; (*d, diamonds*) $u'/u_{x,0}$ = 25.5%, $u_{x,0}$ = 7.2 m/s; (*d, squares*) $u'/u_{x,0}$ = 26.7%, $u_{x,0}$ = 7.1 m/s.

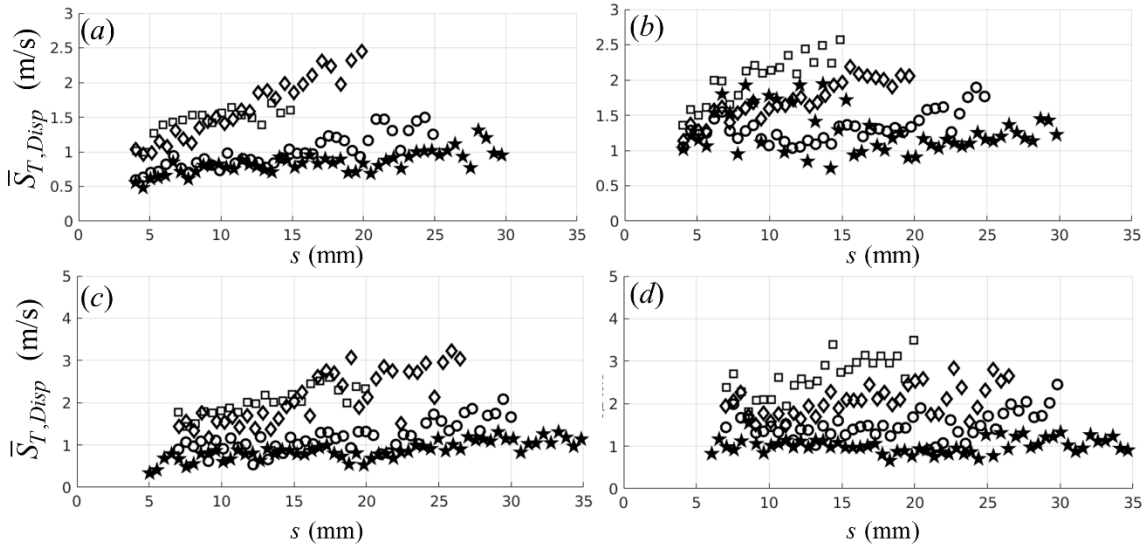

Figure F.2. Average ensemble-averaged turbulent displacement speed at f_0 = 750 Hz (*a, stars*) $u'/u_{x,0}$ = 8.9%, $u_{x,0}$ = 4.9 m/s; (*a, circles*) $u'/u_{x,0}$ = 15.7%, $u_{x,0}$ = 4.7 m/s; (*a, diamonds*) $u'/u_{x,0}$ =29.5%, $u_{x,0}$ =4.1 m/s; (*a, squares*) $u'/u_{x,0}$ =33.1%, $u_{x,0}$ = 3.8 m/s; (*b, stars*) $u'/u_{x,0}$ = 9.3%, $u_{x,0}$ = 4.8 m/s; (*b, circles*) $u'/u_{x,0}$ = 14.6%, $u_{x,0}$ = 4.6 m/s; (*b, diamonds*) $u'/u_{x,0}$ = 24.4%, $u_{x,0}$ = 4.3 m/s;(*b, squares*) $u'/u_{x,0}$ = 26.4%, $u_{x,0}$ = 4.4 m/s; (*c, stars*) $u'/u_{x,0}$ = 9.8%, $u_{x,0}$ = 8.0 m/s; (*c, circles*) $u'/u_{x,0}$ = 14.7%, $u_{x,0}$ = 7.8 m/s; (*c, diamonds*) $u'/u_{x,0}$ = 27.3%, $u_{x,0}$ = 7.0 m/s; (*c, squares*) $u'/u_{x,0}$ = 37.3%, $u_{x,0}$ = 6.0 m/s; (*d, stars*) $u'/u_{x,0}$ = 8.0%, $u_{x,0}$ = 7.8 m/s; (*d, circles*) $u'/u_{x,0}$ = 14.2%, $u_{x,0}$ = 7.7 m/s; (*d, diamonds*) $u'/u_{x,0}$ = 24.7%, $u_{x,0}$ = 7.2 m/s; (*d, squares*) $u'/u_{x,0}$ = 27.4%, $u_{x,0}$ = 7.0 m/s.

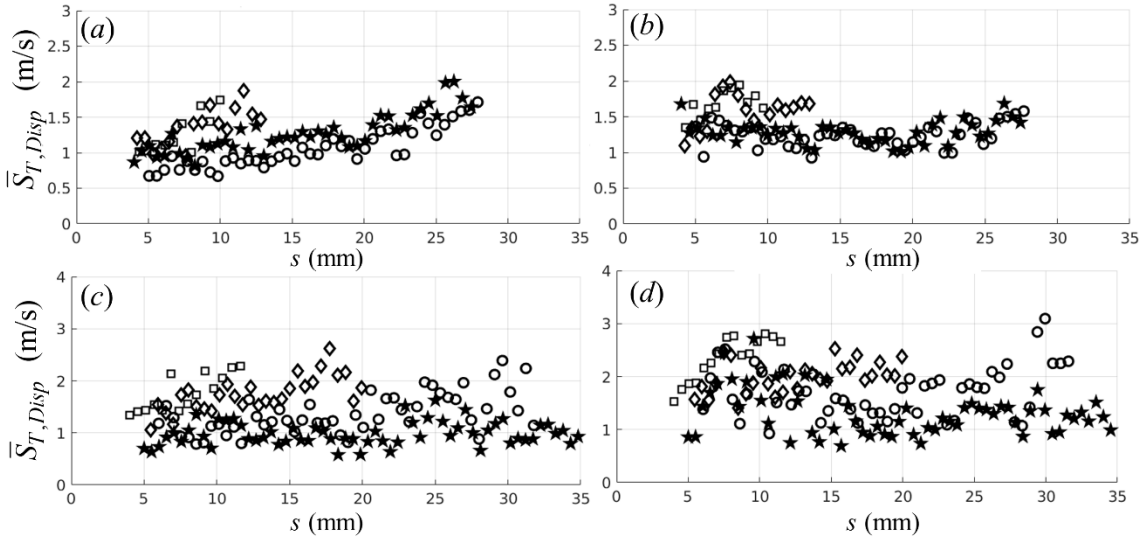

Figure F.3. Average ensemble-averaged turbulent displacement speed at f_0 = 1250 Hz (*a, stars*) $u'/u_{x,0}$ = 13.9%, $u_{x,0}$ = 4.7 m/s; (*a, circles*) $u'/u_{x,0}$ = 14.5%, $u_{x,0}$ = 4.7 m/s; (*a, diamonds*) $u'/u_{x,0}$ = 28.4%, $u_{x,0}$ = 4.1 m/s; (*a, squares*) $u'/u_{x,0}$ = 33.5%, $u_{x,0}$ = 3.7 m/s; (*b, stars*) $u'/u_{x,0}$ = 11.4%, $u_{x,0}$ = 4.5 m/s; (*b, circles*) $u'/u_{x,0}$ = 13.0%, $u_{x,0}$ = 4.6 m/s; (*b, diamonds*) $u'/u_{x,0}$ = 24.5%, $u_{x,0}$ = 4.3 m/s; (*b, squares*) $u'/u_{x,0}$ = 22.0%, $u_{x,0}$ =4.4 m/s; (*c, stars*) $u'/u_{x,0}$ = 7.6%, $u_{x,0}$ = 8.0 m/s; (*c, circles*) $u'/u_{x,0}$ = 14.8%, $u_{x,0}$ = 7.8 m/s; (*c, diamonds*) $u'/u_{x,0}$ = 25.8%, $u_{x,0}$ = 7.1 m/s; (*c, squares*) $u'/u_{x,0}$ = 32.1%, $u_{x,0}$ = 6.2 m/s; (*d, stars*) $u'/u_{x,0}$ = 10.4%, $u_{x,0}$ = 8.0 m/s; (*d, circles*) $u'/u_{x,0}$ = 13.2%, $u_{x,0}$ = 7.7 m/s; (*d, diamonds*) $u'/u_{x,0}$ = 22.0%, $u_{x,0}$ = 7.3 m/s; (*d, squares*) $u'/u_{x,0}$ = 24.3%, $u_{x,0}$ = 7.2 m/s.

APPENDIX G. ENSEMBLE-AVERAGED DISPLACEMENT SPEED CURVATURE CORRELATIONS

This appendix provides a comprehensive set of correlations between the normalized ensemble-averaged turbulent displacement speed, $\mathcal{S}_T$, and the normalized ensemble-averaged flame curvature, $\langle C \rangle u_{x,0}/\omega_d$. The left-hand side of the figure shows a normalized joint probability density plots while the right-hand side of the figure shows the corresponding deweighted correlation plot. Data from the left side of the flame are shown in subplots (*a*) and (*b*), while data from the right side of the flame are shown in subplots (*c*) and (*d*).

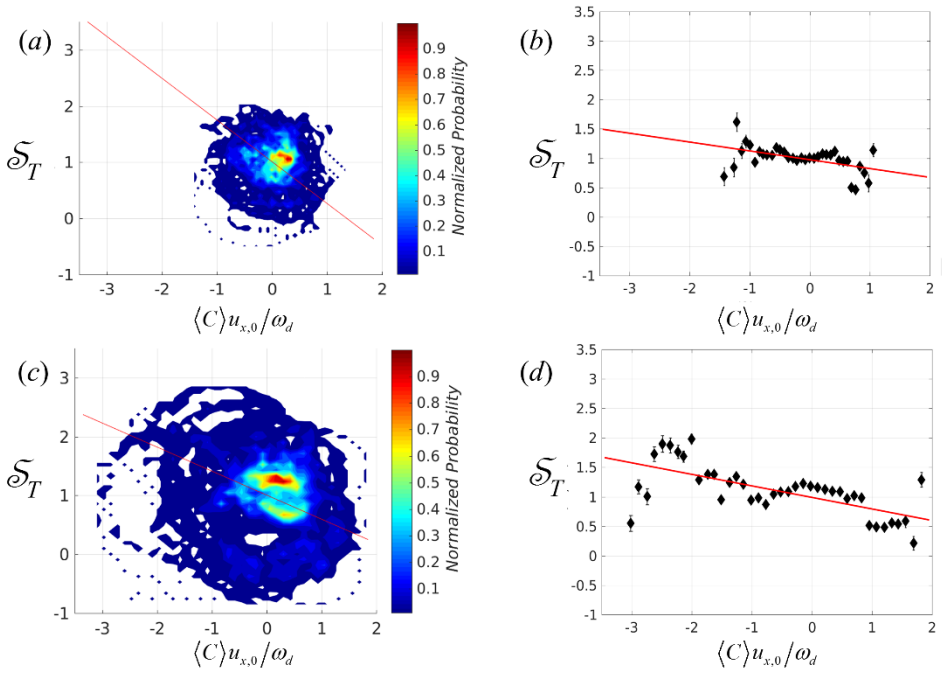

Figure G.1. Normalized ensemble-averaged turbulent displacement flame speed versus curvature shown with (*a, c*) PDF plots and (*b, d*) deweighted plots, at f_0 = 200 Hz at (*a, b*) $u'/u_{x,0}$ = 8.4%, $u_{x,0}$ = 4.8 m/s; (*c, d*) $u'/u_{x,0}$ = 8.6%, $u_{x,0}$ = 4.8 m/s.

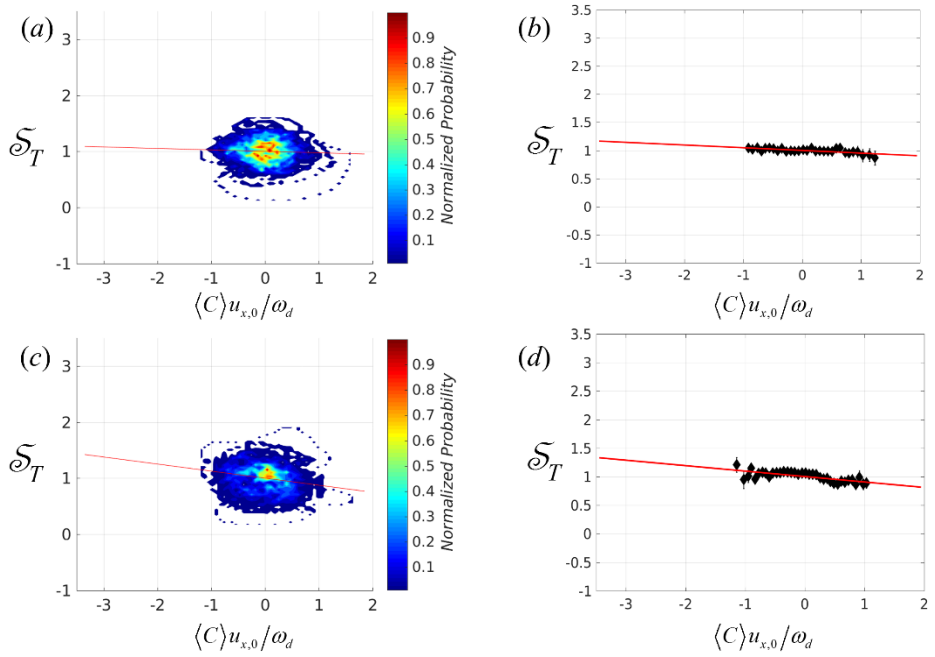

Figure G.2. Normalized ensemble-averaged turbulent displacement flame speed versus curvature shown with (*a, c*) PDF plots and (*b, d*) deweighted plots, at f_0 = 200 Hz at (*a, b*) $u'/u_{x,0}$ = 16.2%, $u_{x,0}$ = 4.7 m/s; (*c, d*) $u'/u_{x,0}$ = 16.6%, $u_{x,0}$ = 4.6 m/s.

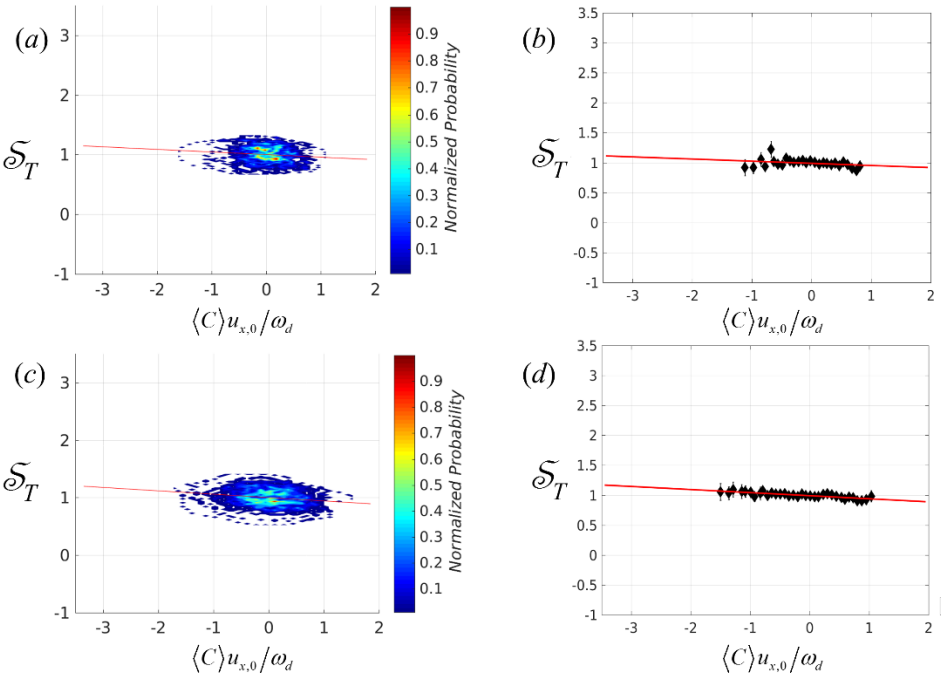

Figure G.3. Normalized ensemble-averaged turbulent displacement flame speed versus curvature shown with (*a, c*) PDF plots and (*b, d*) deweighted plots, at f_0 = 200 Hz at (*a, b*) $u'/u_{x,0}$ = 29.6%, $u_{x,0}$ = 4.0 m/s; (*c, d*) $u'/u_{x,0}$ = 26.3%, $u_{x,0}$ = 4.3 m/s.

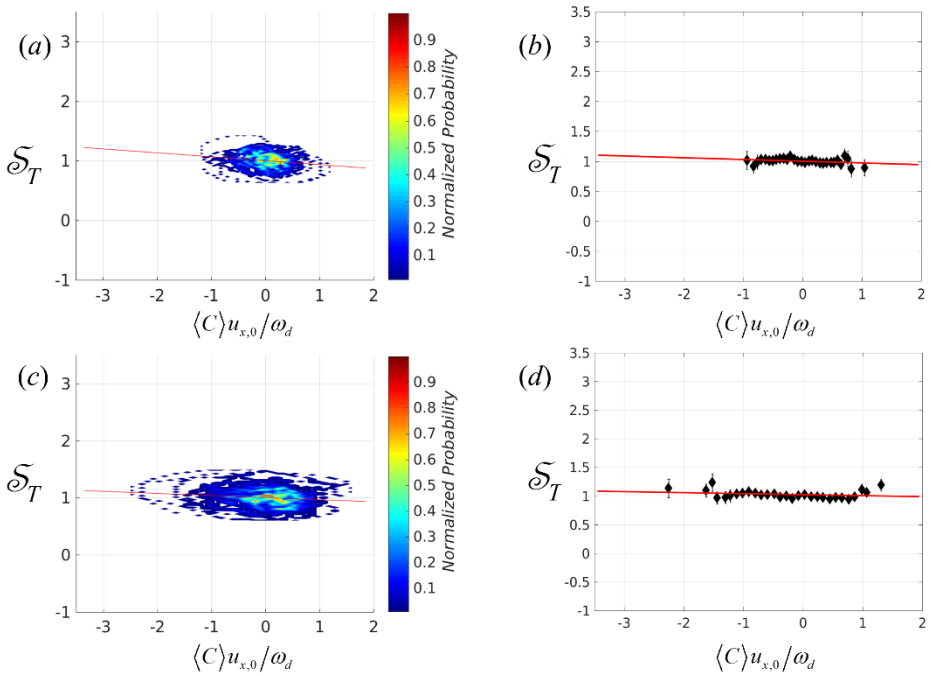

Figure G.4. Normalized ensemble-averaged turbulent displacement flame speed versus curvature shown with (*a, c*) PDF plots and (*b, d*) deweighted plots, at f_0 = 200 Hz at (*a, b*) $u'/u_{x,0}$ = 32.9%, $u_{x,0}$ = 3.8 m/s; (*c, d*) $u'/u_{x,0}$ = 27.4%, $u_{x,0}$ = 4.3 m/s.

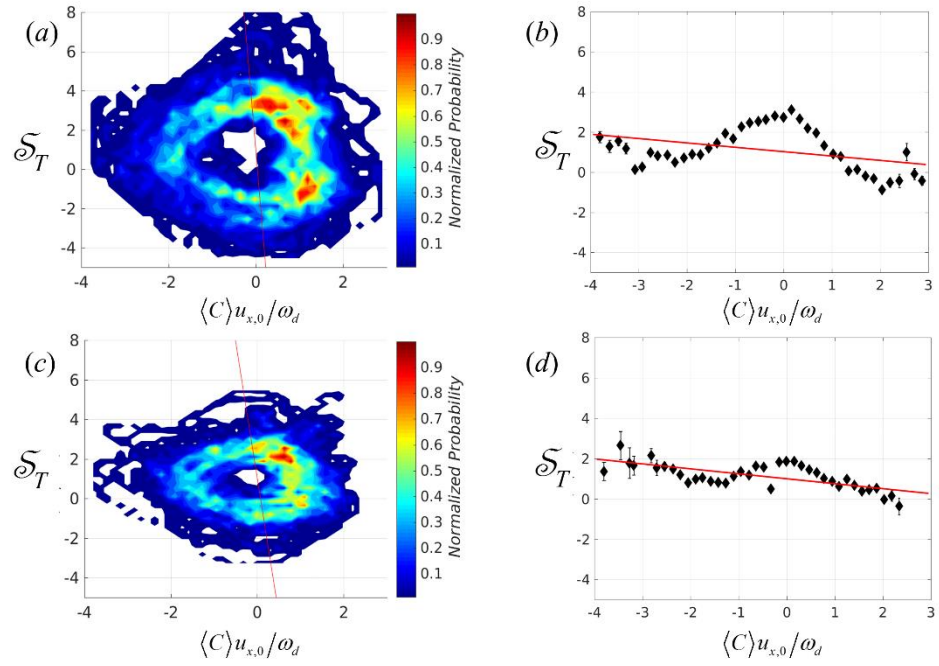

Figure G.5. Normalized ensemble-averaged turbulent displacement flame speed versus curvature shown with (*a, c*) PDF plots and (*b, d*) deweighted plots, at f_0 = 200 Hz at (*a, b*) $u'/u_{x,0}$ = 8.8%, $u_{x,0}$ = 8.14 m/s; (*c, d*) $u'/u_{x,0}$ = 8.4%, $u_{x,0}$ = 8.1 m/s.

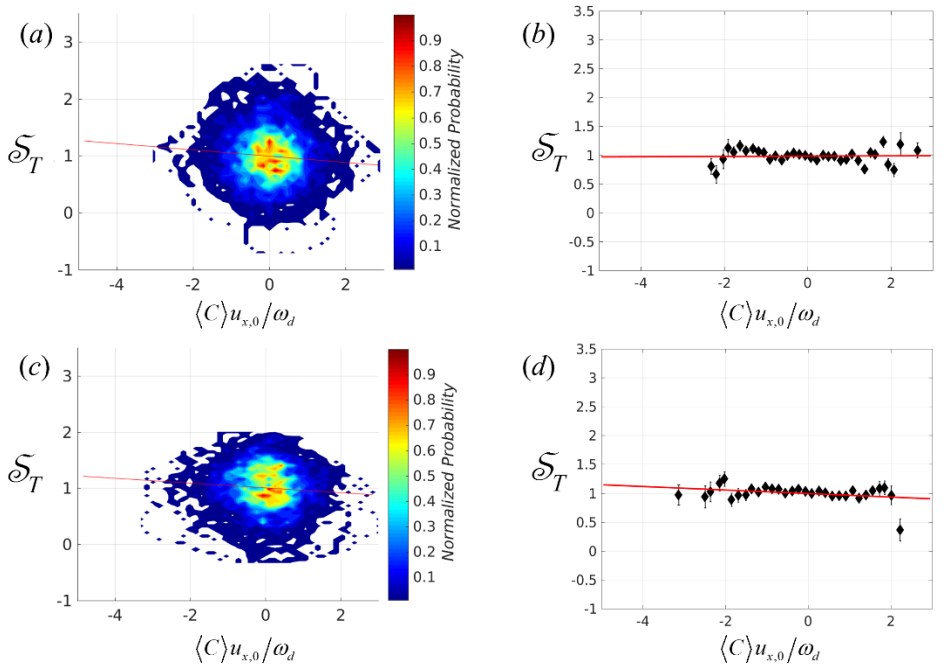

Figure G.6. Normalized ensemble-averaged turbulent displacement flame speed versus curvature shown with (*a, c*) PDF plots and (*b, d*) deweighted plots, at f_0 = 200 Hz at (*a, b*) $u'/u_{x,0}$ = 14.5%, $u_{x,0}$ = 7.8 m/s; (*c, d*) $u'/u_{x,0}$ = 13.1%, $u_{x,0}$ = 7.8 m/s.

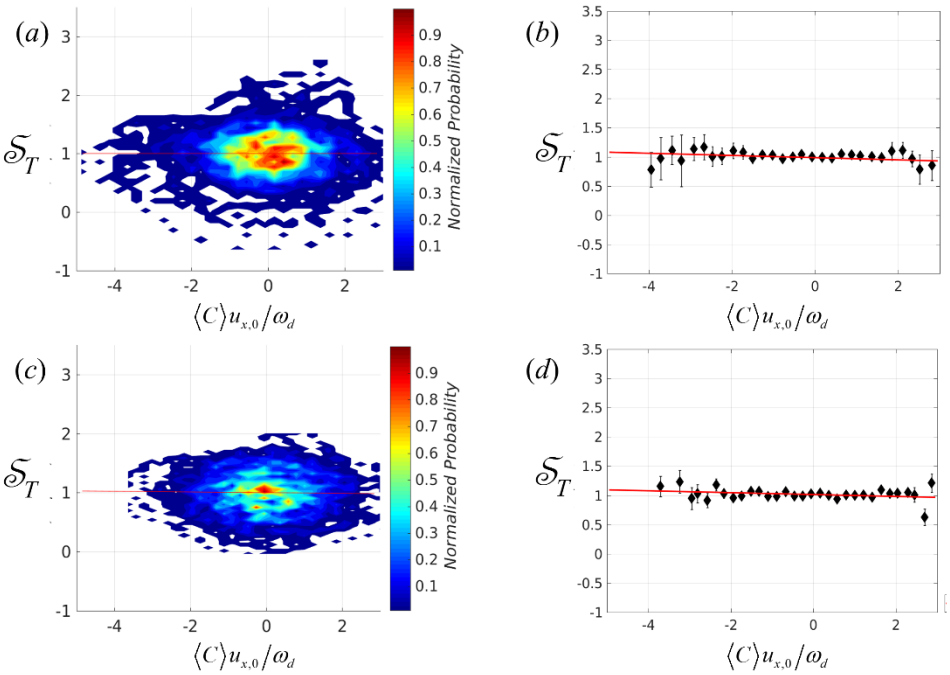

Figure G.7. Normalized ensemble-averaged turbulent displacement flame speed versus curvature shown with (*a, c*) PDF plots and (*b, d*) deweighted plots, at f_0 = 200 Hz at (*a, b*) $u'/u_{x,0}$ = 29.2%, $u_{x,0}$ = 6.8 m/s; (*c, d*) $u'/u_{x,0}$ = 25.5%, $u_{x,0}$ = 7.2 m/s.

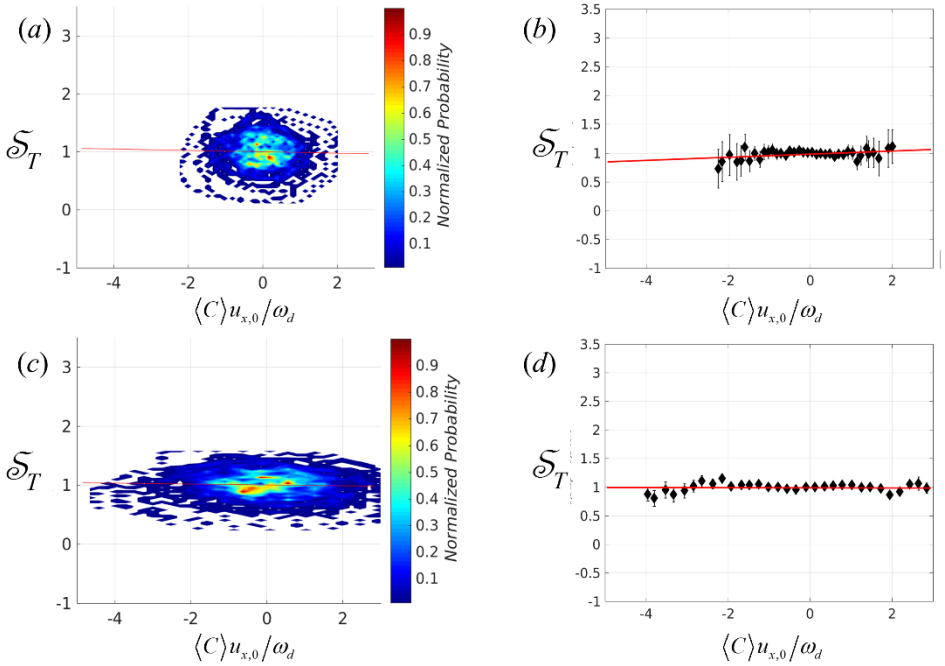

Figure G.8. Normalized ensemble-averaged turbulent displacement flame speed versus curvature shown with (*a, c*) PDF plots and (*b, d*) deweighted plots, at f_0 = 200 Hz at (*a, b*) $u'/u_{x,0}$ = 35.9%, $u_{x,0}$ = 6.1 m/s; (*c, d*) $u'/u_{x,0}$ = 26.7%, $u_{x,0}$ = 7.1 m/s.

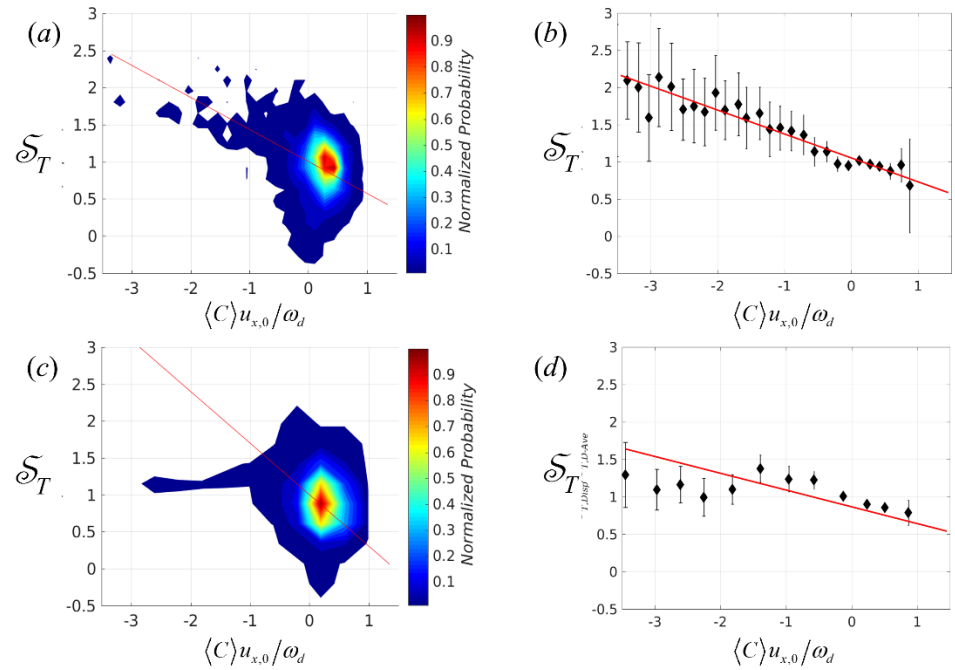

Figure G.9. Normalized ensemble-averaged turbulent displacement flame speed versus curvature shown with (*a, c*) PDF plots and (*b, d*) deweighted plots, at f_0 = 750 Hz at (*a, b*) $u'/u_{x,0}$ = 8.9%, $u_{x,0}$ = 4.9 m/s; (*c, d*) $u'/u_{x,0}$ = 9.3%, $u_{x,0}$ = 4.8 m/s.

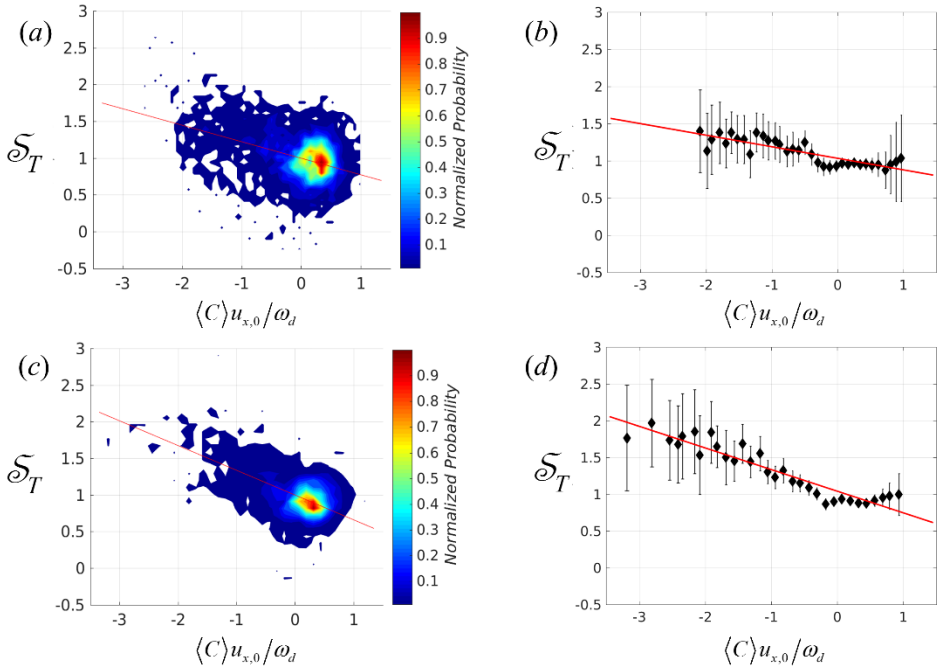

Figure G.10. Normalized ensemble-averaged turbulent displacement flame speed versus curvature shown with (*a, c*) PDF plots and (*b, d*) deweighted plots, at f_0 = 750 Hz at (*a, b*) $u'/u_{x,0}$ = 15.7%, $u_{x,0}$ = 4.7 m/s; (*c, d*) $u'/u_{x,0}$ = 14.6%, $u_{x,0}$ = 4.6 m/s.

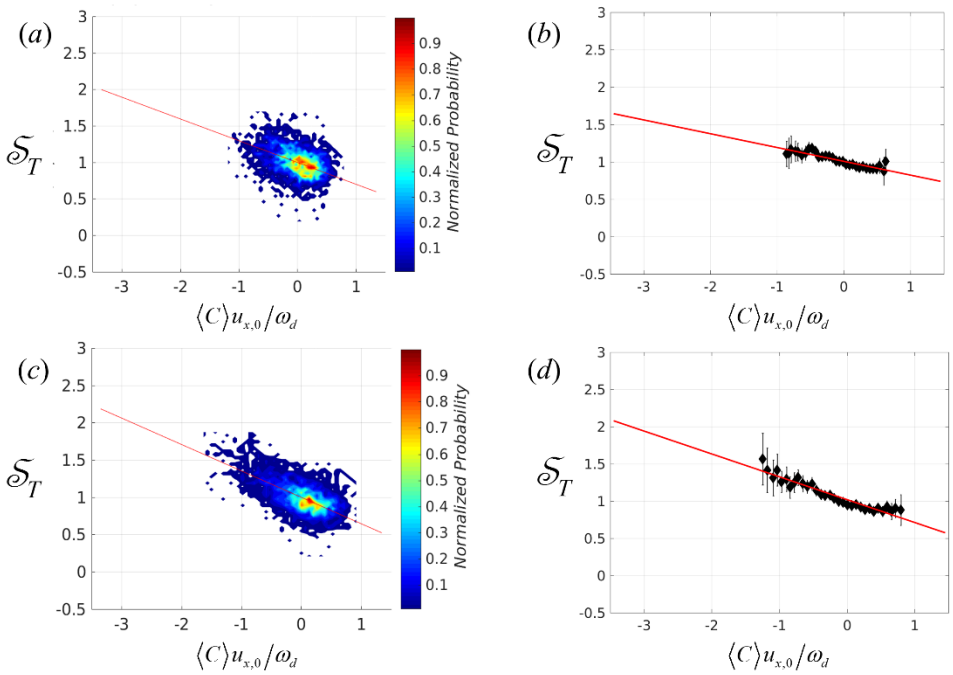

Figure G.11. Normalized ensemble-averaged turbulent displacement flame speed versus curvature shown with (*a, c*) PDF plots and (*b, d*) deweighted plots, at f_0 = 750 Hz at (*a, b*) $u'/u_{x,0}$ = 29.5%, $u_{x,0}$ = 4.1 m/s; (*c, d*) $u'/u_{x,0}$ = 24.4%, $u_{x,0}$ = 4.3 m/s.

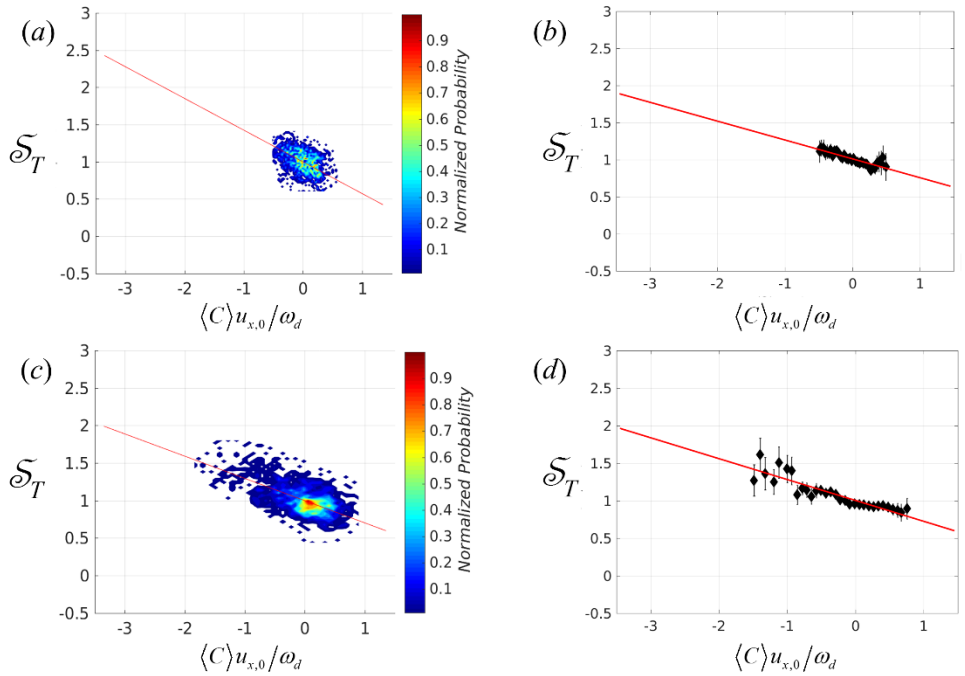

Figure G.12. Normalized ensemble-averaged turbulent displacement flame speed versus curvature shown with (*a, c*) PDF plots and (*b, d*) deweighted plots, at f_0 = 750 Hz at (*a, b*) $u'/u_{x,0}$ = 33.1%, $u_{x,0}$ = 3.8 m/s; (*c, d*) $u'/u_{x,0}$ = 26.4%, $u_{x,0}$ = 4.4 m/s.

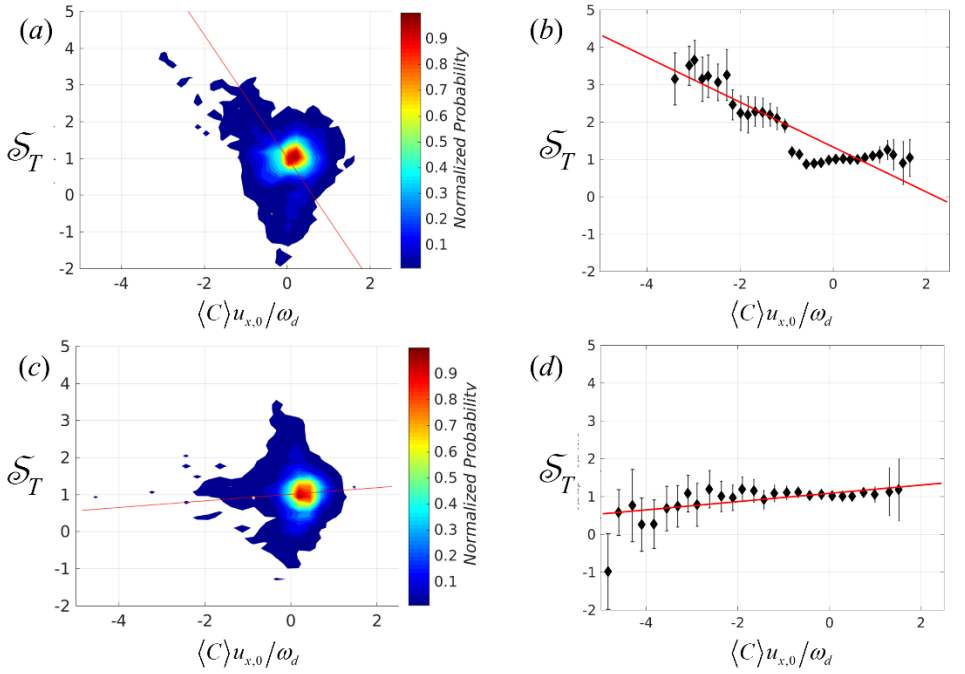

Figure G.13. Normalized ensemble-averaged turbulent displacement flame speed versus curvature shown with (*a, c*) PDF plots and (*b, d*) deweighted plots, at f_0 = 750 Hz at (*a, b*) $u'/u_{x,0}$ = 9.8%, $u_{x,0}$ = 7.94 m/s; (*c, d*) $u'/u_{x,0}$ = 8.0%, $u_{x,0}$ = 7.8 m/s.

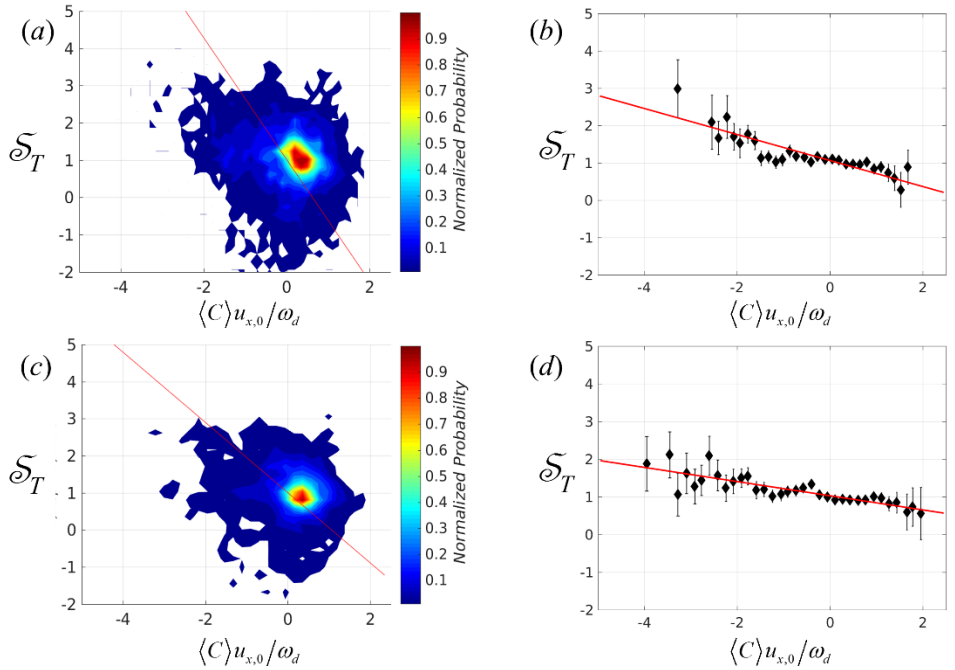

Figure G.14. Normalized ensemble-averaged turbulent displacement flame speed versus curvature shown with (*a, c*) PDF plots and (*b, d*) deweighted plots, at f_0 = 750 Hz at (*a, b*) $u'/u_{x,0}$ = 14.7%, $u_{x,0}$ = 7.8 m/s; (*c, d*) $u'/u_{x,0}$ = 14.2%, $u_{x,0}$ = 7.7 m/s.

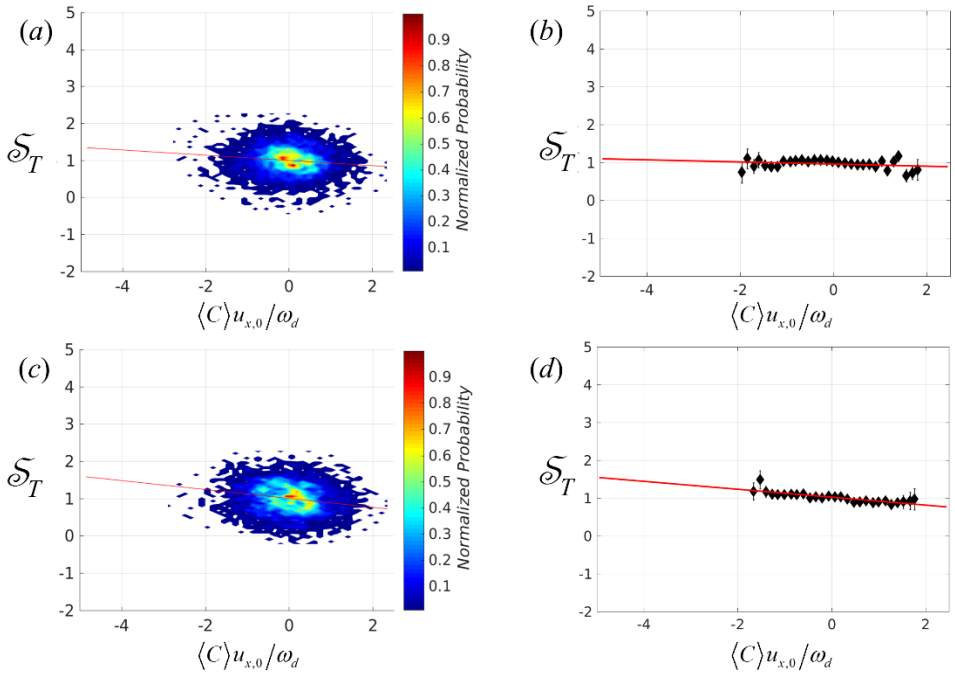

Figure G.15. Normalized ensemble-averaged turbulent displacement flame speed versus curvature shown with (*a, c*) PDF plots and (*b, d*) deweighted plots, at f_0 = 750 Hz at (*a, b*) $u'/u_{x,0}$ = 27.3%, $u_{x,0}$ = 7.0 m/s; (*c, d*) $u'/u_{x,0}$ = 24.7%, $u_{x,0}$ = 7.2 m/s.

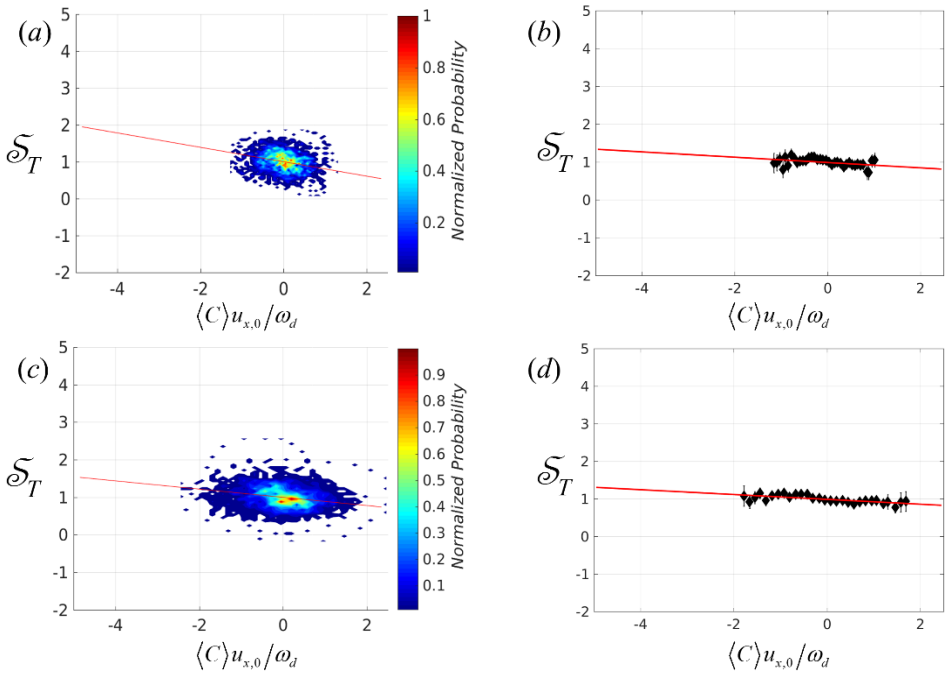

Figure G.16. Normalized ensemble-averaged turbulent displacement flame speed versus curvature shown with (*a, c*) PDF plots and (*b, d*) deweighted plots, at f_0 = 750 Hz at (*a, b*) $u'/u_{x,0}$ = 37.3%, $u_{x,0}$ = 6.0 m/s; (*c, d*) $u'/u_{x,0}$ = 27.4%, $u_{x,0}$ = 7.0 m/s.

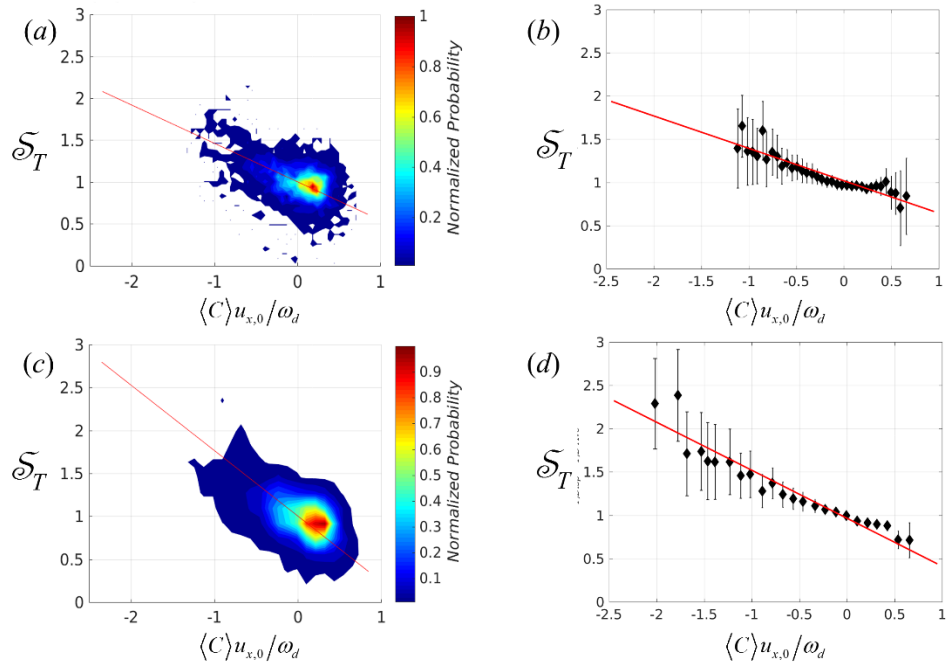

Figure G.17. Normalized ensemble-averaged turbulent displacement flame speed versus curvature shown with (*a, c*) PDF plots and (*b, d*) deweighted plots, at f_0 = 1250 Hz at (*a, b*) $u'/u_{x,0}$ = 13.9%, $u_{x,0}$ = 4.7 m/s; (*c, d*) $u'/u_{x,0}$ = 11.4%, $u_{x,0}$ = 4.5 m/s.

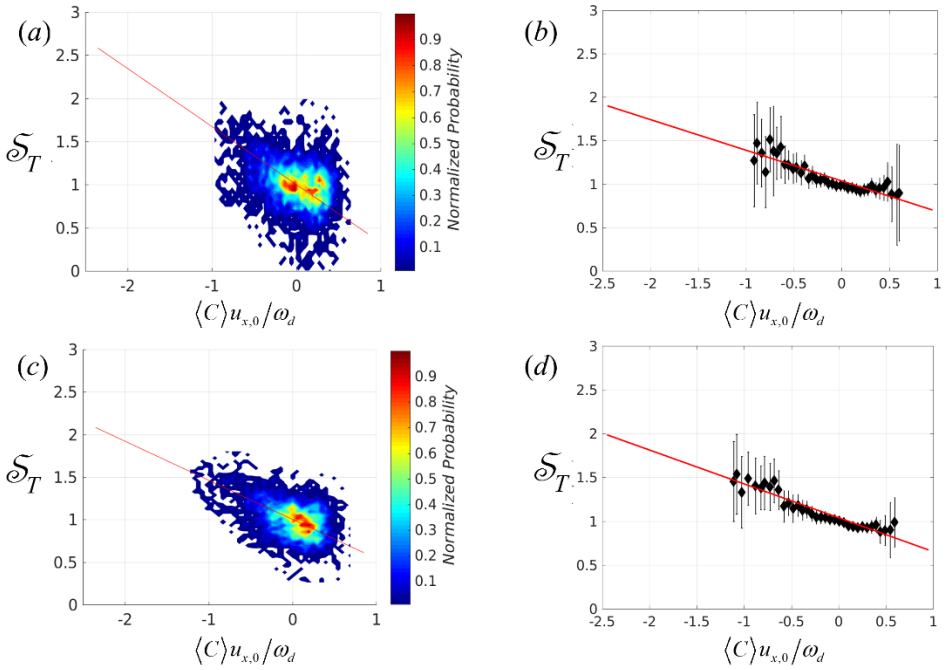

Figure G.18. Normalized ensemble-averaged turbulent displacement flame speed versus curvature shown with (*a, c*) PDF plots and (*b, d*) deweighted plots, at f_0 = 1250 Hz at (*a, b*) $u'/u_{x,0}$ = 14.5%, $u_{x,0}$ = 4.6 m/s; (*c, d*) $u'/u_{x,0}$ = 13.0%, $u_{x,0}$ = 4.6 m/s.

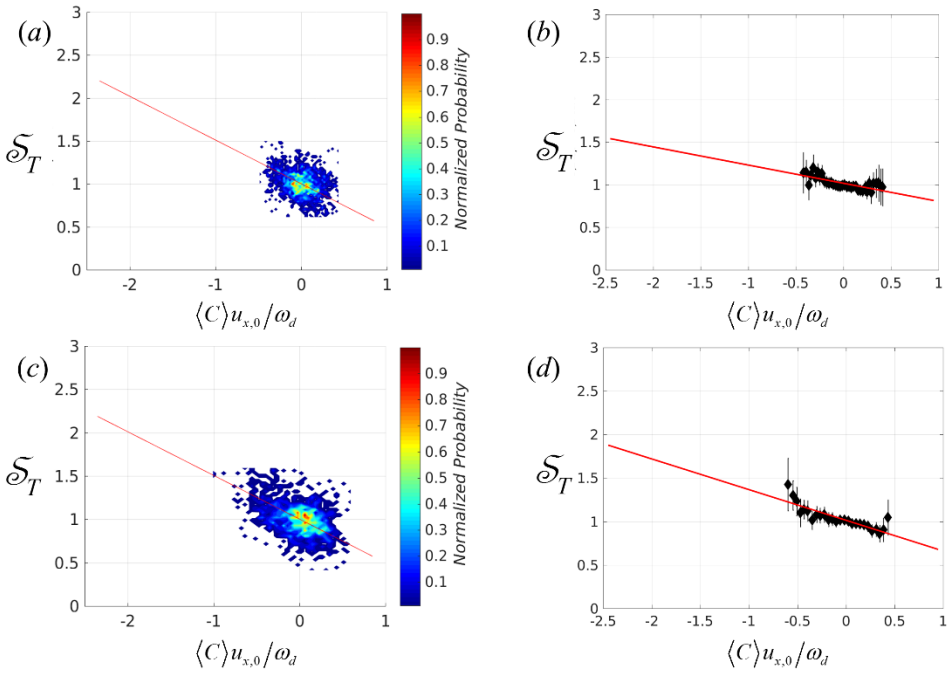

Figure G.19. Normalized ensemble-averaged turbulent displacement flame speed versus curvature shown with (*a, c*) PDF plots and (*b, d*) deweighted plots, at f_0 = 1250 Hz at (*a, b*) $u'/u_{x,0}$ = 28.4%, $u_{x,0}$ = 4.1 m/s; (*c, d*) $u'/u_{x,0}$ = 24.5%, $u_{x,0}$ = 4.3 m/s.

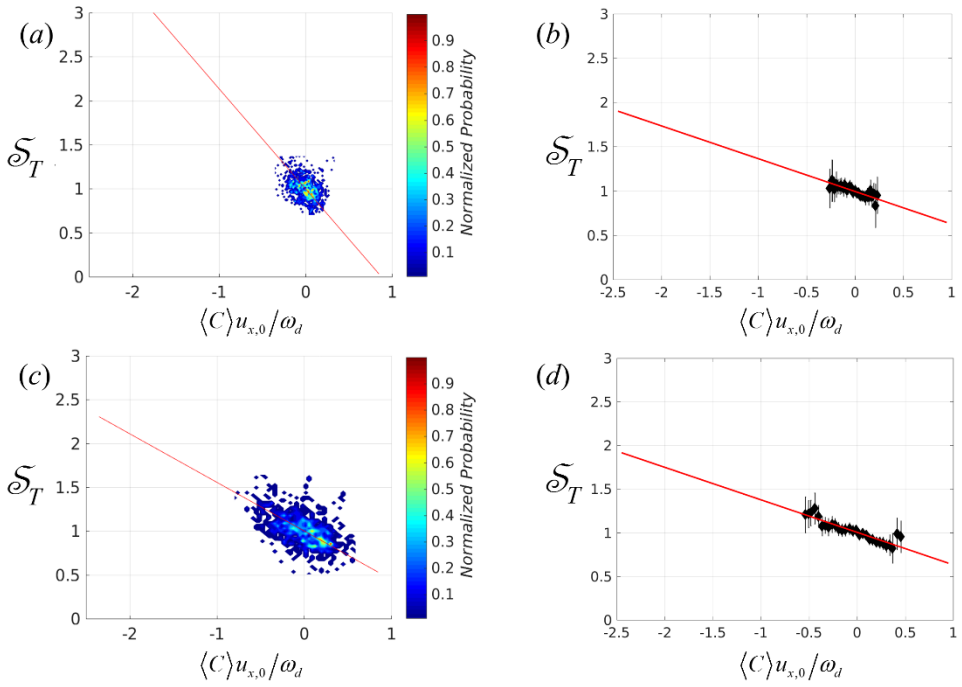

Figure G.20. Normalized ensemble-averaged turbulent displacement flame speed versus curvature shown with (*a, c*) PDF plots and (*b, d*) deweighted plots, at f_0 = 1250 Hz at (*a, b*) $u'/u_{x,0}$ = 33.5%, $u_{x,0}$ = 3.7 m/s; (*c, d*) $u'/u_{x,0}$ = 22.0%, $u_{x,0}$ = 4.4 m/s.

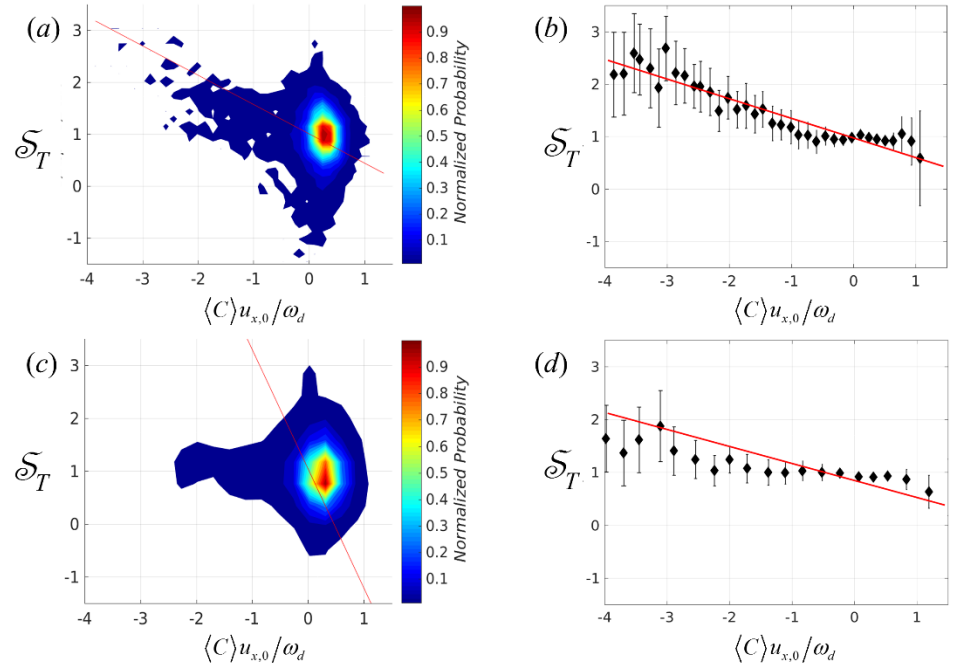

Figure G.21. Normalized ensemble-averaged turbulent displacement flame speed versus curvature shown with (*a, c*) PDF plots and (*b, d*) deweighted plots, at f_0 = 1250 Hz at (*a, b*) $u'/u_{x,0}$ = 7.6%, $u_{x,0}$ = 8.0 m/s; (*c, d*) $u'/u_{x,0}$ = 10.4%, $u_{x,0}$ = 8.0 m/s.

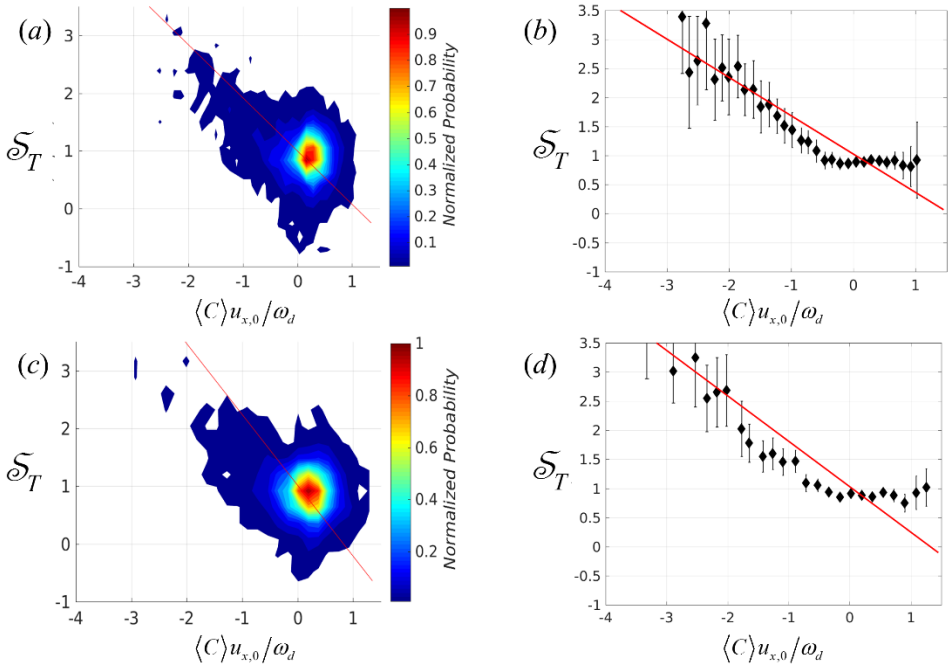

Figure G.22. Normalized ensemble-averaged turbulent displacement flame speed versus curvature shown with (*a, c*) PDF plots and (*b, d*) deweighted plots, at f_0 = 1250 Hz at (*a, b*) $u'/u_{x,0}$ = 14.8%, $u_{x,0}$ = 7.8 m/s; (*c, d*) $u'/u_{x,0}$ = 13.2%, $u_{x,0}$ = 7.7 m/s.

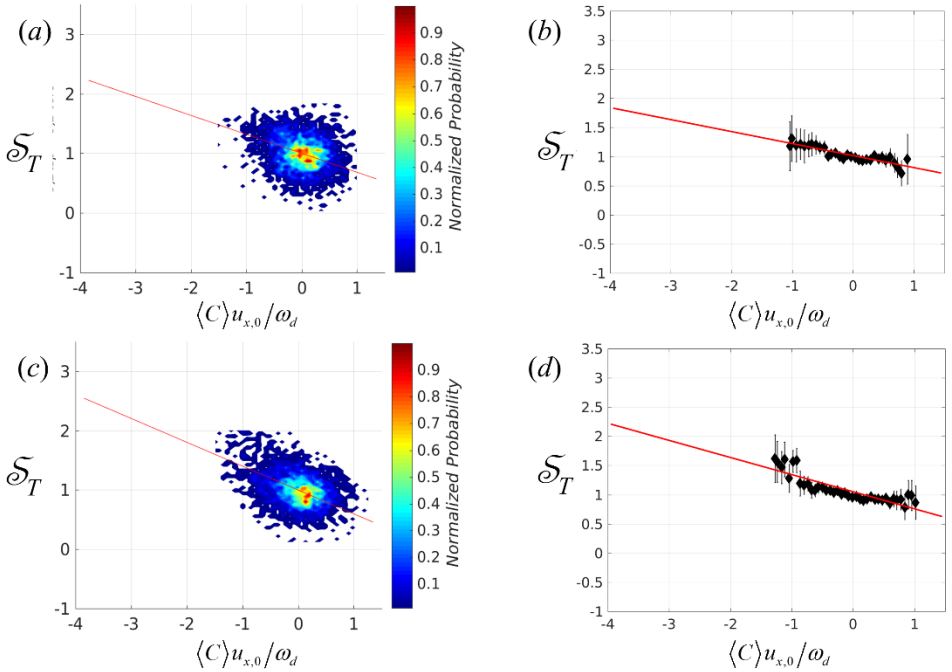

Figure G.23. Normalized ensemble-averaged turbulent displacement flame speed versus curvature shown with (*a, c*) PDF plots and (*b, d*) deweighted plots, at f_0 = 1250 Hz at (*a, b*) $u'/u_{x,0}$ = 25.8%, $u_{x,0}$ = 7.1 m/s; (*c, d*) $u'/u_{x,0}$ = 22.0%, $u_{x,0}$ = 7.3 m/s.

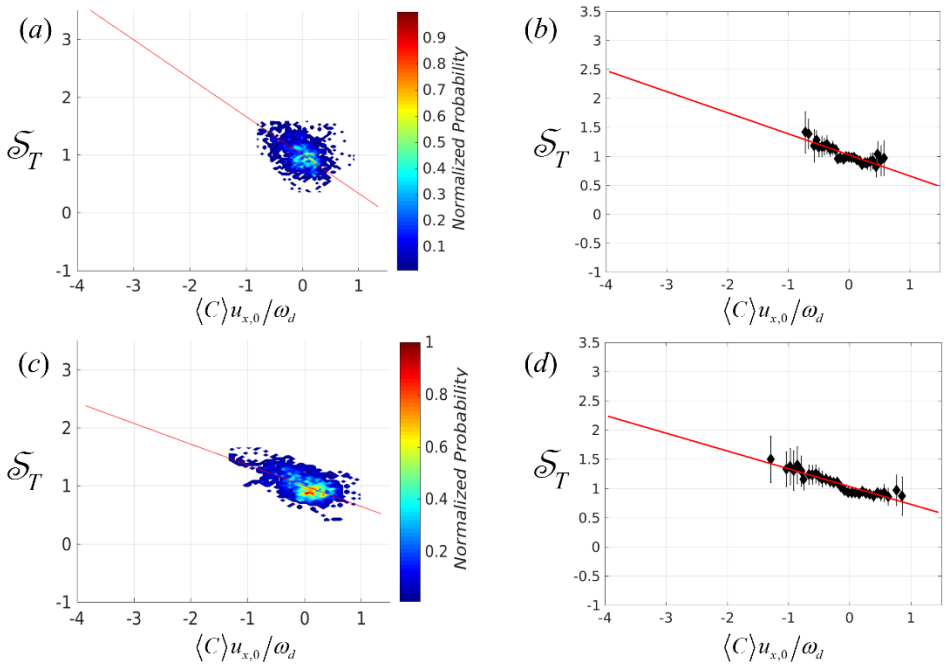

Figure G.24. Normalized ensemble-averaged turbulent displacement flame speed versus curvature shown with (*a, c*) PDF plots and (*b, d*) deweighted plots, at f_0 = 1250 Hz at (*a, b*) $u'/u_{x,0}$ = 32.1%, $u_{x,0}$ = 6.2 m/s; (*c, d*) $u'/u_{x,0}$ = 24.3%, $u_{x,0}$ = 7.2 m/s.

APPENDIX H. AVERAGE CONSUMPTION SPEEDS

This appendix provides plots of the mean ensemble-averaged turbulent consumption speed as a function of the flame coordinate for all cases. Turbulence level generally increases in order of stars, circles, diamonds, to squares. Data from the left side of the flame are shown in subplots (*a*) and (*c*), while data from the right side of the flame are shown in subplots (*b*) and (*d*).

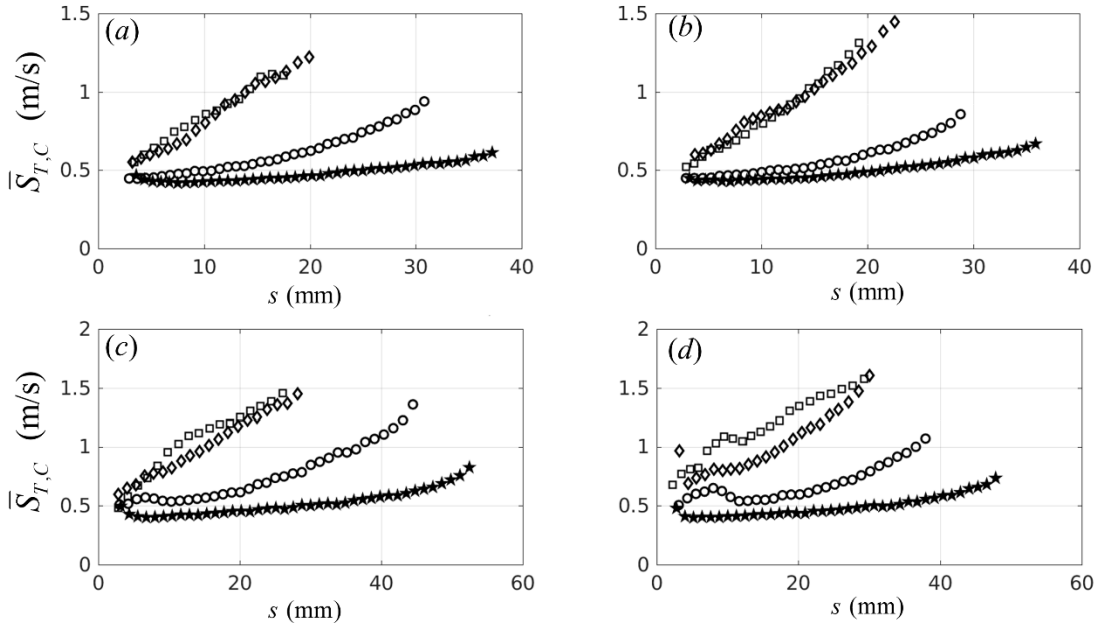

Figure H.1. Average ensemble-averaged turbulent consumption speed at f_0 = 200 Hz (*a, stars*) $u'/u_{x,0}$ = 8.4%, $u_{x,0}$ = 4.8 m/s; (*a, circles*) $u'/u_{x,0}$ = 16.2%, $u_{x,0}$ = 4.7 m/s; (*a, diamonds*) $u'/u_{x,0}$ = 29.6%, $u_{x,0}$ = 4.0 m/s; (*a, squares*) $u'/u_{x,0}$ = 32.9%, $u_{x,0}$ = 3.8 m/s; (*b, stars*) $u'/u_{x,0}$ = 8.6%, $u_{x,0}$ = 4.75 m/s; (*b, circles*) $u'/u_{x,0}$ = 16.6%, $u_{x,0}$ = 4.62 m/s; (*b, diamonds*) $u'/u_{x,0}$ = 26.3%, $u_{x,0}$ = 4.3 m/s; (*b, squares*) $u'/u_{x,0}$ =27.5%, $u_{x,0}$ = 4.35 m/s; (*c, stars*) $u'/u_{x,0}$ = 8.8%, $u_{x,0}$ = 8.14 m/s; (*c, circles*) $u'/u_{x,0}$ = 14.5%, $u_{x,0}$ = 7.8 m/s; (*c, diamonds*) $u'/u_{x,0}$ = 29.2%, $u_{x,0}$ = 6.8 m/s; (*c, squares*) $u'/u_{x,0}$ = 35.9%, $u_{x,0}$ = 6.1 m/s; (*d, stars*) $u'/u_{x,0}$ = 8.4%, $u_{x,0}$ = 8.1 m/s; (*d, circles*) $u'/u_{x,0}$ = 13.1%, $u_{x,0}$ = 7.8 m/s; (*d, diamonds*) $u'/u_{x,0}$ = 25.5%, $u_{x,0}$ = 7.2 m/s; (*d, squares*) $u'/u_{x,0}$ = 26.7%, $u_{x,0}$ = 7.1 m/s.

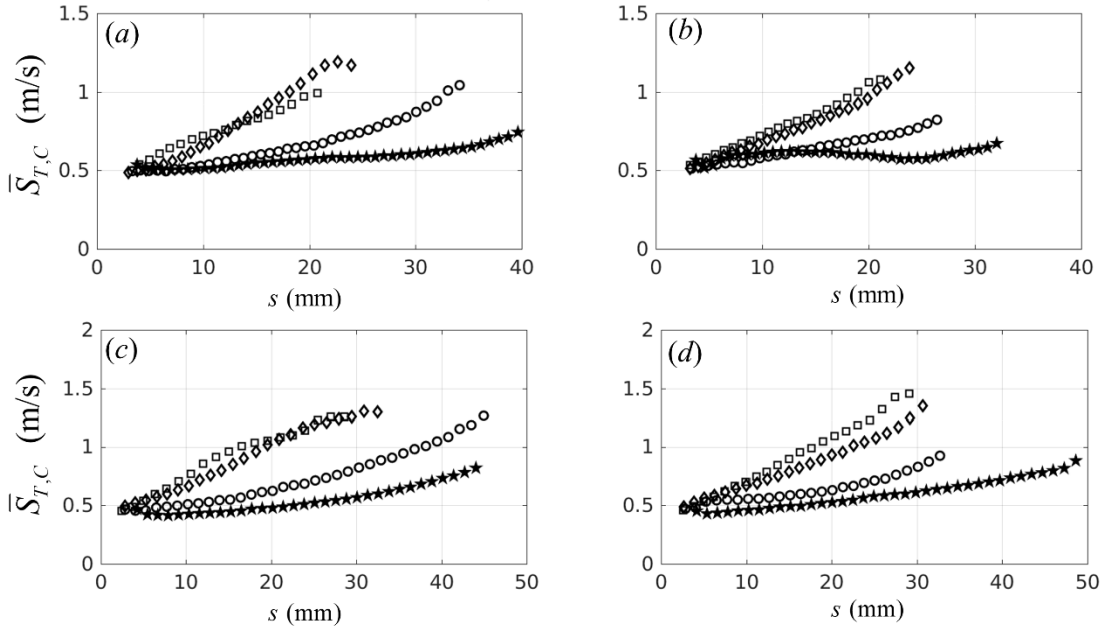

Figure H.2. Average ensemble-averaged turbulent consumption speed at f_0 = 750 Hz (*a, stars*) $u'/u_{x,0}$ = 8.9%, $u_{x,0}$ = 4.9 m/s; (*a, circles*) $u'/u_{x,0}$ = 15.7%, $u_{x,0}$ = 4.7 m/s; (*a, diamonds*) $u'/u_{x,0}$ =29.5%, $u_{x,0}$ =4.1 m/s; (*a, squares*) $u'/u_{x,0}$ =33.1%, $u_{x,0}$ = 3.8 m/s; (*b, stars*) $u'/u_{x,0}$ = 9.3%, $u_{x,0}$ = 4.8 m/s; (*b, circles*) $u'/u_{x,0}$ = 14.6%, $u_{x,0}$ = 4.6 m/s; (*b, diamonds*) $u'/u_{x,0}$ = 24.4%, $u_{x,0}$ = 4.3 m/s;(*b, squares*) $u'/u_{x,0}$ = 26.4%, $u_{x,0}$ = 4.4 m/s; (*c, stars*) $u'/u_{x,0}$ = 9.8%, $u_{x,0}$ = 8.0 m/s; (*c, circles*) $u'/u_{x,0}$ = 14.7%, $u_{x,0}$ = 7.8 m/s; (*c, diamonds*) $u'/u_{x,0}$ = 27.3%, $u_{x,0}$ = 7.0 m/s; (*c, squares*) $u'/u_{x,0}$ = 37.3%, $u_{x,0}$ = 6.0 m/s; (*d, stars*) $u'/u_{x,0}$ = 8.0%, $u_{x,0}$ = 7.8 m/s; (*d, circles*) $u'/u_{x,0}$ = 14.2%, $u_{x,0}$ = 7.7 m/s; (*d, diamonds*) $u'/u_{x,0}$ = 24.7%, $u_{x,0}$ = 7.2 m/s; (*d, squares*) $u'/u_{x,0}$ = 27.4%, $u_{x,0}$ = 7.0 m/s.

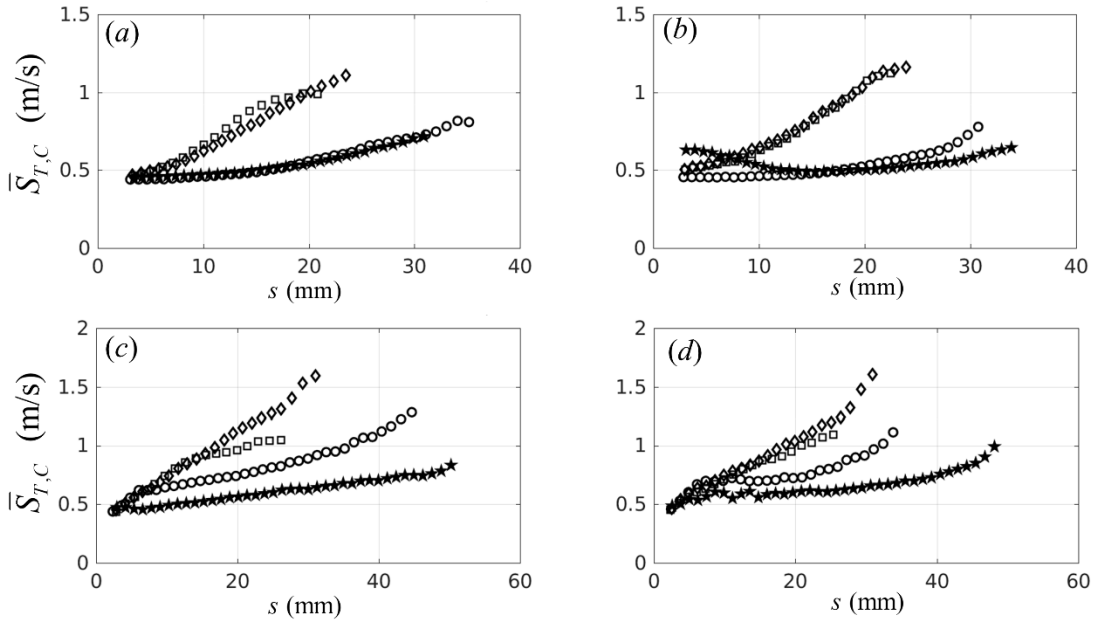

Figure H.3. Average ensemble-averaged turbulent consumption speed at f_0 = 1250 Hz (*a, stars*) $u'/u_{x,0}$ = 13.9%, $u_{x,0}$ = 4.7 m/s; (*a, circles*) $u'/u_{x,0}$ = 14.5%, $u_{x,0}$ = 4.7 m/s; (*a, diamonds*) $u'/u_{x,0}$ = 28.4%, $u_{x,0}$ = 4.1 m/s; (*a, squares*) $u'/u_{x,0}$ = 33.5%, $u_{x,0}$ = 3.7 m/s; (*b, stars*) $u'/u_{x,0}$ = 11.4%, $u_{x,0}$ = 4.5 m/s; (*b, circles*) $u'/u_{x,0}$ = 13.0%, $u_{x,0}$ = 4.6 m/s; (*b, diamonds*) $u'/u_{x,0}$ = 24.5%, $u_{x,0}$ = 4.3 m/s; (*b, squares*) $u'/u_{x,0}$ = 22.0%, $u_{x,0}$ =4.4 m/s; (*c, stars*) $u'/u_{x,0}$ = 7.6%, $u_{x,0}$ = 8.0 m/s; (*c, circles*) $u'/u_{x,0}$ = 14.8%, $u_{x,0}$ = 7.8 m/s; (*c, diamonds*) $u'/u_{x,0}$ = 25.8%, $u_{x,0}$ = 7.1 m/s; (*c, squares*) $u'/u_{x,0}$ = 32.1%, $u_{x,0}$ = 6.2 m/s; (*d, stars*) $u'/u_{x,0}$ = 10.4%, $u_{x,0}$ = 8.0 m/s; (*d, circles*) $u'/u_{x,0}$ = 13.2%, $u_{x,0}$ = 7.7 m/s; (*d, diamonds*) $u'/u_{x,0}$ = 22.0%, $u_{x,0}$ = 7.3 m/s; (*d, squares*) $u'/u_{x,0}$ = 24.3%, $u_{x,0}$ = 7.2 m/s.

APPENDIX I. ENSEMBLE-AVERAGED CONSUMPTION SPEED CURVATURE CORRELATIONS

This appendix provides a comprehensive set of correlations between the normalized ensemble-averaged turbulent consumption speed, $\tilde{S}_{T,C}$, and the normalized ensemble-averaged flame curvature, $\langle C \rangle u_{x,0}/\omega_d$. The left hand side of the figure shows a normalized joint probability density plots while the right hand side of the figure shows the corresponding deweighted correlation plot. Note that due to the y-axis scale the uncertainty bars are not visible in some of the deweighted plots. Data from the left side of the flame are shown in subplots (*a*) and (*b*), while data from the right side of the flame are shown in subplots (*c*) and (*d*).

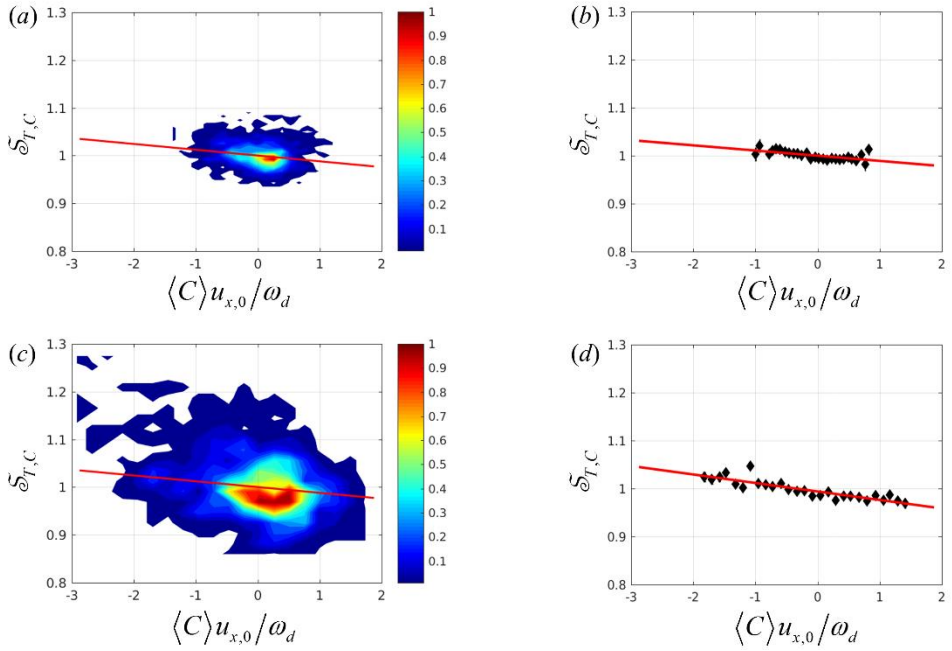

Figure I.1. Normalized ensemble-averaged turbulent consumption flame speed versus curvature shown with (*a, c*) PDF plots and (*b, d*) deweighted plots, at f_0 = 200 Hz at (*a, b*) $u'/u_{x,0}$ = 8.4%, $u_{x,0}$ = 4.8 m/s; (*c, d*) $u'/u_{x,0}$ = 8.6%, $u_{x,0}$ = 4.8 m/s.

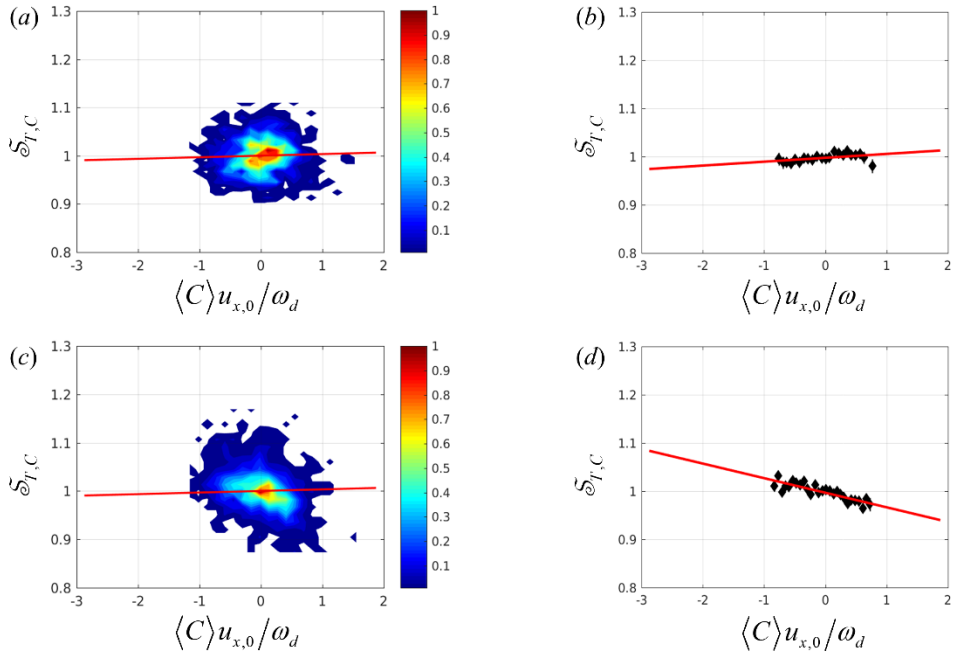

Figure I.2. Normalized ensemble-averaged turbulent consumption flame speed versus curvature shown with (*a, c*) PDF plots and (*b, d*) deweighted plots, at f_0 = 200 Hz at (*a, b*) $u'/u_{x,0}$ = 16.2%, $u_{x,0}$ = 4.7 m/s; (*c, d*) $u'/u_{x,0}$ = 16.6%, $u_{x,0}$ = 4.6 m/s.

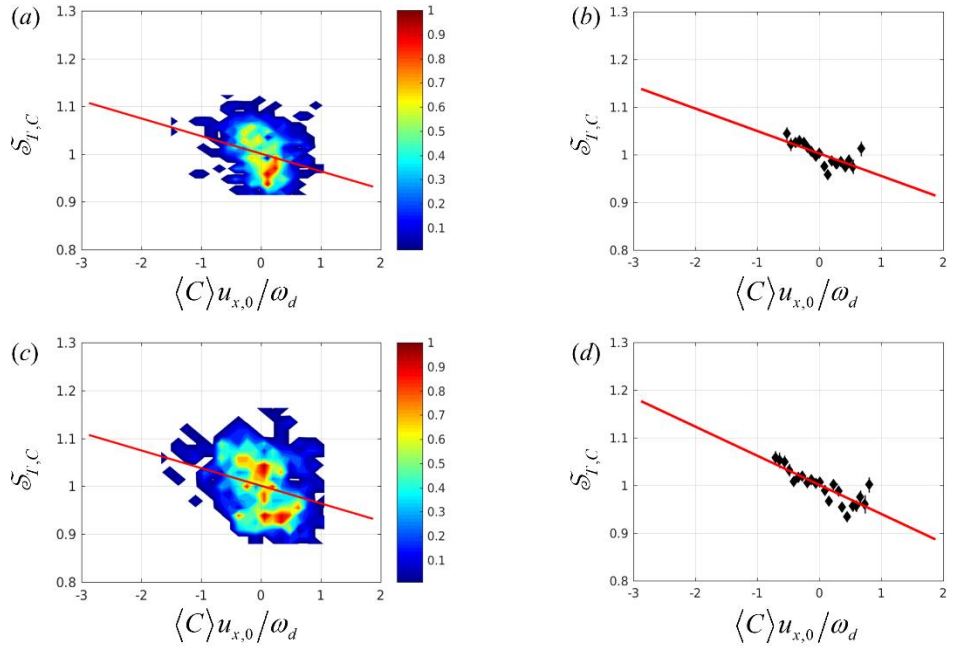

Figure I.3. Normalized ensemble-averaged turbulent consumption flame speed versus curvature shown with (*a, c*) PDF plots and (*b, d*) deweighted plots, at f_0 = 200 Hz at (*a, b*) $u'/u_{x,0}$ = 29.6%, $u_{x,0}$ = 4.0 m/s; (*c, d*) $u'/u_{x,0}$ = 26.3%, $u_{x,0}$ = 4.3 m/s.

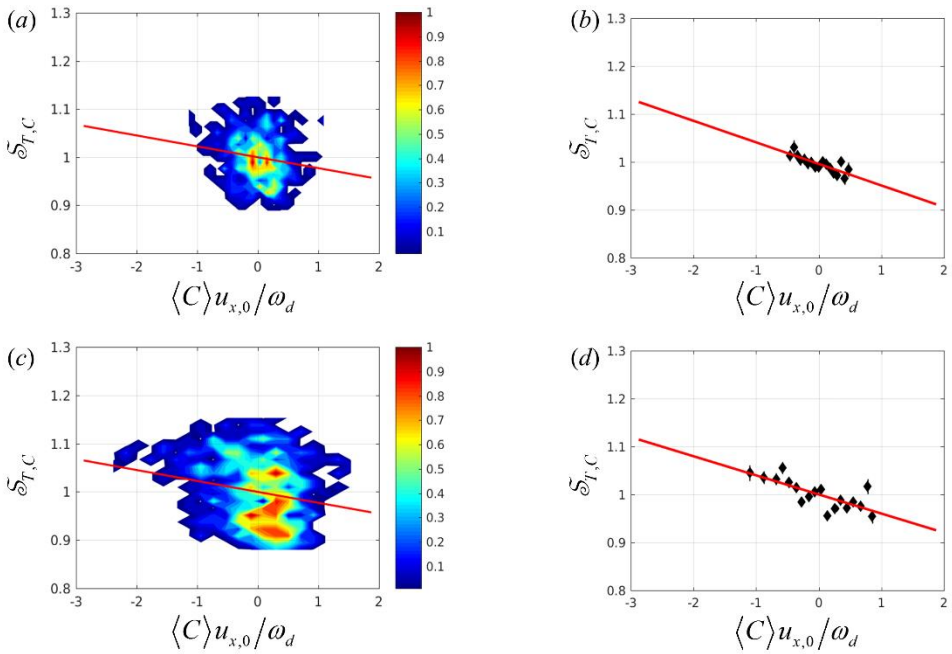

Figure I.4. Normalized ensemble-averaged turbulent consumption flame speed versus curvature shown with (*a, c*) PDF plots and (*b, d*) deweighted plots, at f_0 = 200 Hz at (*a, b*) $u'/u_{x,0}$ = 32.9%, $u_{x,0}$ = 3.8 m/s; (*c, d*) $u'/u_{x,0}$ = 27.4%, $u_{x,0}$ = 4.3 m/s.

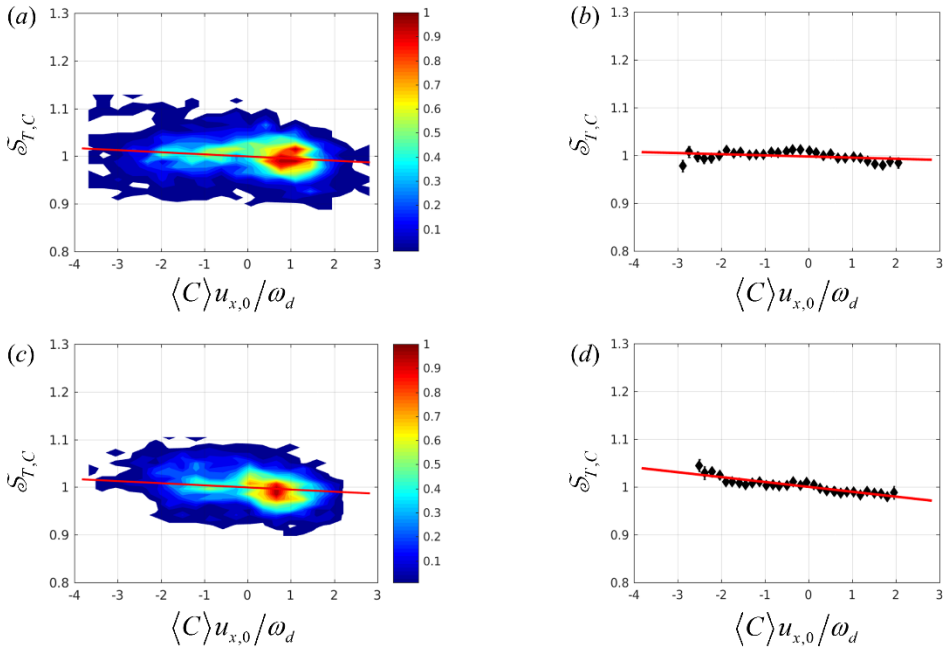

Figure I.5. Normalized ensemble-averaged turbulent consumption flame speed versus curvature shown with (*a, c*) PDF plots and (*b, d*) deweighted plots, at f_0 = 200 Hz at (*a, b*) $u'/u_{x,0}$ = 8.8%, $u_{x,0}$ = 8.14 m/s; (*c, d*) $u'/u_{x,0}$ = 8.4%, $u_{x,0}$ = 8.1 m/s.

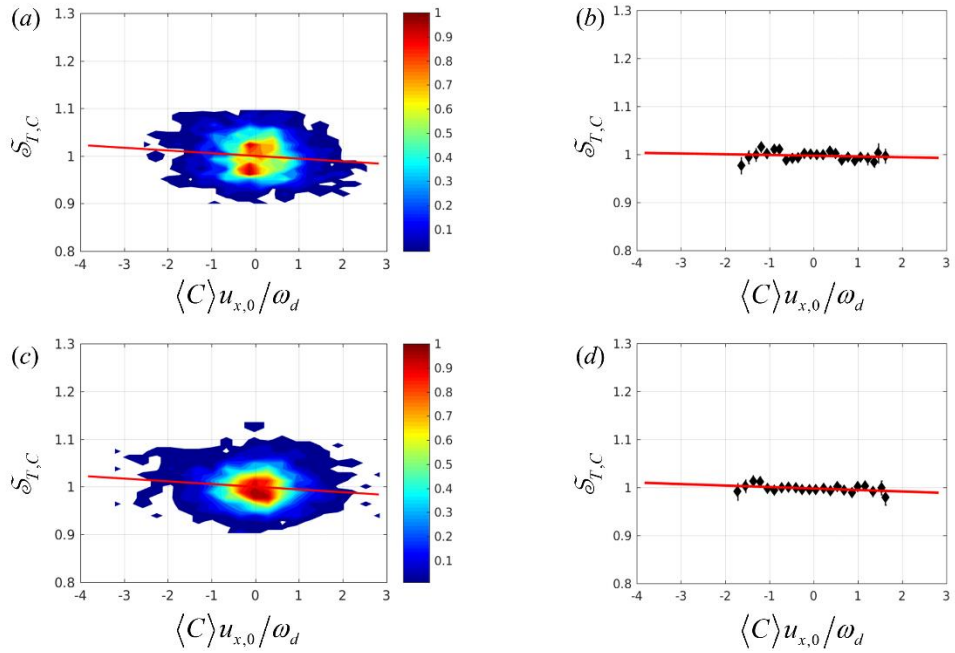

Figure I.6. Normalized ensemble-averaged turbulent consumption flame speed versus curvature shown with (*a, c*) PDF plots and (*b, d*) deweighted plots, at f_0 = 200 Hz at (*a, b*) $u'/u_{x,0}$ = 14.5%, $u_{x,0}$ = 7.8 m/s; (*c, d*) $u'/u_{x,0}$ = 13.1%, $u_{x,0}$ = 7.8 m/s.

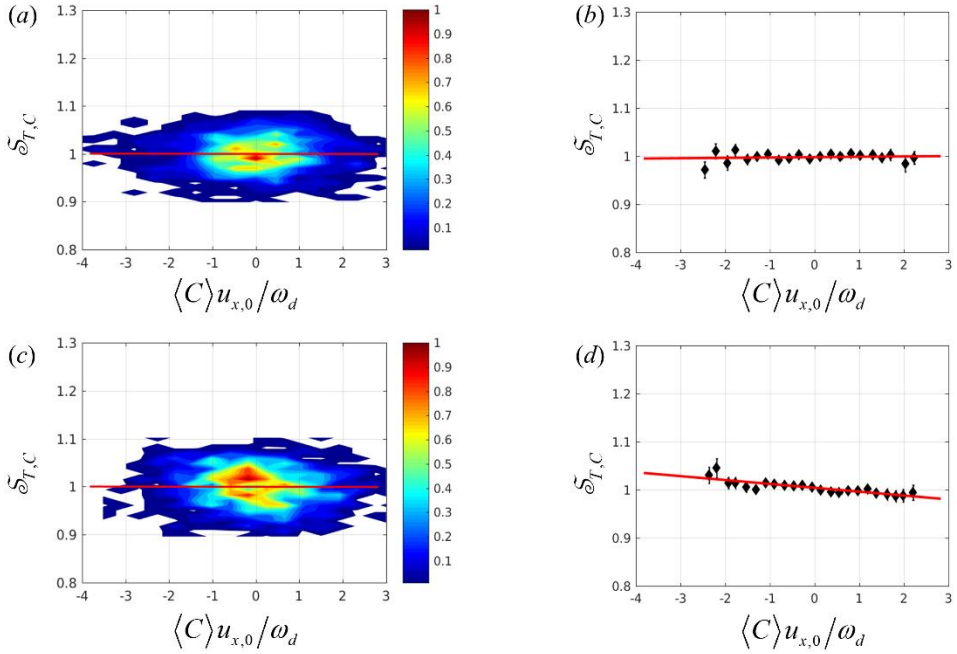

Figure I.7. Normalized ensemble-averaged turbulent consumption flame speed versus curvature shown with (*a, c*) PDF plots and (*b, d*) deweighted plots, at f_0 = 200 Hz at (*a, b*) $u'/u_{x,0}$ = 29.2%, $u_{x,0}$ = 6.8 m/s; (*c, d*) $u'/u_{x,0}$ = 25.5%, $u_{x,0}$ = 7.2 m/s.

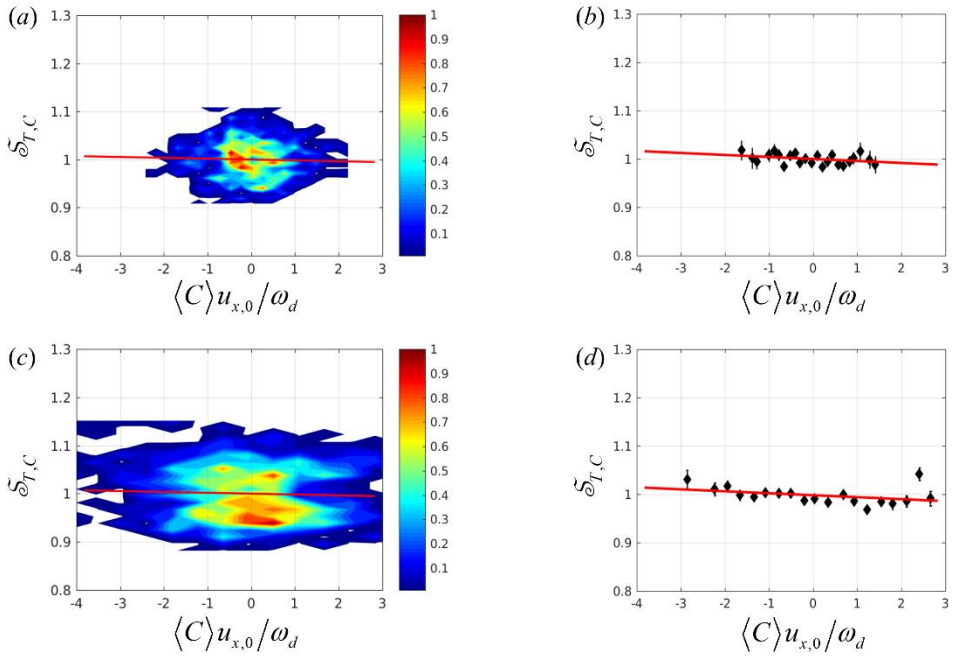

Figure I.8. Normalized ensemble-averaged turbulent consumption flame speed versus curvature shown with (*a, c*) PDF plots and (*b, d*) deweighted plots, at f_0 = 200 Hz at (*a, b*) $u'/u_{x,0}$ = 35.9%, $u_{x,0}$ = 6.1 m/s; (*c, d*) $u'/u_{x,0}$ = 26.7%, $u_{x,0}$ = 7.1 m/s.

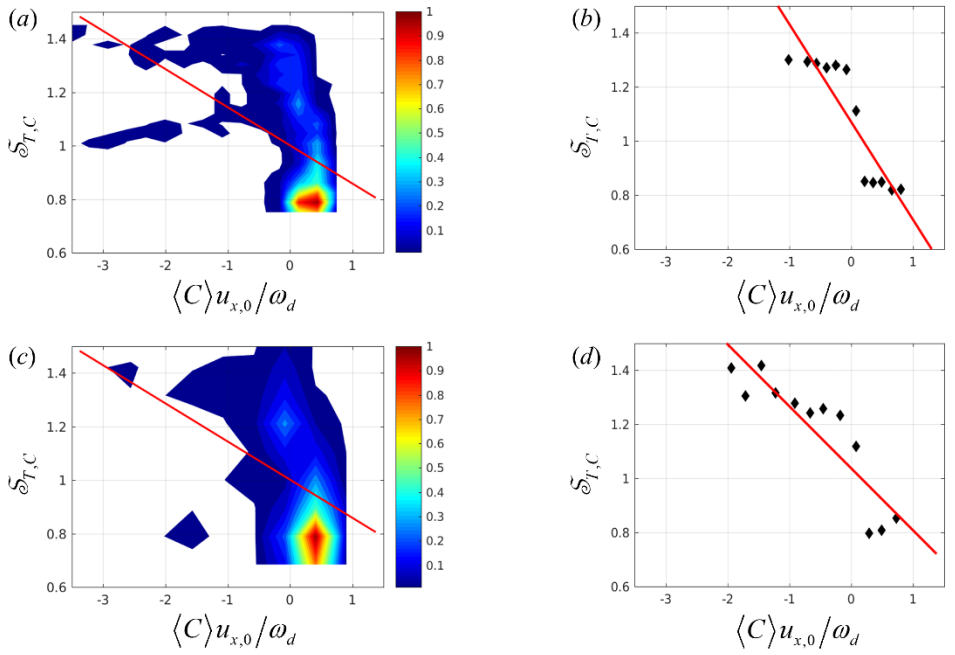

Figure I.9. Normalized ensemble-averaged turbulent consumption flame speed versus curvature shown with (*a, c*) PDF plots and (*b, d*) deweighted plots, at f_0 = 750 Hz at (*a, b*) $u'/u_{x,0}$ = 8.9%, $u_{x,0}$ = 4.9 m/s; (*c, d*) $u'/u_{x,0}$ = 9.3%, $u_{x,0}$ = 4.8 m/s.

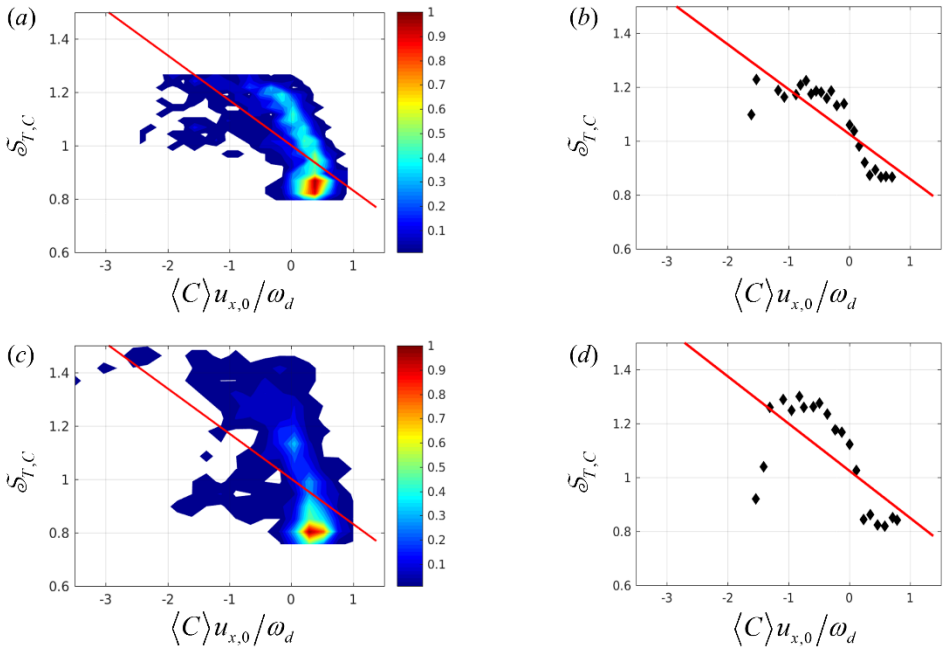

Figure I.10. Normalized ensemble-averaged turbulent consumption flame speed versus curvature shown with (*a, c*) PDF plots and (*b, d*) deweighted plots, at f_0 = 750 Hz at (*a, b*) $u'/u_{x,0}$ = 15.7%, $u_{x,0}$ = 4.7 m/s; (*c, d*) $u'/u_{x,0}$ = 14.6%, $u_{x,0}$ = 4.6 m/s.

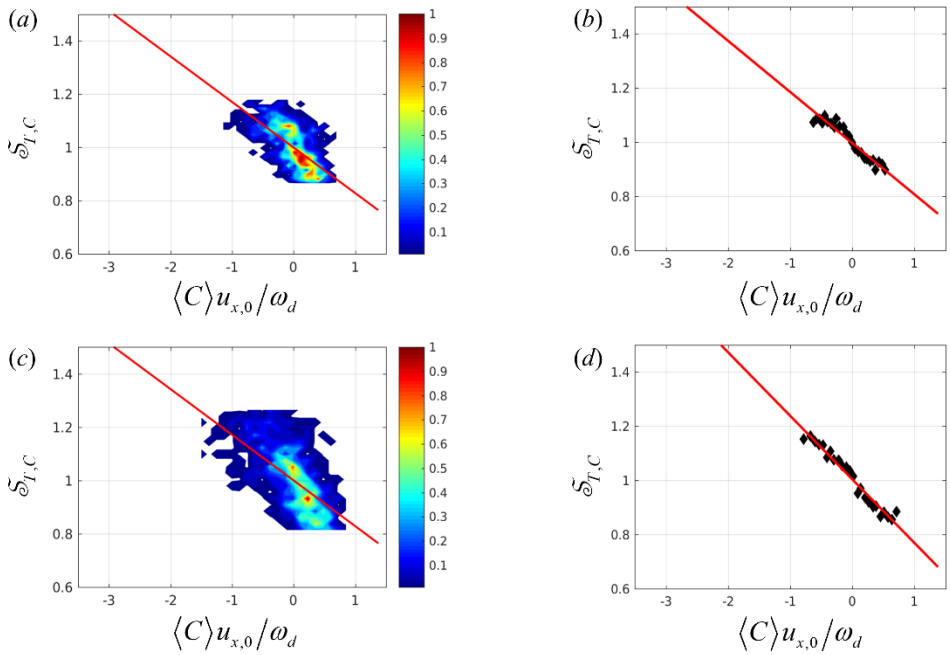

Figure I.11. Normalized ensemble-averaged turbulent consumption flame speed versus curvature shown with (*a, c*) PDF plots and (*b, d*) deweighted plots, at f_0 = 750 Hz at (*a, b*) $u'/u_{x,0}$ = 29.5%, $u_{x,0}$ = 4.1 m/s; (*c, d*) $u'/u_{x,0}$ = 24.4%, $u_{x,0}$ = 4.3 m/s.

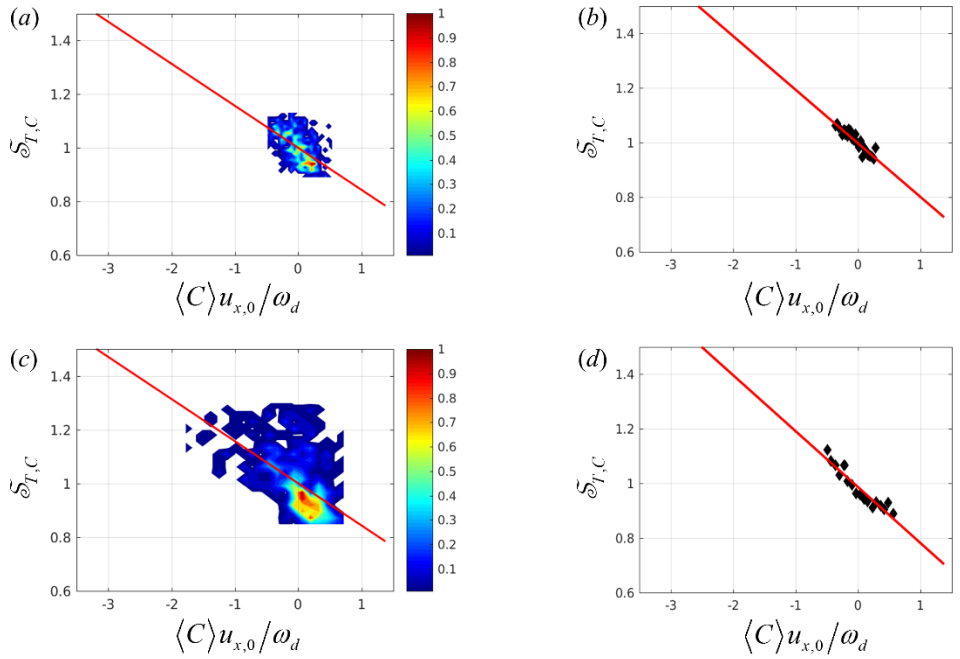

Figure I.12. Normalized ensemble-averaged turbulent consumption flame speed versus curvature shown with (*a, c*) PDF plots and (*b, d*) deweighted plots, at f_0 = 750 Hz at (*a, b*) $u'/u_{x,0}$ = 33.1%, $u_{x,0}$ = 3.8 m/s; (*c, d*) $u'/u_{x,0}$ = 26.4%, $u_{x,0}$ = 4.4 m/s.

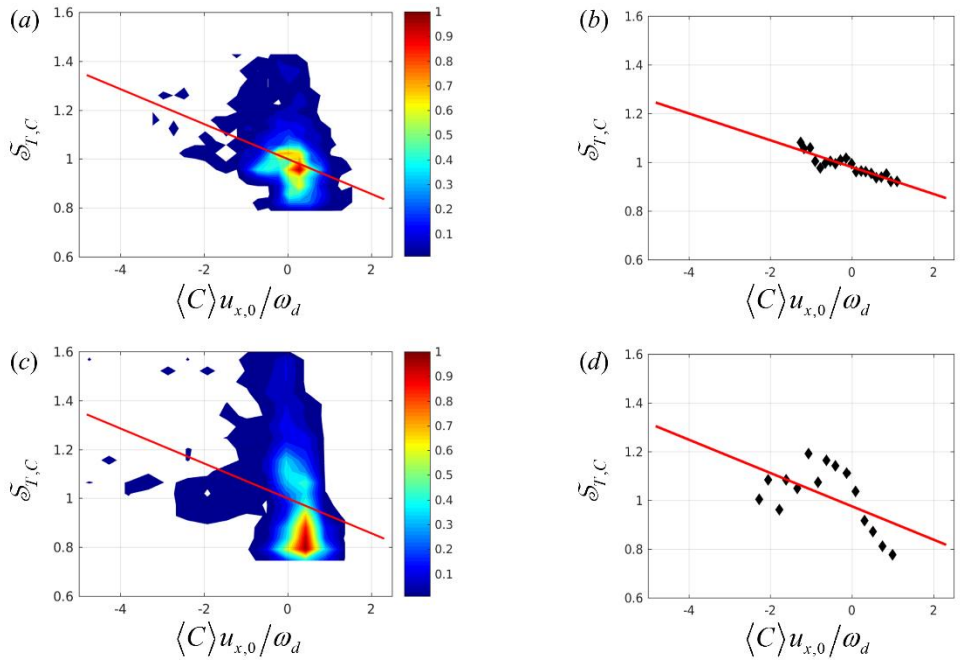

Figure I.13. Normalized ensemble-averaged turbulent consumption flame speed versus curvature shown with (*a, c*) PDF plots and (*b, d*) deweighted plots, at f_0 = 750 Hz at (*a, b*) $u'/u_{x,0}$ = 9.8%, $u_{x,0}$ = 7.94 m/s; (*c, d*) $u'/u_{x,0}$ = 8.0%, $u_{x,0}$ = 7.8 m/s.

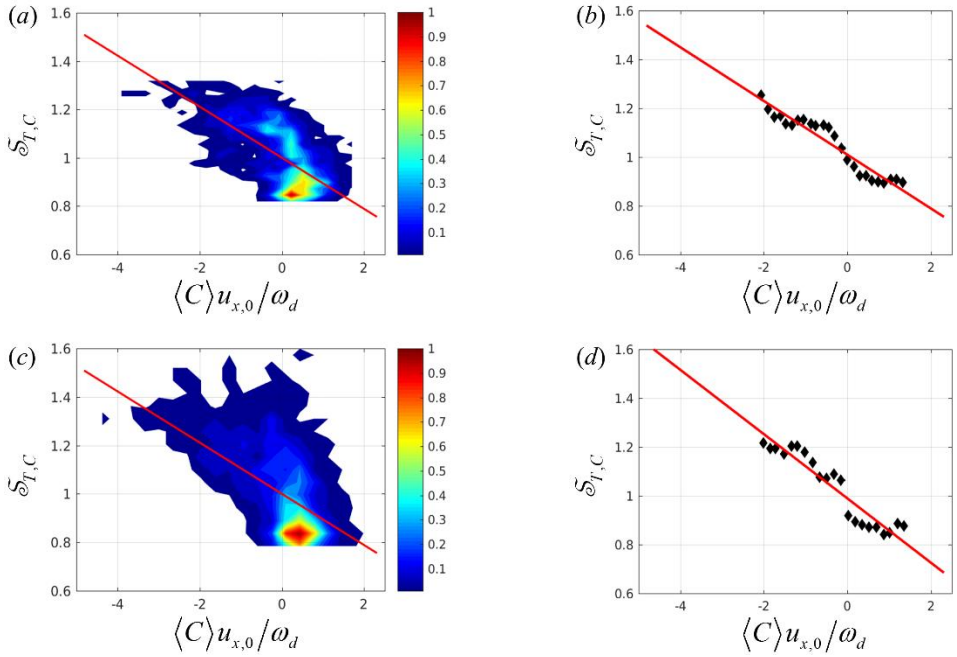

Figure I.14. Normalized ensemble-averaged turbulent consumption flame speed versus curvature shown with (*a, c*) PDF plots and (*b, d*) deweighted plots, at f_0 = 750 Hz at (*a, b*) $u'/u_{x,0}$ = 14.7%, $u_{x,0}$ = 7.8 m/s; (*c, d*) $u'/u_{x,0}$ = 14.2%, $u_{x,0}$ = 7.7 m/s.

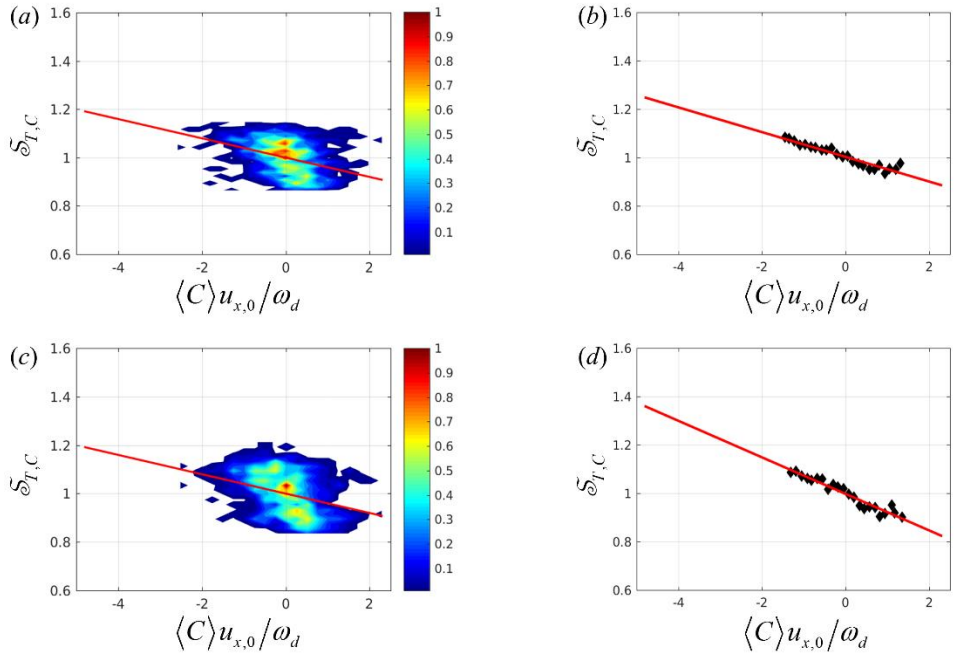

Figure I.15. Normalized ensemble-averaged turbulent consumption flame speed versus curvature shown with (*a, c*) PDF plots and (*b, d*) deweighted plots, at f_0 = 750 Hz at (*a, b*) $u'/u_{x,0}$ = 27.3%, $u_{x,0}$ = 7.0 m/s; (*c, d*) $u'/u_{x,0}$ = 24.7%, $u_{x,0}$ = 7.2 m/s.

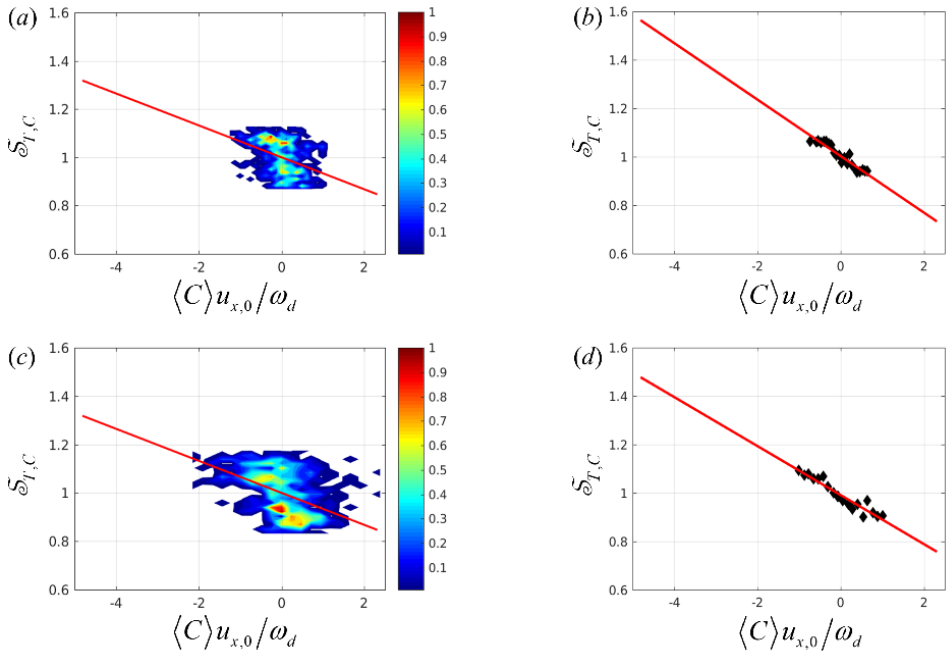

Figure I.16. Normalized ensemble-averaged turbulent consumption flame speed versus curvature shown with (*a, c*) PDF plots and (*b, d*) deweighted plots, at f_0 = 750 Hz at (*a, b*) $u'/u_{x,0}$ = 37.3%, $u_{x,0}$ = 6.0 m/s; (*c, d*) $u'/u_{x,0}$ = 27.4%, $u_{x,0}$ = 7.0 m/s.

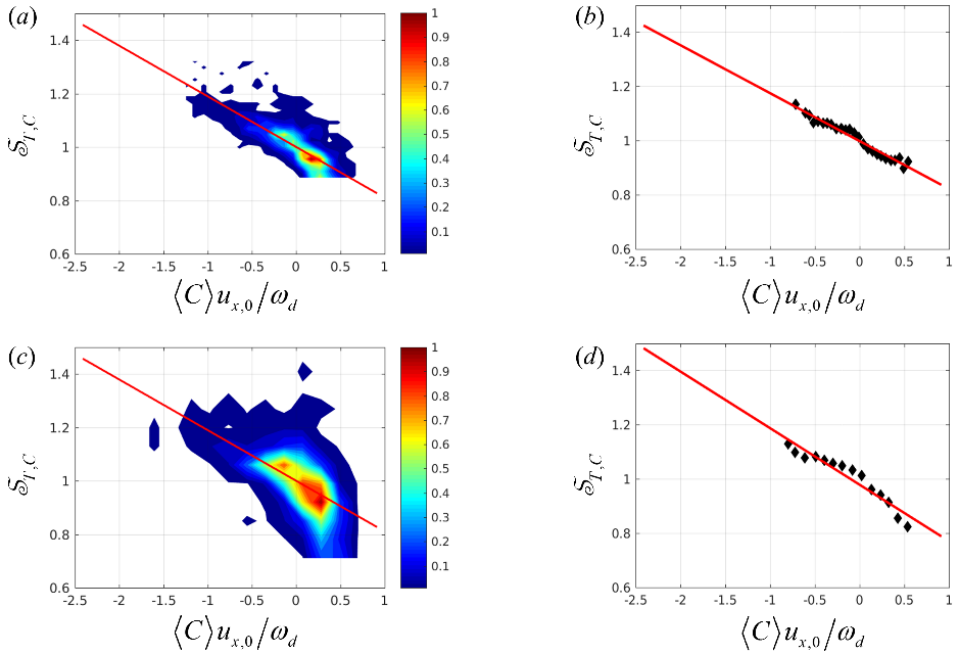

Figure I.17. Normalized ensemble-averaged turbulent consumption flame speed versus curvature shown with (*a, c*) PDF plots and (*b, d*) deweighted plots, at f_0 = 1250 Hz at (*a, b*) $u'/u_{x,0}$ = 13.9%, $u_{x,0}$ = 4.7 m/s; (*c, d*) $u'/u_{x,0}$ = 11.4%, $u_{x,0}$ = 4.5 m/s.

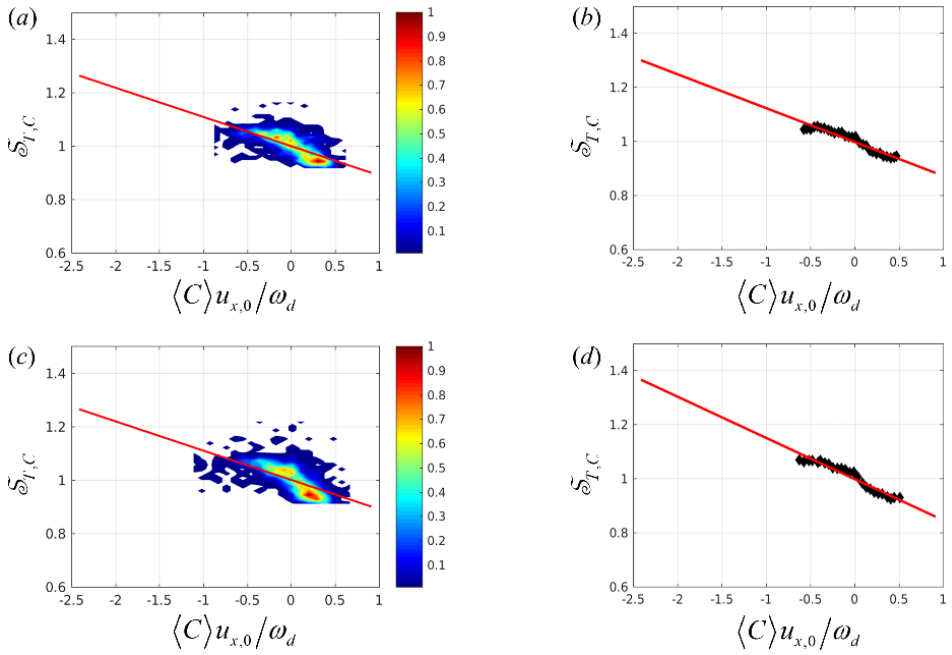

Figure I.18. Normalized ensemble-averaged turbulent consumption flame speed versus curvature shown with (*a, c*) PDF plots and (*b, d*) deweighted plots, at f_0 = 1250 Hz at (*a, b*) $u'/u_{x,0}$ = 14.5%, $u_{x,0}$ = 4.6 m/s; (*c, d*) $u'/u_{x,0}$ = 13.0%, $u_{x,0}$ = 4.6 m/s.

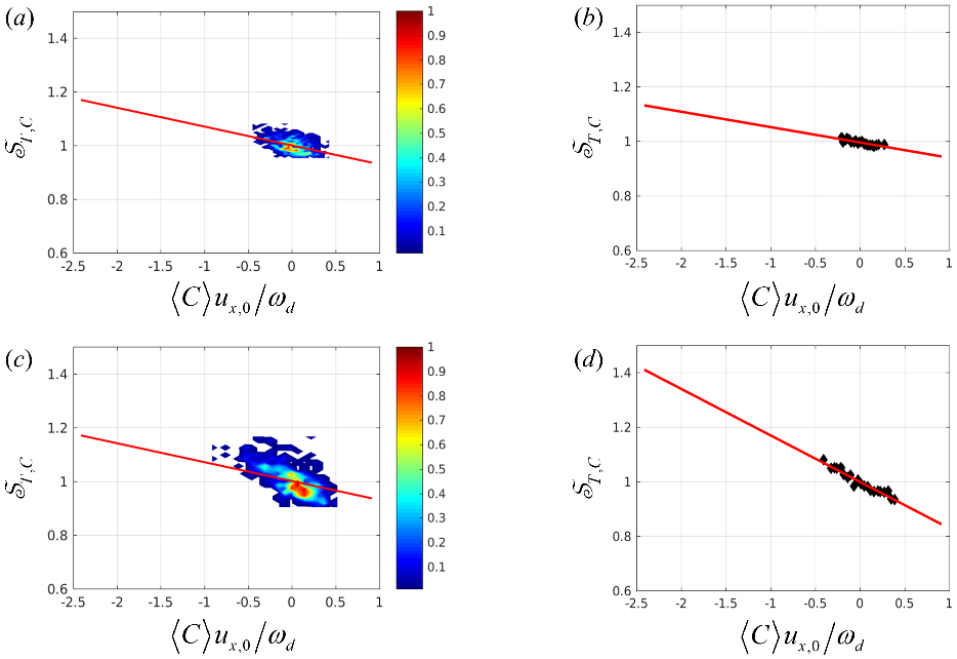

Figure I.19. Normalized ensemble-averaged turbulent consumption flame speed versus curvature shown with (*a, c*) PDF plots and (*b, d*) deweighted plots, at f_0 = 1250 Hz at (*a, b*) $u'/u_{x,0}$ = 28.4%, $u_{x,0}$ = 4.1 m/s; (*c, d*) $u'/u_{x,0}$ = 24.5%, $u_{x,0}$ = 4.3 m/s.

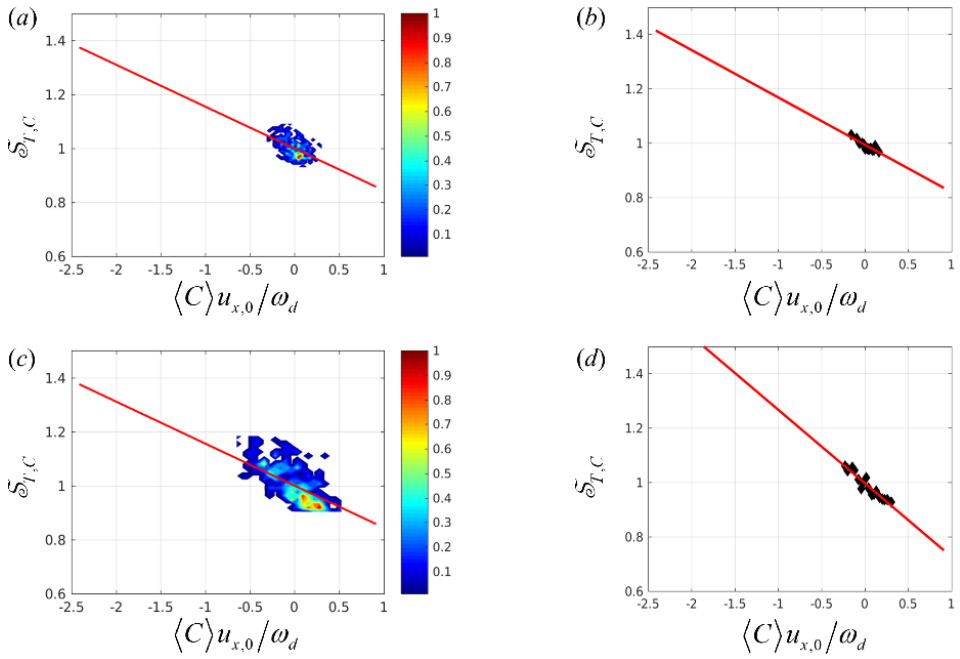

Figure I.20. Normalized ensemble-averaged turbulent consumption flame speed versus curvature shown with (*a, c*) PDF plots and (*b, d*) deweighted plots, at f_0 = 1250 Hz at (*a, b*) $u'/u_{x,0}$ = 33.5%, $u_{x,0}$ = 3.7 m/s; (*c, d*) $u'/u_{x,0}$ = 22.0%, $u_{x,0}$ = 4.4 m/s.

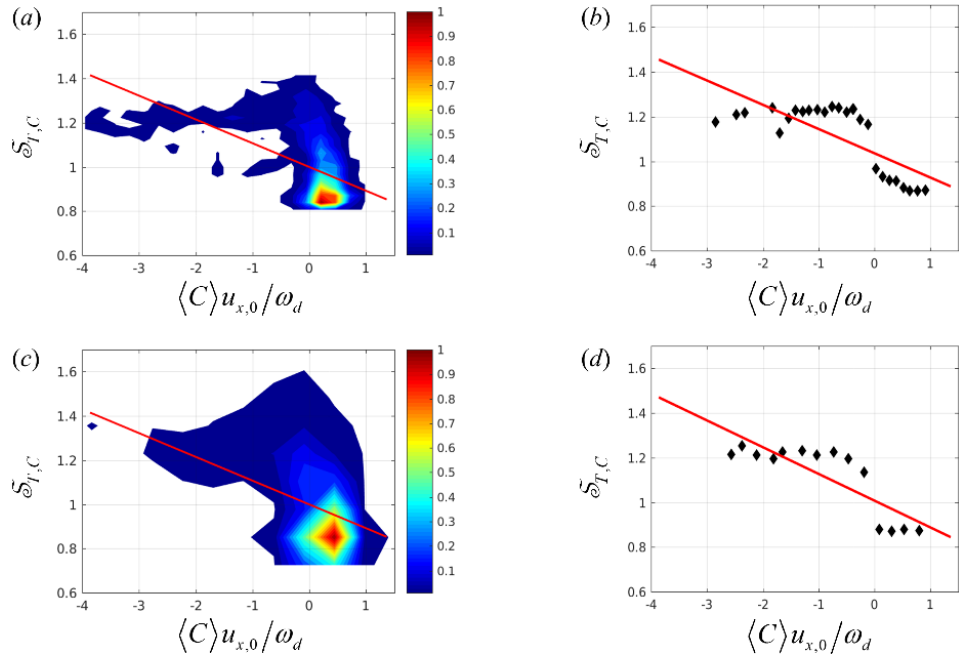

Figure I.21. Normalized ensemble-averaged turbulent consumption flame speed versus curvature shown with (*a, c*) PDF plots and (*b, d*) deweighted plots, at f_0 = 1250 Hz at (*a, b*) $u'/u_{x,0}$ = 7.6%, $u_{x,0}$ = 8.0 m/s; (*c, d*) $u'/u_{x,0}$ = 10.4%, $u_{x,0}$ = 8.0 m/s.

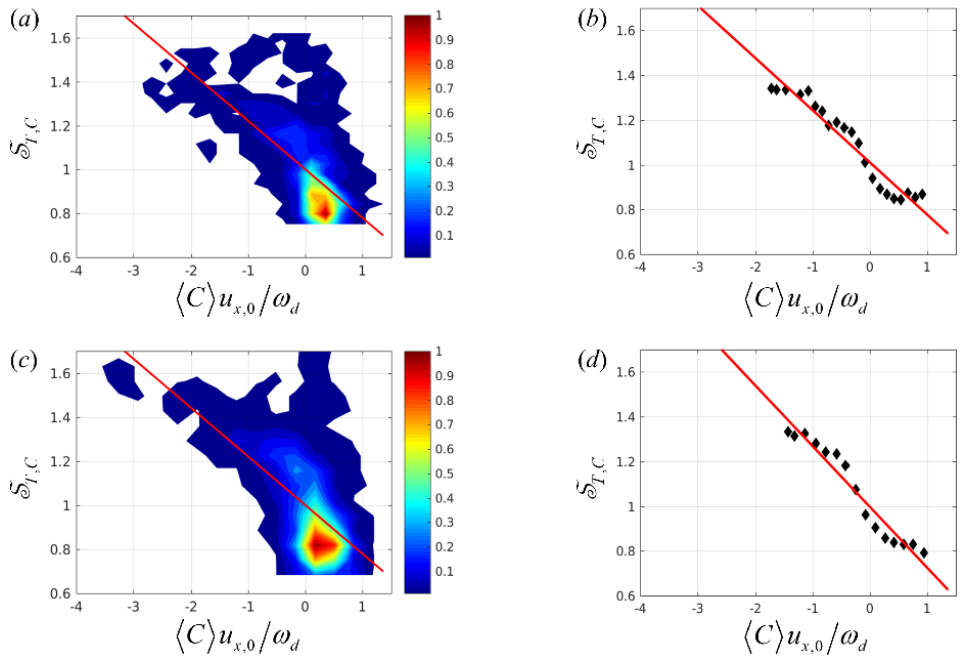

Figure I.22. Normalized ensemble-averaged turbulent consumption flame speed versus curvature shown with (*a, c*) PDF plots and (*b, d*) deweighted plots, at f_0 = 1250 Hz at (*a, b*) $u'/u_{x,0}$ = 14.8%, $u_{x,0}$ = 7.8 m/s; (*c, d*) $u'/u_{x,0}$ = 13.2%, $u_{x,0}$ = 7.7 m/s.

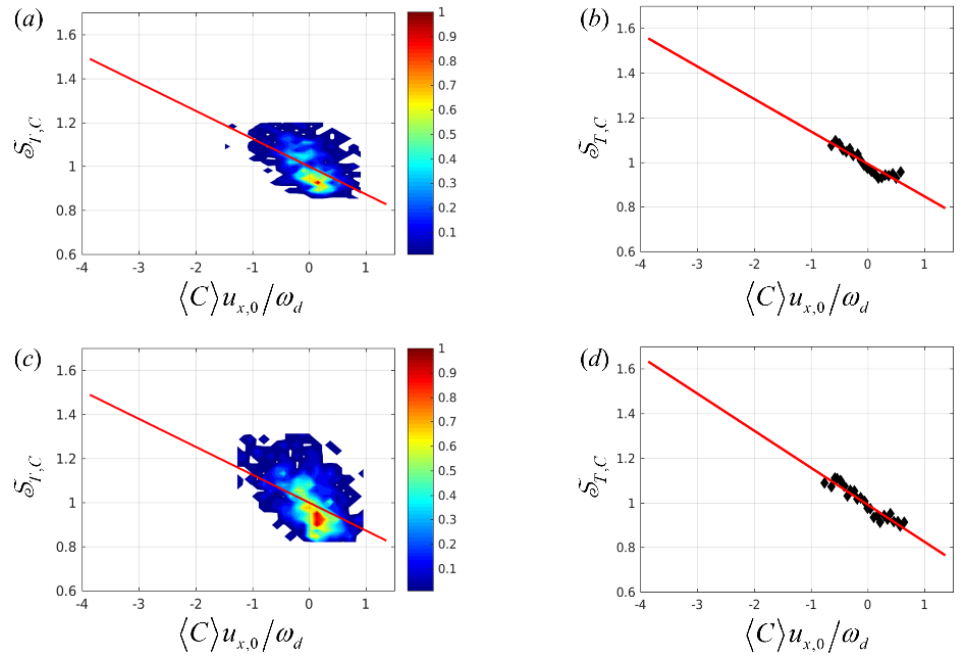

Figure I.23. Normalized ensemble-averaged turbulent consumption flame speed versus curvature shown with (*a, c*) PDF plots and (*b, d*) deweighted plots, at f_0 = 1250 Hz at (*a, b*) $u'/u_{x,0}$ = 25.8%, $u_{x,0}$ = 7.1 m/s; (*c, d*) $u'/u_{x,0}$ = 22.0%, $u_{x,0}$ = 7.3 m/s.

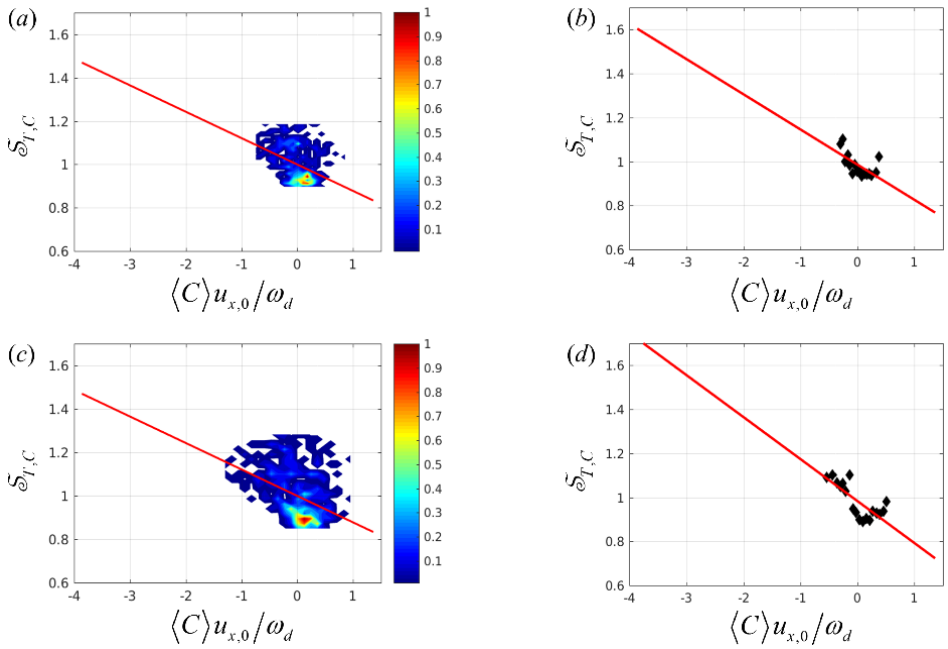

Figure I.24. Normalized ensemble-averaged turbulent consumption flame speed versus curvature shown with (*a, c*) PDF plots and (*b, d*) deweighted plots, at f_0 = 1250 Hz at (*a, b*) $u'/u_{x,0}$ = 32.1%, $u_{x,0}$ = 6.2 m/s; (*c, d*) $u'/u_{x,0}$ = 24.3%, $u_{x,0}$ = 7.2 m/s.

REFERENCES

1. Shin, D.H. and Lieuwen, T.C., *Flame wrinkle destruction processes in harmonically forced, turbulent premixed flames.* Journal of Fluid Mechanics, 2013. **721**: p. 484-513.

2. Berna, F., Goldberg, P., Horwitz, L.K., Brink, J., Holt, S., Bamford, M., and Chazan, M., *Microstratigraphic evidence of in situ fire in the Acheulean strata of Wonderwerk Cave, Northern Cape province, South Africa.* Proceedings of the National Academy of Sciences, 2012. **109**(20): p. E1215–E1220.

3. Choi, C. *History Of Fire Milestone, One Million Years Old, Discovered In Homo Erectus' Wonderwerk Cave*. 2012 cited 2016; Available from: http://www.huffingtonpost.com/2012/04/02/history-fire-million-homo-erectus_n_1397810.html.

4. Radivojević, M., Rehren, T., Pernicka, E., Šljivar, D., Brauns, M., and Borić, D., *On the origins of extractive metallurgy: new evidence from Europe.* Journal of Archaeological Science, 2010. **37**(11): p. 2775-2787.

5. Brinley, T., *The Industrial Revolution and the Atlantic Economy : Selected Essays (1)*. 2002, London, US: Routledge.

6. *The World's First Industrial Gas Turbine Set at Neuchâtel (1939)*. 1988, ASME: New York, NY.

7. NASA. *Engines*. 2016 5/17/2016; Available from: https://www.grc.nasa.gov/www/k-12/UEET/StudentSite/engines.html.

8. *MTT Motorcycles*. 2015 5/17/2016; Available from: http://marineturbine.com/motorcycles/.

9. Turns, S.R., *An Introduction to Combustion, 3rd Ed.* 2012, New York: McGraw-Hill.

10. McKinney, R. and Hoke, J., *Aero Gas Turbine Combustion: Metrics, Constraints, and System Interactions*, in *Gas Turbine Emissions*, T. Lieuwen and V. Yang, Editors. 2013, Cambridge University Press: New York.

11. Gokulakrishnan, P. and Klassen, M., *NOx and CO Formation and Control*, in *Gas Turbine Emissions*, T. Lieuwen and V. Yang, Editors. 2013, Cambridge University Press: New York.

12. *Nitrogen Oxides (NOx), Why and How They are Controlled*, O.o.A.Q.P.a.S. Clean Air Technology Center (MD-12), Editor. 1999, Unisted State Environmental Protection Agency: Research Triangle Park, NC.

13. Skalska, K., Miller, J.S., and Ledakowicz, S., *Trends in NOx Abatement: A review.* Science of The Total Environment, 2010. **408**(19): p. 3976-3989.

14. *Criteria Air Pollutants*. 2016 6.21.16; Available from: https://www.epa.gov/criteria-air-pollutants/naaqs-table#2.

15. *Air Quality Standards*. 2016 6/21/16; Available from: http://ec.europa.eu/environment/air/quality/standards.htm.

16. *China Adopts World-Class Pollutant Emissions Standards for Coal Power Plants*. 2012; Available from: http://www.chinafaqs.org/files/chinainfo/China%20FAQs%20Emission%20Standards%20v1.4_0.pdf.

17. *Nitrogen Dioxide: National Trends in Nitrogen Dioxide Levels*. 2016; Available from: https://www3.epa.gov/airtrends/nitrogen.html.

18. Rutar, T., Lee, J.C.Y., Dagaut, P., Malte, P.C., and Byrne, A.A., *NOx formation pathways in lean-premixed-prevapourized combustion of fuels with carbon-to-hydrogen ratio between 0.25 and 0.88.* Proceedings of the Institution of Mechanical Engineers, Part A: Journal of Power and Energy, 2007. **221**(3): p. 387-398.

19. Myerson, A.L., *The reduction of nitric oxide in simulated combustion effluents by hydrocarbon-oxygen mixtures.* Symposium (International) on Combustion, 1975. **15**(1): p. 1085-1092.

20. Maghon, H., Kreutzer, A., and Termuehlen, H., *The V84 Gas Turbine Designed for Base-Load and Peaking Duty.* Proceedings of the American Power Conference, 1988. **60**: p. 218-228.

21. McDonell, V. and Klein, M., *Ground-Based Gas Turbine Combustion: Metrics, Constraints, and System Interactions*, in *Gas Turbine Emissions*, T. Lieuwen and V. Yang, Editors. 2013, Cambridge University Press: New York.

22. Amato, A., Seitzman, J., and Lieuwen, T., *Emissions from Oxyfueled or High-Exhaust Gas Recirculation Turbines*, in *Gas Turbine Emissions*, T. Lieuwen and V. Yang, Editors. 2013, Cambridge University Press: New York.

23. Rokke, P.E., Hustad, J.E., Rokke, N.A., and Svendsgaard, O.B. *Technology update on gas turbine dual fuel, dry low emission combustion systems*. in *ASME Turbo Expo 2003, collocated with the 2003 International Joint Power Generation Conference*. 2003. American Society of Mechanical Engineers.

24. Huang, Y. and Yang, V., *Dynamics and stability of lean-premixed swirl-stabilized combustion.* Progress in Energy and Combustion Science, 2009. **35**(4): p. 293-364.

25. Hassa, C., *Partially Premixed and Premixed Aero Combustors*, in *Gas Turbine Emissions*, T. Lieuwen and V. Yang, Editors. 2013, Cambridge University Press: New York.

26. Lieuwen, T.C. and Yang, V., eds. *Combustion Instabilities in Gas Turbine Engines: Operational Experience, Fundamental Mechanisms, and Modeling*. Vol. 210. 2005, American Institute of Aeronautics and Astronautics. 659.

27. Lieuwen, T., *Modeling Premixed Combustion-Acoustic Wave Interactions: A Review*. Journal of Propulsion and Power, 2003. **19**(5): p. 765-781.

28. Poinsot, T. and Veynante, D., *Theoretical and Numerical Combustion*. 2005, Philadelphia: RT Edwards, Inc. 522.

29. Lieuwen, T.C., *Unsteady Combustor Physics*. 2012: Cambridge University Press. 488.

30. Candel, S., *Combustion dynamics and control: Progress and challenges.* Proceedings of the Combustion Institute, 2002. **29**(1): p. 1-28.

31. Balachandran, R., Ayoola, B.O., Kaminski, C.F., Dowling, A.P., and Mastorakos, E., *Experimental investigation of the nonlinear response of turbulent premixed flames to imposed inlet velocity oscillations.* Combustion and Flame, 2005. **143**(1–2): p. 37-55.

32. Magri, L. and Juniper, M.P., *A Theoretical approach for passive control of thermoacoustic oscillations: application to ducted flames.* Journal of Engineering for Gas Turbines and Power, 2013. **135**(9): p. 091604.

33. Kabiraj, L. and Sujith, R.I., *Nonlinear self-excited thermoacoustic oscillations: intermittency and flame blowout.* Journal of Fluid Mechanics, 2012. **713**: p. 376-397.

34. Tyndall, J., *On the Sounds Produced by the Combustion of Gases in Tubes.* Philosophical Magazine, Ser.4, 1857. **13**: p. 473-479.

35. LeConte, J., *On the Influence of Musical Sounds on the Flame of a Jet of Coal-Gas.* Philosophical Magazine, Ser.4, 1858. **15**: p. 235-239.

36. Rayleigh, L., *The Explanation of Certain Acoustical Phenomena.* Nature, 1878. **18**(455): p. 319-321.

37. Oefelein, J.C. and Yang, V., *Comprehensive review of liquid-propellant combustion instabilities in F-1 engines.* Journal of Propulsion and Power, 1993. **9**(5): p. 657-677.

38. Blomshield, F., *Historical perspective of combustion instability in motors: Case studies.* 37th Joint Propulsion Conference and Exhibit, 2001.

39. Ingard, U. and Singhal, V.K., *Effect of flow on the acoustic resonances of an open-ended duct.* The Journal of the Acoustical Society of America, 1975. **58**(4): p. 788-793.

40. Lieuwen, T., *Analysis of acoustic wave interactions with turbulent premixed flames.* Proceedings of the Combustion Institute, 2002. **29**(2): p. 1817-1824.

41. Lieuwen, T., Rajaram, R., Neumeier, Y., and Nair, S., *Measurements of incoherent acoustic wave scattering from turbulent premixed flames.* Proceedings of the Combustion Institute, 2002. **29**(2): p. 1809-1815.

42. Ducruix, S., Schuller, T., Durox, D., and Candel, S., *Combustion dynamics and instabilities: Elementary coupling and driving mechanisms.* Journal of Propulsion and Power, 2003. **19**(5): p. 722-734.

43. Strahle, W., *On combustion generated noise.* Journal of Fluid Mechanics, 1971. **49**(2): p. 399-414.

44. Hegde, U.G., Reuter, D., and Zinn, B.T., *Sound generation by ducted flames.* AIAA Journal, 1988. **26**(5): p. 532-537.

45. Marble, F.E. and Candel, S.M., *Acoustic disturbance from gas non-uniformities convected through a nozzle.* Journal of Sound and Vibration, 1977. **55**(2): p. 225-243.

46. Lieuwen, T. and Zinn, B.T., *The role of equivalence ratio oscillations in driving combustion instabilities in low NOx gas turbines.* Symposium (International) on Combustion, 1998. **27**(2): p. 1809-1816.

47. Poinsot, T., Veynante, D., Bourienne, F., Candel, S., Esposito, E., and Surget, J., *Initiation and suppression of combustion instabilities by active control.* Symposium (International) on Combustion, 1989. **22**(1): p. 1363-1370.

48. Williams, F.A., *Combustion Theory*. 2nd ed. Combustion Science and Engineering Series, ed. F.A. Williams. 1985, Menlo Park: Benjamin/Cummings Publishing Company. 665.

49. Schuller, T., Durox, D., and Candel, S., *Dynamics of and noise radiated by a perturbed impinging premixed jet flame.* Combustion and Flame, 2002. **128**(1–2): p. 88-110.

50. Fureby, C., *A computational study of combustion instabilities due to vortex shedding.* Proceedings of the Combustion Institute, 2000. **28**(1): p. 783-791.

51. Schadow, K.C. and Gutmark, E., *Combustion instability related to vortex shedding in dump combustors and their passive control.* Progress in Energy and Combustion Science, 1992. **18**(2): p. 117-132.

52. Petersen, R.E. and Emmons, H.W., *Stability of laminar flames.* Physics of Fluids (1958-1988), 1961. **4**(4): p. 456-464.

53. Preetham, Santosh, H., and Lieuwen, T., *Dynamics of laminar premixed flames forced by harmonic velocity disturbances.* Journal of Propulsion and Power, 2008. **24**(6): p. 1390-1402.

54. Boyer, L. and Quinard, J., *On the dynamics of anchored flames.* Combustion and Flame, 1990. **82**(1): p. 51-65.

55. Fleifil, M., Annaswamy, A.M., Ghoneim, Z.A., and Ghoneim, A.F., *Response of a laminar premixed flame to flow oscillations: A kinematic model and thermoacoustic instability results.* Combustion and Flame, 1996. **106**: p. 487-510.

56. Shanbhogue, S., Shin, D.-H., Hemchandra, S., Plaks, D., and Lieuwen, T., *Flame-sheet dynamics of bluff-body stabilized flames during longitudinal acoustic forcing.* Proceedings of the Combustion Institute, 2009. **32**(2): p. 1787-1794.

57. Shin, D.-H. and Lieuwen, T., *Flame wrinkle destruction processes in harmonically forced, laminar premixed flames.* Combustion and Flame, 2012. **159**(11): p. 3312-3322.

58. Matalon, M., *Flame dynamics.* Proceedings of the Combustion Institute, 2009. **32**(1): p. 57-82.

59. Shin, D.-H., Plaks, D.V., Lieuwen, T., Mondragon, U.M., Brown, C.T., and McDonell, V.G., *Dynamics of a longitudinally forced, bluff body stabilized flame.* Journal of Propulsion and Power, 2011. **27**(1): p. 105-116.

60. Wang, H.Y., Law, C.K., and Lieuwen, T., *Linear response of stretch-affected premixed flames to flow oscillations.* Combustion and Flame, 2009. **156**(4): p. 889-895.

61. Ducruix, S., Durox, D., and Candel, S., *Theoretical and experimental determination of the transfer function of a laminar premixed flame.* Proceedings of the Combustion Institute, 2000. **28**(1): p. 765-773.

62. Kashinath, K., Hemchandra, S., and Juniper, M.P., *Nonlinear thermoacoustics of ducted premixed flames: The influence of perturbation convection speed.* Combustion and Flame, 2013. **160**(12): p. 2856-2865.

63. Humphrey, L., Acharya, V., Shin, D.H., and Lieuwen, T., *Technical note: Coordinate systems and integration limits for global flame transfer function calculations.* International Journal of Spray and Combustion Dynamics, 2014. **6**(4): p. 411-416.

64. Santosh, H. and Sujith, R., *Kinematic coupling effects on heat-release transfer function of a premixed flame.* Journal of Propulsion and Power, 2005. **21**(4): p. 591-599.

65. Schuller, T., Durox, D., and Candel, S., *A unified model for the prediction of laminar flame transfer functions: comparisons between conical and V-flame dynamics.* Combustion and Flame, 2003. **134**(1–2): p. 21-34.

66. Markstein, G.H., *Theory of Flame Propagation*, in *Non-steady Flame Propgation*, G.H. Markstein, Editor. 1964, Pergammon Press Ltd.: New York.

67. Jones, B., Lee, J.G., Quay, B.D., and Santavicca, D.A., *Flame response mechanisms due to velocity perturbations in a lean premixed gas turbine combustor.* Journal of Engineering for Gas Turbines and Power, 2011. **133**(2): p. 021503-021503.

68. Lipatnikov, A.N. and Sathiah, P., *Effects of turbulent flame development on thermoacoustic oscillations.* Combustion and Flame, 2005. **142**(1–2): p. 130-139.

69. Acharya, V., Emerson, B., Mondragon, U., Shin, D.-H., Brown, C., McDonell, V., and Lieuwen, T., *Velocity and flame wrinkling characteristics of a transversely forced, bluff-body stabilized flame, Part II: Flame response modeling and comparison with measurements.* Combustion Science and Technology, 2013. **185**(7): p. 1077-1097.

70. Acharya, V., Malanoski, M., Aguilar, M., and Lieuwen, T., *Dynamics of a transversely excited swirling, lifted flame: Flame response modeling and comparison with experiments.* Journal of Engineering for Gas Turbines and Power, 2014. **136**(5): p. 051503(1)-051503(10).

71. De Goey, L. and ten Thije Boonkkamp, J., *A mass-based definition of flame stretch for flames with finite thickness.* Combustion science and technology, 1997. **122**(1-6): p. 399-405.

72. Karpov, V.P., Lipatnikov, A.N., and Wolanski, P., *Finding the markstein number using the measurements of expanding spherical laminar flames.* Combustion and Flame, 1997. **109**(3): p. 436-448.

73. Bechtold, J. and Matalon, M., *The dependence of the Markstein length on stoichiometry.* Combustion and Flame, 2001. **127**(1-2): p. 1906-1913.

74. Groot, G., Van Oijen, J., De Goey, L., Seshadri, K., and Peters, N., *The effects of strain and curvature on the mass burning rate of premixed laminar flames.* Combustion Theory and Modelling, 2002. **6**(4): p. 675-695.

75. Chung, S.H. and Law, C.K., *An integral analysis of the structure and propagation of stretched premixed flames.* Combustion and Flame, 1988. **72**(3): p. 325-336.

76. Clavin, P. and Williams, F.A., *Effects of molecular diffusion and of thermal expansion on the structure and dynamics of premixed flames in turbulent flows of large scale and low intensity.* Journal of Fluid Mechanics, 1982. **116**: p. 251-282.

77. Mikolaitis, D.W., *The interaction of flame curvature and stretch, part 1: The concave premixed flame.* Combustion and Flame, 1984. **57**(1): p. 25-31.

78. Im, H.G. and Chen, J.H., *Effects of flow transients on the burning velocity of laminar hydrogen/air premixed flames.* Proceedings of the Combustion Institute, 2000. **28**(2): p. 1833-1840.

79. Lipatnikov, A.N. and Chomiak, J., *Molecular transport effects on turbulent flame propagation and structure.* Progress in Energy and Combustion Science, 2005. **31**(1): p. 1-73.

80. Abdel-Gayed, R., Bradley, D., Hamid, M., and Lawes, M. *Lewis number effects on turbulent burning velocity*. 1985. Elsevier.

81. Chen, J.H. and Im, H.G., *Correlation of flame speed with stretch in turbulent premixed methane/air flames.* Symposium (International) on Combustion, 1998. **27**(1): p. 819-826.

82. Echekki, T. and Chen, J.H., *Analysis of the contribution of curvature to premixed flame propagation.* Combustion and Flame, 1999. **118**(1-2): p. 308-311.

83. Gu, X.J., Haq, M.Z., Lawes, M., and Woolley, R., *Laminar burning velocity and Markstein lengths of methane–air mixtures.* Combustion and Flame, 2000. **121**(1–2): p. 41-58.

84. Tseng, L.K., Ismail, M.A., and Faeth, G.M., *Laminar burning velocities and Markstein numbers of hydrocarbonair flames.* Combustion and Flame, 1993. **95**(4): p. 410-426.

85. Law, C.K. and Sung, C.J., *Structure, aerodynamics, and geometry of premixed flamelets.* Progress in Energy and Combustion Science, 2000. **26**(4–6): p. 459-505.

86. Tennekes, H. and Lumley, J., *A first course in turbulence*. 1972: The MIT press.

87. Hinze, J., *Turbulence*. 1975, New York: McGraw-Hill.

88. Borghi, R., *On the structure and morphology of turbulent premixed flames.* Recent advances in the aerospace sciences(A 85-47304 23-31). New York, Plenum Press, 1985, 1985: p. 117-138.

89. Peters, N., *Turbulent Combustion*. Cambridge Monographs on Mechanics, ed. G.K. Batchelor. 2000, Cambridge: Cambridge University Press. 299.

90. Peters, N., *The turbulent burning velocity for large-scale and small-scale turbulence.* Journal of Fluid Mechanics, 1999. **384**: p. 107-132.

91. Meneveau, C. and Poinsot, T., *Stretching and quenching of flamelets in premixed turbulent combustion.* Combustion and Flame, 1991. **86**(4): p. 311-332.

92. Driscoll, J.F., *Turbulent Premixed Combustion: Flamelet Structure and its Effect on Turbulent Burning Velocities.* Progress in Energy and Combustion Science, 2008. **34**(1): p. 91-134.

93. Bradley, D., *How Fast Can We Burn?* Proceedings of the Combustion Institute, 1992. **24**(1): p. 247-262.

94. Abdel-Gayed, R., Bradley, D., and Lung, F., *Combustion regimes and the straining of turbulent premixed flames.* Combustion and Flame, 1989. **76**(2): p. 213-218.

95. Hemchandra, S., Peters, N., and Lieuwen, T., *Heat release response of acoustically forced turbulent premixed flames—role of kinematic restoration.* Proceedings of the Combustion Institute, 2011. **33**(1): p. 1609-1617.

96. Hemchandra, S., Preetham, and Lieuwen, T.C., *Response of turbulent premixed flames to harmonic acoustic forcing.* Proceedings of the Combustion Institute, 2007. **31**(1): p. 1427-1434.

97. Shin, D.H., *Premixed Flame Kinematics in a Harmonically Oscillating Velocity Field*, in *School of Aerospace Engineering*. 2012, Georgia Institute of Techology.

98. Damköhler, G., *The effect of turbulence on the flame velocity in gas mixtures.* Zeitschrift Electrochem, 1940. **46**: p. 601-626.

99. Lipatnikov, A.N. and Chomiak, J., *Turbulent flame speed and thickness: phenomenology, evaluation, and application in multi-dimensional simulations.* Progress in Energy and Combustion Science, 2002. **28**(1): p. 1-74.

100. Matalon, M. and Creta, F., *The "turbulent flame speed" of wrinkled premixed flames.* Comptes Rendus Mécanique, 2012. **340**(11–12): p. 845-858.

101. Verma, S. and Lipatnikov, A.N., *Does sensitivity of measured scaling exponents for turbulent burning velocity to flame configuration prove lack of generality of notion of turbulent burning velocity?* Combustion and Flame, 2016. **173**: p. 77-88.

102. Bell, J., Day, M., Shepherd, I., Johnson, M., Cheng, R., Grcar, J., Beckner, V., and Lijewski, M., *Numerical simulation of a laboratory-scale turbulent V-flame.* Proceedings of the National Academy of Sciences of the United States of America, 2005. **102**(29): p. 10006.

103. Zimont, V.L. and Battaglia, V., *Joint RANS/LES Approach to Premixed Flame Modelling in the Context of the TFC Combustion Model.* Flow, Turbulence and Combustion, 2006. **77**(1): p. 305-331.

104. Zimont, V., *Gas premixed combustion at high turbulence. Turbulent flame closure combustion model.* Experimental Thermal and Fluid Science, 2000. **21**(1-3): p. 179-186.

105. Bray, K.N.C. and Moss, J.B., *A unified statistical model of the premixed turbulent flame.* Acta Astronautica, 1977. **4**(3): p. 291-319.

106. Bray, K.N.C., Libby, P.A., and Moss, J.B., *Unified modeling approach for premixed turbulent combustion—Part I: General formulation.* Combustion and Flame, 1985. **61**(1): p. 87-102.

107. Marble, F.E. and Broadwell, J.E., *The Coherent Flame Model for Turbulent Chemical Reactions*, in *Project Squid*. 1977.

108. Bray, K. and Cant, R., *Some applications of Kolmogorov's turbulence research in the field of combustion.* Proceedings: Mathematical and Physical Sciences, 1991. **434**(1890): p. 217-240.

109. Lipatnikov, A. and Chomiak, J., *Global stretch effects in premixed turbulent combustion.* Proceedings of the Combustion Institute, 2007. **31**(1): p. 1361-1368.

110. Bradley, D., Haq, M.Z., Hicks, R.A., Kitagawa, T., Lawes, M., Sheppard, C.G.W., and Woolley, R., *Turbulent burning velocity, burned gas distribution, and associated flame surface definition.* Combustion and Flame, 2003. **133**(4): p. 415-430.

111. Cuquel, A., Durox, D., and Schuller, T., *Impact of flame base dynamics on the non-linear frequency response of conical flames.* Comptes Rendus Mécanique, 2013. **341**(1–2): p. 171-180.

112. Humphrey, L.J., Acharya, V.S., Shin, D.-H., and Lieuwen, T.C., *Modeling the Response of Turbulent Flames to Harmonic Forcing.* Combustion Science and Technology, 2017. **189**(2): p. 187-212.

113. Matalon, M. and Matkowsky, B.J., *Flames as gasdynamic discontinuities.* Journal of Fluid Mechanics Digital Archive, 1982. **124**(1): p. 239-259.

114. Williams, F.A., *Turbulent combustion*, in *The Mathematics of Combustion*, J.D. Buckmaster, Editor. 1985, Society for Industrial and Applied Mathematics: Philadelphia. p. 267-294.

115. Kerstein, A.R., Ashurst, W.T., and Williams, F.A., *Field equation for interface propagation in an unsteady homogeneous flow field.* Physical Review A, 1988. **37**(7): p. 2728.

116. Peters, N., Wenzel, H., and Williams, F.A., *Modification of the turbulent burning velocity by gas expansion.* Proceedings of the Combustion Institute, 2000. **28**(1): p. 235-243.

117. Dowling, A.P., *A kinematic model of a ducted flame.* Journal of Fluid Mechanics, 1999. **394**: p. 51-72.

118. Lieuwen, T., *Nonlinear kinematic response of premixed flames to harmonic velocity disturbances.* Proceedings of the Combustion Institute, 2005. **30**(2): p. 1725-1732.

119. Barkley, D., *Linear analysis of the cylinder wake mean flow.* Europhysics Letters, 2006. **75**(5): p. 750-756.

120. Meliga, P., Pujals, G., and Serre, É., *Sensitivity of 2-D turbulent flow past a D-shaped cylinder using global stability.* Physics of Fluids, 2012. **24**(6).

121. Mettot, C., Sipp, D., and Bézard, H., *Quasi-laminar stability and sensitivity analyses for turbulent flows: Prediction of low-frequency unsteadiness and passive control.* Physics of Fluids, 2014. **26**(4).

122. Lee, D.-H. and Lieuwen, T.C., *Premixed flame kinematics in a longitudinal acoustic field.* Journal of propulsion and power, 2003. **19**(5): p. 837-846.

123. Creta, F., Fogla, N., and Matalon, M., *Turbulent propagation of premixed flames in the presence of Darrieus–Landau instability.* Combustion Theory and Modelling, 2011. **15**(2): p. 267-298.

124. Tammisola, O. and Juniper, M.P., *Coherent structures in a swirl injector at Re = 4800 by nonlinear simulations and linear global modes.* Journal of Fluid Mechanics, 2016. **792**: p. 620-657.

125. Kornilov, V.N., Schreel, K.R.A.M., and de Goey, L.P.H., *Experimental assessment of the acoustic response of laminar premixed Bunsen flames.* Proceedings of the Combustion Institute, 2007. **31**(1): p. 1239-1246.

126. Kanthasamy, C., Raghavan, V., and Srinivasan, K., *Effect of low frequency burner vibrations on the characteristics of premixed flames.* International Journal of Spray and Combustion Dynamics, 2012. **4**(3): p. 239-254.

127. Dupont, T.F. and Liu, Y., *Back and forth error compensation and correction methods for Semi-Lagrangian schemes with application to level set interface computations.* Mathematics of Computation, 2007. **76**(258): p. 647-668.

128. Pope, S., *Turbulent flows*. 2000, New York: Cambridge Univ Press.

129. Jiang, G.-S. and Peng, D., *Weighted ENO schemes for Hamilton-Jacobi equations.* SIAM Journal on Scientific Computing, 2000. **21**(6): p. 2126-2143.

130. Shin, D.H., Lieuwen, T.C., and Shanbhogue, S., *Premixed flame kinematics in an axially decaying, harmonically oscillating vorticity field*, in *44th AIAA/ASME/SAE/ASEE Joint Propulsion Conference & Exhibit*. 2008, American Institute of Aeronautics and Astronautics.

131. Preetham, T., Thumuluru, S.K., Santosh, H., and Lieuwen, T., *Linear response of laminar premixed flames to flow oscillations: Unsteady stretch effects.* Journal of Propulsion and Power, 2010. **26**(3): p. 524-532.

132. Kee, R.J., Rupley, F.M., Miller, J.A., Coltrin, M.E., Grcar, J.F., Meeks, E., Moffat, H.K., Lutz, A.E., Lewis, G.D.-., Smooke, M.D., Warnatz, J., Evans, G.H., Larson, R.S., Mitchell, R.E., Petzold, L.R., Reynolds, W.C., Caracotsios, M., Stewart, W.E., Glarborg, P., Wang, C., and Adigun, O., *CHEMKIN 10112*. 2011, Reaction Design: San Diego.

133. Smith, G.P., Golden, D.M., Frenklach, M., Moriarty, N.W., Eiteneer, B., Goldenberg, M., Bowman, C.T., Hanson, R.K., Song, S., Gardiner Jr, W.C., Lissianski, V.V., and Qin, Z. *GRI-Mech 3.0*. 2016; Available from: http://www.me.berkeley.edu/gri_mech/.

134. Marshall, A., Venkateswaran, P., Noble, D., Seitzman, J., and Lieuwen, T., *Development and characterization of a variable turbulence generation system.* Experiments in Fluids, 2011. **51**(3): p. 611-620.

135. LaVision. *FlowMaster PIV/ PTV-systems*. 2016; Available from: http://www.lavision.de/en/products/flowmaster/index.php.

136. Otsu, N., *A Threshold Selection Method from Gray-Level Histograms.* IEEE Transactions On Systems, Man, And Cybernetics, 1979. **9**(1): p. 62-66.

137. Wheeler, A.J. and Ganji, A.R., *Introduction to engineering experimentation*. 3 ed. 1996: Prentice Hall New Jersey.

138. Lipatnikov, A., *Fundamentals of Premixed Turbulent Combustion*. 2012: CRC Press. 548.

139. Ling, L., Tianyi, Z., Lawrence, K., and Wei, Z., *Ordinary least square regression, orthogonal regression, geometric mean regression and their applications in aerosol science.* Journal of Physics: Conference Series, 2007. **78**(1): p. 012084.

140. Gran, I.R., Echekki, T., and Chen, J.H., *Negative flame speed in an unsteady 2-D premixed flame: A computational study.* Symposium (International) on Combustion, 1996. **26**(1): p. 323-329.

141. Sohrab, S.H., Ye, Z.Y., and Law, C.K., *An experimental investigation on flame interaction and the existence of negative flame speeds.* Symposium (International) on Combustion, 1985. **20**(1): p. 1957-1965.

142. Lipatnikov, A.N., Li, W.Y., Jiang, L.J., and Shy, S.S., *Does Density Ratio Significantly Affect Turbulent Flame Speed?* Flow, Turbulence and Combustion, 2017: p. 1-20.